

Cylindrical Energy Analyzer for Heavy Ion Beam Diagnostics

Ridhima Sharma

Universidad Carlos III de Madrid

A dissertation submitted in partial fulfilment of the requirements for
the degree of Doctor of Philosophy in Plasmas y Fusion Nuclear

Supervisors

Doctor Artur Jorge Louzeiro Malaquias

Doctor Carlos Hidalgo

Promotors

Prof. Horácio Joao Matos Fernandes

Prof. José Ramón Martín Solís

June 2020

This thesis is distributed under license “Creative Commons **Attribution – Non Commercial – Non Derivatives**”.



FACSIMILE COVER THESIS



Universidad
Carlos III de Madrid



**Universidade de Lisboa
Instituto Superior Técnico (IST)**

Universidad Carlos III de Madrid

**JOINT RESEARCH DOCTORATE IN FUSION SCIENCE AND
ENGINEERING**

Cycle XXXI

And

**ERASMUS MUNDUS International Doctoral College in Fusion
Science and Engineering**

**Cylindrical Energy Analyzer for Heavy Ion Beam
Diagnostics**

Promotor at Instituto Superior Técnico (Home Institution): Prof. Horácio Fernandes
Supervisor at Instituto Superior Técnico (Home Institution): Prof. Artur Malaquias

Promotor at Universidad Carlos III de Madrid (Host Institution): Prof. José Ramón Martín Solís
Supervisor at Universidad Carlos III de Madrid (Host Institution): Prof. Carlos Hidalgo

Ph.D. student: Ridhima Sharma

Lisbon, June 2020

Resumo

O estudo de fenómenos de transporte e turbulência em plasmas é fundamental para a compreensão e controle do confinamento de partículas e energia em máquinas de fusão nuclear do tipo ‘Tokamak’ ou ‘Stellarator’. O diagnóstico de feixe de iões pesados (DFIP) é uma ferramenta única que pode medir localmente várias quantidades de grande interesse tais como a densidade do plasma (n_e), o potencial do plasma (ϕ), a temperatura electrónica (T_e) e o campo magnético poloidal (B_p), ao longo de todo o raio do plasma com uma resolução espacial de alguns mm e até aos microsegundos de resolução temporal (centenas de kHz).

O objectivo da tese é o de desenvolver um Analizador Electroestático Cilíndrico de 90° (AEC- 90°) e demonstrar a sua capacidade para medir o potencial do plasma com uma resolução de energia aceitável (poucas dezenas de Volt). A geometria particular deste analisador electroestático foi escolhida por forma a permitir as medidas do potencial de plasma em paralelo com as medidas da densidade do plasma e campo magnético poloidal obtidos com o DFIP sem necessitar de se alterar a trajectoria do feixe sonda durante a descarga de plasma.

O trabalho apresentado versa a concepção, desenho e simulação (utilizando o código SIMION) de um analisador multi-canal do tipo AEC- 90° . A operação é baseada num modo inovador de desaceleração tirando partido do retardamento e focagem do feixe de prova por um campo electroestático apropriado aplicado à entrada do analisador. A operação no modo de desaceleração demonstrou vantagens significativas na resolução das medidas da energia do feixe e nas características de aberração angular quando comparado com o modo convencional de operação do AEC- 90° .

As previsões obtidas pela simulação foram verificadas experimentalmente por meio de um protótipo AEC- 90° com $\frac{1}{2}$ das dimensões lineares usando um feixe de electrões numa montagem dedicada a este fim. Uma unidade intermédia adicional, denominada modulo de entrada electroestático (MEE), responsável pela deflexão e focagem dos feixes secundários provenientes do plasma até à entrada do AEC- 90° , foi igualmente desenhada e otimizada no programa SIMION. A montagem combinada do MEE e do protótipo $\frac{1}{2}$ AEC- 90° foi instalada e comissionada no tokamak ISTTOK (Portugal) onde foram obtidas com sucesso as medidas do potencial no centro do plasma. O analisador foi calibrado usando um método indireto com o fim de determinar o valor absoluto do potencial do plasma.

A segunda parte desta tese compreende as experiências coduzidas pela autora na dupla Sonda de Feixe de Iões Pesados (SFIP) no ‘Stellarator’TJ-II na CIEMAT (Espanha). O trabalho desenvolvido no TJ-II demonstra a importância das medidas do perfil de potencial e densidade afim de melhor compreender o comportamento do plasma. As experiências foram desenvolvidas em torno de três objectivos: (i) Os perfis centrais do potencial do plasma foram investigados durante a polarização da periferia do plasma com o fim de identificar assimetrias, medindo com duas sondas SFIP separadas toroidalmente; (ii) Medições utilizando o SFIP de linhas de nível 2D do potencial de plasma e densidade e das suas flutuações num regime novo de rastreamento de energia, em plasmas de baixa densidade sustentados por ‘ECRH’; (iii) Medidas do perfil do potencial do plasma quando sujeito a aquecimento por feixes de neutros (FN) injectados em contra e em paralelo à corrente de plasma e sua comparação afim de investigar a correlação entre confinamento de partículas e injeção de feixes de neutros com as predições teóricas.

Palavras chave: *Diagnóstico de Feixe de Iões Pesados, analisador electrostático cilíndrico, medidas de transporte em plasmas, medição do potencial de plasma.*

Abstract

The study of plasma turbulence and transport is crucial to understand and control the particle and energy confinement in fusion devices such as tokamak or stellarators. The Heavy Ion Beam Diagnostic (HIBD) is a unique tool that can provide the local measurement of the quantities of interest such as plasma density (n_e), the plasma potential (ϕ), the electron temperature (T_e) and the poloidal magnetic field (B_p), along a radial scan in the plasma with a spatial resolution of several mm and down to the microsecond range temporal resolution (hundreds of kHz).

The aim of the thesis is to develop a high resolution 90° cylindrical energy analyzer (CEA) and demonstrate its capability to measure plasma potential with sufficient energy resolution (in the order of tens of Volt). The particular analyzer geometry is chosen to provide the plasma potential measurements along with the profiles of plasma density and poloidal magnetic field obtained by the HIBD without the need to scan the probing beam during the plasma discharge.

The present work covers the conceptualization, design and simulation (using SIMION code) of a multiple channel 90° CEA. The operation is based in an innovative deceleration mode which takes advantage of the beam retardation and focusing property of a customized electrostatic field at the input of the analyzer. The deceleration mode has demonstrated significant improvements in the beam energy measurements resolution and angle aberration characteristics as compared to conventional CEA operation.

The simulation predictions were verified by experimental results obtained by testing a half-size 90° CEA prototype with an electron beam installed in a dedicated test facility. An additional intermediate unit, named electrostatic input module (EIM), responsible to focus and deflect the secondary beams from plasma output to CEA input, was also designed and optimized in SIMION. The combined set-up of EIM and half-size 90° CEA prototype was installed and commissioned in ISTTOK tokamak (Portugal) to successfully obtain the measurements of plasma potential from the core. The analyzer has been calibrated using an ‘indirect calibration’ approach in order to determine the absolute plasma potential.

The second part of this thesis work covers the experiments performed by the author on the dual heavy ion beam probe (HIBP) at TJ-II stellarator at CIEMAT (Spain). The work at TJ-II investigates and demonstrates the significance of potential and density profile measurement to understand the behavior of the plasma. The experiments were developed around three experimental objectives: (i) The plasma core potential profiles were investigated during external plasma edge biasing in order to probe asymmetries by observing the plasma potential response measured by two toroidally separated HIBP’s; (ii) 2D poloidal contour plots of plasma potential and density and their fluctuations have been measured by HIBP in a new energy scanning mode in low density plasmas sustained by ECRH; (iii) The plasma potential profiles for plasmas heated by counter- and co- neutral beam current drive injection (NBI) are obtained and compared in order to correlate the fast particle confinement with NBI current drive injection as predicted theoretically.

Key words: *Heavy ion beam diagnostic, cylindrical energy analyzer, plasma transport measurements, plasma potential measurements*

Acknowledgment

I would like to start by expressing immense gratitude to my supervisor, Prof. Artur Malaquias. Thank you for the motivation and your constant feedback. Thank you for guiding me at every step of the thesis work. Your acknowledgment and appreciation of small achievements to milestones have been very supportive throughout the Ph.D. You have encouraged me to work harder while maintaining a healthy work-life balance. Muito obrigado por tudo!

I would like to thank my co-supervisor Dr. Igor Nedzelskiy for helping me throughout the thesis work. I consider myself fortunate to work under your supervision and learn from your expertise. The journey of developing simulations from scratch to experimental confirmations has been a very exciting and rewarding experience with you. Thank you for your constant efforts and endless ideas.

I would also express gratitude to my supervisor Dr. Carlos Hidalgo for mentoring the thesis work in Ciemat. Thank you for entertaining several doubts and explaining them in the easiest manner. Your assessment and evaluation of the results has been crucial for the thesis work. Thank you for your contagious motivation and endless encouragement.

I want to thank Prof. Alexander Melnikov for welcoming me in the HIBP team at TJ-II. Thank you for your great advices and nudging me to towards correct direction. I would also like to thank HIBP team at TJ-II for helping me constantly during the experimental campaign.

I would also like to thank Prof. Horácio Fernandes for coordinating the thesis work and your support as a promoter of this joint doctorate from Instituto Superior Técnico.

I would also like to express gratitude to José Ramón Martín Solís for his help as a promoter of this thesis representing University Carlos III de Madrid.

I would like to thank my colleagues at IPFN for providing a healthy work environment and a readily helping attitude. It would not have been possible to do without the support that I received from my colleagues and friends.

I would like to acknowledge that this work was supported by the European Commission in the framework of the Erasmus Mundus International Doctoral College in Fusion Science and Engineering (FUSION-DC). I would also like to acknowledge Fundação para a Ciência e a Tecnologia (FCT) and EuroFusion for the funding for latter part of this thesis work.

I want to thank my fiancé Carlos for his constant encouragement, support and cooking during this period. Last, but most importantly, I want to thank my parents for everything. Thank you for teaching me to be humble, patient and compassionate. Thank you for the strong support from miles away.

Published and Submitted Content

The Doctoral candidate has authored the following articles that have been published (or submitted) in a scientific journal. Sections of the following articles have been included in the thesis.

- R. Sharma, I.S. Nedzelskiy, A. Malaquias and R. Henriques; Characterization of modified 90° cylindrical energy analyzer with electron beam. *Journal of instrumentation* **15** C01018 (2020)
- R. Sharma, I.S. Nedzelskiy, A. Malaquias and R.B. Henriques; Design and optimization of the electrostatic input module for the ISTTOK Tokamak HIBD cylindrical energy analyzer. *Journal of instrumentation* **12** C11018 (2017)
- R. Sharma, P.O. Khabanov, A.V. Melnikov, C. Hidalgo et.al; Measurements of 2D poloidal plasma profiles and fluctuations in ECRH plasmas using the Heavy Ion Beam Probe system in the TJ-II stellarator. *AIP physics of plasma* **27**, 062502 DOI: 10.1063/1.5142996 (2020)
- R. Sharma, I. S. Nedzelskiy, A. Malaquias, R. Henriques; Absolute plasma potential and fluctuations measurements by HIBD with 90° cylindrical energy analyzer on the ISTTOK tokamak. *Fusion Engineering and Design* (submitted).

The author has also co-authored in following peer-reviewed publications during the thesis work.

- I.S. Nedzelskiy, A. Malaquias, R. Sharma, R. Henriques; 90° cylindrical analyzer for the plasma potential fluctuations measurements by heavy ion beam diagnostic on the tokamak ISTTOK, *Fusion Engineering and Design*, 123 DOI 10.1016/j.fusengdes.2017.03.097 (2016)
- A. Malaquias, R.B Henriques, C. Silva, H. Figueiredo, I.S. Nedzelskiy, H. Fernandes, R. Sharma, V. V. Plyusnin, Edge electrode biasing assisted AC operation in ISTTOK. *Nuclear Fusion* **57** 116002 (2017)
- I.S. Nedzelskiy , A. Malaquias, R.B. Henriques, R. Sharma; Recent developments in the ISTTOK heavy ion beam diagnostic; Proceedings of the International Conference and School on Plasma Physics and Controlled Fusion Kharkov, Ukraine, September 12-15, 2016, *journal "Problems of Atomic Science and Technology"*, Series: Plasma Physics (2016) 106. 297-301.

Conferences participation

Conferences and events attended by the author during the thesis work are mentioned below.

- 3rd European Conference on Plasma Diagnostics ‘Characterization of modified 90° cylindrical energy analyzer with electron beam’ Poster, 6-9 May 2019 Lisbon (Portugal)

- Fusenet PhD event ‘Cylindrical Energy Analyzer for Heavy Ion Beam Diagnostics for measurements in tokamaks and stellarators’ oral presentation, *6-9 November 2018 ITER, Cadarache (France)*
- 45th European Physical Society Conference on Plasma Physics, ‘Poloidal 2D scans to investigate potential and density profiles in the TJ-II stellarator using Heavy Ion Beam Probing’, Poster, *2-6 July 2018; Prague (Czech republic)*
- 2nd European Conference on Plasma Diagnostics, ‘Design and optimization of the electrostatic input module for the ISTTOK Tokamak HIBD cylindrical energy analyzer’ Poster, *18-21 April 2017 Bordeaux (France)*.

Contents

Chapter 1	1
Introduction.....	1
1.1. Heavy ion beam probe.....	2
1.2. Heavy ion beam diagnostic at ISTTOK tokamak	6
1.2.1. HIBD ISTTOK.....	9
1.2.2. Schematics.....	7
1.2.3 Retrieving plasma parameters at ISTTOK HIBD	9
1.3. Relevance of plasma potential measurement for fusion plasma	11
1.4. Motivation for upgrading the ISTTOK HIBD	12
1.5. Thesis outline	13
Chapter 2.....	15
High resolution 90° Cylindrical Energy Analyzer	15
2.1. Introduction.....	15
2.2. Plasma potential measurements in other devices	15
2.2.1. 30° Proca-Green Analyzer.....	15
2.2.2. The 127° cylindrical analyzer.....	16
2.2.3. TOF energy analyzer.....	16
2.3. The 90° Cylindrical Energy Analyzer (CEA) for ISTTOK.....	17
2.3.1. Overview of the 90° Cylindrical Energy Analyzer.....	18
2.3.2. Normal mode operation of 90° CEA	20
2.4. CEA Deceleration mode operation	22
2.4.1. Characterization and optimized beam trajectories	23
2.4.2. Detector parameters for position Split-plate detection.....	24
2.5. The 3D Simulation of the analyzer	27
2.5.1. Guard rings: Design and optimization.....	28
2.5.2. Optimization of beam trajectories	30
2.6. Experimental Characterization of the CEA ½ size prototype	31
2.6.1. Experimental setup.....	31
2.6.2. Design of guard rings for the test prototype.....	32
2.6.3. Modified detection	34
2.6.4. Experimental Results.....	36
2.6.5. Experimental comparison between normal and deceleration operation modes	37
2.6.6. Analysis and comparison with simulations	39

2.7. Conclusions.....	39
Chapter 3	41
Electrostatic Input Module.....	41
3.1 Introduction.....	41
3.2 Electrostatic Input Module descriptions.....	42
3.2.1. Front detector	42
3.2.2. Cylindrical and parallel plates.....	42
3.2.3. Einzel lens	43
3.2.4. Back MCAD.....	44
3.3 Optimization: Geometry and operating voltages of the EIM internal components.....	44
3.3.1 Voltage at central and strip electrodes	45
3.3.2. Optimizing the distance from the entrance of CEA	45
3.3.3. Distance between the end guard plates and inner HV plates.....	45
3.3.4. Shape of the input aperture of the Einzel lens.....	45
3.4. Experimental Characterization of EIM in ISTTOK.....	47
3.4.1. Experimental set up.....	47
3.4.2. Experimental results.....	49
3.5. Conclusions.....	54
Chapter 4	55
Installation and commissioning of the detection system.....	55
4.1. Introduction.....	55
4.2. Experimental setup description	56
4.2.1. Electrostatic input module (EIM).....	56
4.2.2. Cylindrical electrostatic Analyzer (CEA)	58
4.2.3. Detectors location.....	59
4.2.4. Beam Alignment	59
4.3. Characterization of 1/2-size 90° CEA	60
4.3.1. Dependence of energy and angular coefficients with deceleration coefficient	61
4.3.2. Range of CE and $C\theta$ values under experimental uncertainties	62
4.4. CEA Experimental characterization in ISTTOK.....	64
4.4.1. Beam alignment at the SPD	64
4.4.2. Sensitivity curves	65
4.5. Analyzer Calibration	69
4.5.1. Description of indirect calibration.....	70

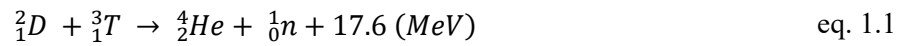
4.5.2. Application of indirect calibration	71
4.6. Measurement of Core plasma potential.....	73
4.6.1. Plasma Potential profile	73
4.6.2. Dependence of local potential with respect to the plasma parameters	74
4.7. Plasma fluctuation measurements: Density and current.....	76
4.7.1. Current Fluctuations.....	76
4.7.2. Plasma Potential fluctuation measurements	77
4.8. Conclusions.....	78
Chapter 5	79
TJ-II Experiments.....	79
Dual HIBP at TJ-II stellarator	79
5a. Effect of edge biasing on core plasma potential and plasma potential flux surface asymmetries in the TJ-II stellarator.....	83
5a.1. Introduction	83
5a.2. Experimental setup	83
5a.3 Influence of edge biasing on core plasma potential in ECRH and NBI scenarios	84
5a.4 Core plasma response to edge plasma biasing and dependence on plasma parameters	86
5a.5 Conclusion.....	89
5b. Measurements of 2D poloidal plasma profiles and fluctuations in ECRH plasmas using the Heavy Ion Beam Probe system in the TJ-II stellarator.....	90
5b.1 Introduction.....	90
5b.2 Experimental set up.....	91
5b.3. Experimental results and discussion.....	92
5b.4 Conclusions	99
5c. Plasma potential profiles for co and counter NBI operation in the TJ-II stellarator	100
5c.1. Introduction	100
5c.2. Influence of co and counter NBI scenarios on plasma potential profiles	100
5c.3. Conclusion.....	103
Conclusions.....	104
Conclusiones	107
Bibliography.....	110

Appendix 1	118
Appendix 2	119
Appendix 3	121
Appendix 4	126

Chapter 1

Introduction

An ever-increasing demand for energy production without the burden of greenhouse effect gases or long-living nuclear waste disposal calls for an alternative and for sure innovative source of energy. Controlled thermonuclear fusion is one of the prime candidates for electricity generation in a clean and sustainable manner. Nuclear fusion reaction consists in fusing two light nuclei together to form heavier nuclei. The difference in the mass between the input and resultant nuclei is released as energy, using Einstein's mass-energy equation ($E = mc^2$). Deuterium-Tritium (D-T) is the most preferred fusion reaction for a power plant (eq. 1.1) due to a higher cross-section of collision at relatively low temperature [1.1].



The Deuterium can be found in sea water and Tritium can be processed from lithium (widely available element throughout the Earth's crust). Therefore, abundant availability of Deuterium and tritium in nature makes it a promising fuel for future fusion plasma reactors.

In order to obtain conditions that allow the fusion reactions on earth, fully ionized plasma is created from the fuel atoms. In order to develop a commercially viable reactor, the plasma should satisfy the so-called Lawson criterion [1.2], which states that for plasma with 10 keV temperature (approx. 100 million °C), eq. 1.2

$$\langle n_e \tau \rangle > 10^{20} \text{ (m}^{-3}\text{s)} \quad \text{eq. 1.2}$$

Where $\tau_e \sim 1\text{sec}$, and the plasma density $n \sim 10^{20} \text{ m}^{-3}$

There are two main confinement routes under investigation for achieving nuclear fusion: Magnetic confinement fusion (MCF) and inertial confinement fusion (ICF). In MCF the fully ionized plasma is confined by both the resultant helical magnetic field created by the plasma current itself and external magnetic field coils. Whereas in ICF a millimeter size fuel pellet composed of D-T frozen mixture is compressed up to a thousand times the atmospheric pressure using high energy (several hundred thousand to million Joule) laser beams.

Presently, the two most relevant magnetic confinement fusion devices are the Tokamak and the Stellarator. In tokamaks hot plasma is contained in a toroidal vessel that acts as the secondary winding of a transformer, created and sustained by the combination of the plasma current and an additional external toroidal and poloidal magnetic field. In stellarators, the expected confining helical magnetic field is all provided by the external winding (the plasma current is null or in some conditions just a very small fraction of the current in the coils that generate the external field) [1.1]. One of the key issues for the success of fusion is to understand energy and particle confinement in the plasma. Some of the most important plasma parameters required to understand the physical picture of several magnetic modes generated in the plasma that affect the turbulence and transport of energy and particles are: the plasma density (n_e), the plasma

potential (ϕ), the electron temperature (T_e), the poloidal magnetic field (B_p) and their respective profiles.

Plasma diagnostics play a key role in understanding the behavior for fusion plasmas. Most of the diagnostics for fusion plasma provide indirect measurements of all these quantities requiring a combination of several diagnostics to obtain the direct plasma parameters of interest. Among various plasma diagnostics for fusion plasmas, Heavy ion beam probe (HIBP) is a powerful tool that can uniquely provide the local measurement of the quantities of interest (plasma density - n_e or plasma pressure-like measurements, plasma magnetic field - B_p and plasma potential - ϕ). Depending on the configuration of the diagnostic, this data is obtained in the whole plasma diameter at once or along a 2D radial scan in the plasma, with spatial resolution of several millimeters and down to the micro-second range temporal resolution (hundreds of kHz).

One of the most elusive plasma parameter to be measured is the plasma potential. The interplay between plasma density and plasma potential and its fluctuations can provide insights into the transport properties of the plasma.

In the present configuration of the Heavy Ion Beam Diagnostic (HIBD) at ISTTOK the local plasma parameters such as: n_e , B_p and T_e were retrieved in previous experiments (details are given hereinafter). The objective of the present thesis work is to upgrade the HIBD of the ISTTOK tokamak to measure the plasma potential profile and its fluctuations. The goal is to provide the possibility for measuring the plasma potential along with the above parameters. This thesis presents the design, construction and commissioning of a new detection system based on a combination of a multiple-cell detector and an innovative electrostatic energy analyzer. The upgraded detection system will allow in principle the measurement of radial profiles of n_e , B_p , and ϕ together with their fluctuation spectra providing an unprecedented unique tool for the study of turbulence and MHD in fusion devices as all information is obtained over a full plasma radius/diameter at once (covering the frequency range of $< 250\text{kHz}$, limited by the amplifier's bandwidth).

Complementarily, this thesis work also exploits the unique Dual HIBPs installation in TJ-II stellarators to measure the 2D poloidal structure of density and potential plasma profiles. The TJ-II innovative experimental set-up developed using a dual HIBP diagnostic pave the way for model validation on core plasma potential asymmetries and particle transport under positive radial electric field scenarios in the TJ-II stellarator. The plasma potential response to external biasing was investigated to search for asymmetries for different plasma heating scenarios.

This chapter introduces the working principle of the heavy ion beam probe and gives an intuitive description for the plasma parameters retrieval. Section 2 describes the heavy ion beam diagnostic in ISTTOK in detail and the methods for retrieval of the plasma parameters. The relevance of plasma potential measurements for fusion plasmas are summarized in section 3. The motivation for upgrading the HIBD to measure plasma potential is explained in section 4. The chapter is concluded with the outline of the thesis in section 5.

1.1. Heavy ion beam probe

Present tokamaks and stellarators aim to study the plasma parameters that control particle and energy confinement and instabilities. The experimental results from the diagnostics provide input for the theory and modelling for more realistic plasma scenarios of the future fusion reactors. Heavy ion beam probe (HIBP) is unique and powerful plasma diagnostic that provides direct measurements of local plasma potential, along with determination of plasma density, electronic temperature and poloidal magnetic field. The HIBP was proposed in the late 60s by Robert L. Hickok, at Rensselaer Polytechnic Institute in the US, which was based on the

molecular ion break up to measure local plasma density and its fluctuations [1.3]. F. C. Jobs and R. Hickok in 1970 for the first time developed heavy ion beam probe to measure directly the plasma potential [1.4]. Since then, various developments have been implemented in order to take full advantage of the capabilities inherent to this diagnostic. Table A.1 in the Appendix 1 summarizes the fusion devices (tokamaks, stellarators and reverse field pinch) in which HIBP has been installed during past years.

Working principle

The basic working principle of Heavy ion beam probe (HIBP) is demonstrated Figure 1.1. A beam of single charged ions, or primary beam (eg Cs^+ , Tl^+ , etc.), is injected into the plasma across the confined magnetic field. The primary beam upon encounter with plasma particles undergoes collision within the plasma (electrons and ions) generating ions of double charged state, called the secondary ions. For the temperatures of operation in ISTTOK the ionization of the beam is largely due to collisions with plasma electrons. The secondary beam ions are separated from the primary beam by the action of the toroidal magnetic field, exhibiting semi-circular trajectories whose Larmor radius is half of the primary beam (Figure 1.1). The primary and the secondary beams are collected by a suitable detection system capturing the local parameters of HIBP measurements.

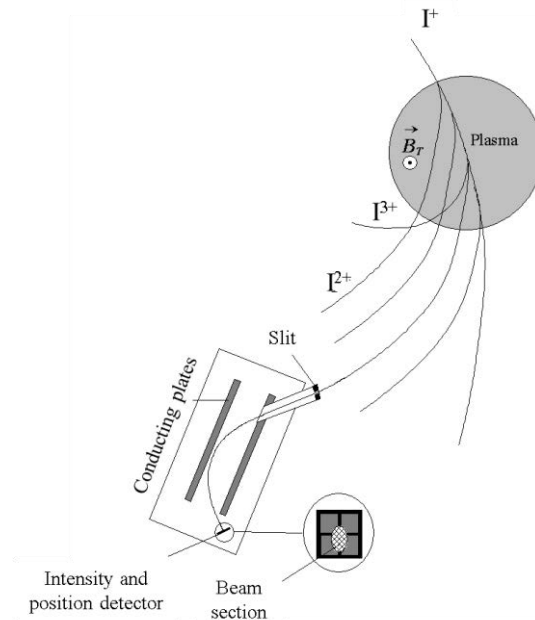


Figure 1.1 HIBProbe working principle: the trajectories of primary (I^+) and secondary ions (I^{2+}) in the presence of confining toroidal magnetic field (B_T) (Figure from [1.12])

The measurement of plasma parameters is based on the intensity of the beams (primary and secondary ion beams), and their relative positions. The relationship between the measured secondary ion current signals in detector and the plasma parameters determined by HIBP are described briefly.

Plasma density: The intensity of each secondary ion beam is directly related to the number of ionizations that the primary beam underwent along a given path element dl , which in turn is proportional to the local electron density (n_e), and the effective impact ionization cross-section (σ_{12}).

Electron temperature: *The electron temperature can be estimated by the ratio of two different generation factors ($n_e \sigma_{12}$) measured at the same sample volume. This can be achieved by using single or two ion method (as explained in sec. 1.2.1. HIBD ISTTOK*

The heavy ion beam diagnostic (HIBD) in ISTTOK is based on the unique concept of Multiple Cell Array Detection (MCAD). The multi-channel detection concept of HIBD facilitates the diagnosis of the secondary ion beams generated from entire sample volumes along the path of primary beam inside plasma. The collection of all the fan of secondary ion beams exiting the plasma allows the determination of radial profile of plasma parameters, such as, plasma density, plasma potential and poloidal magnetic field; from the entire plasma diameter at once with high spatial and temporal resolution [1.7, 1.8]. Furthermore, the HIBP at ISTTOK is unique as it collects the primary ion beam current, which can be used for the absolute density profile reconstruction [1.9]. The ability to collect all the secondary ions simultaneously instead of probing each sample volume successively distinguishes it from the conventionally used HIBProbe to the HIBDiagnostic.

Working principle: A schematic of the diagnostic operation at ISTTOK and underlying physics is presented in Figure 1.4. The primary beam of single charged heavy ions (Xenon, Cesium, etc.) is injected across the plasma in the direction perpendicular to the toroidal magnetic field. The primary beam ions are further ionized inside plasma upon action by plasma electron and are ionized doubly (secondary beam) and to some extent to triply (tertiary beam) or more charged ions. Due to the presence of the magnetic field and the difference of the ion charge, the secondary beam trajectories are separated from the primary one. The primary beam and secondary ion beams (which are generated along the primary beam path in the plasma) are collected by multiple cell array detectors.

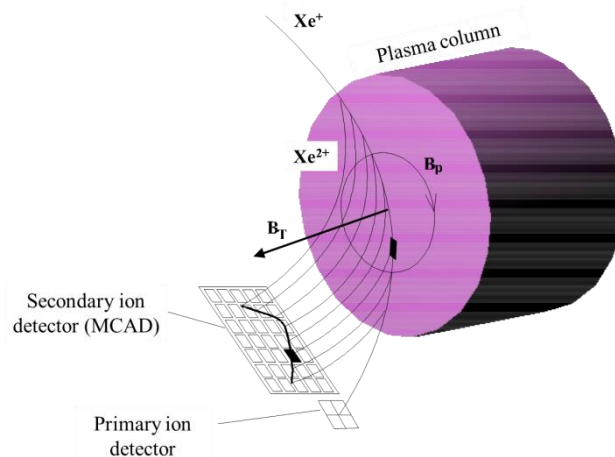


Figure 1.4 Shows a schematic representation of the primary and secondary ion beam trajectories, together with the detectors and plasma for the ISTTOK HIBD configuration (Figure from [1.12]).

1.2.3).

Magnetic poloidal field: The plasma current (I_p) generated inside the tokamak creates a poloidal magnetic field (B_p), with components in the plane perpendicular to its direction. This field causes the secondary ions deflection along the toroidal direction. Thus, information about B_p

can in principle be obtained by measuring the z deviation of the ions in the toroidal direction; such that: $z \propto f(\vec{B}_p)$.

Plasma Potential: The local plasma potential can be measured directly by determination of secondary ions energy originating from the same sample volume. Ability to measure the plasma potential is directly translated from the law of conservation of total energy at the point of ionization.

The measurements of each of the above parameters are discussed in sec. 1.2.1. HIBD ISTTOK

The heavy ion beam diagnostic (HIBD) in ISTTOK is based on the unique concept of Multiple Cell Array Detection (MCAD). The multi-channel detection concept of HIBD facilitates the diagnosis of the secondary ion beams generated from entire sample volumes along the path of primary beam inside plasma. The collection of all the fan of secondary ion beams exiting the plasma allows the determination of radial profile of plasma parameters, such as, plasma density, plasma potential and poloidal magnetic field; from the entire plasma diameter at once with high spatial and temporal resolution [1.7, 1.8]. Furthermore, the HIBP at ISTTOK is unique as it collects the primary ion beam current, which can be used for the absolute density profile reconstruction [1.9]. The ability to collect all the secondary ions simultaneously instead of probing each sample volume successively distinguishes it from the conventionally used HIBProbe to the HIBDiagnostic.

Working principle: A schematic of the diagnostic operation at ISTTOK and underlying physics is presented in Figure 1.4. The primary beam of single charged heavy ions (Xenon, Cesium, etc.) is injected across the plasma in the direction perpendicular to the toroidal magnetic field. The primary beam ions are further ionized inside plasma upon action by plasma electron and are ionized doubly (secondary beam) and to some extent to triply (tertiary beam) or more charged ions. Due to the presence of the magnetic field and the difference of the ion charge, the secondary beam trajectories are separated from the primary one. The primary beam and secondary ion beams (which are generated along the primary beam path in the plasma) are collected by multiple cell array detectors.

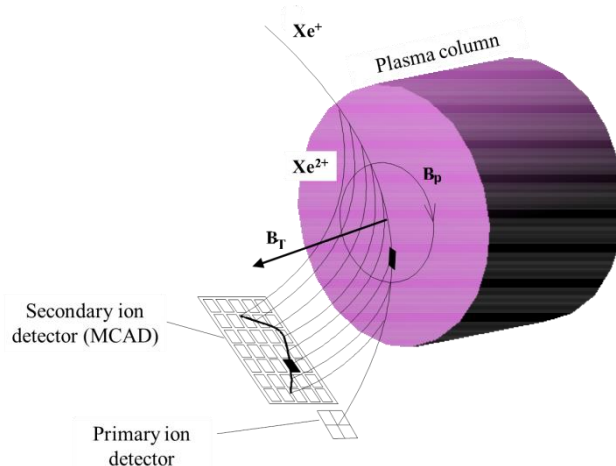


Figure 1.4 Shows a schematic representation of the primary and secondary ion beam trajectories, together with the detectors and plasma for the ISTTOK HIBD configuration (Figure from [1.12]).

1.2.3 in details in reference to HIBD at ISTTOK.

1.2. Heavy ion beam diagnostic at ISTTOK tokamak

ISTTOK is a large aspect ratio circular cross-section tokamak with iron core transformer [1.5] (Figure 1.2). The plasma is limited by a circular limiter (12 blocks of graphite evenly distributed in a poloidal plane) located in a fixed radial position at $r = 0.085$ m. ISTTOK plasmas are ohmically heated and its typical parameters are presented in Table 1.1 . The standard plasma operation presently is by alternate current (AC) discharges [1.4]. In such discharges the plasma current direction is alternated periodically to avoid saturation of iron core transformer and extend the discharge time. The AC discharges at ISTTOK can go up to 40 cycles (positive and negative) with each AC cycle (positive + negative plasma current) lasting usually up to 50 ms.

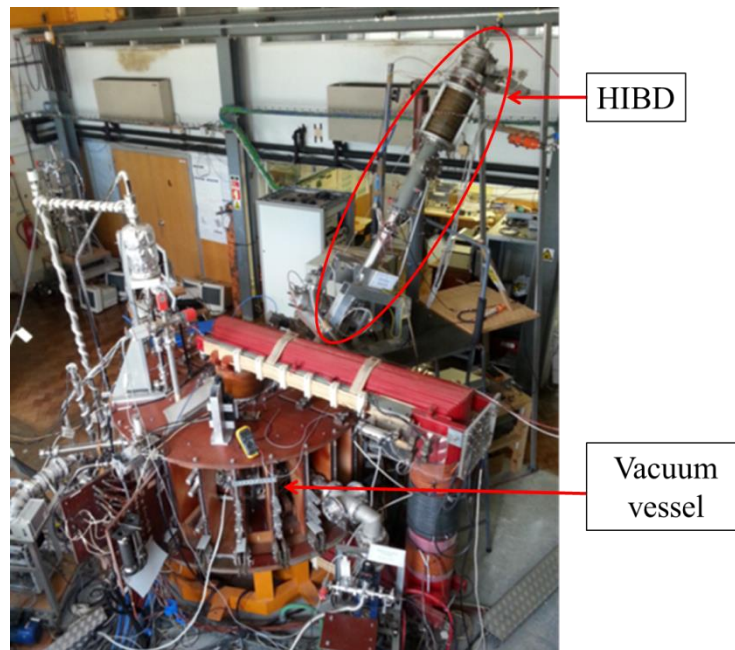


Figure 1.2 ISTTOK picture indicating injector of HIBD [1.10]

ISTTOK Parameters	
Minor R	0.085 m
Major R	0.46 m
Plasma current	4kA
B_p	0.5T
Density	$4 \times 10^{18} \text{ m}^{-3}$
Temperature (keV)	$< 120\text{eV}$
Transformer flux	0.25 V.s
Discharge duration	600 ms

Table 1.1 presents the typical plasma parameters for the discharges in ISTTOK used for the present experiments.

1.2.2. Schematics

This subsection describes the overall diagnostics setup and schematics of heavy ion beam diagnostic installed at ISTTOK. The schematics of HIBD can be divided in three sections: i) injector, ii) detectors and iii) amplifiers (as shown in Figure 1.3).

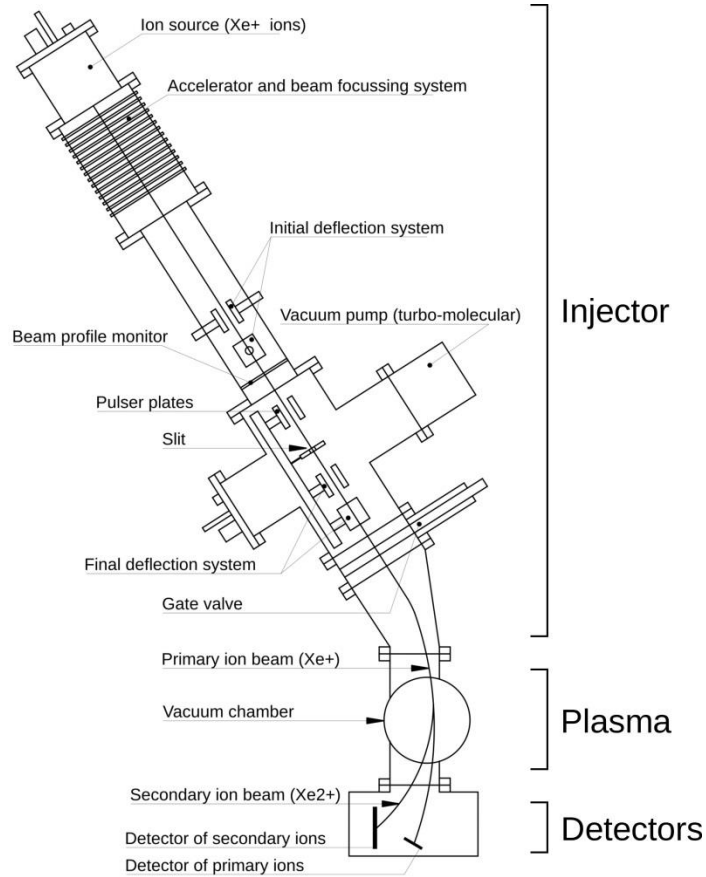


Figure 1.3 Schematics of HIBD ISTTOK (Figure from ref [1.10]).

(i) Injector

The injector is responsible to create the beam of primary ions to be injected into the plasma. The HIBD injector at ISTTOK consists of following components: an ion source; an extraction, acceleration and beam focussing system; an initial deflection system; a beam profile monitor; a pulser and slit; a final deflection system; a vacuum pump; and a gate valve. These components are briefly described below.

Ion source

The ion source (Figure 1.3) is responsible to create plasma of Xe (or Hg, Cs) gas from which the ionized beam is extracted. A tungsten filament (inside the chamber) carrying an electrical current (~50 A) emits thermo-electrons into the ion source chamber filled with gas (Xe, Hg or Cs). The filament is biased with respect to the chamber wall to accelerate the electrons and creates an arc current that ionizes the gas to produce plasma. The electron generated are confined by two permanent magnets in a dipole configuration (with 20 G in the center) placed outside the chamber. The arc voltage (voltage between filament and chamber) is chosen such that only singly ionized charged state (Cs⁺, Hg⁺ or Xe⁺) are generated.

Extraction, acceleration and beam focusing system [1.11]

The ion extraction is performed using quasi-Pierce electrode geometry located at the base of the ion source chamber. An additional electrode is also present to suppress the electrons originated due to ion-electrode collisions. The beam acceleration and focusing system constitutes multiple disc shaped electrodes stacked one over the other to form an electrode acceleration tube (Figure 1.3). The top segment of the tube is dedicated to beam acceleration due to the electric field created by resistive divider (up to 25 kV). The ion optics for lower section is devoted to focus the beam. This section is of extreme importance in defining the final beam current as well as its divergence and dimension of the beam.

Initial deflection system

The initial deflection system constitutes of two pairs of parallel conducting plates oriented toroidally (upper) and radially (lower) for radial and toroidal deflection, respectively. This deflection system is responsible for tuning the beam through the slit. It is also used to measure the spatial distribution of beam current by accessing ‘beam profile monitor’ [1.10].

Slit and pulser system

This system is dedicated to define the beam diameter (by ‘slit’) and chops the beam (using pulser). The slit is essentially a circular pinhole with 3 mm of diameter. The pulser consists of two parallel conducting plates toroidally oriented. When voltage is applied to the plate the beam is deviated away from the slit and for no applied voltage the beam passes through the slit.

Final deflection system

Similarly arranged as the initial deflection system, the final deflection system is responsible for adjusting the beam injection angle in the plasma such that the beam reaches the detector.

Vacuum pump

The HIBD at ISTTOK has an independent and dedicated vacuum system provided by a turbo-molecular vacuum pump providing a vacuum base pressure in the range of 4×10^{-7} mBar.

Gate valve

A gate valve located between the diagnostic and tokamak allows an independent vacuum system for the two systems. Usually the gate valve is opened only during short time for discharges (to inject the primary beam into the plasma) and remains closed otherwise. It permits the operation of the diagnostic without affecting the tokamak operation.

(ii) Detector

The heavy ion beam diagnostic at ISTTOK employs 2-Dimensional Multiple Cell Array Detectors (MCAD) for radial profile measurements. The detector is made from conducting material, such as copper, to detect the heavy ions from primary and secondary beams. The principle of detection is as follows: when an ion strikes a conducting surface it is neutralized by removing an electron from the material surface. The impact process can also lead to the ejection of secondary electrons, thus generating a secondary electron emission (SEE) current due to the successive removal of the electron from the detector surface. Depending upon the incident beam energy, beam uniformity on the detector, and its relative incident angle with respect to the detector, the generated SEE current can amplify the signal [1.17]. Therefore, the total current collected at the detector is sum of direct ion current and SEE current. Two detector configurations can be used to avoid or compensate for this effect when absolute values are required.

Depending on the parameter of interest, the geometry of the MCAD can be customized to be radially and/or toroidally divided. The position and dimension of each cell on the MCAD (used in the HIBD operation) defines the size and the location of sample volume probed inside the

plasma, which can be retrieved by the trajectory simulation codes [1.12]. The MCADs used in the experiments for this thesis are explained later in the chapters.

(iii) *Amplifiers*

Due to the low amplitude (< 10 nA) of the secondary ions on the detectors, the current has to be amplified to acquire the signals on the ISTTOK data acquisition system. The new low noise small size trans-impedance amplifiers [1.16] and the commercial amplifier [1.18] were employed for the experiments reported in this thesis.

1.2.1. HIBD ISTTOK

The heavy ion beam diagnostic (HIBD) in ISTTOK is based on the unique concept of Multiple Cell Array Detection (MCAD). The multi-channel detection concept of HIBD facilitates the diagnosis of the secondary ion beams generated from entire sample volumes along the path of primary beam inside plasma. The collection of all the fan of secondary ion beams exiting the plasma allows the determination of radial profile of plasma parameters, such as, plasma density, plasma potential and poloidal magnetic field; from the entire plasma diameter at once with high spatial and temporal resolution [1.7, 1.8]. Furthermore, the HIBP at ISTTOK is unique as it collects the primary ion beam current, which can be used for the absolute density profile reconstruction [1.9]. The ability to collect all the secondary ions simultaneously instead of probing each sample volume successively distinguishes it from the conventionally used HIBProbe to the HIBDiagnostic.

Working principle: A schematic of the diagnostic operation at ISTTOK and underlying physics is presented in Figure 1.4. The primary beam of single charged heavy ions (Xenon, Cesium, etc.) is injected across the plasma in the direction perpendicular to the toroidal magnetic field. The primary beam ions are further ionized inside plasma upon action by plasma electron and are ionized doubly (secondary beam) and to some extent to triply (tertiary beam) or more charged ions. Due to the presence of the magnetic field and the difference of the ion charge, the secondary beam trajectories are separated from the primary one. The primary beam and secondary ion beams (which are generated along the primary beam path in the plasma) are collected by multiple cell array detectors.

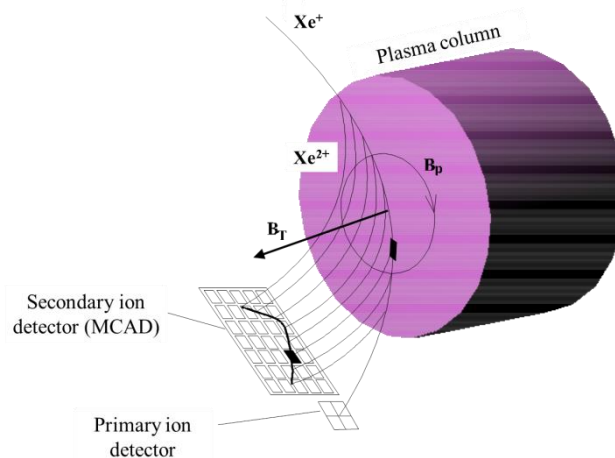


Figure 1.4 Shows a schematic representation of the primary and secondary ion beam trajectories, together with the detectors and plasma for the ISTTOK HIBD configuration (Figure from [1.12]).

1.2.3 Retrieving plasma parameters at ISTTOK HIBD

HIBD provide direct measurement of primary and secondary ions current on the MCAD. The intensity of these currents and their toroidal shift obtained on the multi-channel detectors provides the information about various plasma parameters. The plasma parameters that can be obtained using HIBD at ISTTOK are: generation factor- $n_e \hat{\sigma}(T_e)$, plasma electron temperature - T_e and density- n_e , the poloidal magnetic field- B_p and the plasma potential- ϕ . The measurements of these parameters as obtained in ISTTOK are explained briefly in this section.

(iv) Generation Factor - $n_e \hat{\sigma}(T_e)$

The generation factor ($n_e \hat{\sigma}(T_e)$) is the product of the plasma electron density average over the sample volume ($n_e(r_j)$) and the effective ionization cross-section $\sigma(T_e)$ (function of the plasma electron temperature). The generation factor indicates the ionization rate per unit length and contains the convoluted information of the plasma electron density and temperature. For secondary beam currents I_j^{2+} in the sample volume j of length dl_j for single ionization of singly ionized primary beam, the generation factor is given by eq. 1.3

$$n_e(r_j) \hat{\sigma}_{12}(T_e(r_j)) = \frac{I_j^{2+}}{2I_j^+ dl_j} \quad \text{eq. 1.3}$$

Where, $\hat{\sigma}_{12}$ is the single ionization cross-section for singly ionized heavy ion beam, r_j represents the sample volume radial location along the primary beam path and I_j^+ is the primary ion beam current available at the sample volume j. For typical ISTTOK plasma density and temperature ranges the $n_e \hat{\sigma}(T_e)$ can be considered as proxy to plasma pressure [1.19].

It should be noted that actual primary (I_j^{2+}) and secondary (I_j^{2+}) ion beam current generated at the sample volume j cannot be measured directly. The detected secondary ($I_{j(\text{det})}^{2+}$) and primary ($I_{j(\text{det})}^+$) ion beam on the detector are lower in value than the actual current generated at the sample volume (i.e. I_j^+ and I_j^{2+}) due to the beam attenuation in the plasma. Ref [1.12] presents three methods to recover the absolute $n_e \hat{\sigma}_{12}(T_e)$ profile categorized according by the degree of attenuation taken into account: simplified, intermediate and advanced.

(v) Electron temperature

The electron temperature can be estimated by two methods:

- a. One of the methods to determine electron temperature is by injection of two beams of different ionic species (A and B). The injection energy of the beams is chosen such that both species covers the same path within the plasma. The ratio of the two currents (one from each species) collected from the same sample volume in the plasma is proportional to the ionization cross-sections' ratio, which in turn is a function of electron temperature, $f(T_e)$ (eq. 1.4). The two ion species method has been employed for determination of T_e in ISTTOK [1.9, 1.12].

$$\frac{I_A^{2+}}{I_B^{2+}} \propto \frac{n_e(r) \sigma_{12}^A(T_e)}{n_e(r) \sigma_{12}^B(T_e)} = f(T_e) \quad \text{eq. 1.4}$$

- b. An alternative method is to use single ion species and collect the ions from different ionization reactions. The ratio between the currents of the secondary ions (A^{2+}) and tertiary (A^{3+}) from the same point of ionization is proportional to the ratio between the cross-section of their respective ionization reactions, which in turn is a function of electron temperature function $f'(T_e)$ (eq. 1.5).

$$\frac{I_A^{2+}}{I_A^{3+}} \propto \frac{n(r)\sigma_{12}^A(T_e)}{n(r)\sigma_{13}^A(T_e)} = f'(T_e) \quad \text{eq. 1.5}$$

(vi) *Electron density*

The electron density is obtained from the deconvolution of the experimental generation factor. eq. 1.3 provides the plasma electron density measurements with known effective ionization cross-section and plasma electron temperature.

For plasma with T_e in the range of $T_e > 150$ eV, the effective cross-sections usually have a weak dependence on T_e [1.12]. Thus, secondary beam intensity is solely dependent on plasma electron density and we can use the approximation: $n_e \propto n_e \hat{\sigma}(T_e)$.

Whereas, for the plasma with lower electron temperature ($T_e < 150$ eV), the $n_e \hat{\sigma}(T_e)$ product is usually measured and analysed using eq. 1.3. The electron temperature (T_e) can be estimated (as described above) and the value of $\hat{\sigma}(T_e)$ can be obtained; thus, plasma density can be retrieved [1.9, 1.12].

(vii) *Plasma poloidal magnetic field (B_p)*

A deviation in Z (toroidal) direction is observed due to a force generated by the cross product of beam velocity (\vec{v}_b) and poloidal magnetic field (\vec{B}_p): $\vec{v}_b \times \vec{B}_p$. The poloidal magnetic field can be estimated from the z deviation of the primary and secondary beam on the MCAD. At ISTTOK, the experimental evolution of the poloidal magnetic field profile with the HIBD has previously been reported in [1.13]. The determination of local poloidal magnetic field was possible with beam toroidal deviation (z) measurements and with trajectory simulations [1.12].

(viii) *Plasma potential*

HIBP has a unique capability to measure local plasma electrostatic potential by direct measurements of secondary ion energy. The basic principle behind the measurements is the energy conservation. The potential at the sample volume (φ_{SV}) can be related to the kinetic energy of the primary beam (K_{I^+}) and secondary beam ($K_{I^{2+}}$) as represented in eq. 1.6.

$$\varphi_{SV} = K_{I^{2+}} - K_{I^+} \quad \text{eq. 1.6}$$

Hence, the local plasma potential can be obtained from the measurements of the difference between the energies of primary and secondary ions originating from corresponding sample volume. A multi-channel time-of-flight (ToF) energy analyzer to measure plasma potential was proposed [1.14] and tested [1.15] for HIBD at ISTTOK. However, the results indicated a lack of resolution for plasma potential fluctuations measurements in the $\Delta E/E < 10^{-3}$ range.

1.3. Relevance of plasma potential measurement for fusion plasma

Transport and turbulence in fusion plasma are the key parameters to understand and control energy and particle confinement in fusion devices. Measurement and characterization of

magnetic fluctuations along with density and electric field local perturbations are important ingredients to the physical picture in order to understand the interplay between transport and turbulence [1.20] on one side and fast ions and Alfvén Eigen modes instabilities [1.21] on the other. The measurement of plasma potential [1.22] is crucial to characterize Alfvén Eigen modes [1.23, 1.24] and Geodesic acoustic mode (GAM) [1.25, 1.26]. It also plays an important role in determining turbulence and transport measurements [1.27]. Few examples from the literature emphasizing the relevance of plasma potential measurements are presented below.

The direct measurement of the local electric potential of the plasma is of primary importance for understanding the role of the radial electric field (E_r) in plasma turbulence and confinement improvement mechanisms. Reference [1.28] suggests that the best performance scenario takes place in a fusion device where $\vec{E}_r \times \vec{B}_t$ shear stabilization mechanism has been achieved. Reference [1.29] presents the radial plasma potential profiles obtained in the TJ-II by HIBP and indicates the possibility to modify global confinement and edge plasma parameters with limiter illustrating the direct effect of radial electric fields on confinement properties.

Alfvén Eigen modes (AE) can be excited by the energetic particles injected during heating by neutral beam injection (NBI) or ion cyclotron resonance [1.30]. These modes can cause loss of energetic and thermal particle from the plasma bulk [1.31]. This is particularly crucial for externally heated plasmas and fusion grade plasmas where Alfvén Instabilities triggered by fast ions can potentially degrade confinement and limit the performance of future reactors. The fast fluctuations measurement by plasma potential measured by HIBP characterizes turbulent nature of this Alfvén Eigen mode [1.24].

Geodesic Acoustic Modes (GAMs) are radially localized structures of plasma radial electric field component, E_r (or plasma potential) [1.32]. GAMs can suppress the plasma's micro-turbulence eddies and they can be considered as mechanisms of self-regulation of turbulence, hence, they are relevant for studies of plasma confinement. The identification of GAMs in the power spectral density of plasma-potential oscillations using HIBP has been reported in TJII [1.33], T-10 [1.34] and LHD [1.35].

Other diagnostics that can measure the plasma potential are Langmuir probes for the edge plasma [1.36]. The probes perturb the plasma locally and therefore the retrieval of the plasma potential is complicated and measurements are limited to the edge and affected by local plasma temperature [1.37].

1.4. Motivation for upgrading the ISTTOK HIBD

Experiments in ISTTOK [1.9, 1.13, 1.15, 1.16], TJ-II [1.24, 5.3], T-10 [1.38, 5.3] and in the LHD device [1.39] have all together demonstrated the capabilities of the HIBP in determining plasma density and potential and its fluctuations measurements allowing for MHD and turbulence characterization including AE modes (TJ-II) [1.24] and GAMs (T-10) [1.25]. However, the present diagnostic arrangements for the potential fluctuation measurements require a scan in beam energy and/or injection angle to access different radial points in the plasma which limits the time resolution. A first attempt to have a simultaneous measurement of the radial profile of density fluctuations combined with the measurements of plasma potential local fluctuations was made in a design of the HIBD for TJ-II [1.40] (however no experimental results were obtained due to operational constraints).

The aim of the present thesis is to upgrade the ISTTOK HIBD to measure the plasma potential. This covers the conceptual study, construction and commissioning of a new detection system

based on a combination of a multiple-cell detector and an innovative cylindrical electrostatic energy analyzer with the capability to measure plasma density and plasma potential fluctuations with the required accuracy to characterize turbulence and MHD activity. A 90° Cylindrical Electrostatic Analyzer (CEA) prototype operating in an innovative ‘high-resolution deceleration mode’ was designed, constructed and commissioned to measure the plasma potential via secondary ions energy measurements. The ½-size prototype has demonstrated the properties required to build a full plasma coverage detector. This detector combination will be unique as it will allow for the simultaneous measurements of radial plasma profiles of n_e , ϕ , B_p and their fluctuations, in one discharge (multichannel approach) with relatively high temporal and spatial resolution.

The thesis presents also the experimental results obtained in experiments coordinated by the author in using the dual HIBP setup at TJ-II stellarator. For the first time 2D plot contour of the plasma potential and secondary ion current (proxy to plasma density) and their fluctuations have been retrieved for one-third of the poloidal plasma cross-section. The effect of the NBI heating (-co and -counter) on local plasma potential has been examined. The plasma potential asymmetry has been investigated using dual HIBP at TJII for positive and negative E_r under different heating scenarios for impurity transport studies. The Experimental results obtained from the innovative experimental set-up developed using a dual HIBP diagnostic can provide input for the theoretical model validation for future fusion plasma scenarios.

1.5. Thesis outline

The thesis is divided into 5 chapters in total. Chapter 1 is introductory chapter describing the basic of Heavy ion beam diagnostics and motivation behind the thesis work. Chapter 2, 3 and 4 presents the numerical simulations and experimental results regarding the upgrade of the HIBD at ISTTOK to measure plasma potential. Chapter 5 is the compilation of experiments performed using dual-HIBP at TJ-II stellarator concerning the role of plasma potential and its fluctuations measurements on particle transport and confinement under positive radial electric field scenarios in the TJ-II stellarator in different heating scenarios.

Chapter 1 introduces the heavy ion beam diagnostics as fusion plasma diagnostic. A general overview of the diagnostic is followed by the detailed hardware of HIBD at ISTTOK and a description on the retrieval of plasma parameters by secondary ions current measurement. The importance of the plasma potential measurements for plasma turbulence and transport studies has been highlighted along with the results from the other HIBPs. The motivation of the thesis to upgrade HIBD at ISTTOK tokamak to be able to measure plasma potential in addition to density and poloidal magnetic field and their respective profiles in one radial scan using cylindrical energy analyzer is explained.

Chapter 2 introduces the *90° cylindrical energy analyzer (CEA)* to upgrade the HIBD ISTTOK for potential measurements. The characterization and optimization of the analyzer was performed in SIMION software. Sufficient improvements of the energy resolution and angle aberration characteristics were obtained for innovative deceleration mode operation of analyzer as compared to conventional standard operation. The chapter presents the theoretical characterization of analyzer along with experimental results obtained by the half-size 90° CEA

prototype with electron beam. The comparison of the results with SIMION simulations is also included for validation.

Chapter 3 reports on electrostatic input module (EIM) which is a necessary intermediate module to focus and deflect the secondary beam from plasma output to CEA input. The chapter reports on the design, optimization and characterization of the various elements comprising EIM. To verify and validate the simulations, an experimental prototype EIM setup was built and tested in HIBD. The experimental results for the vertical beam profile expected at the analyzer input are presented. The ½-size CEA and EIM (both tested independently) were assembled and installed in HIBD for diagnosing secondary beam corresponding to the sample volume at the core of the plasma.

Chapter 4 presents the integrated design and schematics of the combined setup of EIM + CEA as installed on HIBD at ISTTOK. The preliminary measurement of the core plasma potential and its fluctuations were reported. An indirect method of calibration of the analyzer is also presented.

Chapter 5 presents the results from the Dual HIBP in TJ-II stellarator. This chapter is divided into three subsection sections each presenting three independent experiments as follows:

- a. 2D poloidal scans: For the first time, 2D poloidal contour plots of plasma potential and density and their fluctuations have been measured in low density plasmas with hollow density profiles sustained by ECRH in the TJ-II stellarator. The innovative experimental set-up, developed using a dual HIBP diagnostic, pave the way for model validation on core plasma potential asymmetries and particle transport under positive density gradient scenarios in the TJ-II stellarator.
- b. Biasing: The core plasma potential asymmetries were investigated by measuring core plasma potential response due to external edge biasing. The plasma potential was measured by the means of dual Heavy ion beam probe located at two toroidally separated locations in the stellarator at TJII. The response on the plasma potential due to biasing was also extended to electron [$E_r > 0$] and ion root [$E_r < 0$] scenarios.
- c. NBI 1 and 2: Plasma potential measured by Heavy ion beam probe in TJII for NBI1 (-co) and NBI2 (-counter) heated plasma for similar plasma parameters was investigated. The aim was to correlate fast particle confinement due to counter and co-counter neutral beam current drive injection as predicted theoretically.

The thesis is summarized with final conclusion and future work.

Chapter 2

High resolution 90° Cylindrical Energy Analyzer

2.1. Introduction

The upgrade of the heavy ion beam diagnostic (HIBD) system at ISTTOK to measure the plasma potential required the construction of two major components, i) the electrostatic input module (EIM) and ii) the 90° cylindrical energy analyzer (CEA). The first step to be taken consists in the conceptual design of these components supported by numerical simulation. This chapter centers on the characterization and optimization of the 90° cylindrical energy analyzer. The first part concerns the modeling of the CEA using the SIMION code and the second part is dedicated to the installation and characterization of a test facility based on a half-size ($\frac{1}{2}$ -size) prototype. The simulation and experimental results are compared in view of validating the model and its predictions. As a result of the simulation and optimization work, it was found that a new mode of operation ‘intrinsic deceleration’ results in significant higher energy resolution and higher tolerance to the beam entrance angle. This mode of operation takes advantage of the beam retardation and focusing property of electrostatic field lines at the input of the analyzer and constitutes the basis of the work hereinafter presented.

This chapter starts with a brief introduction describing the energy analyzers that are used in other heavy ion beam probes. Section 3 describes the 90° cylindrical energy analyzer along with the changes incorporated in the design to obtain an innovative CEA biasing scheme allowing for the increased sensitivity as compared to a normal mode of operation. Section 4 includes the optimization and characterization of the intrinsic deceleration mode. Section 5 introduces the additional electrodes required as per the 3-D setup and experimental conditions. In section 6 is presented the experimental setup of the $\frac{1}{2}$ -size prototype of 90° CEA and the results obtain by the tests conducted with an electron beam. The comparison of the results with SIMION simulations is also included for the validation of the model. The chapter is concluded with a summary in section 7.

2.2. Plasma potential measurements in other devices

2.2.1. 30° Proca-Green Analyzer

The 30° Proca-Green analyzer is the most common detector used for the measurement of the plasma parameters in HIPP [2.1]. The parallel plate proca-green analyzer was developed by Proca and Green to make precise particle beam energy measurements [2.2]. A conventionally 30° Proca-Green energy analyzer is shown in Figure 2.1. The analyzer consists of two parallel plates, the top plate is positively biased and the bottom plate is grounded. The bottom plate contains the input slits and the exit window. A positively charged ion beam entering into the input slit encounters a retarding field and is therefore deflected towards the bottom plate. The voltage on the top plate is optimized to deflect the beam to the exit slit. A split plate detector placed at the exit window collects the beam and the relative currents on the detector provide information that can be related to plasma parameters, namely plasma potential and density. By preserving the electric field between the plates any change in the energy of the entering beam can be measured accurately by the position of the beam at the split plate detector.

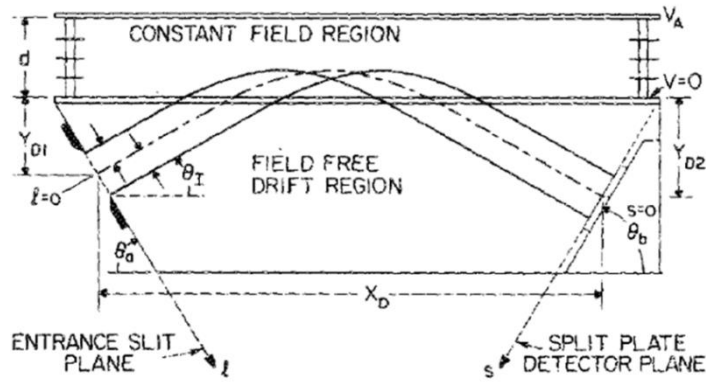


Figure 2.1 Proca-Green Analyzer schematics [2.1]

2.2.2. The 127° cylindrical analyzer

Such analyzers are commonly used in the energy analysis of fast ion and electron beams due to its simple design. Hughes and Rojansky studied the trajectory of a charged particle in a cylindrical electrostatic field [2.3, 2.4]. Figure 2.2 presents three particle trajectories, starting from the same point at radius r_0 with three different energies. At an intermediate angle of 127° the trajectories of different energy groups are uniquely separated and independent of the initial beam divergence (Figure 2.2). A position sensitive detector placed at this angular position can provide information about the particles energy [2.5].

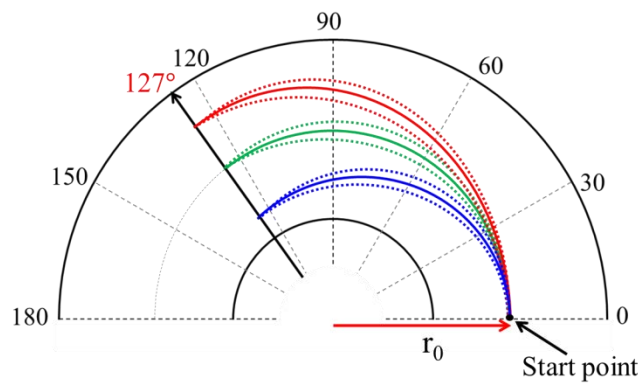


Figure 2.2 127° cylindrical analyzer: the trajectories of ions starting from a same point (r_0) but with different energies and different incident angles. The ions of same bunch (same color) belong to same energy group with angle divergence. The energy of the central trajectory of each bunch is, 0.8 (blue), 1.0 (green) and 1.2 (red) time of the circular orbit energy, the divergence of the incident angle between two neighboring trajectories (shown by dotted lines) is 4°. The figure is was built based on the information given in ref [2.5]

2.2.3. TOF energy analyzer

The Time of flight (TOF) technique basically measures the beam energy (velocity) through the measurement of the time that the beam takes from a start point until a stop point. In TOF method the energy dispersion is created in time, hence, a beam is pulsed to allow the discrimination between the start and stop signals [2.6]. The experimental set-up (Figure 2.3) consists on a start point detector, which could be made from a metallic mesh with some finite

transparency to allow the beam to pass through and a stop point detector. The distance between the detectors is known. The time of flight is measured experimentally using an adequate electronic detection system.

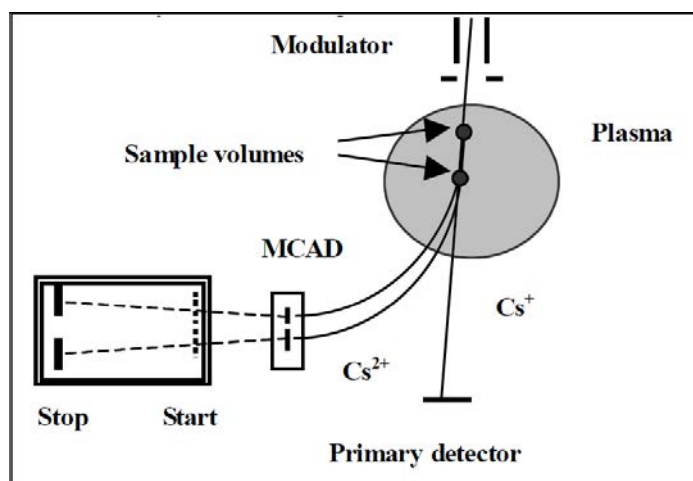


Figure 2.3 Schematics of TOF arrangement for Heavy ion beam diagnostics [2.6]

2.3. The 90° Cylindrical Energy Analyzer (CEA) for ISTTOK

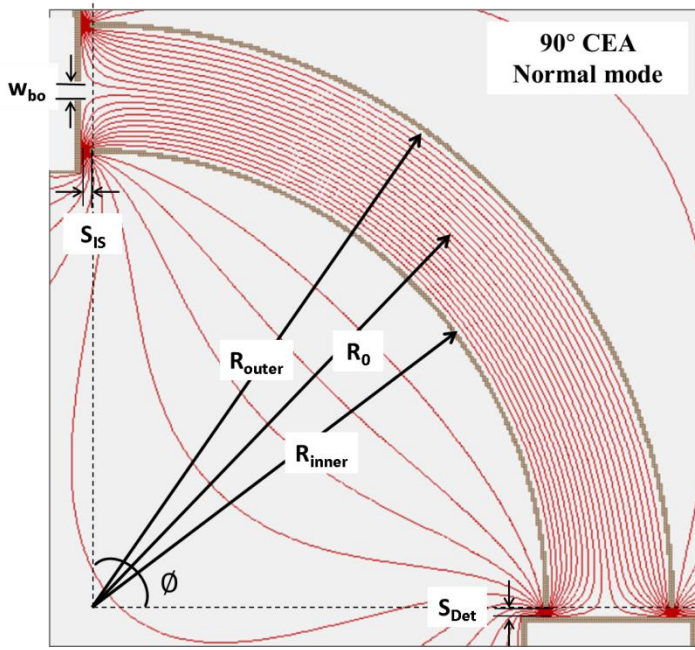
In its original configuration the heavy ion beam diagnostics at ISTTOK is capable of measuring plasma density, poloidal magnetic field and electron temperature [1.9, 1.12]. One first upgrade of the diagnostic to measure the plasma potential and its fluctuation by means of a multichannel TOF method has already been tested in ISTTOK [1.14, 1.15]. However, the TOF measurements have indicated a lack of resolution for investigations of plasma potential fluctuations better than $\Delta E/E < 10^{-2}$ range. In addition, the signal frequency was relatively low due to the need to build up enough statistics. Hence, a new detector system based on the electrostatic method is required to perform the measurements of the plasma potential in the energy resolution range of $\Delta E/E < 10^{-3}$, with frequencies that can be up to the amplifiers bandwidth (300 kHz), more suitable for turbulence and particle transport studies.

The installation of the traditionally used 30° Proca-Green parallel plate analyzer in ISTTOK is anticipated to be very difficult due to the physical and geometrical constraints at the HIBD output port. Moreover, for the intended multichannel mode of operation, Proca-Green parallel plate analyzer is of limited applicability due to its limitation to collect the secondary ions from the whole plasma cross-section. Therefore, a novel design of a 90° cylindrical energy analyzer with a multi-aperture input slit has been proposed to measure the plasma potential fluctuations by HIBD in ISTTOK.

The possibility to use a single long entrance slit in the energy analyzer facilitates the collection of the secondary beams fan and therefore accessing plasma fluctuations from a larger region of the plasma. Another advantage of using a cylindrical configuration is the efficient logarithmic potential gradient distribution making the cylindrical analyzer more compact in size [2.8] as compared to biased parallel plate Proca-Green analyzer. Due to compactness and applicability in multichannel operation the cylindrical energy analyzer has been chosen for the upgrade of the HIBD in ISTTOK.

2.3.1. Overview of the 90° Cylindrical Energy Analyzer

A 90° cylindrical energy analyzer (CEA) consists of two 90° curved inner and outer electrodes with radii R_{inner} and R_{outer} respectively, combined with an entrance slit and an end detector plate (as shown in Figure 2.4, left). For chosen voltages on the inner and outer electrodes (V_{inner} and V_{outer} , respectively), the beam entering the analyzer input slit is deflected by the electrostatic field to the end detector center due to the symmetrically biased curved electrodes.



90° CEA: Normal mode	
$V_{\text{outer}} / V_{\text{inner}}$	2.4kV/-2.4kV
ψ_0 / V_{Det}	0kV/0kV
V_{IS}	0V
$R_{\text{outer}}/R_{\text{inner}}$	240/190 mm
R_0	215mm
$S_{\text{IS}}/S_{\text{Det}}$	3/3 mm

Table 2.1

Figure 2.4 90° CEA equipotential field lines in normal mode operation (left), the values of the parameters is given in Table 2.1 on the right; where R_0 , R_{outer} , R_{inner} are the central, outer plate and inner radii of analyzer respectively; $S_{\text{IS}} / S_{\text{Det}}$ is the distances between analyzer and entrance slit/ deceleration plate respectively, Φ is the azimuthal angle of the analyzer (90° for present case), w_{bo} is the width of then input slit of the analyzer. V_{inner} and V_{outer} are the voltages applied to the inner and outer radii of the analyzer plates; V_0 and V_{Det} are the voltages on the central radii (R_0) and the detector.

Theoretical background

The electric field strength, $E(R)$ and the potential $\psi(R)$ between the curved plates at a radius R is given by eq. 2.1 and eq. 2.2, respectively [2.10];

$$E(R) = E_0(R_0/R) \quad \text{eq. 2.1}$$

$$\psi(R) = E_0 R_0 \ln\left(\frac{R}{R_0}\right) + \psi_0 \quad \text{eq. 2.2}$$

Where, $E(R)$ is electric field strength at the position R taken inside the plates, E_0 is electric field at the central standard line trajectory with radius R_0 (Figure 2.4) and $\psi(R)$ is the potential at the radius R , inside the curved plates. The values of E_0 and ψ_0 are given by eq. 2.3 and eq. 2.4, respectively,

$$E_0 = (V_{outer} - V_{inner}) / (R_0 \ln \left(\frac{R_{outer}}{R_{inner}} \right)) \quad \text{eq. 2.3}$$

$$\psi_0 = \frac{[V_{inner} \ln \left(\frac{R_{outer}}{R_0} \right) - V_{outer} \ln \left(\frac{R_{inner}}{R_0} \right)]}{\ln(R_{outer}/R_{inner})} \quad \text{eq. 2.4}$$

Where V_{inner} , and V_{outer} are the voltages applied to the inner (R_{inner}) and outer (R_{outer}) radii of the analyzer plates, respectively; $R_0 = \frac{1}{2}(R_{outer} + R_{inner})$ is the radius of standard (central) trajectory and ψ_0 is the potential at R_0 . Figure 2.4 presents the 2D view of the analyzer in SIMION with indicated notations.

The potential difference necessary to guide an ion with energy E_0 on the R_0 orbit can be obtained by equating the electrostatic force and the centrifugal force as given in eq. 2.5 [2.11]:

$$V_{outer} - V_{inner} = 2[(E_0 - q\psi_0)/q] (d/R_0) \quad \text{eq. 2.5}$$

Where, q and d are the charge of the particle and the distance between the CEA plates, respectively.

With potential applied to the curved electrodes, the trajectory of the input ion, at the analyzer entrance, is deflected by the electrostatic fields to the end detector (Figure 2.4). The ion displacement at the end detector from standard trajectory (R_0) is dependent on the initial input conditions namely, beam energy, input angular dispersion and the intrinsic energy resolution properties of the detector. The first order estimation for the ion displacement Δr from the central standard trajectory (R_0) at the analyzer collector is given by the following equation [2.9].

$$\Delta r = \delta r + C_\theta \delta \theta + C_E \delta E \quad \text{eq. 2.6}$$

where $\Delta r = \Delta R_{det}/R_0$ is the beam normalized shift at the detector, $\delta r = \Delta R_{slit}/R_0$ is the normalized input slit position corresponding to the initial position of the beam relative to standard trajectory, C_θ is the first-order angular aberration coefficient, $\delta \theta$ is the angle of beam trajectory relative to the standard trajectory, C_E is the first-order energy dispersion coefficient and $\delta E = \Delta E/E_0$ is the normalized ion energy variation.

The dispersion relation in the first order does not include the influence of the electric field irregularities due to input slit and end detectors at the CEA entrance and exit, respectively. For an *Ideal cylindrical analyzer*, the coefficients C_θ and C_E are given by eq. 2.7 [2.9],

$$\begin{aligned} C_\theta &= 2^{-1/2} \sin(2^{1/2} \phi) \\ C_E &= 2^{-1} [1 - \cos(2^{1/2} \phi)] \end{aligned} \quad \text{eq. 2.7}$$

Where ϕ is the CEA's azimuth angle ($= 90^\circ$) (Figure 2.4).

eq. 2.7 gives $C_E = 0.8$ and $C_\theta = 0.56$ for the energy and angle dispersion coefficients of the 90° CEA. The equipotential between the CEA plates for the ideal mode has been simulated in SIMION [2.7] is presented in Figure A2.1 (Appendix 2). The coefficients for energy and angle dispersion as obtained from the simulations are in very good agreement with the theoretical

value (Figure A2.2). The next section presents the numerical simulations for the traditionally used *Normal mode* operation for 90° CEA.

2.3.2. Normal mode operation of 90° CEA

The conventional operation of cylindrical analyzer is in normal mode. In this mode the potential for central line trajectory (ψ_0) is maintained at 0V by applying symmetric voltages on the curved electrodes. Figure 2.4 (left) shows the schematic and equipotential field lines for normal mode of the 90° CEA with the geometric parameters as indicated in the Table 2.1. It should be noted that equipotential lines are symmetric at the input and the exit of the analyzer. The following section presents the numerical simulations for normal mode.

SIMION [2.7] software was used for simulating the secondary ion beam trajectory inside the cylindrical analyzer. The simulations were aimed to provide the numerical estimation of energy and angular dispersion coefficients. Figure 2.5 shows the energy and angle dispersion coefficients determined from the characteristic plots for normal mode operation. On the left graph is plotted the energy dispersion (C_E) for three input energies 19.7, 20, 20.3 keV and for 3 different initial positions: central $\Delta R_{\text{slit}} = 0$ and $\Delta R_{\text{slit}} = \pm 2$ mm above and below the central line. On the right graph is depicted the angular characteristic plot for the nominal angle (zero degree) and an input angle change from $+2^\circ$ to -2° for the same three input positions ($\Delta R_{\text{slit}} = 0$ and $\Delta R_{\text{slit}} = \pm 2$ mm). The coefficient for energy dispersion (C_E) and angle dispersion (C_θ) were calculated as follow.

Using eq. 2.6, for three input beams with no angle dispersion ($\delta\theta = 0$) at the input, we can re-write it as eq. 2.8,

$$\Delta r = C_E \delta E + \delta r \quad \text{eq. 2.8}$$

From eq. 2.8, C_E is the linear slope for the plot of Δr vs δE (Figure 2.5, left).

Similarly, for determination of angular dispersion coefficient for three input beams with no energy dispersion ($\delta E = 0$) at the input, we can re-write eq. 2.6 as eq. 2.9,

$$\Delta r = C_\theta \delta\theta + \delta r \quad \text{eq. 2.9}$$

From eq. 2.9, C_θ is the linear slope for the plot of Δr vs $\delta\theta$ (Figure 2.5, right).

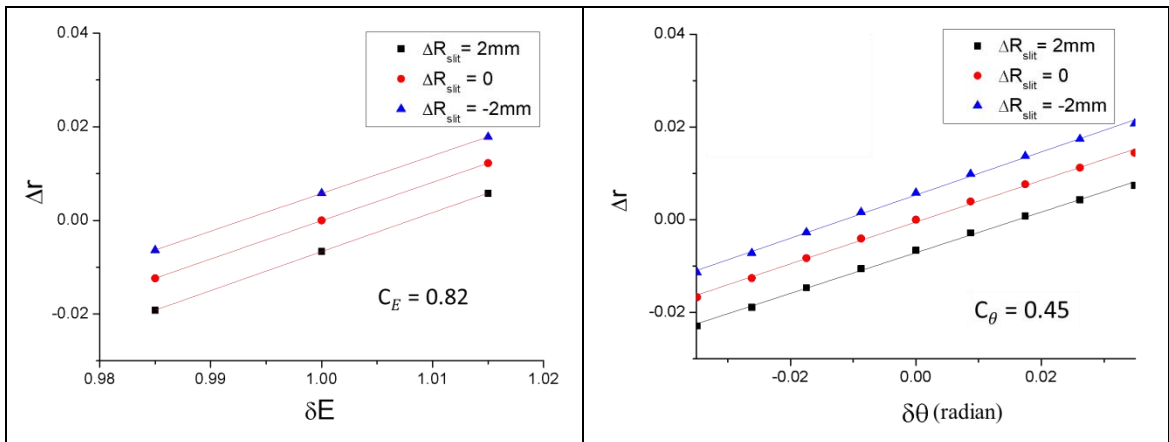


Figure 2.5 Characterization graphs for the normal mode operation showing the relative beam position at the end of CEA as a function of a) input energy and b) input angle.

Figure 2.6 depicts the ion beam trajectories simulated in SIMION software. Figure 2.6 (left) shows the trajectories of 3 beams with energy $20 \text{ keV} \pm 0.3 \text{ keV}$ without any angular dispersion at the input and $\Delta R_{slit} = 0$. The ΔR_{det} measured gives is used to compute $\Delta r = \Delta R_{det} / R_0$, Δr is then plotted with respect to $\delta E = \Delta E / E_0$ to obtain C_E (eq. 2.8) as shown in Figure 2.5 (left graph, red circles). The measurements were repeated for $\Delta R_{slit} = \pm 2 \text{ mm}$ to obtain the blue and black points in Figure 2.5 (left graph).

Similarly, Figure 2.6 (right) shows the 3 trajectories of mono-energetic beam (20 keV) with input angle dispersion of $\pm 2^\circ$ ($\sim 0.07 \text{ radian}$) and $\Delta R_{slit} = 0$. The normalized shift at the detector, Δr , measured in this case was plotted with respect to $\delta \theta$ to obtain C_θ (eq. 2.9) as shown in Figure 2.5 (right). The measurements were repeated for $\Delta R_{slit} = \pm 2 \text{ mm}$ to obtain the blue and black scatter points.

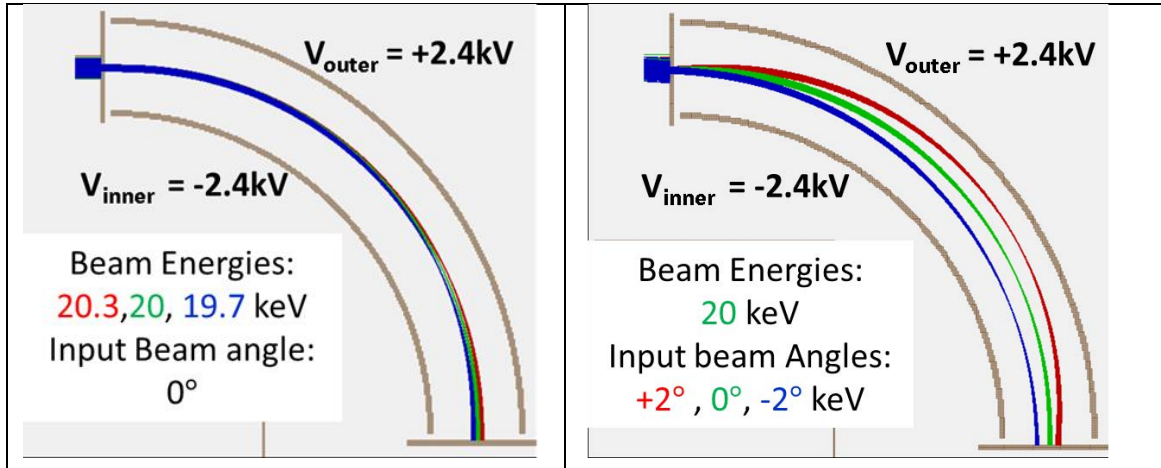


Figure 2.6 Simulation for energy (left) and angular (right) dispersion for 90° ideal CEA normal mode (+2.4/-2.4 KeV) with grounded central line trajectory.

The dispersion coefficients for the normal mode operation are given as $C_E = 0.82$ and $C_\theta = 0.45$ from Figure 2.5. It should be noted that the angle dispersion coefficients for normal mode ($C_\theta = 0.45$) is lower if to compare with ideal analyzer ($C_\theta = 0.56$). The decrease in the C_θ is attributed due to inclusion of electric field disruption (fringing fields) at the entrance and exit of the analyzer in normal mode (Figure 2.4) as opposite to the equipotential field lines for the ideal analyzer (Figure A2.1). However, the comparable value of C_E and C_θ for normal mode operation is undesirable for an ideal energy analyzer as described below.

In the normal operation of the 90° CEA, the value of energy coefficient is $C_E = 0.8$. Assuming a mono-energetic parallel ion beam entering at the slit center, $\delta r = 0$, and at zero angle with the analyzer axis, $\delta \theta = 0$, we find that for the target energy resolution $\delta E \sim 10^{-3}$, the corresponding value of Δr is $\Delta r = 10^{-3}$, which implies beam position measurements in the range of 0.215 mm (for $R_0 = 215 \text{ mm}$). This is rather demanding in experimental environment. Moreover, the angular aberration of the beam and input angle range (from the different sample volumes in the plasma) will contribute to the uncertainty in Δr via the coefficient C_θ . The fact that the energy coefficient is not strongly distinct from the angular coefficient for normal operation mode implies that the input angle dispersion will mask the detected positions Δr which for our application shall be only dependent of beam input energy dispersion. Therefore an optimization of this geometry was required and the goal of the simulations hereinafter presented is to develop improved energy analyzer geometry in order to reduce C_θ and maximize C_E such that the normalized beam displacement at the end of analyzer is predominantly dependent on the energy of the beam.

New approach:-

However if to reconsider eq. 2.5, if an ion with energy E_0 enters the CEA with a $\psi_0 \neq 0$, it will be decelerated along the central line trajectory and will reach the detector plate (also biased to ψ_0) with energy $E_{0det} = E_0/k_E$, where k_E is the deceleration coefficient, such that, $k_E = (1 - q\psi_0/E_0)^{-1}$.

In such case, the energy term in eq. 2.5 should therefore be rewritten to include a factor that reflects the energy coefficient of a beam with reduced energy. Hence Δr from eq. 2.6 shall be re-written as,

$$\Delta r = (C_E \delta E)_{deceleration} = k_E (C_E \delta E)_{normal} \quad \text{eq. 2.10}$$

eq. 2.10 indicates k_E times effective increase of sensitivity to the energy change as compared to normal mode.

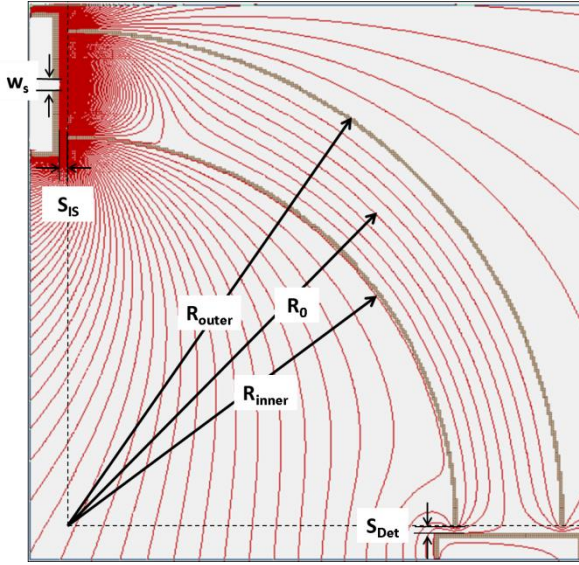
An estimation of the analyzed beam shift on the detector relative centerline (ΔR_{det}) for energy resolution of $\delta E = 10^{-3}$, gives a value $\Delta R_{det} \sim 0.17$ mm for normal mode ($k_E = 1$) and four times higher values ($\Delta R_{det} \sim 0.68$ mm) for double charged ions in two-times deceleration mode ($k_E = 2$). This opens the possibility of CEA operation in higher resolution deceleration mode besides the traditional normal mode operation ($\psi_0 = 0$). The next section investigates the deceleration mode in details.

2.4. CEA Deceleration mode operation

As mentioned in the previous section the use of the 90° CEA in the normal mode operation is not suitable as a high sensitivity energy analyzer due to relative low energy dispersion and competing angular dispersion. The prime requisite for the energy analyzer choice is to maximize the divergence at the end predominantly due to the energy fluctuations and tolerate input angles in the range of $\pm 2^\circ$ as determined by simulation on beam scans in practical energy and position ranges. Therefore, the aim is to minimize the angular aberration (C_θ) and increase the energy dispersion (C_E) beyond the normal mode. To that end, a new 90° CEA operation mode has been proposed [2.12] based on a decelerating longitudinal electric field. This deceleration mode takes advantage of the strong lensing properties of fringing fields generated at the entrance imposing a controlled deceleration of the beam inside the CEA with minimal angular dispersion.

This new CEA potential distribution is a combination of the retarding parallel plate and the cylindrical plate analyzers. The CEA entrance (grounded) and the detector (biased) are kept at different potentials in order to impose an internal retarding field along the beam trajectory. The outer and inner curved electrodes are biased symmetrically around the reference voltage of the retarding potential (ψ_0), which was zero in the normal operation and takes now some positive value. The role of the imposed deceleration is to subject the beam to the analyzer electrostatic forces for a longer time as compared with the non-decelerated beam.

In Figure 2.7 (left) is depicted the equipotential lines for a practical choice of electrode voltages. Two regions are well defined, the initial deceleration region with a clear lensing effect that focus the beam and the final analyzing region with a selected central average positive potential which bends and retards the beam until the detector. The values of the parameters indicated in the Figure are given in the Table 2.2 (on the right).



90° CEA: Deceleration mode	
V_{outer} / V_{inner}	8.59kV/7.61kV
ψ_0 / V_{Det}	8.1kV/8.1kV
V_{IS}	0V
R_{outer}/R_{inner}	240/190 mm
R_0	215mm
S_{IS}/S_{Det}	3/3 mm

Table 2.2

Figure 2.7 (left) Equipotentials of the CEA operation in Deceleration mode;(right) Table 2.2 presenting the values of the parameters indicated in the left. Where, V_{outer}/ V_{inner} are the voltages on outer and inner curved plates, V_0 / V_{Det} are voltages on central line and detector plate, V_{IS} is voltage at the input slit; R_{outer}/R_{inner} is the radii of outer and inner curved plate, R_0 is the radius of central line beam; S_{IS} is the distance between the input slit and input of the curved plate and S_{det} is the distance between the detector and end of analyzer (curved plates).

2.4.1. Characterization and optimized beam trajectories

Following the same approach as for the normal mode of operation (sec. 2.3.2.) the graphs for the energy and angle sensitivity for deceleration operation are plotted in Figure 2.8. The energy dispersion coefficient (left graph) is increased from 0.82 in normal mode to 4.02 in deceleration mode. The angular dispersion coefficient (right graph) is reduced from 0.45 to 0.01. Hence, the energy sensitivity increased 5 times and angular sensitivity decreased by 45 times as compared to the normal mode. This is quite clear by comparing the values of Δr between Figure 2.5 and Figure 2.8.

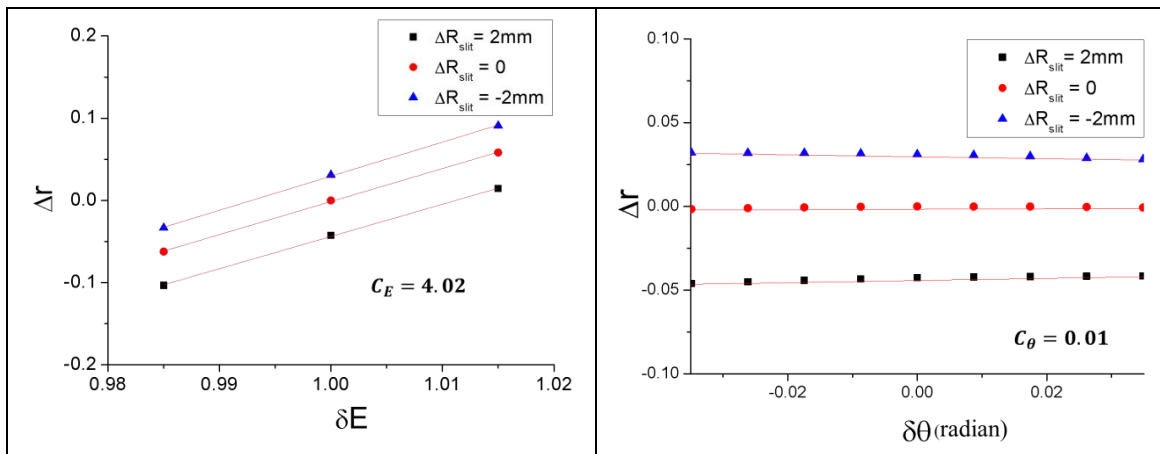


Figure 2.8 Detector relative position graphs vs. Energy (left) and angle (right) for three different beam input coordinates indicating the improved coefficients values, C_E and C_θ , in deceleration mode operation. The three scatter plots in each plot (red, blue and green) correspond to $\Delta R_{slit} = 0, \pm 2$ mm i.e. deviation of the input beam from the standard central line.

In the simulation results of Figure 2.9 (a) the input initial angle was kept ($\theta_{in} = 0^\circ$), while changing the beam input energy $E_0 = 20 \pm 0.3$ keV which corresponds to the typical mean plasma potential variation in ISTTOK. The beam separation at the detector is relatively large and certainly more evident than in Figure 2.6 (left). Figure 2.9 (b) presents the beam trajectories obtained for $E_0 = 20$ keV beam under a change of input angle of $\pm 2^\circ$ degrees to the initial angle ($\theta_{in} = 0^\circ$). As expected from the value of the angular coefficient obtained, the beam position at the analyzer end is practically insensitive to the input angle change of $\pm 2^\circ$ deg. The beam footprint is also larger as shown in Figure 2.9c (it increased from 2.5 mm to 10 mm) as a consequence of the strong lensing effect which moves backwards the focal point of the trajectories. If required, this effect can be compensated by additional guard rings, as will be shown later.

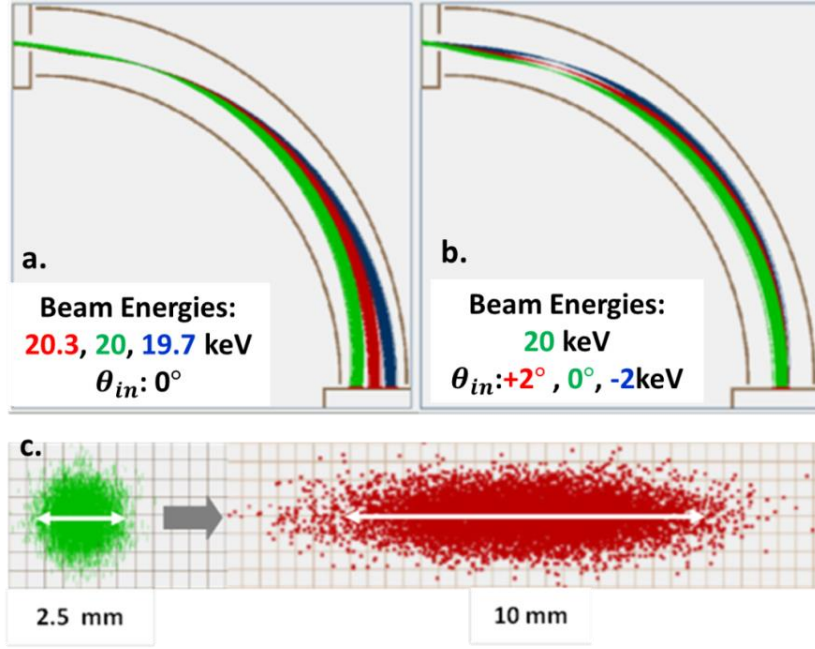


Figure 2.9 Simulated beam trajectories for deceleration mode; Presents the simulation of three beam trajectories as follows (a) three beam energy with no input angle variation and (b) single beam energy with three input angle as indicated; (c) shows the magnification of the beam in the energy dispersion direction from input (2.5mm) to output (10mm). The biasing voltages on the electrodes is the same as mentioned in Figure 2.7 (right) [2.12]

2.4.2. Detector parameters for position Split-plate detection

The HIBD standard split-plate (i.e. dual cell) detection [2.1] is schematically depicted in Figure 2.10. For a homogenous square beam, of width w_b on the detector, the shift (Δr) on split-plate due to energy change can be translated to the difference of beam current on the right, i_R , and left, i_L , plates can be presented as eq. 2.11.

$$\Delta r = (i_R - i_L) / (i_R + i_L) (w_b / 2R_0) = \delta i (w_b / 2R_0) \quad \text{eq. 2.11}$$

Where $\delta i = (i_R - i_L) / (i_R + i_L)$ is the normalized beam current indicating the effective shift of the beam from standard central position, w_b is the width the beam at the split-plate and R_0 is the radius of central standard trajectory.

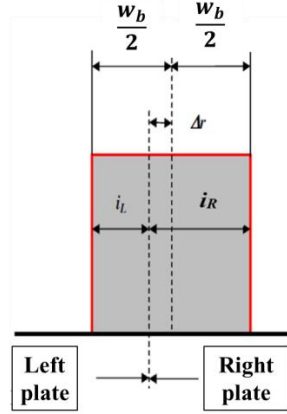


Figure 2.10 Split-plate detection principle.

The corresponding energy difference, δE , can be extracted from eq. 2.6 and eq. 2.11, for $\delta r = 0$ (central beam input position) and $\delta\theta = 0$ (zero input angle), and written as

$$\delta E = (d/2R_0) \delta i C_E^{-1} \quad \text{eq. 2.12}$$

Or for the plasma potential, φ ($\Delta E = \varphi$), where $\delta E = \Delta E / E_0$ (eq. 2.6), we can re-write eq. 2.12 as:

$$\varphi = (d/2R_0) \delta i E_0 C_E^{-1}. \quad \text{eq. 2.13}$$

From eq. 2.13 the dynamic range of the analyzer for a square uniform beam on the split-plate detector, $\Delta\varphi_{DR}$, can be determined by eq. 2.14 (within the limit of $\delta i = \pm 1$)

$$\Delta\varphi_{DR} \leq 2[(w_b/2R_0)/C_E] E_0 \quad \text{eq. 2.14}$$

The minimum detectable change in plasma potential for split-plate ($\Delta\varphi_{min}$)_{SP}, is determined by the signal-to-noise ratio (SNR) of the current on the detector plate. By replacing $\delta i = (\text{SNR})^{-1}$ in eq. 2.14, we obtain ($\Delta\varphi_{min}$)_{SP} (eq. 2.1):

$$(\Delta\varphi_{min})_{SP} \geq [(w_b/2R_0)/C_E](\text{SNR})^{-1} E_0, \quad (\delta i = (\text{SNR})^{-1}) \quad \text{eq. 2.15}$$

Estimations for dynamic range ($\Delta\varphi_{DR}$), and resolution ($\Delta\varphi_{min}$) of the analyzer in absolute values and beam energy of $E = 20$ keV for normal and deceleration mode are presented in Table 2.3 (for $\text{SNR} = 2$). Also, as an illustration, Figure 2.11 presents a visual representation of two Gaussian beams $w_{b0} = 1.5$ mm of width and $\Delta\theta = \pm 0.5^\circ$ of divergence differed in energy on 20 V (20 keV top and 20.02 keV bottom).

Operation	C_θ	k_E	C_{Eeff}	$\Delta\varphi_{DR} / \Delta\varphi_{min}$ (V/V) ($w_b = 10$ mm)	$\Delta\varphi_{DR} / \Delta\varphi_{min}$ (V/V) ($w_b = 6$ mm)
90° CEA					
Normal	0.56	1	0.8	$\pm 500/50$	$\pm 300/30$
Deceleration	0.01	5	4.02	$\pm 116/12$	$\pm 70/7$

Table 2.3

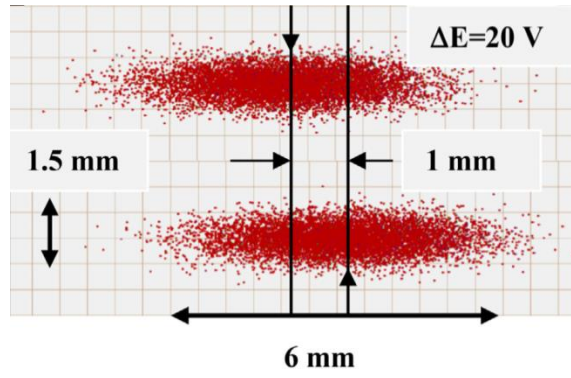


Figure 2.11 Beam energy sensitivity: the image shows the shift in the beam mean position for the change in energy of 20V in the beam input energy.

2.5. The 3D Simulation of the analyzer

The previous results characterized the properties of the 90° CEA analyzer in the 2D geometry. This section will cover the 3D design for optimized 90° CEA geometry as determined by the real HIBD beam trajectory from plasma to the detector as well as by the geometric constraints of the detection system (vacuum chamber layout).

Figure 2.12 presents the optimized design for 90° CEA resulting from the SIMION simulations. The following design modifications in regard to the 2D approach were introduced:

- The proposed 90° CEA is designed to measure the absolute plasma potential and its fluctuations in multichannel operation mode. The experimental set up consists of an input CEA single long slit (Figure 2.12a) that collects the probing beams from the 4 different plasma positions, each corresponding to different radii. A corresponding end Multiple Channel Analyzer Detector (Figure 2.12 a, b) (MCAD) is also added. The parameters of the CEA electrodes are given in Table 2.4.
- The CEA is installed inside a grounded stainless steel 6 way cross flange 200CF (Figure 2.12a). The height of the analyzer and the radii of the curved electrodes were chosen in order to fit inside the cross flange.
- Guard rings are placed on top and bottom of the CEA to preserve and control the equipotential at the top and bottom end (Figure 2.12c).

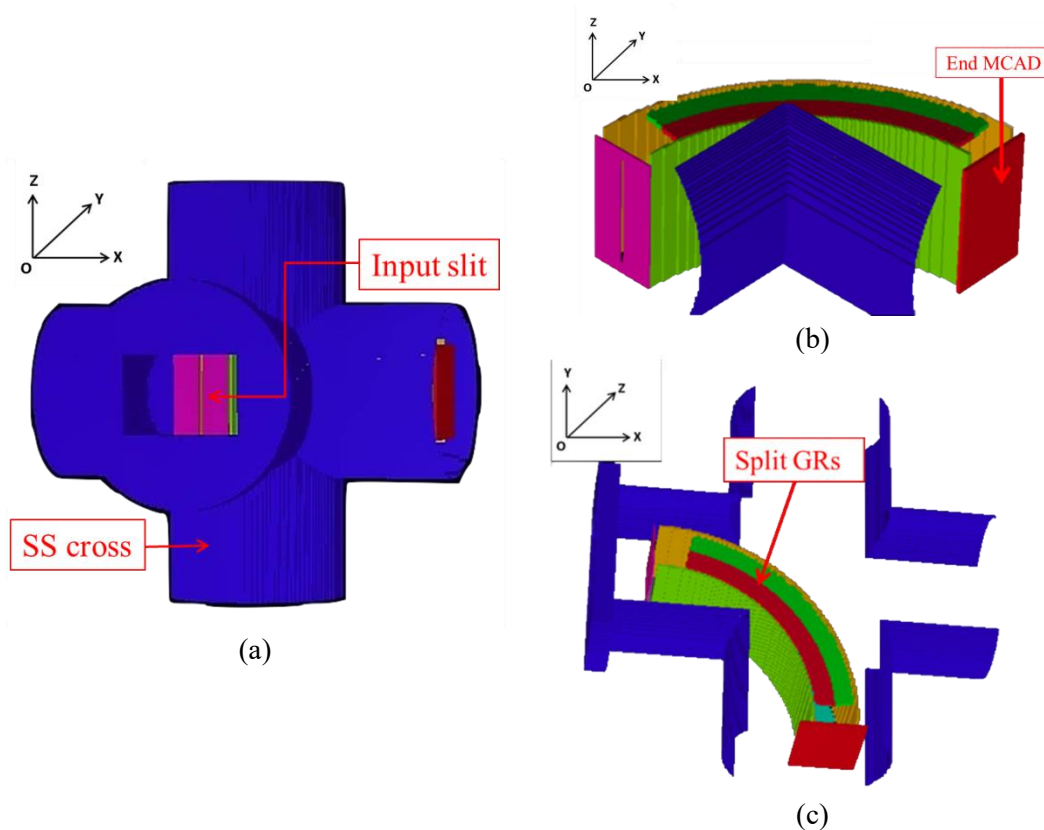


Figure 2.12 Modified 3D 90° CEA design in SIMION software. The CEA is installed inside the 6 way cross vacuum chamber (a); input slit (b), end detector (MCAD) and (c) longitudinal split guard rings.

R_{outer} (mm)	R_{inner} (mm)	R_{mean} (mm)	Electrodes Height (mm)	Vertical distance b/w guard rings (mm)
240	190	215	120	110

Table 2.4

The following subsection explains the design and the advantage of using guard ring. It is also presented the optimization of the beam trajectories for the 4 beam channels in multi-channel mode of operation.

2.5.1. Guard rings: Design and optimization

The proximity of the grounded vacuum chamber walls disturbs the electric field between the CEA plates, as compared to ideal standalone case. SIMION simulations confirmed this has an effect on the beam trajectories inside the CEA. To minimize the perturbations introduced by housing chamber walls, a pair of double Guard Rings (GRs) has been added between the CEA curved electrodes. In Figure 2.13 are shown the four beam trajectories under the influence of the grounded SS cross chamber (a) and after the equipotential correction introduced by the GRs (b).

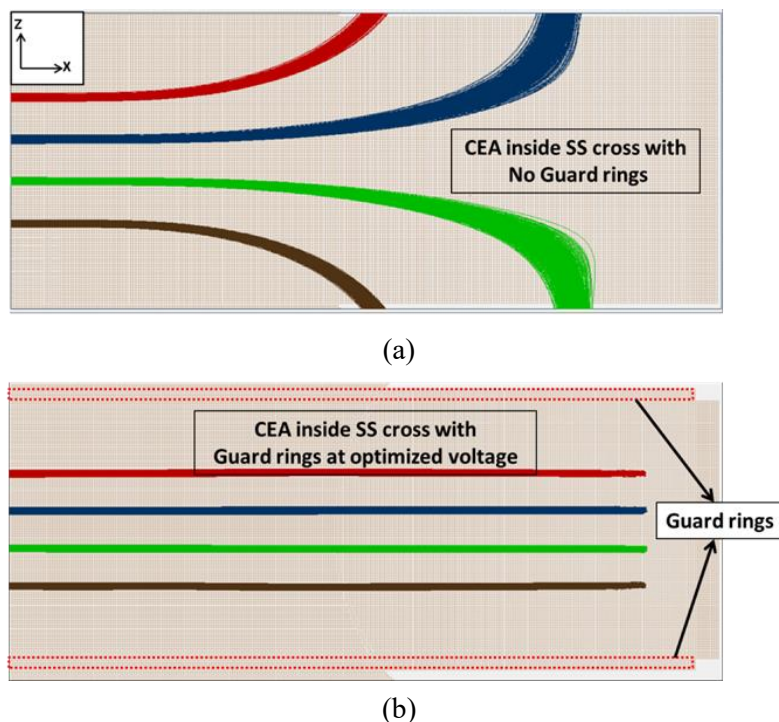


Figure 2.13 Influence of vacuum vessel; Influence of the SS cross chamber (at ground potential) on the trajectory of the 4 beam channels without guard ring (a) and in the presence of Guard ring with optimized voltage (b)

It is interesting to visualize the equipotential distribution inside the CEA. In Figure 2.14 a vertical cross-section of the CEA is shown with the equipotential field lines between the cylindrical electrodes for three cases: (a) CEA without the enveloping vacuum chamber (standalone CEA), (b) CEA inside the vacuum chamber and (c) CEA with guard rings added on top and bottom of the analyzer and inside the vacuum chamber. It can be observed that in the case (b) the analyzer field lines are perturbed (biased) towards the position of the detector,

unlike in the ideal case (a). By choosing the guard rings geometry and optimized voltage one can recover the symmetric analyzing field pattern (c).

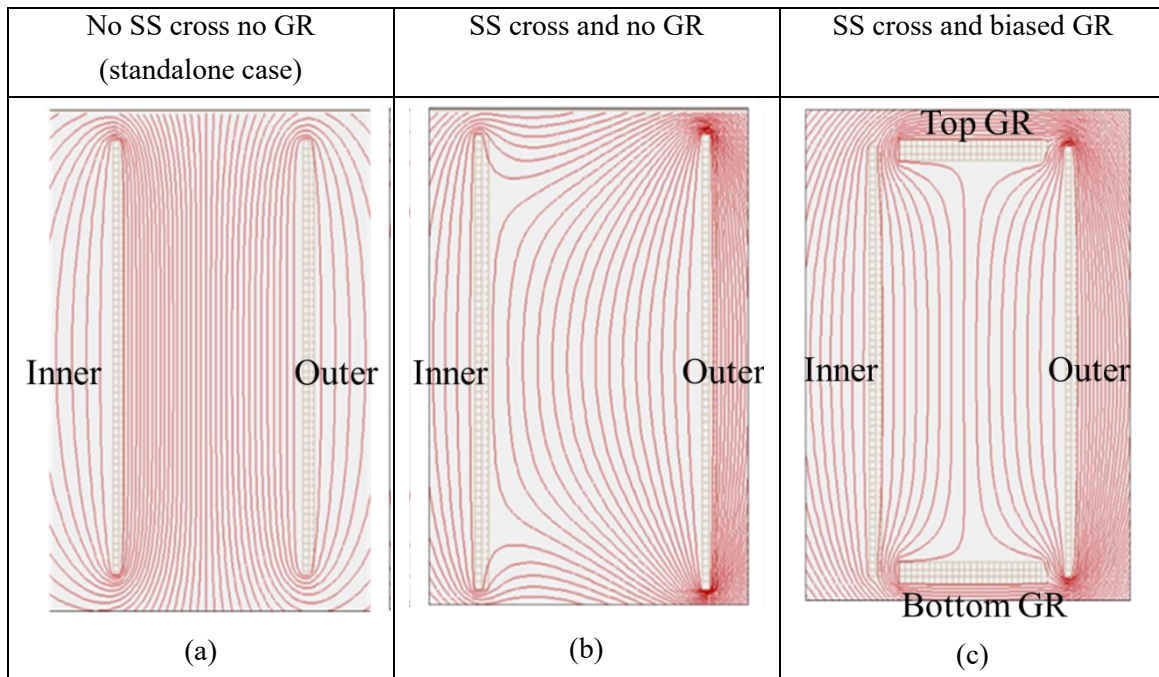


Figure 2.14 Map of equipotential lines in a transverse plane inside the CEA curved plates ('inner' and 'outer' refers to electrodes plates position) for three cases: (a) without SS cross and guard rings - uniform field lines at the edge, (b) with SS vacuum chamber and no guard ring - shows the effects of fringing fields at the edge and (c) SS chamber and optimized GRs - restores the equipotential as in (a).

Furthermore, in order to achieve a more uniform voltage distribution at the edge of the curved plates the guard rings are split into two pair, each element can be operated independently with optimized voltages (Figure 2.15). The Guard ring is split in order to better approximate the logarithmic distribution of equipotential field lines between the analyzer electrodes. The GR elements are placed inside the analyzer 5mm from each electrode. The GRs do not cover the whole 90° sector of CEA (GR azimuth angle is $\varphi = 75^\circ$), keeping gaps of $\varphi = 10^\circ$ at the entrance and 5° at the exit. This gap is of particular importance at the entrance of the CEA to maintain the lensing properties of fringing field, being optimized by simulations.

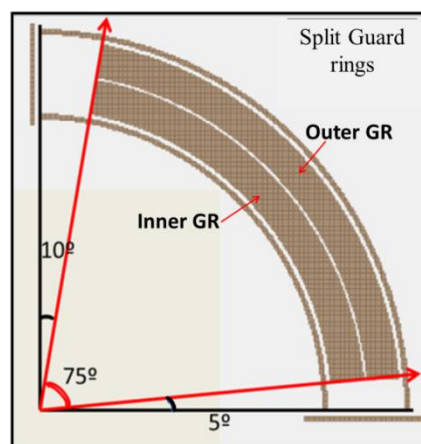


Figure 2.15 Displays the top pair of split guard ring as modelled in SIMION.

2.5.2. Optimization of beam trajectories

This section concerns the study of the reference beam trajectories obtained for the 4 beam channels by optimizing the voltage on the CEA electrodes. The optimization was performed to obtain maximal energy dispersion and minimal angular aberration at the detection position – MCAD position.

Figure 2.16 shows trajectories from four beam channels in the two planes, Z-X (a) and Y-X (b), of CEA. Each channel consist of 3 beam different energies: 19.7 (blue), 20 (green), 20.7 (red) keV. The beam dispersion at the end MCAD for each channel is presented in Figure 2.16c. Optimized voltage on the various electrodes is presented in Table 2.5.

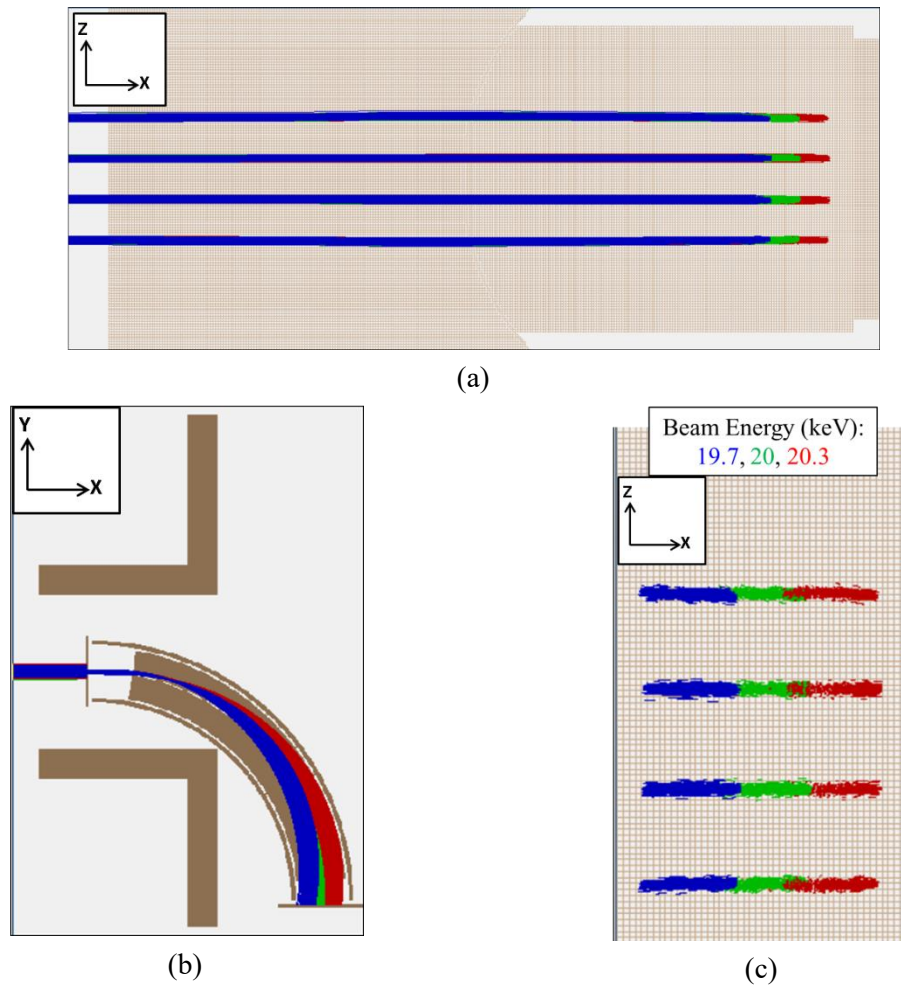


Figure 2.16 Presents the optimized trajectories for four beam channels (each with three beam energies as mentioned in c) for CEA inside SS grounded cross flange in Z-Y (a) and Y-X (b) planes. The beam dispersion position at the end MCAD for the 4 channels with energy 19.7, 20, 20.3 keV is shown in c.

Electrodes	Voltage (kV)
$V_{\text{outer}} / V_{\text{inner}}$	8.69 / 7.66
$V_{\text{GR-inner}} / V_{\text{GR-outer}}$	7.95 / 8.46
V_{MCAD} / V_0	8.175 / 8.0

Table 2.5 Optimized Voltage on electrodes for CEA electrodes for Figure 2.16. Where $V_{\text{GR-inner}} / V_{\text{GR-outer}}$ are the voltage for inner and outer GR pair, respectively.

2.6. Experimental Characterization of the CEA ½ size prototype

This section presents the design, simulation and experimental validation of the proposed CEA deceleration operation mode. A CEA prototype of 1/2 scale has been designed and built in order to investigate this new type of operation as described in previous sections and predicted by SIMION simulations. The characterization of the prototype CEA was experimentally conducted using an energy adjustable 2 keV electron beam [2.13].

2.6.1. Experimental setup

The 3-dimension mockup of CEA is shown in Figure 2.17 (simulation) and Figure 2.18 (as installed) indicating the arrangement of various electrodes. Due to the reduced dimensions, the ½ size-CEA was used only for a single central beam channel. The dimensions of the prototype are shown in the Table 2.6. The detection of the beam during biased deceleration voltage was modified to allow detection at ground potential by adding two grids in front of the (now) grounded detector. The first grid is the deceleration grid (DG) (mesh 1) and the second is the secondary electron emission (SEE) suppression grid (SG) (mesh 2). The split plate guard ring proposed for the full size CEA is replaced here by a single pair of guard rings (top and bottom) which is sufficient for the present case as the beam travels in the inner central part of the analyzer. The CEA is housed inside a smaller 6 way cross CF100 vacuum chamber (replicating the CF 200 version). The entrance slit of the CEA is located at 100 mm from the last extraction electrode of the electron gun. In Figure 2.18 it is shown the picture of the ½ size-CEA built for the experiments. On the left is possible to see a phosphorus screen detector used in the initial test experiments before the implementation of the split-plate detector. The split-plate detector was later added to the central part of the phosphorus screen to collect the beam current while allowing for the visualization of the beam distribution.

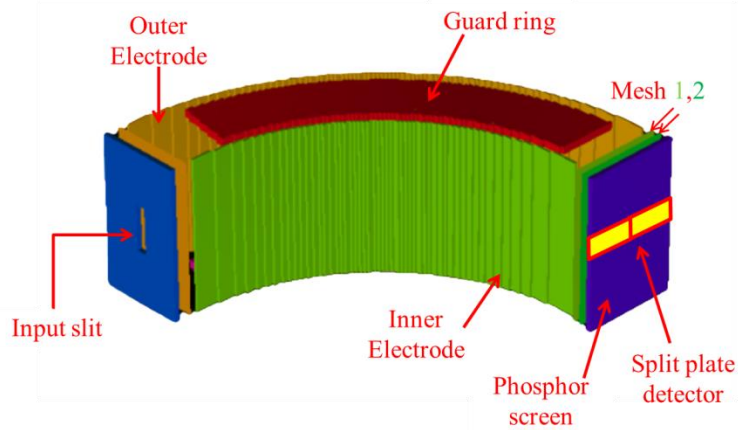


Figure 2.17 Model of the ½ mock up CEA implemented in SIMION.

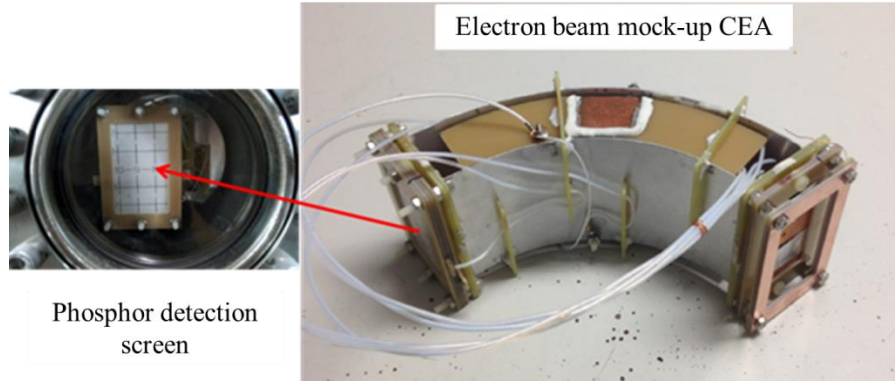


Figure 2.18 Experimental test prototype (right) end detection Phosphor screen (left)

EG^*	R_{inner}	R_{outer}	R_0	H_{CEA}	S_{EG}	S_{DG}
$16 \times 30 \text{ mm}^2$	90 mm	120 mm	105 mm	60 mm	3 mm	3 mm

Table 2.6

Where, EG is dimension of the whole entrance window in respectively vertical and horizontal (energy dispersion) directions;

R_{inner} , R_{outer} , R_0 are the inner, outer and central CEA radii;

H_{CEA} is the CEA height;

S_{EG} is the longitudinal distance between the entrance slit and CEA electrodes;

S_{DG} is the longitudinal distance between CEA electrodes and deceleration grid (DG).

2.6.2. Design of guard rings for the test prototype

As discussed before, in the absence of guard rings the proximity of vacuum chamber walls causes disturbance in electric field between the CEA plates which in turn affects the analyzer operation. Such influence on the beam transmission inside CEA prototype is shown in Figure 2.19. It shows the simulated trajectories of electron beams in the two planes (XZ and XY) and the beam images at the CEA exit detector for (a) normal and (b) deceleration mode. The electron beam is simulated as a uniform parallel rectangular input shape ($4 \times 4 \text{ mm}^2$) with energies $E_0 = 1.7 \pm 0.1 \text{ keV}$ propagating along the CEA centerline for respectively normal (Figure 2.19 a) and deceleration (Figure 2.19b) operation modes. The voltages applied to the CEA for normal and deceleration mode are presented in Table 2.7

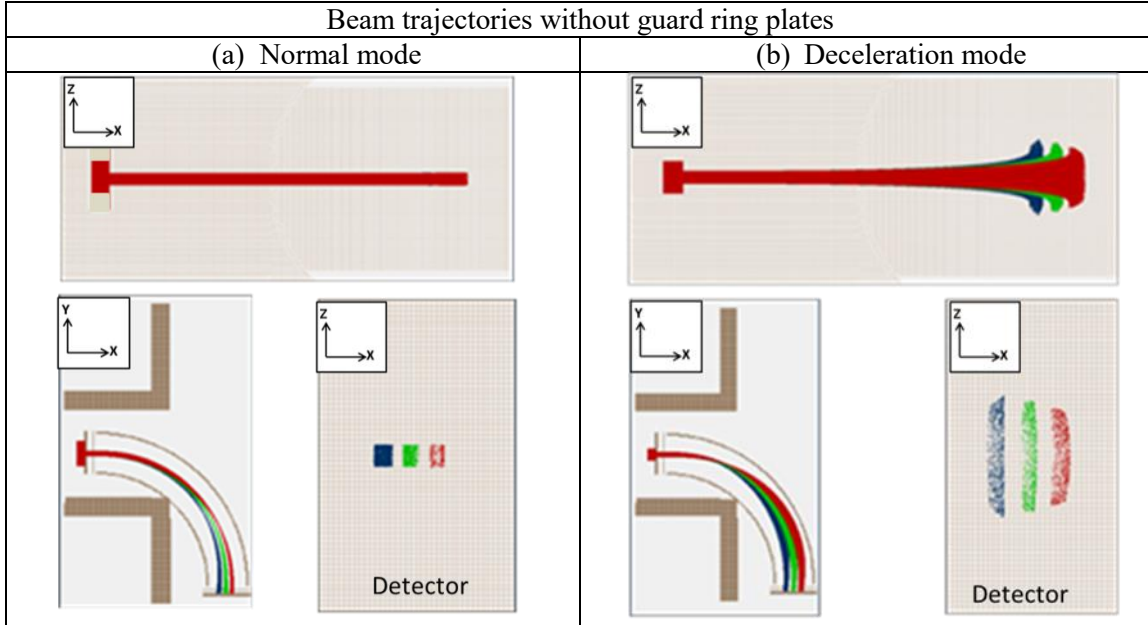


Figure 2.19 Electron beam trajectories (for $E_b = 1.6$ (blue), 1.7 (green), 1.8 (red) keV) (without GRs) inside the CEA and the corresponding images at the exit of the CEA in normal (left), $\psi_0 = 0$ kV (a), and deceleration (right), $\psi_0 = -0.85$ kV (b), modes.

Electrodes	Normal	Deceleration
V_{inner}	+0.44 kV	-0.65 kV
V_{outer}	-0.51 kV	-1.05 kV
$*V_{DG}$	0 kV	-0.85 kV

Table 2.7 $\frac{1}{2}$ -CEA electrodes voltages for Figure 2.19

* V_{DG} is the voltage on the deceleration grid (DG)

From Figure 2.19(a) it can be seen that for normal mode the beam shape and size are unchanged. Whereas in Figure 2.19(b) for deceleration mode a strong effective amplification of the beam size in vertical direction is observed due to the integral-length effect of the electric field distortion between CEA plates introduced by the vacuum chamber.

Simulations, like those presented in the Figure 2.19 have been repeated for the CEA with biased guard rings in normal and deceleration modes. The respective results for the GR voltages $V_{GR} = 0$ V in normal mode and $V_{GR} = -0.85$ kV in deceleration mode (equal to the voltage on DG) are shown in Figure 2.20. For normal mode (Figure 2.20a) the beam size is slightly elongated in vertical direction. Whereas for deceleration mode (Figure 2.20b) the beam size in vertical direction is almost unchanged, while, there is an effective magnification of beam size in horizontal (energy dispersion) direction as compared to the case without guard rings (Figure 2.20b). Such magnification was also observed in the results of [2.12].

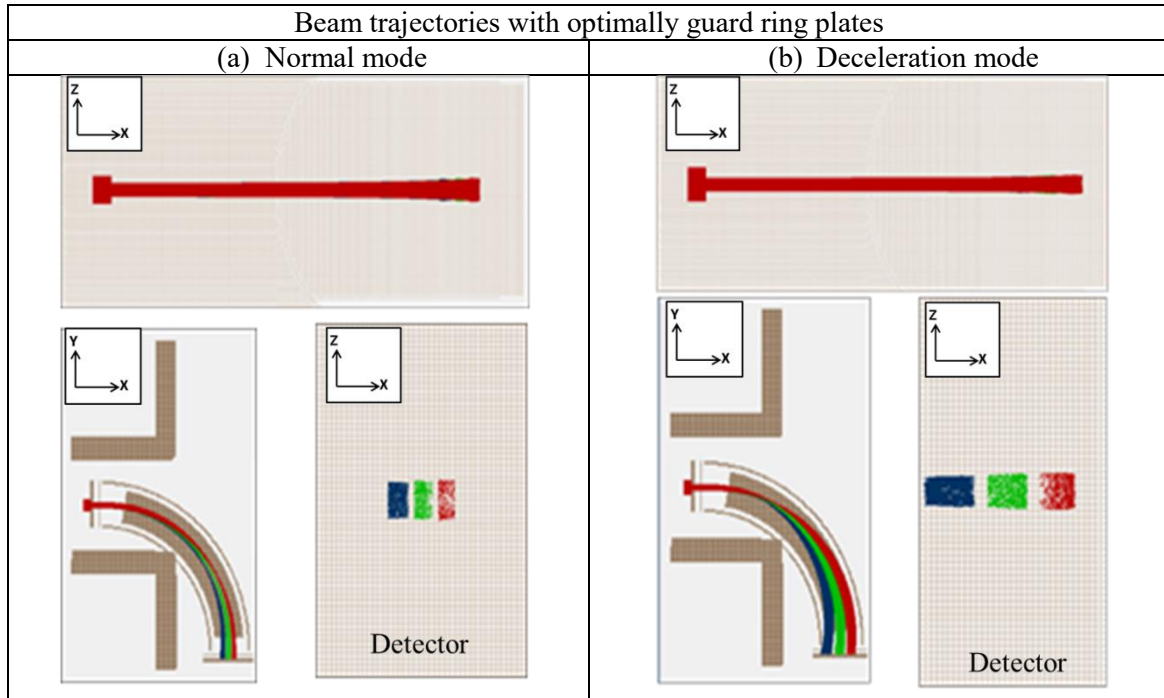


Figure 2.20 Electron beam trajectories (for $E_b = 1.6$ (blue), 1.7 (green), 1.8 (red) keV) inside and images at the exit of the CEA with guard rings in normal, $\psi_0 = 0$ kV (a), and deceleration, $\psi_0 = -0.85$ kV (b), modes.

2.6.3. Modified detection

The measurement of beam energy by the current difference between split-plates, or SPD (Ref [2.1]), biased to the deceleration potential was considered. As mentioned earlier, this approach was modified by an additional deceleration grid (DG) biased at deceleration voltage and followed by detection at the SPD (grounded). This approach allows the simplification of detection at ground potential. However, in such detection approach the Secondary Electron Emission (SEE) effect can lead to wrong results whether the CEA is used for the energy analysis of ion or electron beams. SEE refers to the emission of electrons from the metal surface, which occurs when the high-speed electrons or ions hit the metal cells of the detector. To overcome the SEE effect, the single detector end plate has been modified to accommodate two additional grids/meshes: the decelerating (mesh1) and the SEE suppressing (mesh 2) while the detector is maintained at ground potential as shown in Figure 2.21.

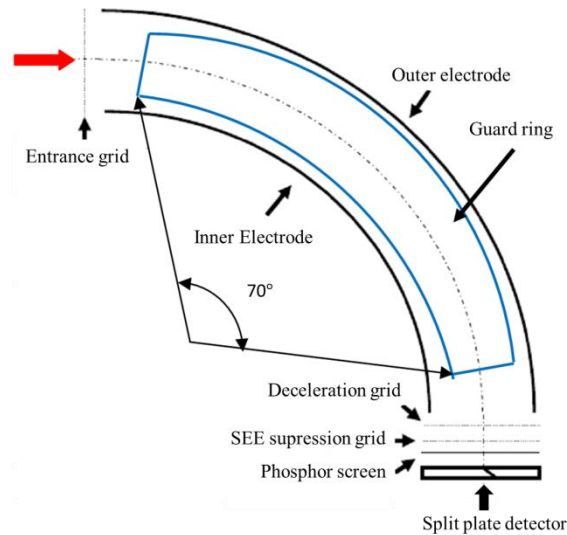


Figure 2.21 Schematics of prototype analyzer for detection at zero potential with additional two meshes.

Detection at deceleration grid

Figure 2.22a demonstrates the case when the beam is detected in the absence of any secondary electron suppression grid (SG). In Figure 2.22a are depicted the trajectories of 5 eV secondary electrons ejected from the surface of the deceleration grid (mesh1) held at the deceleration voltage of $V_{DG} = -850$ V. The applied voltages in the inner (-650 V) and outer electrodes (-1050 V) are indicated in the figure. There are three possibilities of the analyzed beam in split-plate detector being influenced by SEE:

- If the electron beam is completely on the right high energy side, the secondary electrons will be accelerated by the potential of the CEA outer plate and the detected signal will be determined by the current of the probing electron beam plus the secondary grid emission.
- If the analyzed electron beam is completely on the left low energy side, the secondary electrons will be collected by inner CEA plate and the signal will simply be the electron beam current.
- If the beam partially occupies both regions near the centerline an intermediate SEE contribution has to be considered.

For all of the above cases the measurement at the detection plate will be incorrect. Similar properties also characterize the normal mode of CEA operation.

To overcome the SEE effect, a secondary electron emission suppression grid (SG) is added between the deceleration grid (DG) and split plate detector (SPD) as shown in Figure 2.22b. The SEE suppression grid is biased more negative than the deceleration grid and the split plate detector is kept at ground potential. In such modified configuration of the detector part, applying the potential on the SG more negative than on DG, the SEE effect influence is completely avoided as demonstrated in Figure 2.22b.

Both meshes used in the experimental setup have 75 percent transparency. However, It should be noted that in such modified detector, the gap between the deceleration grid and detector plate at zero potential should be as small as possible (much smaller than beam trajectory length inside analyzer) to minimize beam shape distortions. The dimensions of the modified detector part of CEA are specified in Table 2.8

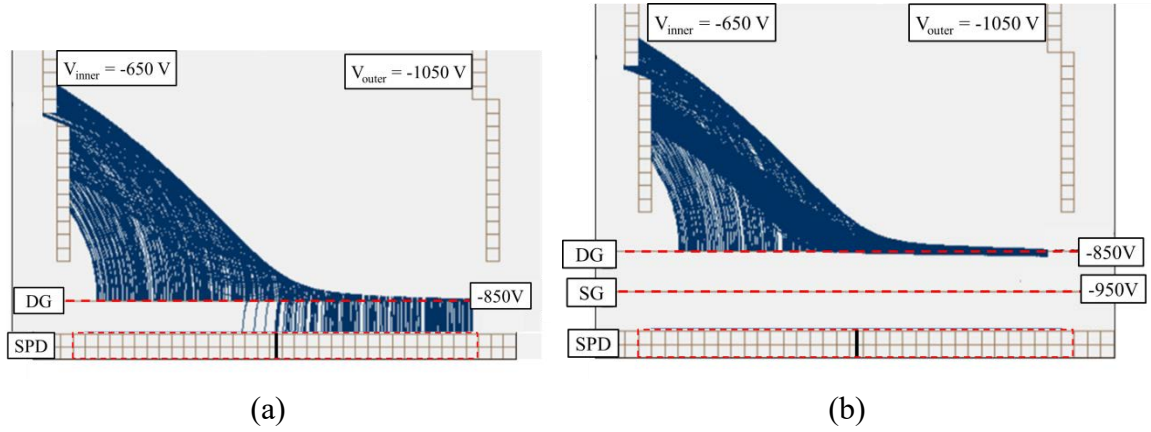


Figure 2.22 Secondary electrons trajectories from deceleration grid inside non-modified (a) and from deceleration grid of modified (b) CEA at deceleration mode. Where, DG = deceleration grid, SG = SEE suppression grid, SPD = split plate detector.

S_{DG}	S_{SG}	S_{PS}	S_{SPD}
3 mm	4.5 mm	6 mm	7.5 mm

Table 2.8

S_{DG} is the distance between CEA electrodes and deceleration grid;
 S_{SG} is the distance between CEA electrodes and SEE suppression grid;
 S_{PS} is the distance between CEA electrodes and phosphor screen;
 S_{SPD} is the distance between CEA electrodes and split-plate detector.

2.6.4. Experimental Results

The experiments with prototype CEA have been performed on test facility with strip-like shaped electron beam ($0.3 \times 12 \text{ mm}^2$ extraction slit). The mounting of the electron gun to the 6-way cross vacuum chamber allowed for $\theta_{in} \sim \pm 1^\circ$ adjustment of the input beam angle. The electron beam geometrical characteristics at the CEA entrance have been investigated by visual observation of beam image on the phosphor screen. The image dimensions indicate a beam size of 4 mm in horizontal (energy dispersion) direction and 16 mm in vertical (extraction slit orientation) direction with $\sim \pm 1^\circ$ divergence. The use of strip-like electron beam allows the simultaneous visualization of the beam shape and current collection by the SPD.

Figure 2.23a presents the electron beam image on the phosphor screen (top) and the corresponding simulated images (bottom) of $4 \times 16 \text{ mm}^2$ uniform electron beam (bottom) with $\sim \pm 1^\circ$ divergence (in horizontal and vertical directions). The experimented was conducted for 3 different beam energies of $E_0 = 1.7 \pm 0.1 \text{ keV}$ in normal mode. Considering the tolerances of prototype CEA fabrication, assembling and installation, the data in Figure 2.23c shows that the beam position, determined by beam energy and beam dimensions are in good agreement with simulations.

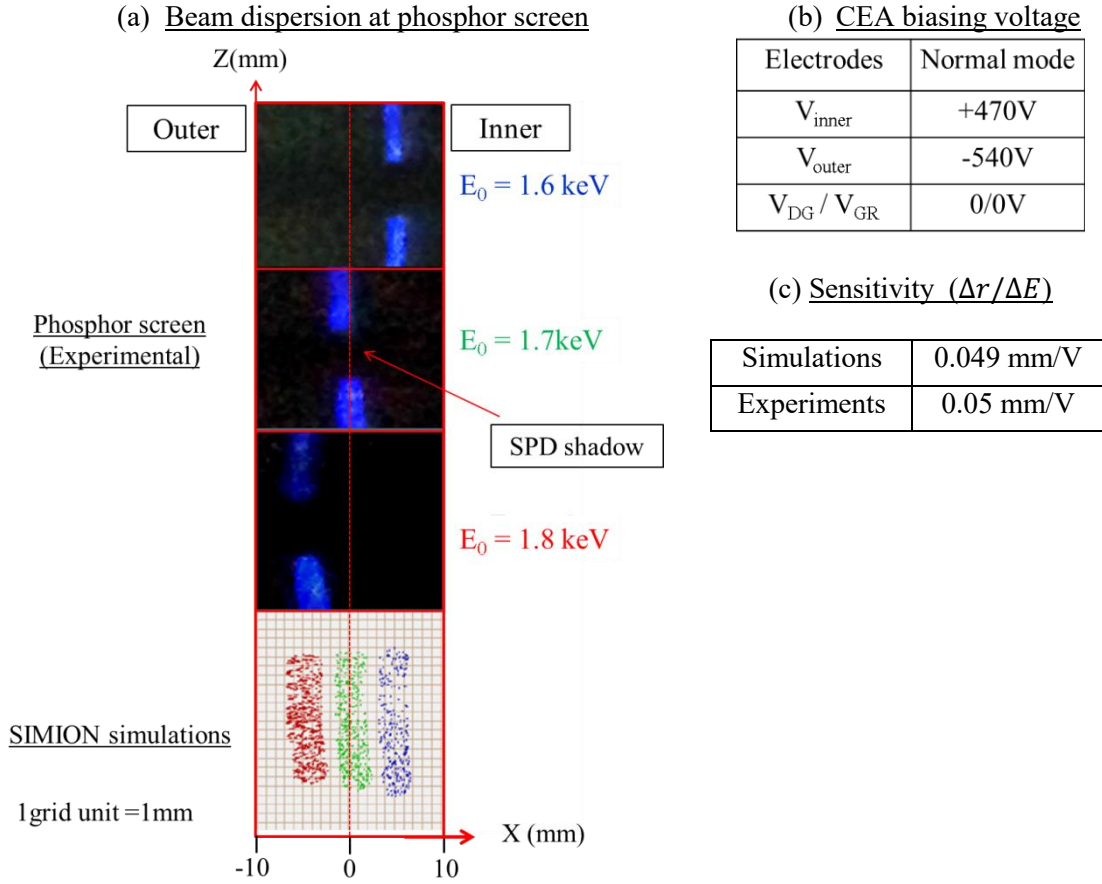


Figure 2.23 (a) Electron beam as observed on phosphor screen (photograph) for three beam energies (images stacked vertically) and (left bottom) simulated beam positions (overlapped) for same energies (on the bottom); The shadow on the middle of the phosphor images is due to the SPD incorporated in front of the phosphor screen; (b) table on the top mentioning the voltages on different electrodes and the (c) presents the $\Delta r / \Delta E$ (sensitivity) as obtained for simulation and experiment.

2.6.5. Experimental comparison between normal and deceleration operation modes

The eq. 2.6 gives the first order estimation of dispersion relation for the 90° CEA and eq. 2.11 provides the effective split-plate current-to-energy change characteristic (I - E characteristic) for $\Delta\theta_{in} = 0$. eq. 2.11 can be rewritten for deceleration mode (k_E) as:

$$\delta i = k_E C_E (w_b / 2R_0)^{-1} \Delta E / E_0 (\Delta\theta_{in} = 0) \quad \text{eq. 2.16}$$

Where, $\delta i = (i_R - i_L) / (i_R + i_L)$ is the normalized beam current indicating the effective shift of the beam from standard central position. C_E is the first order energy dispersion coefficient, $\delta E = \Delta E / E_0$ is the normalized ion energy, R_0 is the radius of standard trajectory, w_b is beam width at the detector plate and k_E is the degree of deceleration as described in eq. 2.10.

From eq. 2.16, the I - E characteristic depends on the beam width in energy dispersion direction, and, for the same beam widths, it should have steeper slope in deceleration mode. The slope of the I - E characteristic designates the energy resolution, $(\Delta E / E_0)_{res}$, being k_E -times better in

deceleration mode for the unaltered minimal resolved current δi_{min} . For the k_E -times decelerated beam, or a non-decelerated beam with k_E -times lower initial energy, the I - E characteristics should coincide. Also, the I - E characteristics should saturate at $\delta i = \pm 1$ when the beam is completely on one of the split plates, hitting the limit of the dynamic range of the measurements.

Figure 2.24 shows the I - E characteristics obtained for the beam energies of $E_0 = 1.8$ keV (B, black) and $E_0 = 0.9$ keV (C, red) in normal mode, and for the beam energy of $E_0 = 1.8$ keV in deceleration (D, blue) ($E_{dec} = \frac{1}{2}E_0 = 0.9$ keV) mode. The beam width in energy dispersion direction have been maintained at $w_b = 4$ mm by manipulation of the voltage applied to the Guard rings. The respective CEA voltages are specified in Table 2.9. The ΔV on the X axis refers to the change in beam energy in electron volts from the reference value for respective configurations: B, C and D (as mentioned in the graph).

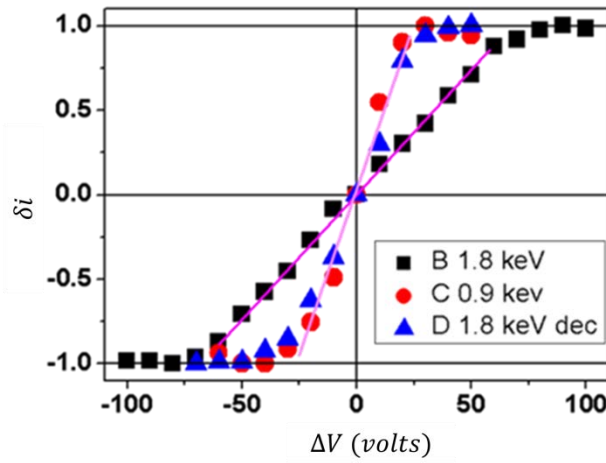


Figure 2.24 I - E characteristics: Split-plate I - E characteristics in normal and deceleration modes. B (black squares) and C (red circles) refers to normal mode operation with $E_0 = 1.8$ keV and 0.9 keV, respectively and D (blue triangles) refers to the deceleration mode ($k=2$). The voltages specification for the 3 cases is presented in Table 2.9.

Reference in fig.2.25	E_0 keV	V_{inner} kV	V_{outer} kV	V_{DG} kV	V_{SG} kV	V_{GR} kV	ψ_0 kV
B	1.8	+0.470	-0.540	0	-0.2	0	0
C	0.9	+0.240	-0.270	0	-0.2	0	0
D	1.8 (deceleration)	-0.650	-1.150	-0.9	-1	-0.72	-0.9

Table 2.9 Voltages applied to the CEA electrodes.

Where, V_{inner} and V_{outer} is the voltage applied on the inner and outer curve plate of the analyzer, respectively. V_{DG} , V_{SG} and V_{GR} are the voltage on deceleration grid, SEE suppression grid and pair of guard rings, respectively. ψ_0 is the mean potential at the central line trajectory.

The results in Figure 2.24 indicate that the dynamic range $(\Delta E/E_0)_{DR}$ is identical for beam energies 1.8 keV and 0.9 keV, being $(\Delta E/E_0)_{DR} \sim 6.7 \times 10^{-2}$, and the I - E characteristics for the beam energy of 0.9 keV and two times decelerated beam with energy of 1.8 keV coincide. Estimation with eq. 2.16 gives a value of $w_b \sim 5.8$ mm, which is in quite good agreement with simultaneous observations on phosphor screen and results of the respective simulations by

SIMION code shown in Figure 2.23. Results presented in Figure 2.24 completely confirm the expected features of the I - E characteristics and demonstrate the principle of the k_E -times energy resolution improvement by deceleration of the analyzed beam inside the CEA.

2.6.6. Analysis and comparison with simulations

Energy dispersion

Estimation of the energy dispersion, $\Delta r/\Delta E$, from the beam shifts in Figure 2.23 gives the value of $\Delta r/\Delta E \sim 0.05$ mm/V. Using eq. 2.6 with $\Delta\theta_{in} = 0$, the value of energy dispersion coefficient C_E can be estimated as $C_E = 0.81$ for $k_E = 1$ (normal mode), $R_\theta = 105$ mm and $E_0 = 1.7$ keV. The value of C_E and C_θ as given by SIMION code are mentioned in Table 2.10 and the dispersion graphs are added in Figure A2.3 and Figure A2.4. All the obtained C_E values are within $\sim 3\%$ of the theoretical value $C_E = 0.8$.

	Normal ($k_e = 1$)	Deceleration ($k_e = 2$)
C_θ	0.2	0.04
C_E	0.78	1.66

Table 2.10 Dispersion coefficients for angle (C_θ) and energy (C_E) for normal and deceleration mode.

Energy resolution

The eq. 2.16 gives the value of $\delta i_{min} \sim 0.2$ (limitation due to power supply, $\Delta V > 10$ eV) as reliable current difference resolution in experiment with electron beam and Figure 2.24 provide the calibration. For $w_b = 4$ mm, $R_\theta = 105$ mm, $C_E = 0.8$, eq. 2.16 gives $(\Delta E/E_0)_{res} \sim 4.8 \times 10^{-3}$ and $(\Delta E/E_0)_{res} \sim 2.4 \times 10^{-3}$ energy resolutions in normal and deceleration modes, respectively.

Angle aberration

Simulations by SIMION code give $C_\theta = 0.2$ and $C_\theta = 0.04$ for the angle aberration coefficient in respectively normal and deceleration modes. From eq. 2.6, the equivalent of effective energy change due to angle aberration can be estimated by equating $\Delta r/R_\theta = 0$. It gives respectively $(\Delta E/E_0)_\theta = 4.3 \times 10^{-3}$ and $(\Delta E/E_0)_\theta = 4.3 \times 10^{-4}$ in normal and deceleration modes for $\Delta\theta_{in} = 1^\circ$ of the experiments entrance angle variation range. The obtained values of $(\Delta E/E_0)_\theta$ are within the respective values of energy resolution, $(\Delta E/E_0)_{res}$, in normal and deceleration modes and explain the experimental observations of the respectively weak and the absence of sensitivity to the change of beam entrance angle inside the experimentally available range.

2.7. Conclusions

SIMION code has been used to investigate the applicability of 90° cylindrical energy analyzer as an energy analyzer for ISTTOK tokamak. A new approach for operation of the analyzer-deceleration mode was introduced. The new mode was based on beam retardation inside the analyzer by elevating the central line potential along with detection at deceleration bias voltage. The coefficient of energy dispersion was increased 4 times and angle aberration coefficient was decreased 45 times in deceleration operation as compared to normal operation of the analyzer.

Double guard rings were introduced on the top and bottom of the analyzer to compensate for the fringing field distorting the equipotential at the end due to the external SS cross chamber. The detection part of the analyzer was modified by adding deceleration grid (DG) and secondary electron emission suppression (SG) grid before the detection plate for maintaining the deceleration voltage till the CEA end while suppressing the SEE. As result of numerical simulations, the energy resolution of $\Delta E/E = (3-5) \times 10^{-4}$ has been obtained with strong decrease of the angular aberration in the range of $\theta = \pm 2^\circ$.

A prototype $\frac{1}{2}$ -size 90° CEA has been investigated both numerically and in experiments with electron beam in real operational conditions. A reasonably good agreement between the experimental results and the numerical simulation predictions was obtained. The CEA operation in deceleration mode has been demonstrated and confirmed experimentally. The energy resolution of $(\Delta E/E_0)_{\text{res}} \sim 2.4 \times 10^{-3}$ has been obtained in $k_E = 2$ deceleration mode of operation insensitive to the change of the analyzed beam entrance angle in the range of $\Delta\theta_m = \pm 1^\circ$. The prototype 90° CEA will be applied for the plasma potential and potential fluctuations measurements by HIBD on the ISTTOK tokamak (chapter 4).

Chapter 3

Electrostatic Input Module

3.1 Introduction

The installation of the cylindrical electrostatic energy analyzer (CEA) in ISTTOK requires the utilization of an intermediate module in order to control the secondary beams' trajectories. The Electrostatic Input Module (EIM) is used to collect, deflect and focus four beams emerging from four different plasma radii into the input of the CEA.

The main elements of the EIM [3.1] are:

- i) The front Multi Cell Array Detector (MCAD) containing the four collection input slits (each defining a plasma sampling volume).
- ii) Four pairs of short deflecting electrostatic cylindrical plates for beam bending followed by a set of parallel plates for beam steering.
- iii) The multiple aperture electrostatic Einzel-like lens.
- iv) The back Multi Cell Array Detector.

The EIM internal elements dimensions and the voltages applied were optimized by simulating the geometry using the SIMION code. In Figure 3.1(a) is depicted the global geometry of secondary beams trajectories and the location of the EIM-CEA modules. In the same figure it is presented (b) the general view of the integration of the EIM-CEA geometry in SIMION.

The following sections cover the EIM design description and optimization followed by its experimental characterization under the ISTTOK operating conditions.

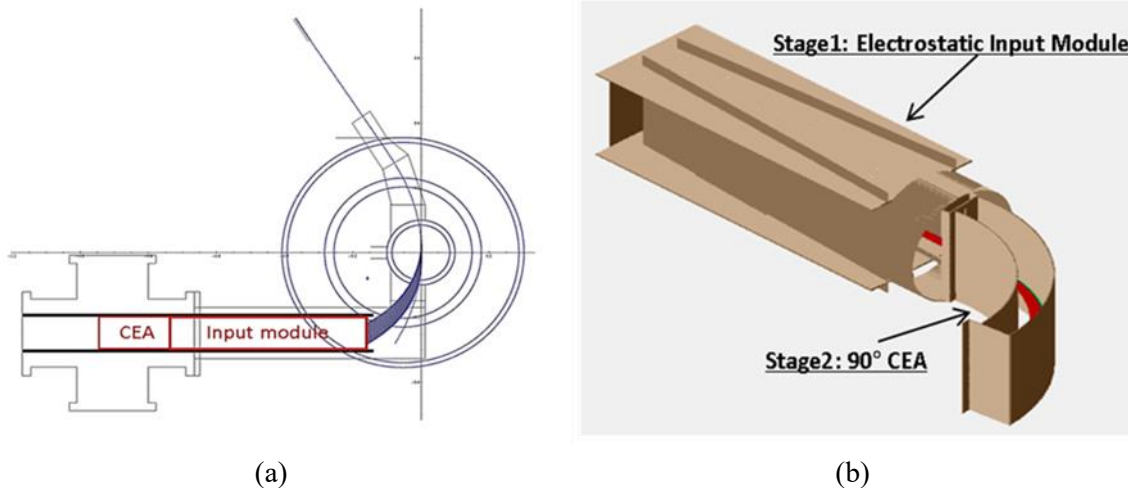


Figure 3.1 a) geometry of secondary ions trajectories and location of the EIM-CEA modules; b) detection system geometry consisting of Electrostatic input module (EIM) and 90° cylindrical energy analyzer (CEA) simulated in SIMION.

3.2 Electrostatic Input Module descriptions

3.2.1. Front detector

The front detector is a Multi Cell Array Detector (MCAD) based on a flat matrix of copper cells composed of 11 rows (height = 8 mm and width = 16 mm), with four of them equally split toroidally in three columns: 2 edge cells and one middle slit (Figure 3.2(a)). Each detector row corresponds to a unique radial position of the plasma sample volume. The four input slits ($8 \times 4 \text{ mm}^2$) on the front detector define the selection of four secondary beams (from four different plasma radii to be transmitted into the EIM. This front detector allows to obtain the toroidal position of the four probing secondary beams (used for the poloidal magnetic field measurements [1.13]) and also the $n\sigma(T)$ quantity (by measuring directly the collected secondary beam currents and in addition the passing four beam currents measured at the CEA back end detector, as will be shown). Each of the four EIM input slits define the sample volume vertical dimension of 8 mm and the vertical slit separation determines a plasma sample volume radial separation of circa 15 mm.

3.2.2. Cylindrical and parallel plates

The front MCAD detector slits are followed by four pairs of 30° electrostatic cylindrical plates aligned in a tandem arrangement with four pairs of parallel plates (Figure 3.2 (b)). The purpose of this arrangement is to bend and provide steering control of the secondary beams into the four aperture electrostatic Einzel-like lens. The secondary ions arrive at the front detector at a given angle to the normal of the detector surface (as calculated by the HIBD numerical code). This angle being different for each entrance slit requires specific voltages for each electrostatic pair to bend and steer the beam to the quasi-zero degree condition. The 30° cylindrical plates also provide some intrinsic focus of the beam in the vertical direction (YY). The ZZ direction focus is controlled later on other section of the beam line. The combination of the electrostatic cylindrical and parallel plates allows collecting and bending the beam within the required geometric constraints.

(a) Front MCAD

(b) Cylindrical and parallel plates (SIMION software)

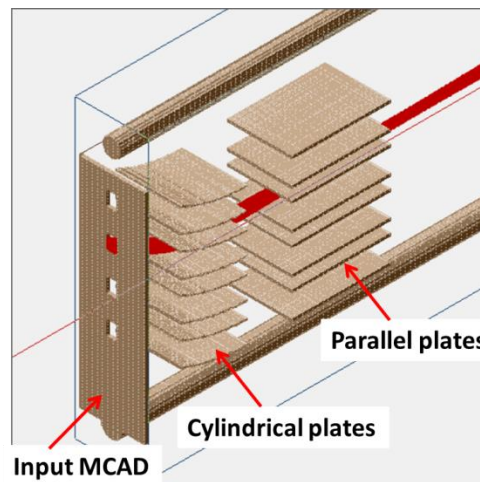
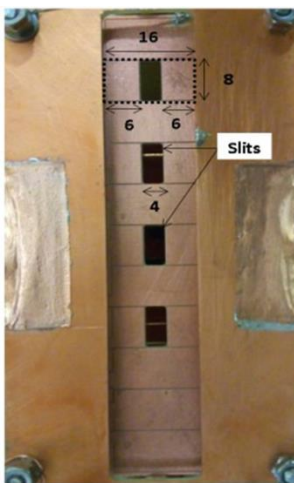


Figure 3.2 EIM components (a) input MCAD installed in EIM (b) Input MCAD, Cylindrical and parallel plates set as designed in SIMION software.

3.2.3. Einzel lens

The requirement for beam focusing can be better visualized from Figure 3.3 (top). The simulation shows the trajectory of the secondary beams, passing through 4 pairs of cylindrical and parallel plates. The natural beam divergence leads to some partial overlapping of the beams coming from different slits (corresponding to different plasma radii) as they reach the plane that defines the entrance of the CEA (not shown). Hence, a beam focusing unit is required to keep the four beams channels' trajectories from overlapping. To that end, a new design for a multi-aperture Einzel lens was proposed.

The multiple aperture Einzel-like lens in Figure 3.4 (b) consists of four planar vertical electrodes with four apertures. The voltages are specifically tuned to provide the required electric field gradient for shaping the four passing beams. In addition, there are four pairs of strip-like electrodes integrated on the sides along the beam trajectory allowing for beam fine shaping and deflection in the horizontal direction. Figure 3.3 (bottom) presents the four beams focused by the multi-aperture Einzel lens for optimized voltages. The Einzel lens is a crucial element for the EIM in order to shape the secondary beams into the required dimensions and ensure the required current density at the energy analyzer input slit (not shown).

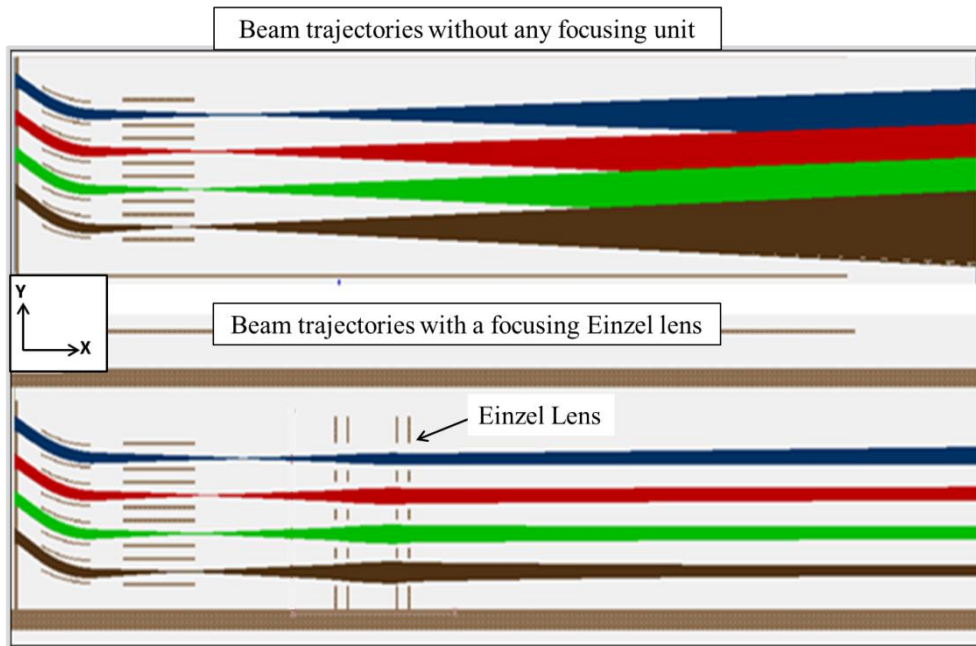


Figure 3.3 Comparison of the beam trajectories (in XY plane) Secondary beam (20 keV) passing through 4 pairs of cylindrical and parallel plates without any focusing unit (upper) and focused beam in presence of multiple aperture Einzel lens (lower). The optimized voltages on the elements are given in Table A3.1.

Figure 3.4 shows the equipotential map for a four channel conventional Einzel lens and the multiple aperture Einzel lens used in this experiment. The equipotential distribution is quite similar in both cases. The geometry of multi-aperture Einzel-like lens provides larger geometric acceptance and flexibility in beam shaping as compared with traditional Einzel lens. Another advantage of the multi-aperture Einzel lens is the simpler fabrication and the possibility to use internal pairs of strip electrodes for individual beam shaping and deflection (as previously noted).

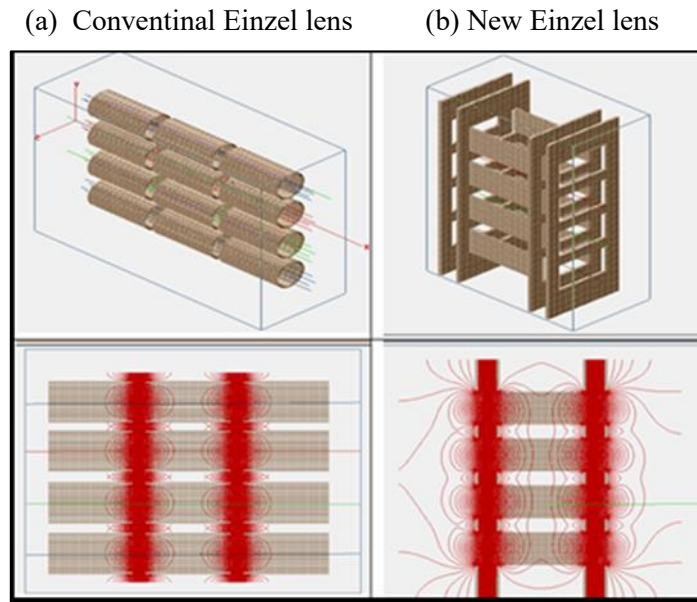


Figure 3.4 Illustration of similar equipotential map for a four channel conventional einzel lens [3.2] (a) and the new multiple aperture Einzel lens used in this module (b).

3.2.4. Back MCAD

The last element of the EIM is the Multiple Cell Array Detector. This detector is located (in the experimental setup) at a distance of 44cm from the front MCAD and is composed of a matrix of eleven rows and three columns (very similar to the front MCAD, but without apertures). The cell dimensions are 8 mm height and 4 mm width. The four secondary beams will be detected in current and in position (Y and Z).

3.3 Optimization: Geometry and operating voltages of the EIM internal components

The cells dimensions of the front and back MCADs were chosen based on information regarding the secondary beam current density and beam cross-section dimensions. The large experience accumulated in the operation of the HIBD in ISTTOK indicates that a 1 cm radial spatial resolution and a minimal 2 nA current detection (after filtration) could be achieved by the typical vertical cell size of 8 mm. The secondary beam width in toroidal direction is found to be between 12 and 15 mm (depending on injection parameters and tokamak pressure conditions). Therefore, a 4 mm cell width allows collecting the beam in 3 to 4 cells array which allows determining the average center of beam charge and its geometrical profile (keeping the 2 nA minimal current detection). These parameters are required to ascertain on the beam toroidal position and its fluctuations.

The voltages on the cylindrical plates and front parallel plates are chosen aiming at obtaining a longitudinally aligned beam. The focal point of this beam (Figure 3.3) and the position of the Einzel lens are set to provide an optimum size parallel beam at the detector (back MCAD).

The following parameters were optimized for einzel lens design to focus and optimize the beam position and shape at the back MCAD

3.3.1 Voltage at central and strip electrodes

The strip electrodes on the side of the Einzel lens (Figure 3.5 a,b) are added in the design and they assist with the beam shaping and focusing:

- By applying equal non-zero voltages on the strip plates the toroidal shape of the beam can be manipulated at the back MCAD. Figure 3.6 shows how the beam dispersion at the back MCAD can be changed in shape for the four channels as the voltage of strip electrode is equally changed by +120V to -120V from its reference voltage. The importance of optimization of the beam toroidal dimensions for each channel is to achieve an optimized signal to noise ratio while avoiding “optical aberrations” that could introduce non-linear effects in the determination of the beam toroidal position.
- The intrinsic focus by the 30° cylindrical plate in Y-axis is achieved at different location at X axis for each of the 4 beam channel (can be seen in Figure 3.3). The unequal beam dimension at the input of multiple-aperture einzel lens can be compensated by optimizing the biasing voltage for each channel of side strip electrodes to obtain similar beam dispersion at the input of analyzer.
- In addition, the strip electrodes are used to deflect each beam in the ZZ direction (for centering at the entrance slit of the CEA). In that case a voltage difference is imposed between the corresponding pairs. All the voltages have been individually optimized (as well as the width and length of the strip electrodes).

3.3.2. Optimizing the distance from the entrance of CEA

The distance between the front MCAD detector and the CEA entrance slit is fixed $L=60\text{cm}$. From one hand, the closer is the Einzel-lens from the CEA entrance the less voltage is required to focus the beam. On the other hand, as seen from Figure 3.3 (top), the secondary beams spread along the path therefore the lens must be placed closer to the focus point of the beams in order to avoid loss at the entrance of the lens.

3.3.3. Distance between the end guard plates and inner HV plates

The first and last plate of the Einzel-lens is kept at ground potential (Figure 3.5 b) avoiding global beam energy changes after the lens. The distance between the grounded end plates and the inner biased plates (d_1, d_2) (Figure 3.5b) were also optimized in simulations in order to provide a quasi-parallel beam path.

3.3.4. Shape of the input aperture of the Einzel lens

The Einzel lens consists of four rectangular shaped apertures of dimensions $8\text{mm} \times 12\text{mm}$ ($Y \times Z$). Circular apertures were also simulated exhibiting the same focusing-like effect. However, due to space constrain (and optimization requirements) the circular aperture cannot have a diameter larger than 12 mm, which limits the beam steering in the Z direction. Therefore the rectangular aperture was adopted.

The parameter scan for optimized voltages and dimensions of the Einzel-lens is summarized in Figure 3.5. The choice of the present geometry was driven by the minimal beam angular spread in the ZZ direction (ΔZ) (for maximizing the beam current entering the CEA input slit) and keeping also an acceptable beam spread in the YY direction (ΔY) (avoiding beam overlap and keep a relatively higher current density). All the parameters, voltages on the einzel lens electrodes, distance between the einzel lens plate (d_1, d_2) and width (w) of the strip plates are mentioned in the Table 3.1.

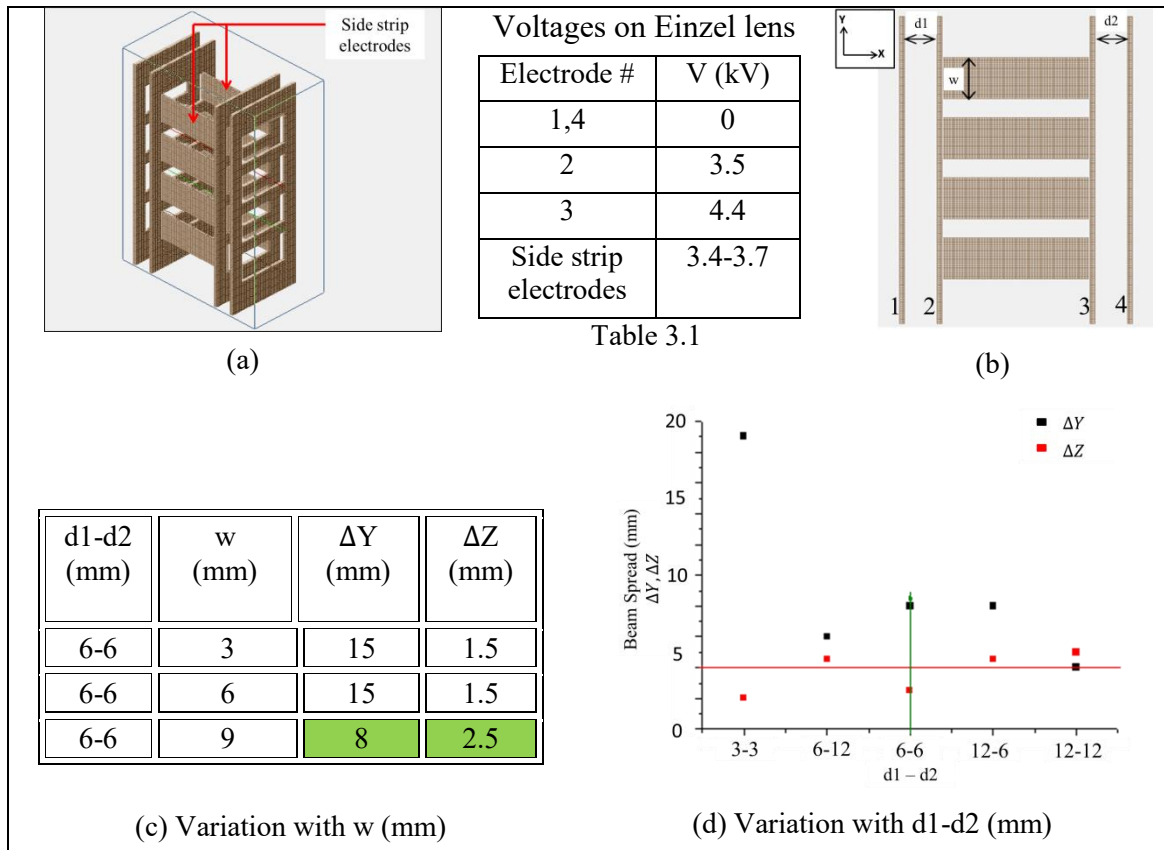


Figure 3.5 shows the 3D view (a) and XY plane (b) of the multiple aperture Einzel lens, the optimized voltages on the electrodes are shown in the table 3.1 in the center; table (c) presents the beam spread due to variation in width (w) of strip electrodes; graph (d) presents the optimization of d1-d2 with respect to the beam spread at the CEA entrance, the lens is optimized for beam spread $[8(\Delta Y) \times 2.5(\Delta Z)]$ mm at the entrance of analyzer for $[d1, d2] = [6, 6]$ mm. Electrode # in the table are mentioned in (b).

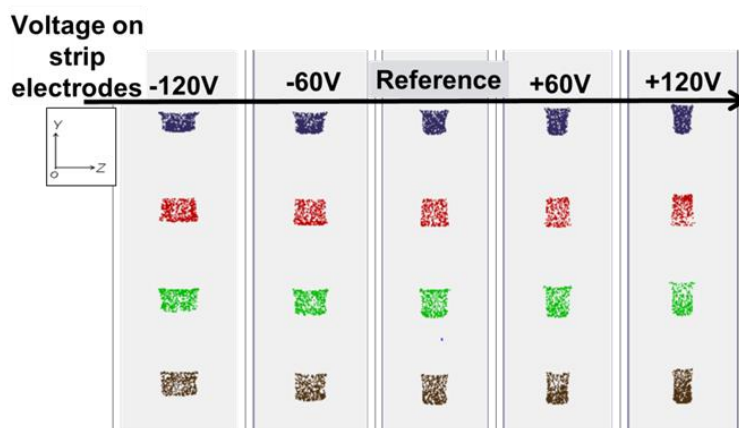


Figure 3.6 Beam shaping in YZ plane at the present MCAD position in the EIM, reference voltage at the strip electrode are, 3.4, 3.6, 3.57, 3.5 kV, respectively.

The simulation shows that by changing the reference 20 keV beam energy by the expected plasma potential value, the beam suffers a vertical shift of 1mm at the back MCAD (Figure 3.7, right). This vertical shift is due to the intrinsic energy analyzing properties of the EIM input 30° cylindrical plates (Figure 3.7, left a). This shift can be recovered by changing the voltage on the front parallel plate arrangement by 40V. In practice, the determination of the plasma potential is

not affected by this shift as it occurs in the vertical direction which is perpendicular to the direction of the measurements (toroidal). The flexibility and tolerance of the “optic” system was tested successfully for the expected $\pm 0.5^\circ$ angular uncertainty of each secondary beam at the entrance of the EIM (Figure 3.7, left b) and for the expected energy change of the beam (± 200 V), corresponding to different plasma positions inside the tokamak (i.e. different plasma potential).

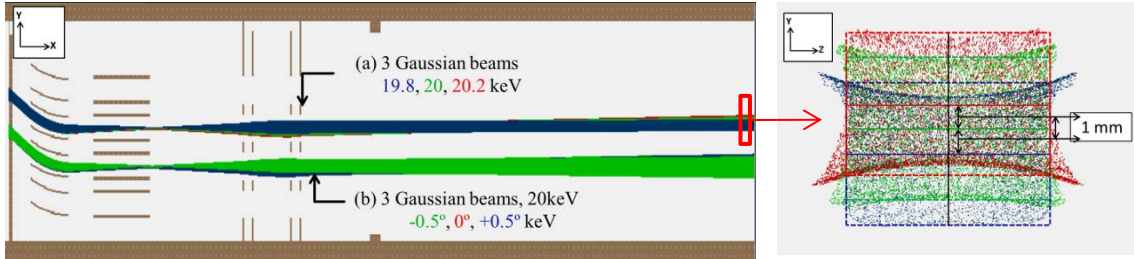


Figure 3.7 (left, a) Trajectories of three Gaussian beams with different energies: 20keV (green), 19.8 (blue) and 20.2keV(red), (right) overlapped beam footprint at the analyzer entrance for the three beam energies differing by 200V showing a shift of 1mm in the YY direction; (left, b) trajectories of 3 beams with input angle variation of $\pm 0.5^\circ$ (as expected angular uncertainty). The biasing voltage on the EIM components are mentioned ion Table A3.1.

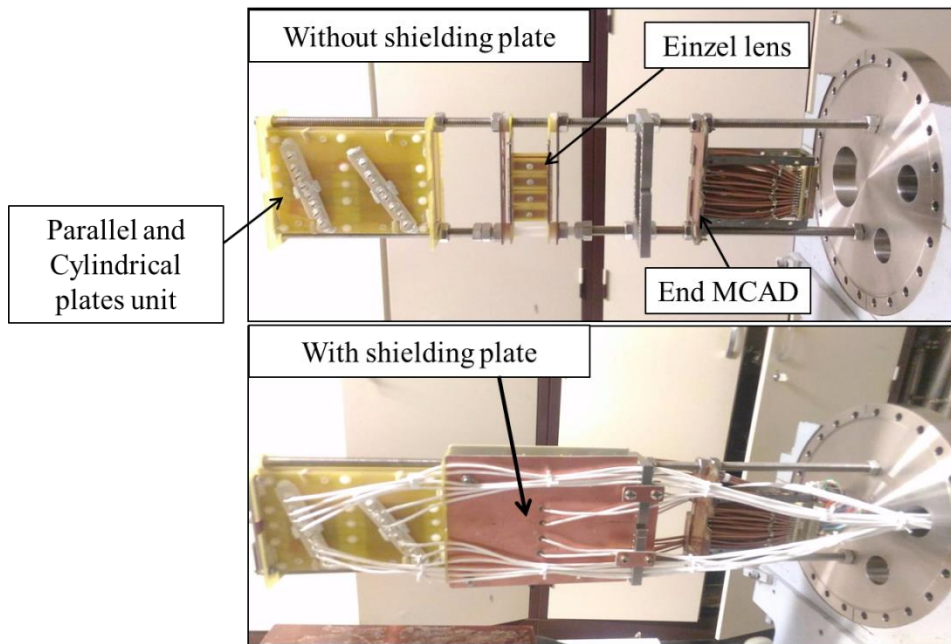
3.4. Experimental Characterization of EIM in ISTTOK

3.4.1. Experimental set up

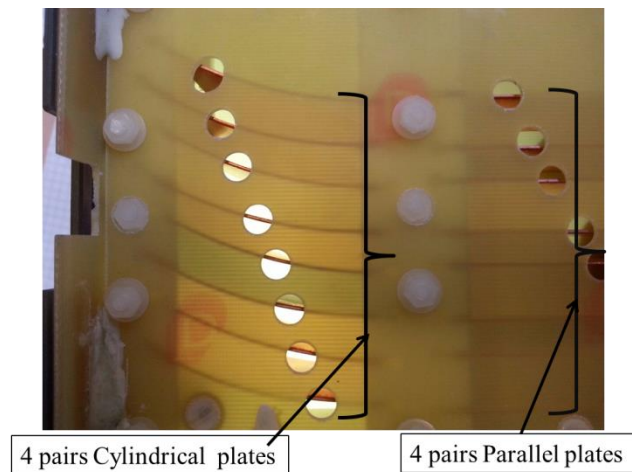
In order to verify and validate the above simulations, an experimental EIM setup was built and tested. The pictures of the experimental arrangement are shown in Figure 3.8.

In order to produce more realistic simulation results, several peripheral components were added into the simulation. These components could only be added in the simulation after assembling the EIM (for a realistic representation). The list of boundary elements added in the simulation is given below.

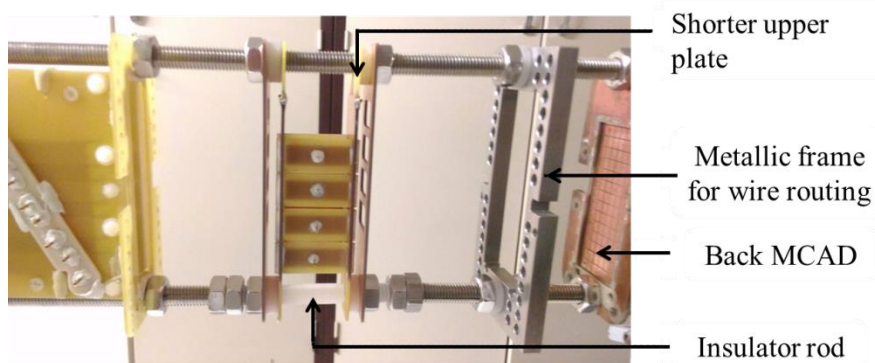
1. The whole set up is enclosed in a grounded enclosure as shown in the simulations in Figure 3.1b). The enclosure geometry corresponds to the shape of the ISTTOK port that will house the whole EIM setup. This port enclosure is grounded (is connected to the ISTTOK vessel).
2. Two stainless steel (SS) rods used for supporting the EIM elements were added (Figure 3.8).
3. The field lines of the lower aperture of Einzel lens were getting distorted due to the close proximity of the lower rod affecting the corresponding beam alignment. Thus, a part of the grounded SS rod was replaced with an insulator section (Figure 3.8, c).
4. Because of the top SS conducting rod physical location the inner electrodes of the einzel lens are shortened on the upper region (Figure 3.8, c).
5. The simulations have also shown deviations in the beam trajectory (in the Einzel less section) due to the grounded shield of the wires used for signal collection and also due to the bias voltage connectors. Therefore, two grounded plates were added on each side of the Einzel lens to avoid arbitrary influence of wires (Figure 3.8, c).
6. A grounded stainless steel metal frame was added after the Einzel-lens in order to route the wires properly (Figure 3.8, c), as well included in the simulation.
7. All remaining metallic surroundings like the flange and vacuum chamber were grounded and accounted for.



(a)



(b)



(c)

Figure 3.8 Picture of the Electrostatic ion setup without (a, top) and with (a, bottom) the ground shield plate in the sides of einzel lens; (b) see through view of the four pairs of cylindrical and parallel plates, (c) displays einzel lens with the incorporated insulator between the inner bottom plates, metallic frame to route the cables and back MCAD.

Figure 3.9 shows the picture of the assembled EIM from side (a) and front (b) views. In the side view, the location of the primary detector, front MCAD and back MCAD can be seen along with the Einzel lens inside the shielding plates.

There are 3 detectors installed on the EIM prototype used to detect the beam and are summarized in Table 3.2. These detectors are shown in Figure 3.9.

Detector	Beam detected	No. of cells
Primary	Primary	3
Front MCAD	Secondary	14
Back MCAD	Secondary	33

Table 3.2

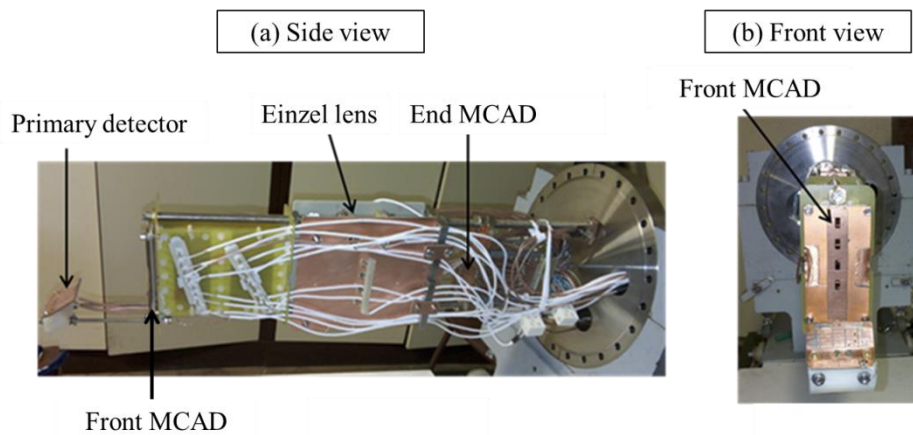


Figure 3.9 Pictures depicting the detectors location in the EIM experimental setup from the side (a) and front (b) view.

3.4.2. Experimental results

The EIM was installed in the HIBD detection port of ISTTOK. The experiments on the EIM prototype were performed to test and optimize the EIM electrodes voltages in order to collect the secondary beam at the back multiple cell array detector (MCAD). Figure 3.10 depicts the plasma current (I , in green) and plasma density (n , in red) evolution for standard AC plasma discharges. The particular ISTTOK discharge considered is a sequence of positive plasma cycles (except for the first one which is negative). The experimental conditions in the EIM were optimized for the positive plasma current cycles. The secondary beam passing through the second channel of the front MCAD was chosen to perform the trajectory alignment characterization.

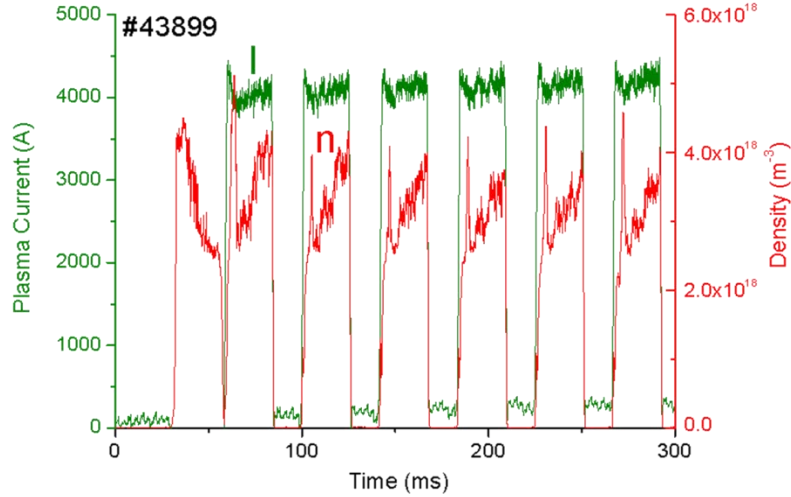


Figure 3.10 plasma current (green) and plasma density (red) evolution for plasma discharge #43899 at ISTTOK.

(i) *Beam Alignment*

A primary beam of Xe^+ ions with 23.5 keV energy and circa $1.3 \mu\text{A}$ current was injected into the tokamak. This primary beam current is collected in the primary detector (Figure 3.11a). The secondary beam (emerging from the plasma) alignment along the EIM was achieved by optimizing the voltage for each element of the EIM in a stepwise approach, in each tokamak discharge. The resulting optimized voltages on the EIM plates are presented in Table 3.3 .

Shot #	2 nd beam channel pair		
	Cylindrical $V_{\text{upper}}/V_{\text{lower}}$ (V)	Parallel $V_{\text{upper}}/V_{\text{lower}}$ (V)	Strip Einzel-lens $V_{\text{left}}/V_{\text{right}}$ (V)
43925	-1700/0	600/0	330/0
43927	-1700/0	600/0	380/0
43928	-1700/0	547/0	400/0
43929	-1700/0	547/0	400/0

Table 3.3 optimized voltage parameters on EIM prototype for 2nd beam channel.

(ii) *Signal detection*

The signals (from primary and secondary beam) observed on the detectors are presented in Figure 3.11. The plasma load on the detectors offsets the beam signal (Figure 3.11 a ,b). However the beam signal can be recovered by background subtraction due to the 200 Hz pulsed operation. The signals shown in Figure 3.11 were obtained after applying a low pass filter of 5kHz.

The secondary beam current (Xe^{2+}) collected on the front MCAD cell #29 (Figure 3.11b) is of the order of 60-100nA, depending on plasma temperature, density and primary beam current. The signal obtained on cell #11 of the back MCAD (is depicted in Figure 3.11c) ranges from 2 to 5 nA (20 times less than the front MCAD). This is because only a partial fraction of this current passes through the slit below the cell #29 on the front MCAD (for practical purposes here it is assumed that a similar secondary beam current reaches the detector line containing the

slit). In addition, the beam area is toroidally and vertically distributed in the back MCAD occupying several cells while only one cell-current is showed.

It is possible to evaluate some characteristics between both MCAD. The signal fluctuation divided by the signal amplitude is similar for both detectors, around 10-11%. This is expected if the collected signal comes from the same sample volume and its amplitude is determined mainly by the plasma fluctuations (including some primary beam fluctuation contribution). The background noise level ratio (measured when there is no plasma) between back MCAD and the front MCAD is about 10. This indicates that even without plasma some larger source of noise affects the front detector noise by about 10 times higher than the back detector. This could be attributed to the existence of some radiation coming from the background gas that is continuously bombarded with the primary source of electrons produced by the filament kept inside the tokamak chamber. This light does not reach the back MCAD. Finally, concerning Signal to Noise (S/N) ratio the front detector presents an $S/N = 12.8$ while the back MCAD presents $S/N = 3.8$. One must note that in the back MCAD the signal is spread between 4 cells (Figure 3.12) and if was collected in one single cell the S/N would become very similar to the front MCAD. The conclusion is that all relative detection properties seem to be conserved between the two detectors showing consistency in the detected signal properties.

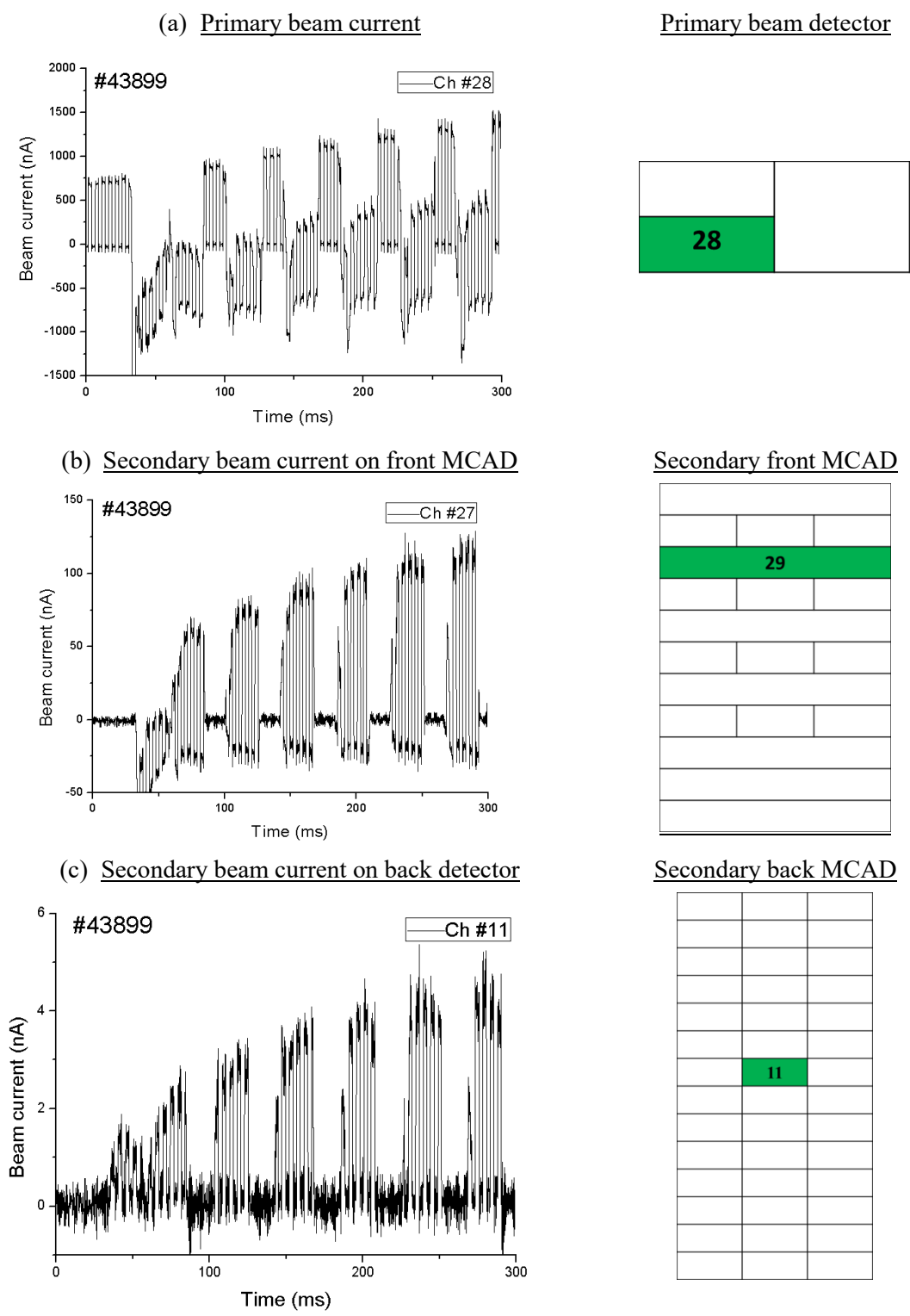


Figure 3.11 Signals on various EIM detectors primary (a), front MCAD (b), back MCAD (c) the right shows the position of the cell for the each corresponding detector. (a) primary beam (Xe^+) on primary detector during ISTTOK AC plasma operation (x - time in ms), (b) the secondary beam (Xe^{3+}) on front MCAD (b) detector and back detector (c) only existing for the periods where there is plasma.

(iii) *Beam Vertical Profile*

Figure 3.12 shows the secondary beam current for two plasma cycles. The beam covers vertically for 4 cells on the back detector. The position of these cells (#10, #11, #12, and #13) on the end MCAD is shown on the right. Figure 3.13 shows the secondary ion beam vertical distribution at the back multiple cell detectors. The distribution in the vertical direction (Y) gives information about the beam size and divergence at the input slit of the CEA. This data can be used to determine the beam size expected at the end of the CEA analyzer.

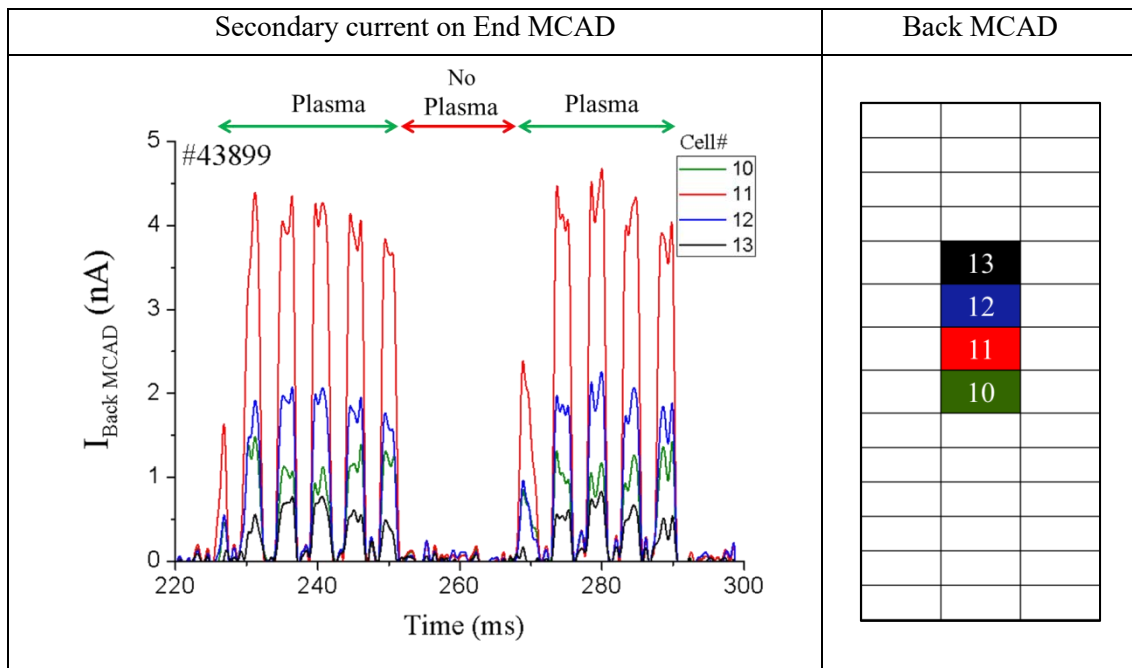


Figure 3.12 (left) Shows the secondary beam current on the end MCAD for two positive plasma current cycles for the four cells (#10, #11, #12, and #13). The location on the cell on the end MCAD is shown on the right.

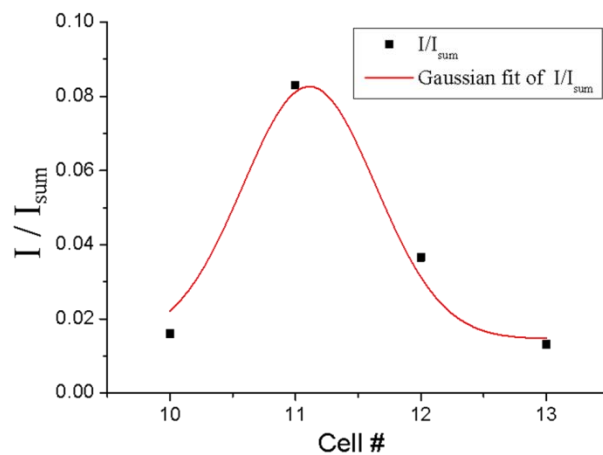


Figure 3.13 Normalized secondary ion beam current (I / I_{sum}) distribution in the vertical plane in the MCAD for the cell position on the MCAD (as shown in Figure 3.12 right).

3.5. Conclusions

This chapter summarizes the design, optimization and experimental results for the intermediate electrostatic input module unit. The simulations were performed to optimize the geometry and biasing voltages on the internal units in order to achieve a secondary beam dimension of $8 \text{ mm} \times 2.5 \text{ mm}$ without any overlapping between the four beams from different slits and without any loss of current at the CEA entrance slit. The beam distribution at the input of the analyzer can be further modified using the modified multi-aperture Einzel lens unit. The simulations indicate that changing the beam energy by 200V from 20KeV, shows a vertical shift of 1mm due to the initial 30° cylindrical plates. This shift can be recovered by changing the voltage on the parallel plate arrangement by 40V. The flexibility and tolerance of the optic system were tested successfully for the expected angular uncertainty of the beam by $\pm 0.5^\circ$ at the entrance and with the expected energy spread of the beam corresponding to different plasma positions inside the tokamak.

A prototype EIM setup was built and installed on HIBD at ISTTOK to verify and validate the simulations. The final design of the EIM prototype consisted of additional elements necessary during real installation and was verified with simulations. The secondary beam was aligned to observe the primary beam at the primary detector, secondary beam at the front detector and at the back detector at the end MCAD for the second channel. The vertical beam profile was obtained for the back MCAD placed at 44cm from the front detector. The alignment parameters obtained in this chapter were crucial to provide reference biasing values for the combined operation of the EIM and 90° CEA (as described in chapter 4).

Chapter 4

Installation and commissioning of the detection system

4.1. Introduction

This chapter presents the installation of the sub-systems previously described and the commissioning of the combined operation of the EIM and $\frac{1}{2}$ size prototype CEA (Figure 3.1). The first results of ISTTOK core plasma potential measurements comparing classical and deceleration operation of CEA are also discussed. The $\frac{1}{2}$ -size CEA is capable of confining only one beam channel at a time thus the EIM has been experimentally aligned and optimized for the second beam channel of the front MCAD (out of four), which's sample volume position is close to plasma center as indicated in Figure 4.1.

This chapter is divided as follows. The schematics of the experimental detection setup in the tokamak are presented in section 2 and the figures from simulations are added to describe the design clearly. The characterization parameters for $\frac{1}{2}$ -size CEA and the mode of analyzer's operation (degree of deceleration) are presented in section 3. Section 4 presents the sensitivity of the analyzer as measured experimentally and makes comparison with simulations for both operation modes. Section 5 describes the indirect calibration of the analyzer for estimation of the plasma potential. Section 6 presents the core plasma potential measurement using the indirect calibration to obtain radial plasma potential profile and its evolution during a discharge. Section 7 focuses on fast fluctuation measurement for secondary ion current and plasma potential. The chapter is concluded with a summary in section 8.

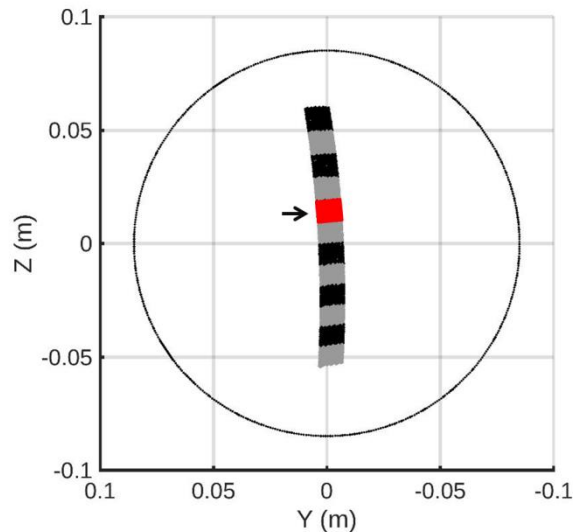


Figure 4.1 Poloidal cross-section view of ISTTOK indicating the sample volume location (in red) corresponding to second beam channel along primary beam trajectory [1.10].

4.2. Experimental setup description

Figure 4.2 depicts the experimental arrangement of the detector chain (assembled outside) to be installed at ISTTOK. The arrangement is the combination of EIM and CEA which is enclosed inside a SS conflat 6 way cross chamber. The following subsection will describe various elements of EIM and CEA in the experimental setup. The simulations in SIMION are presented in parallel with the experimental pictures for clarity.

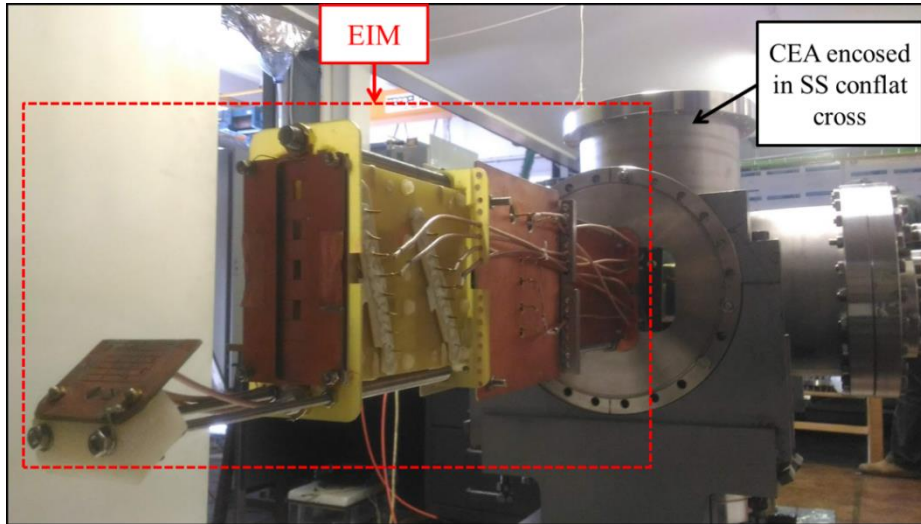


Figure 4.2 EIM+CEA: Assembled experimental setup of combined CEA and EIM to be installed in HIBD.

4.2.1. Electrostatic input module (EIM)

Updated Simulations

The EIM design used in chapter 3 was modified to be used in combination with CEA experimental setup. The SIMION simulation model for the EIM as it is used in the present experimental arrangement is presented in Figure 4.3. The end MCAD used in the previous EIM setup (sec. 3.4.1) was removed and an additional pair of horizontal Z plates was added to perform the horizontal deflection of the beam. This deflection helps to center the beam at the entrance of the CEA.

Figure 4.3 shows the EIM geometry simulated in SIMION for the second beam channel in 2D plane. Figure 4.3b,c shows the same beam trajectory and components in a perspective projection. The secondary beam enters the second input slit of the front MCAD and is horizontally aligned by the cylindrical plates and the corresponding pair of parallel plates (b). The bias voltage on these set of electrodes controls the vertical beam propagation. The beam then enters into the second channel of Einzel lens and propagates further between the pair of Z plates (c).

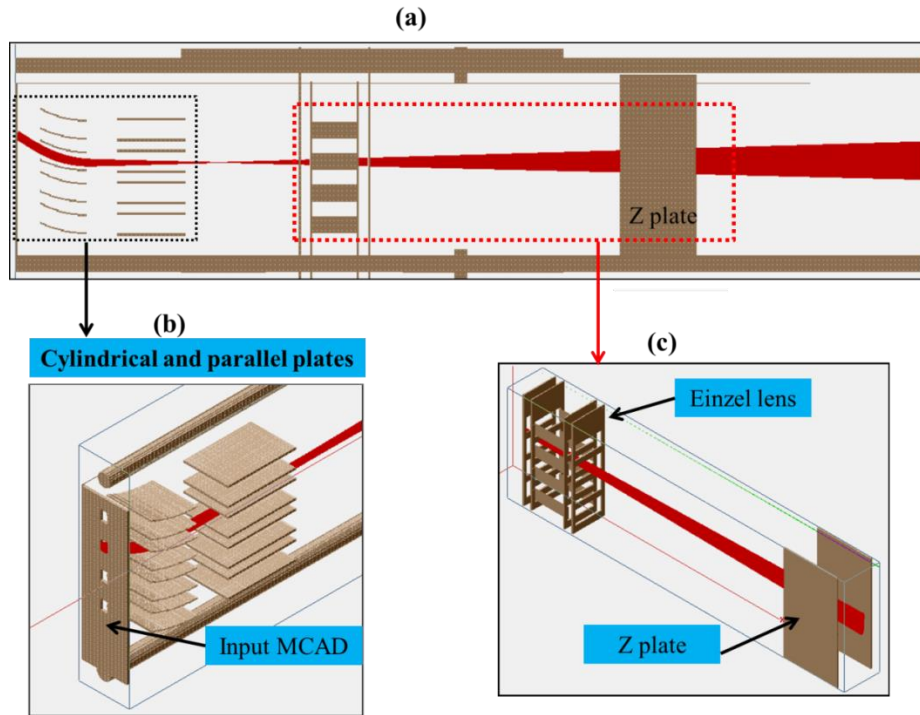


Figure 4.3 (a) EIM setup designed in SIMION describing different components (b) perspective visualization of (b) input MCAD, cylindrical and parallel plates and (c) Einzel lens and Z plate.

Modified experimental EIM setup

Figure 4.4 shows the picture of the experimental setup of the EIM for three views (front, side and top) and its components. The propagation region after the Einzel lens up to the entrance of the CEA is shielded with a grounded enclosure (this enclosure was included in the computation). The ground plate around the Einzel lens also provides shielding against the stray electric field of cables.

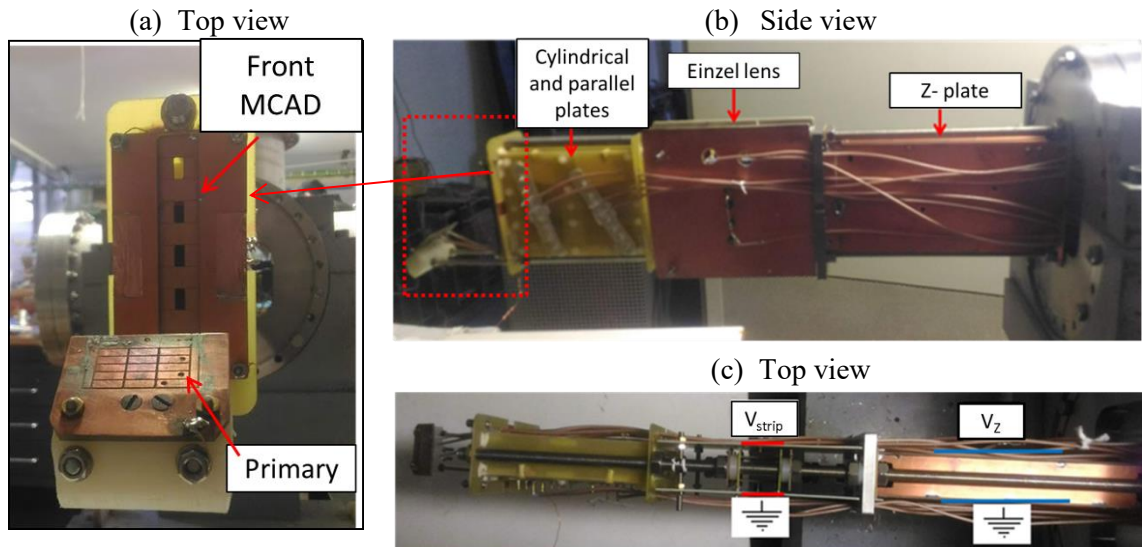


Figure 4.4 Presents pictures of EIM experimental setup - (a) front view; (b) side and (c) top view and various components as mentioned in Figure 4.3 are indicated.

4.2.2. Cylindrical electrostatic Analyzer (CEA)

Updated Simulations

Figure 4.5 presents the 3D geometry of CEA as implemented in SIMION software. The CEA electrodes, input slit, Deceleration Grid (DG), Secondary electron suppression Grids (SG) and end Split Plate Detector (SPD) (the cells of the end MCAD were combined to form a two cell split plate detector) are indicated in the Figure. The beam emerging from the EIM is aligned to the center of the input slit of the energy analyzer. A 2x1 detector is placed at each side of the input of the CEA for this purpose (Figure 4.6).

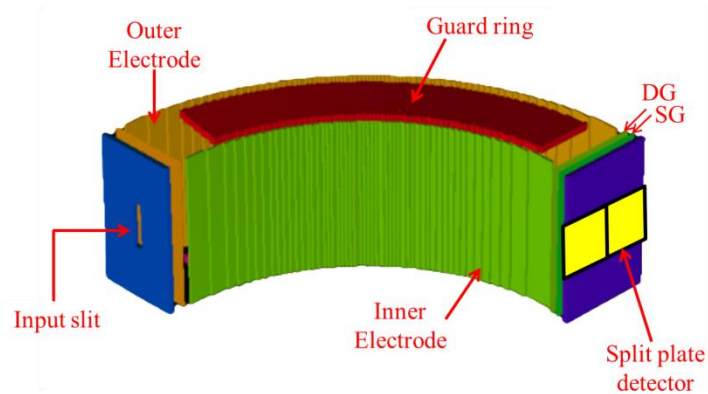


Figure 4.5 90° CEA in designed in SIMION simulation.

Modified 1/2-size 90° CEA

Figure 4.6 shows the picture of the 1/2-size CEA as used in the test facility with modified input and output to be used in the HIBD. Figure 4.6 indicates the input slit (a) to the analyzer with the input detector (with 4 cells) and on the right is shown the rear of the split plate detector (b) (MCAD with all cells combined in two halves). Figure 4.7 shows the arrangement of CEA installed inside the SS 6 way cross vacuum chamber. The dimensions of the 1/2 -size CEA is given in Table 2.6

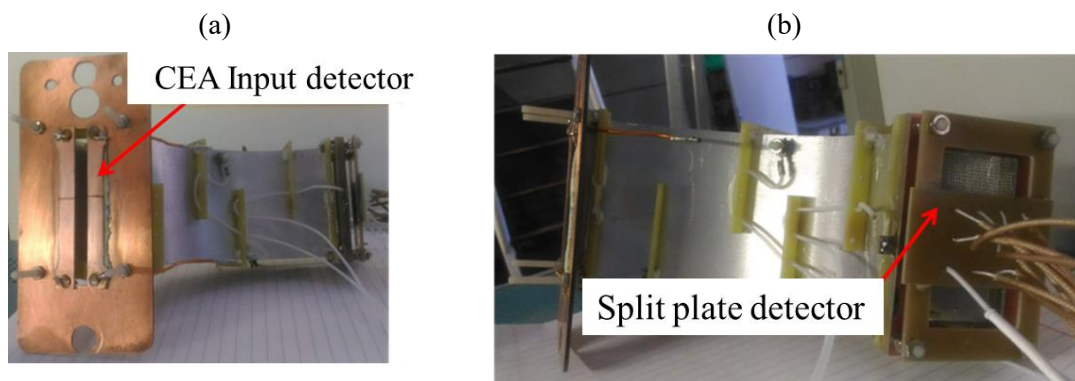


Figure 4.6 CEA before installation in the SS cross displays the input detector (a) and back side of end SPD (b).

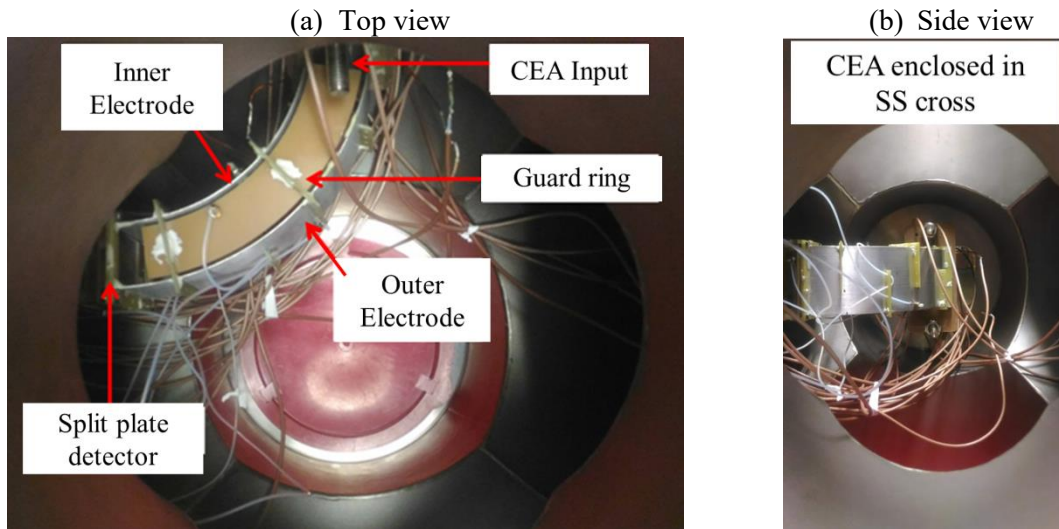


Figure 4.7 CEA inside SS conflat cross; the top view (a) and side view (b) indicating the various electrodes and its arrangement inside the cross.

4.2.3. Detectors location

To detect the beam at different positions in the secondary beam line several detectors have been placed at different locations. One detector is used to measure the primary beam position and current and other three are employed for detecting secondary ion beam in the EIM +CEA setup. Figure 4.8 displays the primary beam detector and three secondary ion beam detectors used. More information about the detectors and their connection to the acquisition system can be found in Appendix 4.

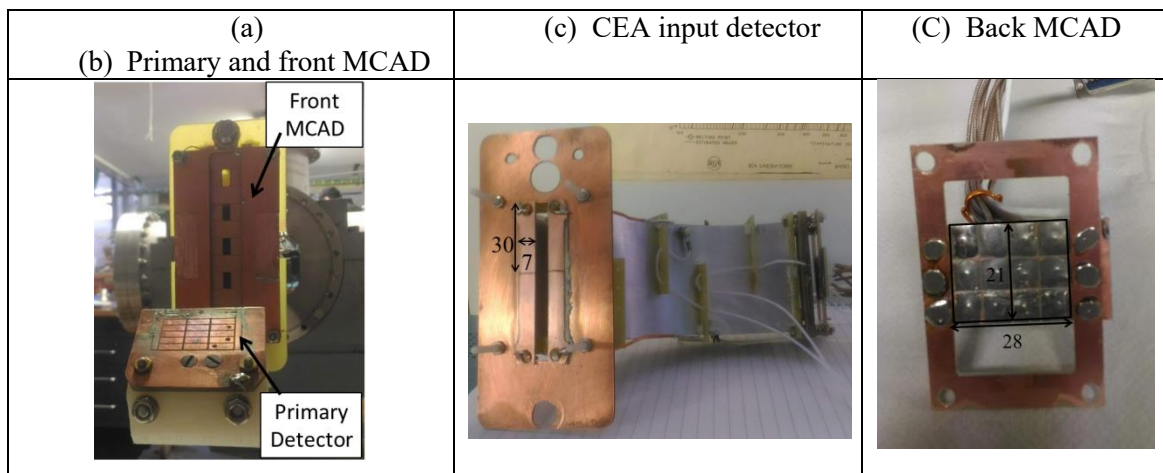


Figure 4.8 show the primary beam detector (a) and secondary beam detectors (a, b, c) installed at different positions. The dimensions of the cells as indicated in (b) and (c) are in millimeters (mm).

4.2.4. Beam Alignment

The alignment of the secondary beam inside the EIM was performed during plasma discharge at ISTTOK. This is a time consuming activity as it requires a stepwise approach, electrode by electrode, and can only be done under acceptable plasma conditions to ensure a proper S/N

ratio. The initial results obtained during the experimental alignment of the second channel of EIM in chapter 3 were used as the starting parameters for the combined EIM+CEA setup alignment. The voltage on the cylindrical plates (V_{cyl}), parallel plates (V_{pp}), side strip electrodes (V_{strip}) and Z plate (V_z) were optimized to obtain a uniform centered beam at the CEA entrance. In Table 4.1 are presented the set values for the initial alignment with only the EIM, and with the combined EIM + CEA arrangement.

Alignment	Shot	V_{cyl} (V)	V_{pp} (V)	V_{strip} (V)	V_z (V)
EIM	#43927	-1700	660	380	NA
EIM + CEA	#45192	-1650	350	430	-150

Table 4.1 *EIM alignment voltage set values*

4.3. Characterization of 1/2-size 90° CEA

This section describes the characterization of the 1/2-size 90° CEA using the secondary beams emerging from the plasma (the initial characterization was done with an electron beam in a standalone experiment as described in chapter 2). This section is further divided into two subsections. The first sub-section presents the SIMION simulation results to determine the energy (C_E) and angular (C_θ) coefficients of the analyzer as a function of the deceleration degree (k_E). The second sub-section presents the measurement of the same coefficients as determined by experiment. Recalling eq. 2.6 the first order estimation for the ion displacement Δr from the central standard trajectory for the cylindrical analyzer at the end detector is given by the following relation.

$$\Delta r = \delta r + C_\theta \delta \theta + C_E \delta E \quad \text{eq. 2.6}$$

Where, $\Delta r = \Delta R/R_0$ is the relative position at the detector (back MCAD), $\delta r = \Delta R_{slit}/R_0$ is the normalized initial position of the ion relative to standard trajectory at the analyzer input slit, C_θ is the first-order angular aberration coefficient, $\delta \theta$ is the angle of beam trajectory relative to the standard trajectory, C_E is the energy dispersion coefficient and $\delta E = \Delta E/E_0$ is the normalized ion energy fluctuation (determined by plasma potential fluctuations).

eq. 2.6 forms the basis for obtaining the fundamental analyzer parameters. For an energy analyzer, high energy resolution (C_E) and lower angular aberration (C_θ) are the ideal requirements. Therefore, the coefficients, C_θ and C_E , determine the sensitivity and applicability of the analyzer to measure beam energy at different toroidal input angles. The secondary beam toroidal input angle depends on the poloidal field created by the plasma current. As it happens to act on the same direction (zz) used to measure the plasma potential, the goal is to achieve low sensitivity to this angle. The two modes of operation can be described as follows:

- a. Normal mode: This operation mode is characterized by near zero potential on the central line trajectory of the CEA (it means \pm symmetric biasing of the analyzer electrodes). As a consequence, detection of the beam is at ground potential (as the central line potential). This is the conventional utilization of the CEA.
- b. Deceleration mode (This is the innovative operation mode proposed in this thesis): In this operation mode the central line trajectory is kept at a positive potential causing

beam deceleration. In practice, the inner and outer analyzer electrodes are positively biased (same sign as beam charge). The detection is at ground potential but a polarizing mesh kept at the intermediate voltage between inner and outer electrodes is placed in front of the detector (few mm in front) to maintain deceleration of the beam near the detector.

As expected from eq. 2.10 and verified in experiments with electron beam (sec 2.6); for a 90° CEA operated in deceleration mode with deceleration coefficient ($= k_E$), a k_E times effective increase in sensitivity to the energy change is observed.

Where, $k_E = (1 - q\psi_0/E_0)^{-1}$ is the deceleration coefficient, E_0 is the input beam energy and ψ_0 is the central line trajectory voltage and q is the beam charge.

4.3.1. Dependence of energy and angular coefficients with deceleration coefficient

The value of C_E and C_θ depend on the degree of deceleration k_E , and on the geometric dimensions of the analyzer (i.e. analyzing electric field topology). This section presents the simulation results on the dependence of C_E and C_θ with the degree of deceleration, k_E , from no deceleration (normal mode), $k_E=1$, to $k_E=5$ corresponding to 8 kV deceleration voltage.

In chapter 2 were presented the simulation results for the full size analyzer for deceleration factor $k_E = 5$ (Figure 2.16). Energy sensitivity gains of up to four fold times and angular dependency reduction up to seventy times were obtained. As for the 1/2-size prototype, the experiments conducted allowed the characterization up to $k_E = 2$ using an electron beam. In this section an extended characterization is made based on SIMION for the case of double charged positive ions.

In Figure 4.9 is depicted the variation of C_E (a) and C_θ (b) with respect to deceleration factor (k_E) for 1/2-size CEA for beam energy, $E_0 = 23.5$ keV, as used in experiments. The Figure 4.9(a) shows that the energy coefficient increases as the deceleration (k_E) is increased and (b) angular aberration coefficient (C_θ) is near zero value for $k_E \sim 2$. Therefore, as per requirement of high tolerance to angle dispersion for the present CEA experiment, $k_E \sim 2$ is the optimal deceleration coefficient to operate the 1/2-size analyzer.

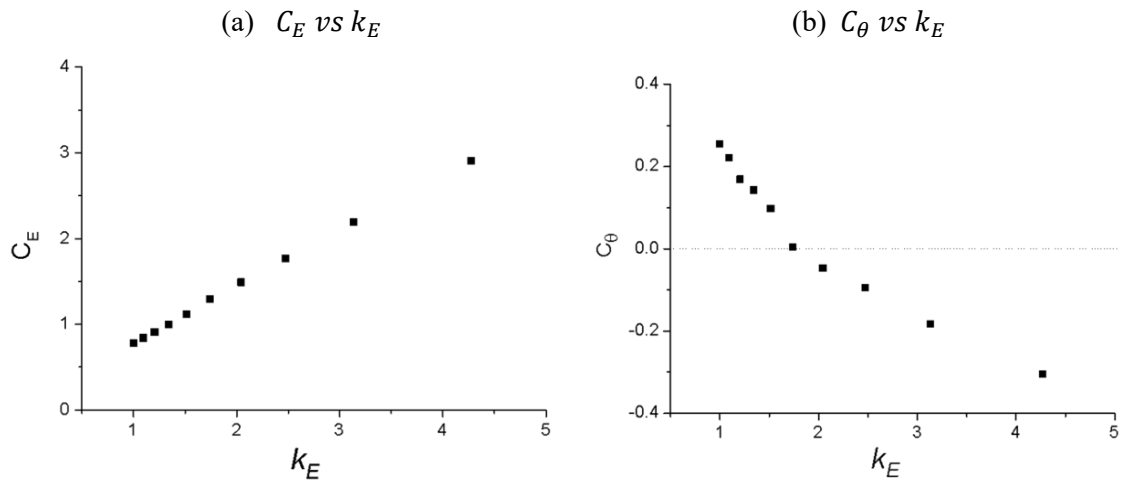


Figure 4.9 Variation of C_E (a) and C_θ (b) with respect to deceleration degree (k_E) for 1/2-size CEA.

4.3.2. Range of C_E and C_θ values under experimental uncertainties

This section presents the SIMION simulation results for C_E and C_θ values obtained for conventional (normal) mode ($k_E = 1$) and deceleration mode ($k_E = 2$) covering uncertainties in the experimental parameters namely, beam position at the CEA entrance, input toroidal angle and beam energy.

In Figure 4.10 is presented the detected beam position (at the back MCAD) as a function of beam energy for three different beam input positions (given in the legend). The energy coefficient (C_E) can be obtained by the slope of the lines. As it can be seen there is no practical dependence of the slopes with beam input relative position neither for the normal neither for deceleration modes. The value of the energy coefficient for $k_E = 2$ is double of the conventional mode value resulting on a two fold increase of detector position sensitivity to beam energy.

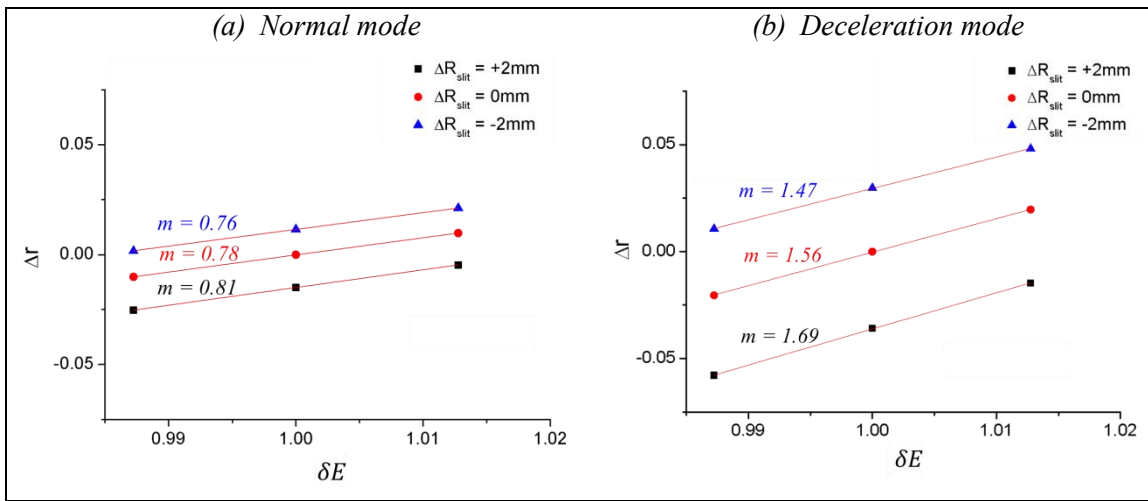


Figure 4.10 energy coefficients, C_E , for normal (left) and deceleration (right) mode for $1/2$ size analyzer. Where ΔR_{slit} is the shift of the beam at input position vertically from the standard central beam input position ($\Delta R_{slit} = 0$) and m is the slope of the linear fit.

In Figure 4.11 is depicted the dependence of the beam position at the detector as the input toroidal angle (at CEA entrance) is changed. Ideally this dependence should be null but in practice has some finite value. In this simulation the beam energy is fixed ($E_0 = 23.5$ keV). The detected beam position dependency with toroidal input angle can be linearized (for practical purposes) and is represented by the 3 lines on each graph (one per relative input position). The angular coefficient (C_θ) is obtained by the slope of these lines. One can see that for the conventional normal mode, C_θ is not constant meaning that the contribution for the detected beam position depends on beam input relative position at the entrance of the CEA. In the case of deceleration operation the angular coefficient (C_θ) reduces to half and is practically independent of beam input position. This means that the influence of toroidal angle induced by the plasma current in the plasma potential measurements is reduced to half (as compared to normal mode) and is the same for all input channels of the CEA, therefore possible to be accounted by means of a unique constant. The value of such fractional contribution, \mathcal{F} can be obtained from the C_E and C_θ values as given in eq. 4.1

$$\mathcal{F} = C_\theta / (C_\theta + C_E) \quad \text{eq. 4.1}$$

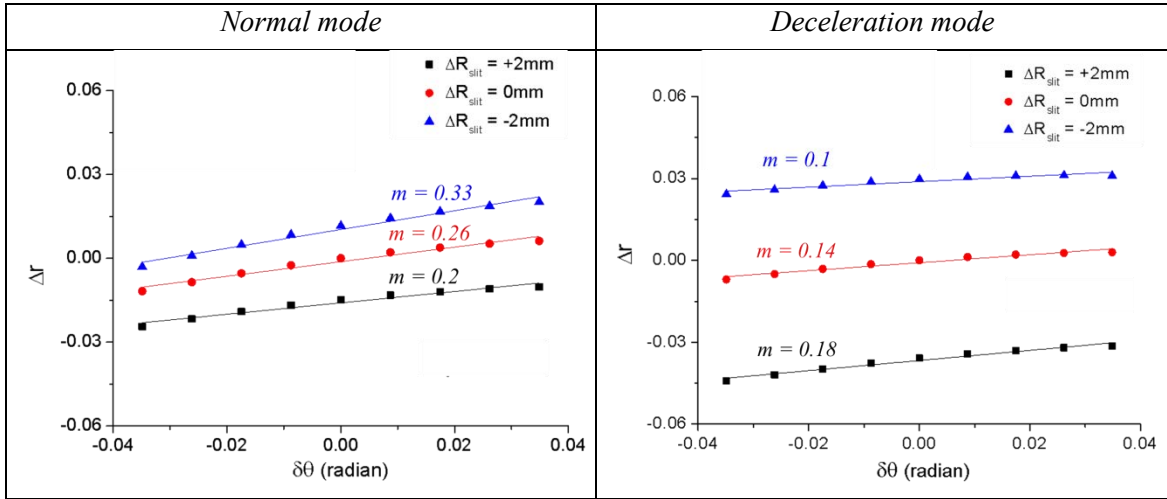


Figure 4.11 Angle coefficients C_θ for normal (left) and deceleration (right) mode for $\frac{1}{2}$ size analyzer; m is the slope of the linear fit.

Table 4.2 summarizes the values of the coefficients for normal and deceleration mode. Here an average value for C_θ in normal mode was used. It is clear that the crosstalk between the beam input toroidal angle (at the CEA entrance) and the beam toroidal position at the back MCAD is largely reduced (three times fold) by the deceleration operation mode. At this point is worth to note that the beam input angle can be determined by the geometric trajectories of the beams and for a given value of plasma current, using the HIBD simulation code. This would allow discounting the contribution of the input angle in the toroidal position at the back MCAD if deemed necessary.

	Normal ($k_E = 1$)	Deceleration ($k_E = 2$)
C_E	0.78	1.56
C_θ	0.26	0.14
\mathcal{F}	0.25	0.08

Table 4.2

For the full size CEA operating with $k_E = 5$ and $C_\theta = -0.033$ the crosstalk fraction is reduced to a negligible $\mathcal{F} = -7 \times 10^{-3}$, where the negative sign means opposition of phase, i.e., the shifts at the back MCAD induced by the input toroidal angle are in opposite direction to the plasma potential induced shifts. The results here presented will be compared with the analyzer experimental results in the next section.

4.4. CEA Experimental characterization in ISTTOK

In this section are presented and analyzed the experimental results obtained in ISTTOK tokamak. After aligning the beam and optimizing the biasing voltages of the various electrodes of the setup, the secondary ion beam current signals were obtained on the CEA back Split Plate Detector (SPD) for both normal and deceleration modes. Sensitivity studies of the analyzer were performed by changing the inner analyzer electrode voltage to obtain parameters; such as dynamic range, beam width and sensitivity. The results are supported by simulations using SIMION. Figure 4.12 presents the reference discharges used in the experiment. The averaged plasma density (red) and plasma current (green) for two typical ISTTOK AC discharges [1.6] are represented for normal (left) and deceleration (right) modes of operation.

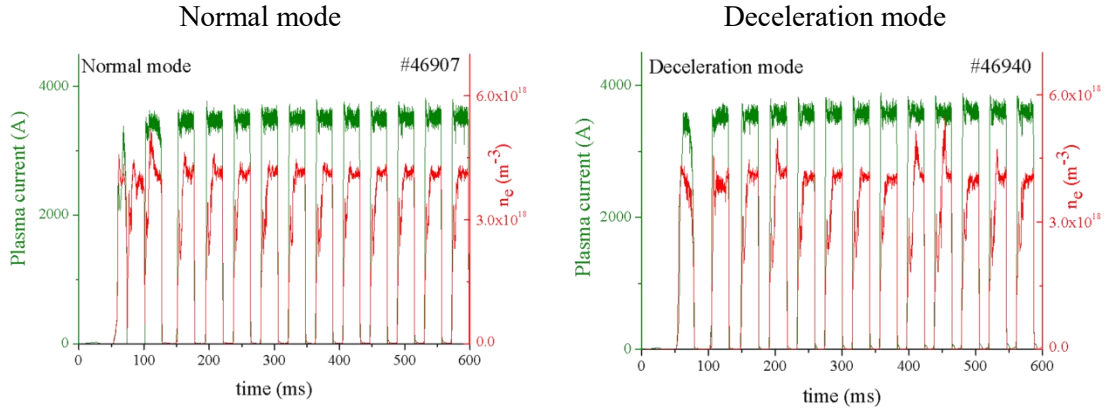


Figure 4.12 (right) Presents plasma density (red) and plasma current (green) with respect to time (0 – 650 ms) for ISTTOK AC discharge with several positive plasma current cycles.

4.4.1. Beam alignment at the SPD

The beam was centered at the input slit of the analyzer by balancing the current on the four side cells located at the entrance. Once the beam is centered at the entrance the biasing on the analyzer electrodes was optimized such that the beam is centered at the end SPD ($i_{13} \approx i_{14}$). Figure 4.13 displays the secondary current obtained at SPD for normal (left) and deceleration (right) mode for several plasma cycles. The location of cell #13 (black line) is closer to inner electrode (low energy side) and cell #14 (red line) is closer to outer electrode (high energy side). The total current, $i_{sum} (=i_{13}+i_{14})$ at the end SPD (in the last cycle) is close to 16nA as observed from the Figure 4.13 for both the modes. The density and the plasma current for the corresponding discharge are shown Figure 4.12. The voltage on the various electrodes of CEA is shown in Table 4.3

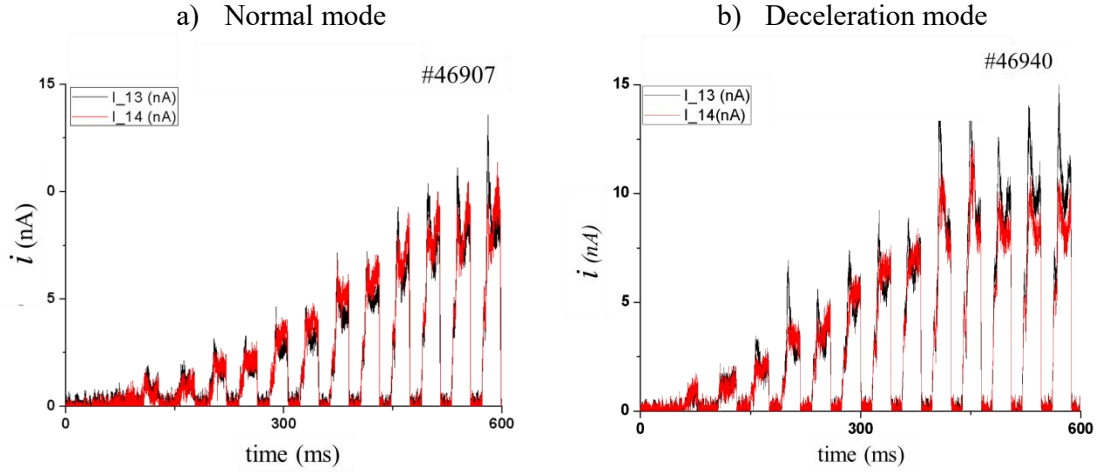


Figure 4.13 Beam balanced on the two cells of SPD observed for normal (left) and deceleration (right) mode. The cell #13 (black) and cell #14 (red) are closer to inner and out electrode of the analyzer, respectively.

$V_{\text{electrode}}$	Normal(kV)	Deceleration (kV)
$V_{\text{inner}} / V_{\text{outer}}$	-3.15/-3.10	3.85/ 7
$V_{\text{GR}}/V_{\text{DG}}/V_{\text{SG}}$	0/ 0/ 0	5.8 /5.7/ 0

Table 4.3 - voltages on the electrodes of the cylindrical analyzer for normal and deceleration mode used in the experimental setup. Where, $V_{\text{inner}} / V_{\text{outer}}$ are the voltages on inner and outer curved plates, $V_{\text{GR}} / V_{\text{DG}}/ V_{\text{SG}}$ are voltages on: guard rings/ deceleration grid/ SEE suppression grid.

4.4.2. Sensitivity curves

This section is divided into two subsections. The first section estimates the sensitivity of the analyzer, as retrieved experimentally. The second section compares and verifies these results with SIMION simulation.

In the experiments, the inner electrode voltage (V_{inner}) is changed stepwise and the beam position at the detector is obtained. However, to obtain the sensitivity of the analyzer, the effective change in inner electrode voltage (ΔV_{inner}) should be converted to the corresponding beam energy change (ΔE_0). Thus, the relation between ΔV_{inner} and ΔE_0 is derived as follows.

The change in ΔV_{inner} can be translated to change in input energy (ΔE_0) using by using eq. 2.5

$$V_{\text{outer}} - V_{\text{inner}} = 2[(E_0 - q\psi_0)/q] (d/R_0) \quad \text{eq. 2.5}$$

Where, V_{inner} and V_{outer} is the voltage in inner and outer electrode; E_0 is the beam energy, ψ_0 is the central line potential, q ($=2$) is the charge of the beam, d is the distance between the inner and outer electrode; R_0 is the central axis radius.

ψ_0 can be obtained by replacing $R = R_0$ (central line radius = R_0) in eq. 2.2 to obtain eq. 2.4, rewritten below,

$$\psi_0 = \frac{[V_{inner} \ln\left(\frac{R_{outer}}{R_0}\right) - V_{outer} \ln\left(\frac{R_{inner}}{R_0}\right)]}{\ln(R_{outer}/R_{inner})} \quad \text{eq. 2.4}$$

Where, R_{inner} and R_{outer} are the radii of inner and outer curved electrode, respectively.

Substituting ψ_0 obtained from eq. 2.4 and replacing in eq. 2.5, we can recalculate the coefficient relating change in inner electrode voltage (ΔV_{inner}) to change in beam energy (ΔE_0), as given by eq. 4.2

$$\Delta E_0 = \left\{ 2 \left[\ln\left(\frac{R_{outer}}{R_0}\right) / \ln\left(\frac{R_{outer}}{R_{inner}}\right) \right] - \frac{R_0}{d} \right\} \Delta V_{inner} \quad \text{eq. 4.2}$$

Replacing the values of R_0 , R_{inner} , R_{outer} and d as mentioned in Table 2.6 and substituting in eq. 4.2 we obtain eq. 4.3.

$$\Delta E_0 = 2.56 \Delta V_{inner} \quad \text{eq. 4.3}$$

It should be noted that eq. 4.3 applies for both, normal and deceleration mode. The coefficient ‘2.56’ in eq. 4.3 is also verified by SIMION simulations.

(i) Experimental Analysis for Analyzer Parameters:

In the present experimental setup, the inner electrode voltage is changed stepwise and the current on the SPD plates (cell #13 and #14) is measured to obtain normalized current (δi) for each V_{inner} . Where, δi is given by eq. 4.4,

$$\delta i = \frac{i_{14} - i_{13}}{i_{14} + i_{13}} \quad \text{eq. 4.4}$$

Where i_{13} and i_{14} are currents on cell #13 and cell #14, respectively. Hence, $\delta i = -1$ corresponds to beam shifted completely to cell#13 (near inner electrode) and $\delta i = +1$ corresponds to beam on cell #14 (near outer electrode). The normalized beam current (δi) can be related to the beam position on the SPD using eq. 2.11:

$$\Delta r = \tilde{\delta i} (w_b / 2R_0) \quad \text{eq. 2.11}$$

Where, $\Delta r = \Delta R_{det}/R_0$, w_b is the beam width at the detector and R_0 is the central radius. eq. 2.11 can be re written in terms of ΔR_{det} as eq. 4.5

$$\Delta R_{det} = \tilde{\delta i} (w_b/2) \quad \text{eq. 4.5}$$

Where, ΔR_{det} is the shift of the beam mean position (in mm) at the SPD from the standard central line; such that $\Delta R_{det} = 0$, for $\tilde{\delta i} = 0 \rightarrow i_{13} = i_{14}$ (beam balance on the two plates).

Dynamic range and beam width

The normalized beam current (δi) on the SPD for both normal and deceleration mode was recorded as the V_{inner} is changed while voltage on rest of the electrodes is fixed. The change on V_{inner} required to shift the beam from one cell of the SPD to another completely ($\delta i = -1$ to $+1$) was recorded as 460V and 560V for normal and deceleration mode, respectively. Hence, using eq. 4.3, the resultant dynamic range for normal and deceleration mode is 1180V (± 590) and 1440 V (± 720 V), respectively.

Recalling the mathematical relation for calculating dynamic range ($\Delta\phi_{DR}$) for a uniform beam at SPD for ($\delta i = \pm 1$) as given by eq. 2.14,

$$\Delta\phi_{DR} \leq 2[(w_b/2R_0)/C_E]E_0 \quad \text{eq. 2.14}$$

Replacing the dynamic range, 1180V and 1440V for normal and deceleration mode, respectively, we can retrieve the beam width at the SPD by substituting the known parameters in eq. 2.14 for normal and deceleration mode to retrieve - $w_{bn} \sim 4$ mm, $w_{bd} \sim 10$ mm.

Where, w_{bn} and w_{bd} are the beam width for normal and deceleration mode at SPD respectively, C_E is the energy dispersion coefficient as given in Table 4.2.

Figure 4.14 plots the beam average position on the detector ΔR_{det} (eq. 4.5) vs inner electrode voltage (V_{inner}) for normal (a) and deceleration (b) mode. The sensitivity (S) for an analyzer can be defined as the change in energy required to shift the beam effectively by 1mm on the detector. The sensitivity ($\Delta E_0/\Delta R_{det}$) can be derived using slope from plots in Figure 4.14 and eq. 4.3, as depicted in eq. 4.6,

$$S = \Delta E_0/\Delta R_{det} = 2.56 (1/slope) \quad \text{eq. 4.6}$$

Where, slope = ($\Delta R_{det}/\Delta V_{inner}$), is the slope of graphs in Figure 4.14 for normal (left) and deceleration mode (right).

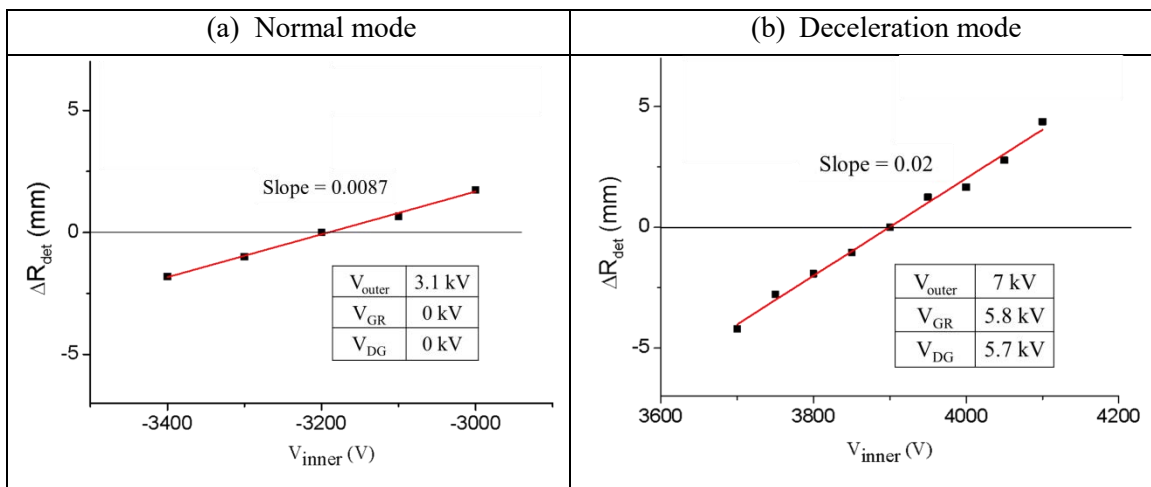


Figure 4.14(a) presents the beam shift (ΔR_{det}) on Y-axis obtained as the voltage on the inner electrode (ΔV_{inner}) is changed for normal (a) and deceleration (b) mode. The voltages on the other CEA electrodes are indented in the graph for each mode. Where, V_{outer} , V_{GR} and V_{DG} are voltages on the outer curved electrode, guard rings and deceleration grid, respectively.

Using eq. 4.6, we can determine sensitivity for normal (S_n) and deceleration (S_d) modes as:

$S_n \sim 295$ V/mm and $S_d \sim 130$ V/mm, respectively.

It should be noted that dynamic range for deceleration mode is higher due to the larger beam width at the SPD as compared to the normal mode. Additionally, if to compare the sensitivity (where the effect of beam width for the two modes is compensated), we obtain 2 times more sensitivity for deceleration mode ($k_E = 2$) in comparison to normal mode ($k_E = 1$). The following section determines these analyzer parameters using simulations in SIMION.

(ii) *Simulations Analysis of Analyzer Parameters:*

Figure 4.15 (similar to Figure 4.14) shows the plot of ΔR_{det} (on Y-axis) with respect to inner electrode voltage (V_{inner}) as the other electrode voltages are kept constants (presented in graph) for normal (a) and deceleration (b) mode, as obtained by simulations in SIMION.

An input Gaussian beam (500 particles) for each V_{inner} is launched and its mean position on the detector is recorded as ΔR_{det} . Inner electrode voltage (V_{inner}) was changed (in step of 100V) and ΔR_{det} was recorded for each ion beam fly to obtain plots in Figure 4.15. Where, $\Delta R_{det} = 0$, infers to beam equally balanced between the two plates of the SPD. Beam width as measured directly from in the simulation for normal and deceleration mode is: $w_{bn} = 5$ mm and $w_{bd} = 10$ mm, respectively (in agreement with experimentally obtained values).

Similar to previous section, the sensitivity for the analyzer can be estimated from the slope of the normal and deceleration mode in Figure 4.15 and using eq. 4.6. We obtain sensitivity for normal (S_n) and deceleration (S_d) modes as: $S_n = 298$ V/mm and $S_d \sim 150$ V/mm, respectively. The sensitivity increases two times in the deceleration mode as compared to the conventional operation mode.

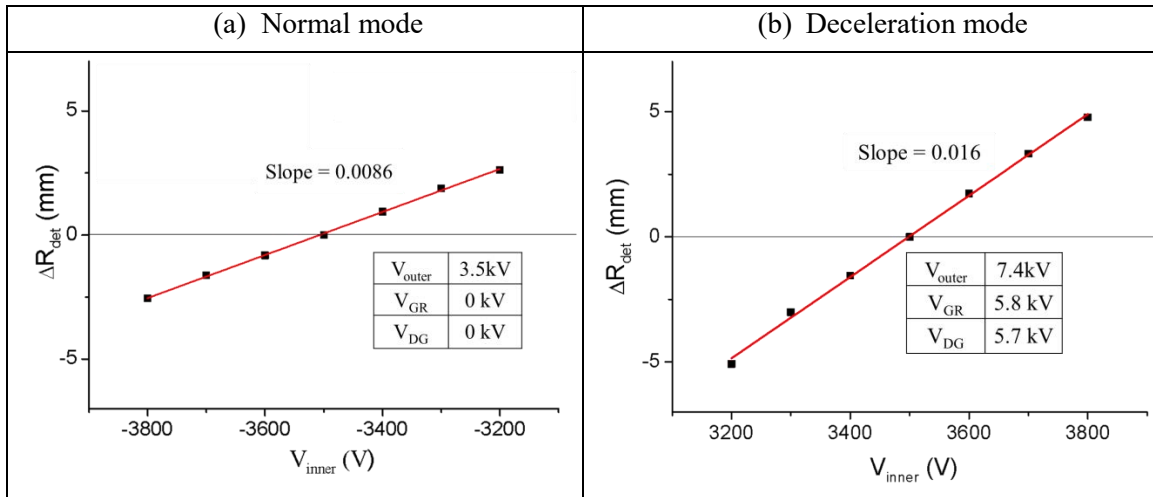


Figure 4.15 present the plots for ΔR_{det} vs. V_{inner} as obtained from simulation for normal (a) and deceleration (b) mode. The biasing voltages on the other electrodes are indented in each plot.

Table 4.4 summarizes and compares the sensitivity from normal and deceleration mode as obtained from experimental results and SIMION simulations.

Operation mode	Experiment	Simulation
	Sensitivity (eV/mm)	
Normal	294	298
Deceleration	130	150

Table 4.4 Analyzer sensitivity

Table 4.4 indicates very good matching of the value of the sensitivity as obtained by simulations and experiments for the normal mode. Whereas, in case of deceleration mode the sensitivity value for simulation and experiment agrees within an error of 15%. This error could be attributed due to the non-uniformity of the beam shape at SPD in the deceleration mode (as also observed in simulations).

In addition, it should also be noted that the CEA Voltage parameters used in the experimental data and simulation are offset by 300V, however the axis line potential ($\psi_0 = 0 / 5.5$ kV, eq. 2.4) is the same in both experiment and simulations. This offset could easily be attributed due to a calibration offset of the HV power supply used to select the beam energy. Other contributions are the construction tolerances of the CEA.

One important note goes for the used alignment procedure. It was chosen to align the beam by choosing the voltages on the analyzer electrode such that the beam is centered on the SPD. It is clear from Figure 4.14a that this condition is attained for -3.2 kV in normal mode whereas the ideal symmetric value should have been -3.1 kV if to keep the geometric axis potential line near 0 V. The same applies in the deceleration mode, the correct alignment would be for a value for $V_{DG} = 5.7$ kV whereas the experimental value for the geometric axis potential line is 5.5 kV (given by eq. 2.6). This geometric distortion of the CEA can be recovered by shifting the detector (SPD) central line to the beam position obtained by setting the appropriated symmetric biasing values. In practice it is not possible to move the detector. However, an alternative way is to use the whole cells of the back detector in MCAD mode, which is position sensitive regardless of beam width, and define the reference beam position as the one obtained by the symmetrically applied voltages. The present experiments had to use SPD configuration due to limitations on number of amplifiers. However, this does not constitute a limitation for the characterization of the dynamic properties of the CEA as the measurements are validated by comparison with SIMION model and calibrated experimentally (as described later).

4.5. Analyzer Calibration

Absolute measurements of plasma potential with HIBD require the calibration of the analyzer used for the secondary beam energy measurements. Generally, the direct calibration of the energy analyzer includes two steps:

- (i) The first step is the calibration on test facility with a beam of varied energy of any charged particles (ions, electrons) to specify the analyzer characteristics (resolution, dynamic range, angle aberrations) in ideal and controlled operation condition;
- (ii) The second step is based on the possibility of performing the calibration in the real installation on the tokamak [4.1]. The usual practice is to use the secondary ions created in collisions with residual or specially puffed gas, without any plasma. The main problem of such calibration is low (one-two orders of magnitude) cross-section of that ionization process, thus determining low intensity of secondary beam and low resolution of the calibration measurements itself.

On ISTTOK, the first step of CEA calibration was realized in the experiments mentioned in Chapter 2 on dedicated test facility with low (2 keV) energy electron beam (sec. 2.6.) [2.13]. The energy resolution of $(\Delta E/E) = 2 \times 10^{-3}$ (limited by the power supplies accuracy) has been demonstrated in two-times deceleration mode and insensitive (in this mode) to the $\delta\theta = \pm 1^\circ$ change of the analyzed beam entrance angle.

As for the second step, the gas calibration is inapplicable due to low intensity primary beam in ISTTOK (\sim few μ A). Instead, in order to estimate the plasma potential absolute value from the CEA measurements, the indirect calibration method described below was used.

4.5.1. Description of indirect calibration

The channel used in the prototype CEA collects secondary beams from the plasma core. The basis for this method relies on the initial phase of the ramp-up of the plasma discharge, where the core plasma potential is expected to be evolving in amplitude. During the initial phase of the discharge the plasma potential is rather low and it is assumed that its value evolves with the plasma current. By following the beam evolution on the SPD one can trace the quasi-linear relation between beam position and time for the early instants of plasma ramp-up. The zero potential is attributed to the beam position on the SPD obtained by reverse extrapolation to the instant $t=0$.

The HIBD standard split-plate detection [2.1] was explained in sec. 2.4.2. As shown before, for an uniform beam of width w_b the shift on the split-plate due to energy change can be translated to the difference of beam currents on the left, i_L , and right, i_R , plates (Figure 2.10), and, for the 90° CEA, the measured plasma potential is determined from eq. 2.13,

$$\varphi = (d/2R_0) \delta i E_0 C_E^{-1} \quad \text{eq. 2.13}$$

Where R_0 is the central radius of the CEA, $\delta i = \Delta i / i_{sum} = (i_L - i_R) / (i_L + i_R)$, E_0 is the beam energy and C_E is the energy dispersion coefficient.

eq. 2.13 expects that at $\varphi = 0$, the normalized currents difference δi is also zero, $\delta i = 0$ (balance of the split-plate currents); therefore, in that case the measurements are absolute. In real conditions (with unknown or poorly specified analyzer installation tolerances, alignment, parameters of a real beam at the analyzer entrance, quality of the power supplies) the normalized currents difference δi at $\varphi = 0$ may not be zero, $\delta i = \delta i_{in} \neq 0$, and eq. 2.13 can be rewritten as,

$$\varphi = (w_b/2R_0) (\delta i - \delta i_{in}) E_b C_E^{-1} \quad \text{eq. 4.7}$$

eq. 4.7 indicates that with unknown reference value of δi_{in} the plasma potential measurements are not absolute; therefore, determination of δi_{in} is necessary for analyzer calibration (note that for the relative plasma potential fluctuations measurements, the absolute analyzer calibration is not required).

In eq. 2.13 the sum of secondary ions current i_{sum} is determined by the plasma ionization rate $n_e \sigma = F_{n\sigma}(t)$, and $F_{n\sigma}(0) = 0$ at $t = 0$. The currents i_L, i_R , in addition to the dependence on $n_e \sigma$, are also functions of the plasma potential φ as follows:

$$\begin{aligned} i_L &= \frac{1}{2} F_{n\sigma}(t) [1 + f_\varphi(t)] \\ i_R &= \frac{1}{2} F_{n\sigma}(t) [1 - f_\varphi(t)] \end{aligned} \quad \text{eq. 4.8}$$

Where $0 > f_\varphi(t) > 1$ is the misbalance beam fractions on the SPD with an opposite (\pm) “response” on the plasma potential change, and $f_\varphi(0) = 0$ at $t = 0$.

From eq. 4.8 the Δi , i_{sum} , and δi can be written as follow:

$$\Delta i = i_L - i_R = F_{n\sigma}(t) f_\varphi(t) \quad \text{eq. 4.9}$$

$$i_{sum} = i_L + i_R = F_{n\sigma}(t) \quad \text{eq. 4.10}$$

$$\delta i = \Delta i / i_{sum} = f_\varphi(t) \quad \text{eq. 4.11}$$

Such that δi dependence is only on the plasma potential (assuming constant beam profile in the small range of shifts).

Considering the initial (or final) phase of plasma discharge, the currents on split plates are distinguishable from the noise background at some time t_{dist} with increasing (decreasing) of plasma electron density and temperature. The idea of indirect calibration is that δi_{in} can be estimated during plasma ramp-up (or termination) phase by extrapolation of δi to $t=0$

In principle, the plasma current may induce an additional toroidal shift in the detector due to current evolution. However, the measurements is limited for low values of the plasma current ($I_p < 2$ kA) and its contribution is not practically measurable as it remains in the sub-millimeter range. In addition, the CEA is quite insensitive to the input angle of the secondary beam.

4.5.2. Application of indirect calibration

On ISTTOK the initial phase of plasma discharge is characterized by strongly unstable plasma column position during rising of plasma current and electron density, as one can see in Figure 4.16. The Figure presents an example of time evolution of the radial (R) and vertical (Z) plasma column positions together with the average electron density (n_e), the plasma current (I_p), the sum secondary current (i_{sum}) and the SPD normalized secondary currents ratio (δi) for one particular plasma cycle for shot #46940. Figure 4.17 shows a time-expanded final phase of this plasma cycle indicating almost linear decay of I_p and n_e during cycle termination after preceded flat-top phase. The time markers by vertical lines in Figure 4.17 (left) are (left-to-right): start of I decay (t_I), time for which n_e decays by 20% of its flat top value (t_n) and the time instant for which δi value is two times the standard deviation of i_{sum} noise ($\delta i = 2\sigma_{i_{sum}}$) (t_{dist}). Note that I decays approximately two times before start of n_e decay and during this time interval, $t_n - t_I$, the value of δi is practically unaltered (demonstrating that the beam position on the split plate detector is not influenced by the change of the plasma current poloidal magnetic field).

Application of indirect calibration to the final stage of that plasma cycle by linear fitting of δi inside time interval $t_{dist} - t_n$ is demonstrated in Figure 4.17 (right). To reduce the noise contribution, the δi data in Figure 4.16 and Figure 4.17 is low-pass filtered at 5 kHz (approximately twice the inverse of the decay time of n_e). From Figure 4.17, the estimated value of δi_{in} at time t_{dist} is $\delta i_{in} = 0.35$ (thus, corresponding to $\varphi = 0$ V). Taking this value as the reference we determine $\delta i_\varphi = (\delta i_{FT} - \delta i_{in}) = 0.45$ for the plasma potential value (δi in potential units) at flat-top phase (where δi_{FT} is the δi value at the initial flat top region in the graph in Figure 4.17 (left)).

The calibration accuracy is estimated by application of calibration procedure to a number of plasma cycles of the same shot. Particularly, for five cycles of the analyzed shot #46940, the estimated mean value is $(\delta i_{in})_{\text{mean}} = 0.37$ with standard deviation of $(\delta i_{in})_{\text{std}} = \pm 0.1$.

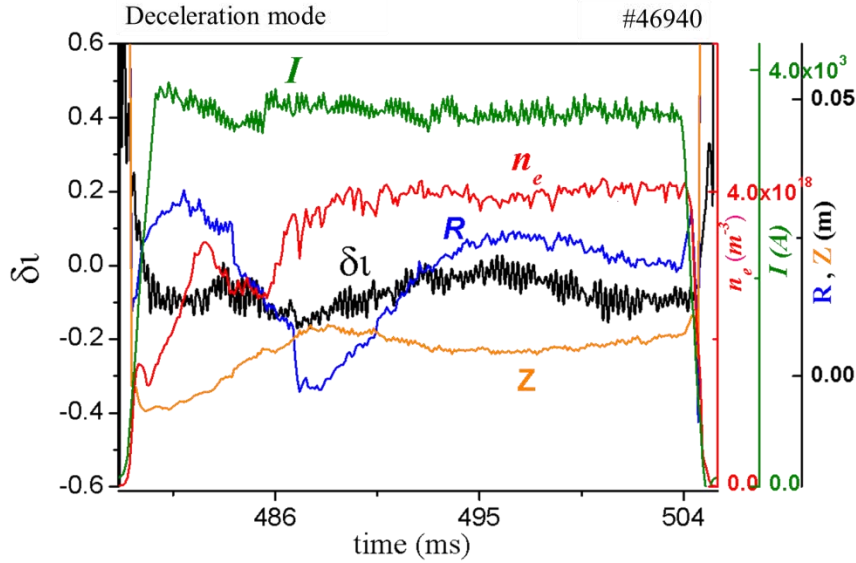


Figure 4.16 Plasma potential (black) evolution in time for single plasma cycle for a discharge plotted with respect to the evolution of averaged plasma density (red), radial (R, blue) and Z (orange) position of the plasma centroid.

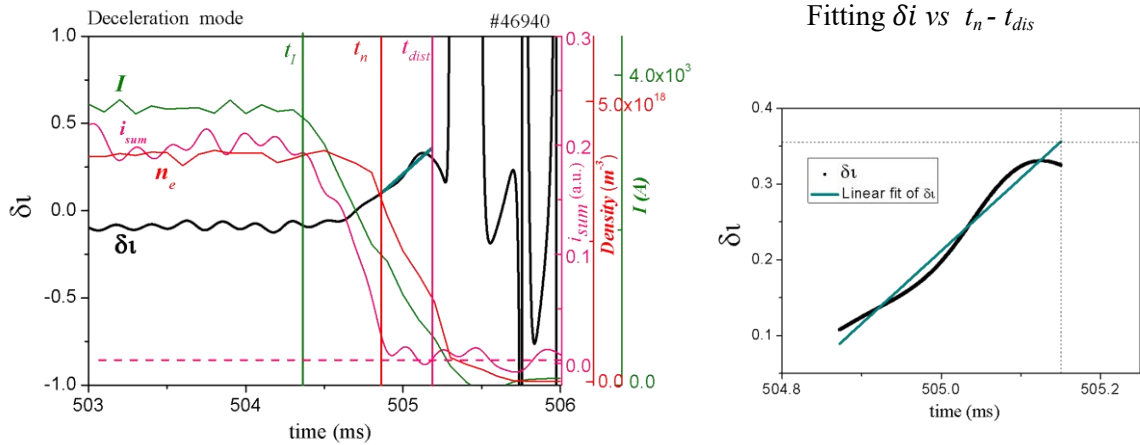


Figure 4.17 (left) present the application of the indirect plasma potential calibration in the final part of the cycle; (right) linear fitting of the δi vs t curve to obtain δi_{in} .

The dependence of the CEA dispersion not only on beam energy, but also on the beam entrance angle, due to the interaction of the diagnostic beam with the poloidal magnetic field of plasma current is estimated as follows. Early experience with HIBD operation on ISTTOK [1.13] and experiments with ToF energy analysis [1.15] showed the respective change of the secondary beam angle in the range of $\delta\theta \sim 0.5^\circ$ for plasma current of 5 kA. Recalculation to the effective energy equivalence by eq. 2.6,

$$(\Delta E/E_0)_\theta = -(C_\theta/C_E)\delta\theta \quad \text{eq. 4.12}$$

gives $(\Delta E/E_0)_\theta \sim 8 \times 10^{-4}$, or $(\Delta E)_\theta \sim 18\text{V}$, being only $\sim 5\%$ of the estimated potential value (340V, as given in next section). This indicates that the misbalance of the secondary ion current on the split-plates (δi) used to determine the reference δi_{in} is mainly determined by the plasma potential.

4.6. Measurement of Core plasma potential

4.6.1. Plasma Potential profile

The values of plasma potential in discharge #46940 during flat-top phase before cycle termination (using $(\delta i_{in})_{\text{mean}} = 0.37$) is $\varphi = -340\text{ V}$ as calculated by eq. 4.7 with estimated calibration offset corresponding to $\delta i = \pm 0.1$ or, $\Delta\varphi = \pm 71\text{ V}$. In Figure 4.16 (left), the plasma column shifts radially during first half of the cycle without changes of n_e , and I . The change of the plasma column position is equivalent to the shift of the sample volume, i.e. to a radial scan of the plasma. In the analyzed cycle, the plasma is scanned to higher radii. Figure 4.18 presents the core plasma potential profile obtained during plasma movement together with data obtained by Langmuir probes on the plasma periphery, for similar plasma density and current.

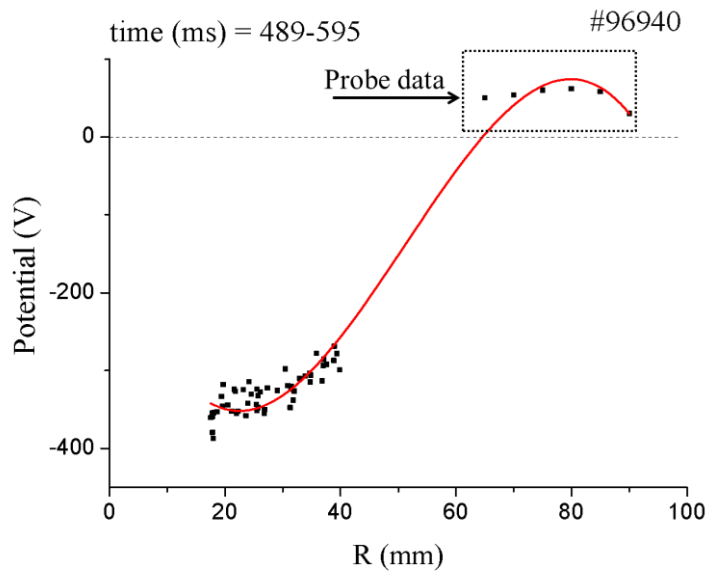


Figure 4.18 Presents the mean plasma potential profiles with respect to the radial position. The mean plasma potential near the core is measured using HIBD and those on the edge are measured using Langmuir probes (as indicated).

Figure 4.19 presents evolution of plasma potential during a discharge as calculated for deceleration mode measured using indirect calibration for 4 plasma cycles. The value of the plasma potential obtained in the last 4 cycles is more reliable due to better signal to noise ratio. The signals are low pass filtered at 5 kHz.

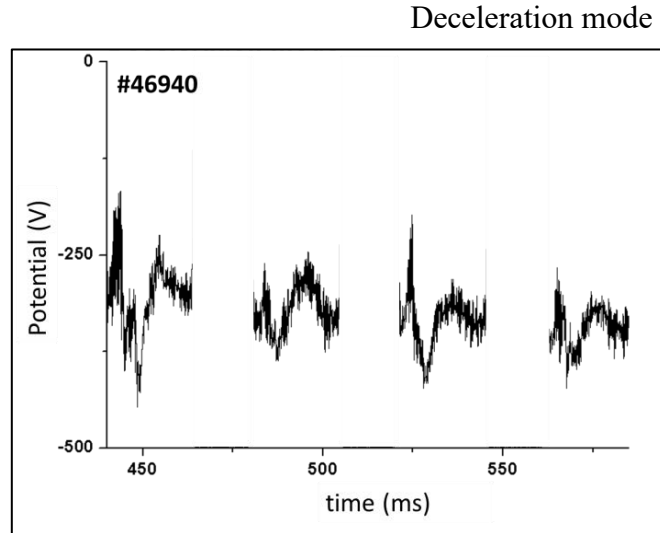


Figure 4.19 Plasma potential measurements using indirect calibration for deceleration operation mode.

4.6.2. Dependence of local potential with respect to the plasma parameters

Figure 4.20a shows the core plasma potential with respect to the plasma density (n_e , red) and plasma current (I , green) for four plasma cycles as observed in deceleration mode. The plasma current is set at 4 kA for each cycle in these discharges. The averaged plasma density increases in the beginning of each cycle and saturates at $4 \times 10^{18} \text{ m}^{-3}$, the plasma potential follows the changes in the averaged plasma density but the trend is not linear. Similarly, Figure 4.20b presents the plasma potential for the four cycles but with respect to the sum current ($i_{sum} = i_{I3} + i_{I4}$). It can be observed that the local plasma potential is more sensitive to the sum current, which is proxy to plasma pressure $\langle n\sigma_e \rangle$ (b), than to the line averaged plasma density (a). In particular this behavior reflects a dependence of plasma potential with plasma temperature (via the effective ionization cross-section σ_e). In Figure 4.20b it is clear that when temperature drops the plasma potential absolute value drops and vice-versa as dictated from the balance between electric potential energy and kinetic energy within the Debye length and ambipolar transport.

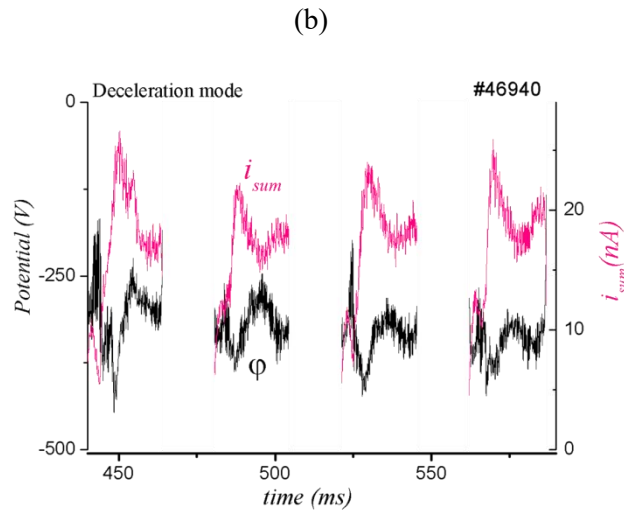
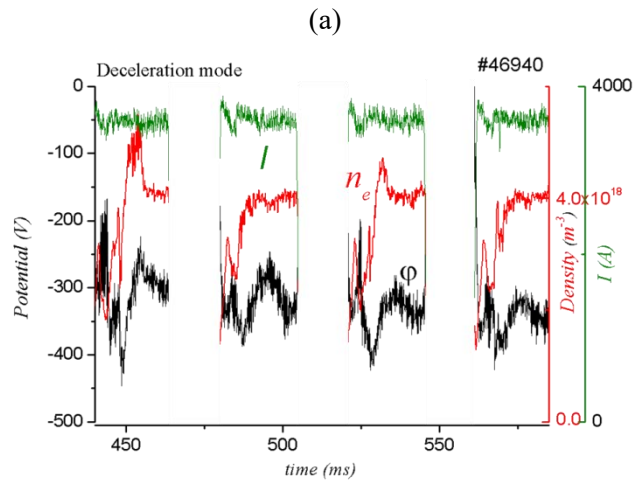


Figure 4.20 (a) Plasma potential, ϕ (black) variation with respect to plasma density, n_e (red) and plasma current, I , (green) (b) Mean potential (black) variation with respect to sum current (i_{sum}) on the SPD (pink) 4 plasma cycles in a discharge. The empty spaces between the cycles are corresponding to the no plasma negative cycle during AC discharges.

4.7. Plasma fluctuation measurements: Density and current

4.7.1. Current Fluctuations

This section presents the fluctuation measurements of the secondary beam current as observed in the lower cylindrical plate (EIM input at secondary beam channel) and at the end SPD of the cylindrical analyzer.

(i) Secondary ion current fluctuation in lower cylindrical plate

The voltages on the EIM were switched off to obtain the secondary ion current from the sample volume corresponding to second beam channel (core) of the plasma on the lower cylindrical plate. The Figure 4.21 shows the PSD for the secondary ion beam current on the lower cylindrical plate. The PSD is presented for 3 plasma cycles; the corresponding current signal (averaged for cell #13 and #14) is shown below the spectra. The gaps between the signals are corresponding to the moments without plasma

The fluctuation in the range of 75-125 kHz can be observed in the spectra along with some low frequency structures (0 - 20 kHz). The intensity of the fluctuations in the high frequency range increases as the signal to noise ratio is improved with time along the discharge.

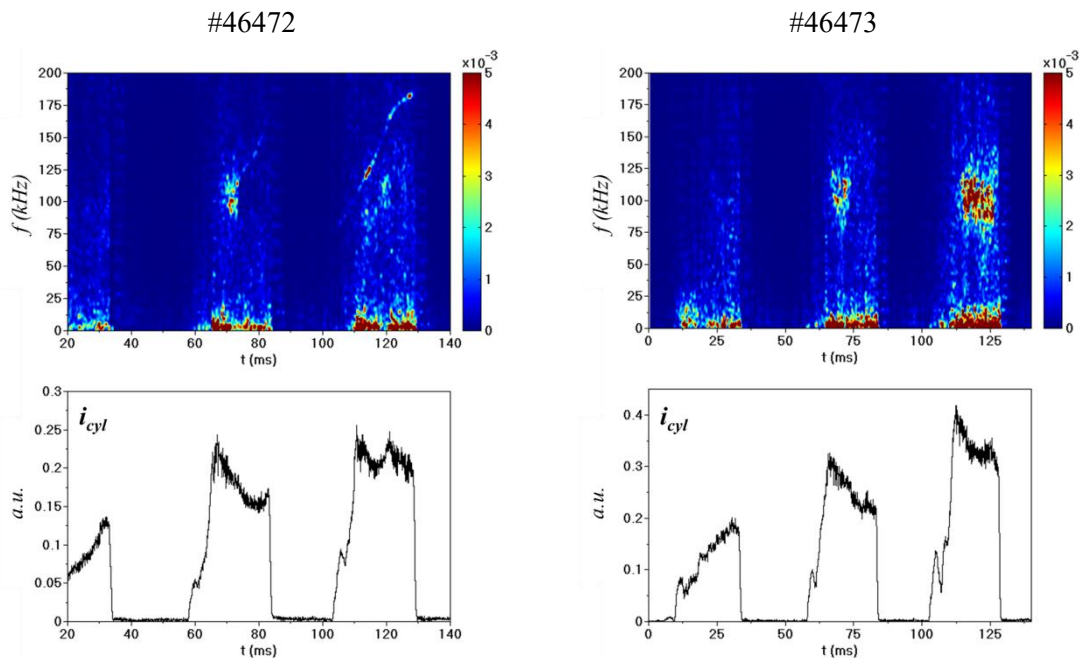


Figure 4.21 PSD (top) of the secondary ion current (lower) obtained at the lower cylindrical plate for two plasma discharges.

(ii) Current fluctuation on CEA back detector (SPD)

The Figure 4.22 below shows the sum current ($i_{sum} = i_{13} + i_{14}$) fluctuation from the split plate detector cells for normal (left) and deceleration (right) mode for 5 plasma cycles. The fluctuation in the secondary beam sum current shows some fluctuations in the low frequency region (0 – 20 kHz) and the high frequency region (75-115 kHz). The low frequency component seems to not vanish completely during both the plasma –on and -off region (particularly in deceleration mode due to higher induced background noise) and the higher frequency (75-125 kHz) fluctuation appears only during the plasma cycles. The intensity of the high frequency fluctuation increases as the sum current increases.

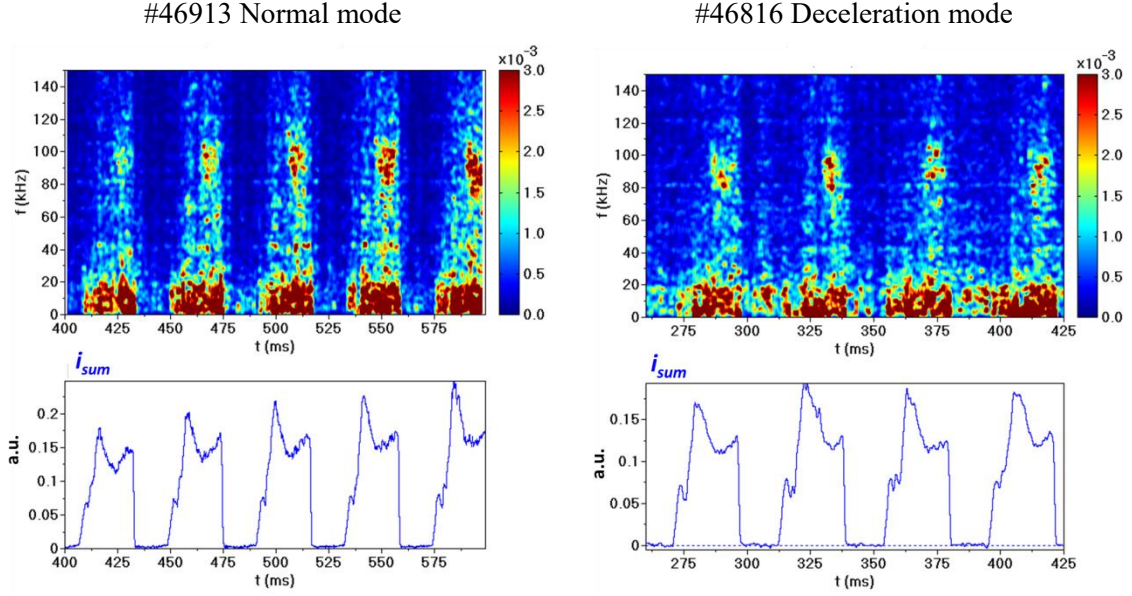


Figure 4.22 PSD of the sum of secondary ion current obtained at the back SPD for normal (left) and deceleration (right) mode.

In face of these results we may conclude that the observed fluctuation spectra in the intensity of the secondary beam signal are the same before and after the EIM + CEA chain.

4.7.2. Plasma Potential fluctuation measurements

As mentioned earlier, measurements of plasma potential fluctuations, being relative, do not require a calibration reference. Estimations of the analyzer sensitivity to the plasma potential fluctuations can be obtained with the external modulation of the beam energy during the plasma shot and considered as the relative calibration of the analyzer.

In order to estimate the CEA resolution several relative calibration experiments using external modulation of the potential at the CEA inner plate have been performed (sec. A4.4). The sinusoidal modulation of 2.5 kHz, 5 kHz and 25 kHz with amplitudes of 10 V and 20 V was applied. Using the conversion coefficient determined by eq. 4.3, these experiments showed a beam energy sensitivity of $\Delta E_{\text{sin}} \sim \pm 26$ V, thus determining $\Delta E/E \sim 2 \times 10^{-3}$ for the CEA sensitivity (resolution) to the plasma fluctuation measurements.

Figure 4.23 shows the PSD of the i_{sum} (related to the plasma $n_e\sigma$) and δi (related to the plasma potential) band-pass filtered at 80-120 kHz for one particular plasma cycle of shot #46913. The standard deviation of the potential fluctuation is $(\tilde{\varphi})_{\text{std}} \sim \pm 40$ V. The evolution of the spectra in this Figure puts in evidence the interplay between local plasma pressure ($PSD-i_{\text{sum}}$) and electric potential ($PSD-\delta\varphi$) for a previously identified by HIBD in similar plasmas [1.19].

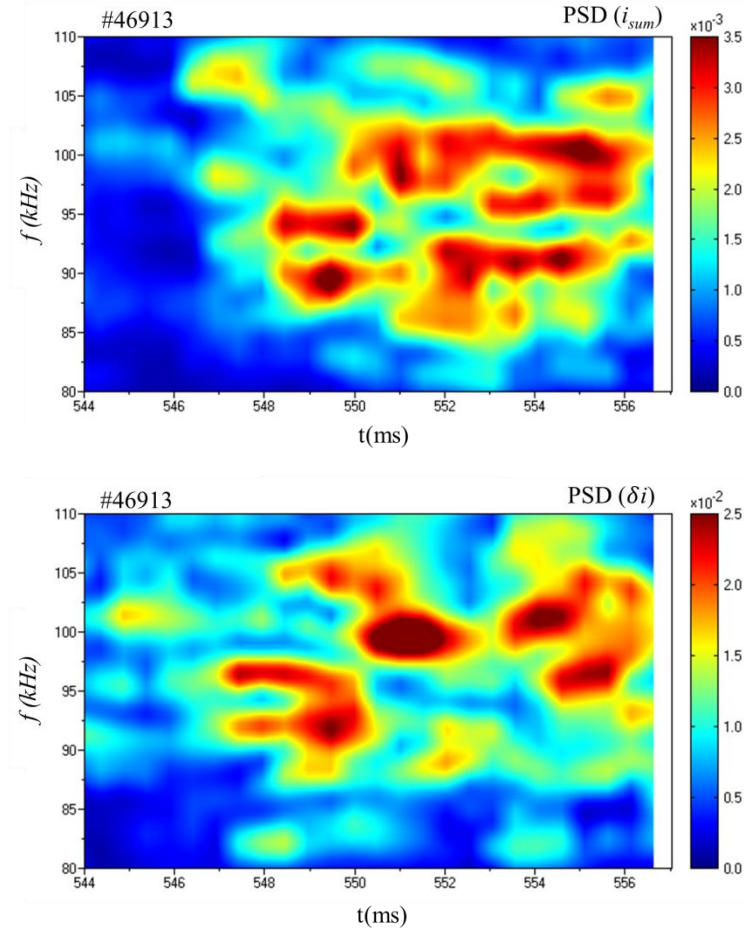


Figure 4.23 presents the power spectral density for frequency range (80-110 kHz) for sum current (i_{sum}) (proxy to plasma pressure) and normalized current (δi) (proportional to plasma potential) for same time interval {544-556 ms} during a plasma discharge for shot #46913.

4.8. Conclusions

The 90° cylindrical energy analyzer was successfully commissioned in the ISTTOK HIBD for performing the measurements of the plasma potential and its fluctuations. The proposed indirect calibration method allows performing the absolute plasma potential measurements. The typical value of plasma potential was found to be $\varphi \sim -340$ V with estimated calibration error $\Delta\varphi = \pm 71$ V, measured in the plasma core. The obtained negative plasma potential values represent the general trend of values observed in tokamaks and its amplitude is in agreement with previously measurements made in ISTTOK by TOF energy analysis [1.15];

Experimental relative calibration established the CEA resolution of $\Delta E/E \sim 2 \times 10^{-3}$ obtained with external sinusoidal modulation of beam energy. Finally, the combined measurements of the plasma pressure-like and plasma potential fluctuations in the core were obtained with an error of $(\Delta\varphi)_{std} \sim \pm 40$ V during a MHD activity. The Plasma potential fluctuations attributed to MHD activity were also observed by HIBD on the TEXT tokamak [1.19] and on the CHS stellarator [4.2, 4.3].

Chapter 5

TJ-II Experiments

This chapter reports on the experiments conducted on dual HIBP installed in TJ-II stellarator during the thesis work. The experimental results relevant to fusion plasmas obtained by plasma potential and its fluctuation measured using Heavy ion beam probe (HIBP) is presented in this chapter. The chapter starts with an introduction that describes the dual HIBP diagnostic system at the TJ-II stellarator. The chapter is further divided into three sections. In the first section is investigated the effect of edge biasing on core plasma potential and plasma potential flux surface asymmetries in the TJ-II stellarator. In the second section is presented the measurements of 2D poloidal plasma profiles and their fluctuations in ECRH plasmas using the HIBP system in the TJ-II stellarator. Finally the third section compares the plasma potential profiles for co- and counter- NBI heating at the TJ-II stellarator.

Dual HIBP at TJ-II stellarator

Stellarator TJ-II [5.1], is a flexible heliac situated in CIEMAT in Madrid, Spain with major radius, $R = 1.5$ m, and minor radius, $a = 0.22$ m. The magnetic surfaces of TJ-II are completely determined by means of external coils before plasma initiation. These coils include: 32 toroidal field coils, two central coils (one circular and one helical) and vertical field coils. The magnetic field generated by these coils generates bean-shaped magnetic flux surfaces. The plasma is heated by Electron cyclotron resonance heating (ECRH) and Neutral beam injection (NBI). Typically, the beam-shaped plasma discharges at TJ-II lasts around 0.25 s. The vacuum vessel is divided into four sectors: A, B, C and D (as indicated in Figure 5.1), corresponding to the four-fold toroidal symmetry of TJ-II stellarator. Each Sector is further divided into 8 regions.

The dual setup of the Heavy Ion Beam Probe (HIBP) system is one of the unique diagnostic installations in TJ-II stellarator [5.2]. The advanced HIBP measures electric potential (ϕ), electron density (n_e) and poloidal magnetic field (B_p) component of the sample volume (SV) inside the plasma. The dual HIBP systems in TJ-II consist of two similar HIBPs that are located at two different toroidal ports separated by 90° (sector A4 / HIBP2 and B4 / HIBP1) in the torus as indicated in Figure 5.1. The two HIBP are located at the equivalent toroidal location assisting the possibility of studying long-range correlations of core plasma parameters.

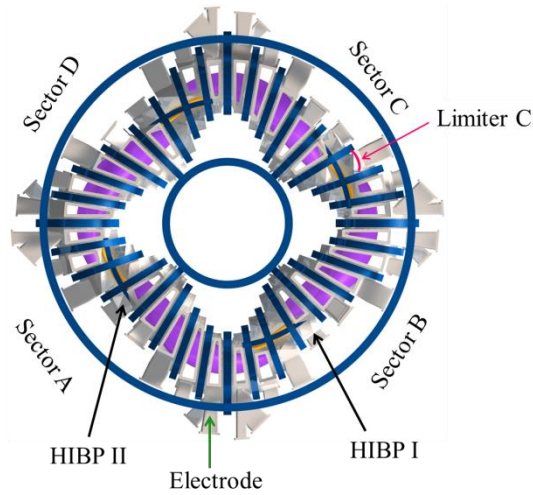


Figure 5.1 Presents the schematics of top view- TJ-II stellarator. The location of the Dual HIBP located in the similar poloidal cross-section separated in the torus by angle of $\pi/2$ is indicated in the figure.

Working principle

The basic principle of operation of Heavy ion beam probe (HIBP) at TJ-II is the same as explained in the sec.1.2. Figure 5.2 presents the schematics of HIBPI (left) and HIBPII (right) as installed in TJ-II stellarator. The primary beam of Cs^+ ions (used in present experiments) is generated and accelerated in the injector. The injector is followed by the beam deflection and steering plates system to inject the primary beam into the plasma. Inside the plasma, the primary beam ions are ionized by the action of plasma electrons generating secondary ions (Cs^{2+}) beam. The double charged ions are deflected by the toroidal magnetic field (B_t) and collected by the energy analyzer [5.3]. The injected ions and their injection energy are selected such that the Larmor radius of the secondary ions is larger than the size of the plasma column, which can be achieved by using heavy ions. The point of ionization or the sample volume (SV) probed by the injected primary beam can be determined by the primary beam energy (E_b) and on the control voltages on the four set of steering plates in the primary beam line to scan the beam from High Field Side (HFS) to Low Field Side (LFS).

The advanced HIBPII consists of two energy analyzers aiming for the extended simultaneous coverage of the plasma cross-section [5.6]. Each analyzer of HIBPII has 5 input slits and HIBPI consists of a single analyzer with two input slits. The five entrance channels of HIBPII correspond to 5 SV's inside the plasma that allows simultaneous measurements of plasma parameters. The low noise electronics allows plasma parameter profiles measurements with the temporal resolution $\sim 10\mu\text{s}$ and spatial resolution $\sim 1\text{cm}$.

The following section is presented the experimental results obtained using HIBP at TJ-II stellarator in this thesis work.

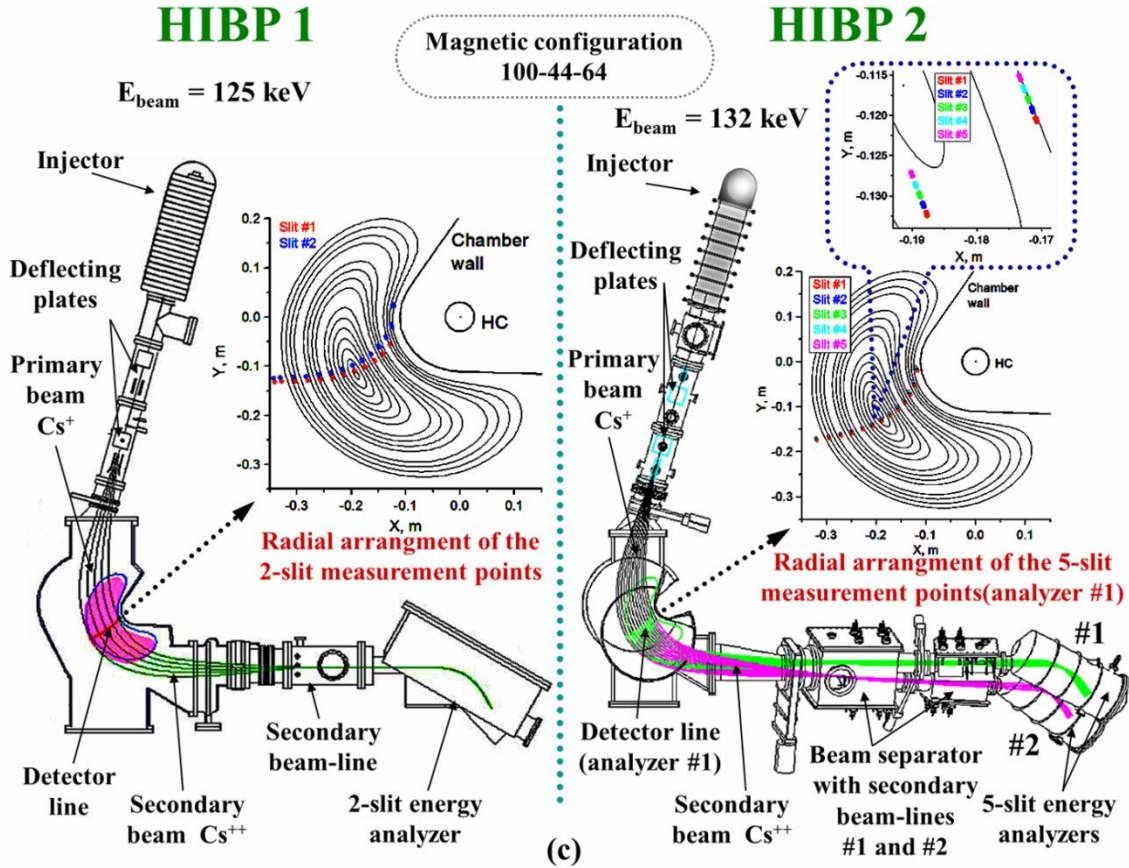


Figure 5.2 Schematics of HIBPI (left) and HIBPII (right) (Figure from [5.7])

The HIBPs at TJ-II obtain direct measurements of local plasma potential (ϕ) by measuring the energy of the secondary ions (as explained in sec.1.2.1. HIBD ISTTOK)

The heavy ion beam diagnostic (HIBD) in ISTTOK is based on the unique concept of Multiple Cell Array Detection (MCAD). The multi-channel detection concept of HIBD facilitates the diagnosis of the secondary ion beams generated from entire sample volumes along the path of primary beam inside plasma. The collection of all the fan of secondary ion beams exiting the plasma allows the determination of radial profile of plasma parameters, such as, plasma density, plasma potential and poloidal magnetic field; from the entire plasma diameter at once with high spatial and temporal resolution [1.7, 1.8]. Furthermore, the HIBP at ISTTOK is unique as it collects the primary ion beam current, which can be used for the absolute density profile reconstruction [1.9]. The ability to collect all the secondary ions simultaneously instead of probing each sample volume successively distinguishes it from the conventionally used HIBProbe to the HIBDiagnostic.

Working principle: A schematic of the diagnostic operation at ISTTOK and underlying physics is presented in Figure 1.4. The primary beam of single charged heavy ions (Xenon, Cesium, etc.) is injected across the plasma in the direction perpendicular to the toroidal magnetic field. The primary beam ions are further ionized inside plasma upon action by plasma electron and are ionized doubly (secondary beam) and to some extent to triply (tertiary beam) or more charged ions. Due to the presence of the magnetic field and the difference of the ion charge, the secondary beam trajectories are separated from the primary one. The primary beam and

secondary ion beams (which are generated along the primary beam path in the plasma) are collected by multiple cell array detectors.

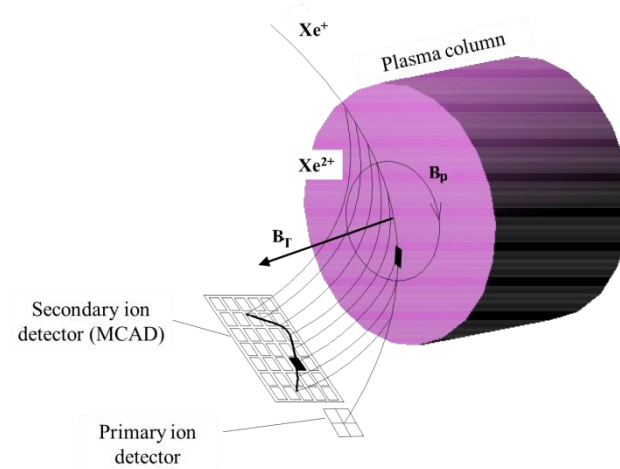


Figure 1.4 Shows a schematic representation of the primary and secondary ion beam trajectories, together with the detectors and plasma for the ISTTOK HIBD configuration (Figure from [1.12]).

1.2.3). Besides measuring ϕ HIBP is also capable of measuring several important plasma quantities (as described in ref [5.4]) such as:

- (i) Determination of radial (E_r) and poloidal (E_{pol}) component of the electric field by measuring potential from neighboring SVs using multichannel detection approach; thus, determining plasma drift velocity across the magnetic field.
- (ii) The density at the sample volume can be retrieved by secondary ion beam current, ionization cross-section at sample volume and primary beam energy. Recently the density profiles were reconstructed using HIBP in ECRH plasma at TJ-II [5.39].
- (iii) Determination of Radial local turbulent flux by simultaneous measurement of fluctuations in density and potential.
- (iv) Plasma broadband turbulence rotation and poloidal mode number of perturbation can be obtained by measurement of the fluctuations in density from different poloidal SVs.
- (v) Magnetic oscillation measurement from core of the plasma by measuring beam shift on the detector due to component of poloidal magnetic field.

The method to obtain these parameters is presented in ref [5.3 and 5.4].

The Dual HIBP in TJ-II has produced results concerning several relevant topics in fusion plasma such as characterization Alfvén Eigen modes [1.24], GAM structure [1.33], effect of radial electric field [5.5], transport and turbulence characteristics [5.4].

5a. Effect of edge biasing on core plasma potential and plasma potential flux surface asymmetries in the TJ-II stellarator

5a.1. Introduction

The accumulation of highly charged impurity ions in the plasma core poses one of serious threats to the realization of fusion power. In the standard neoclassical theory impurity accumulation has been explained as due to the negative (inwards pointing) radial electric field required to satisfy the ambipolarity condition in high density (ion root) regimes in stellarators [5.8]. But there are some experimental observations of outward impurity flux that are not well understood in stellarators [5.9, 5.10] and call for improvements of the neoclassical theory [5.11, 5.12]. In this context, the component of the plasma potential that is non-constant along magnetic flux surfaces can play an important role on impurity transport. Heavy impurity ions are much more sensitive than other plasma particles due to their high charge to the variations in the electrostatic potential.

Direct experimental observations of electrostatic potential variations within the same magnetic flux surfaces have been previously reported in the plasma edge of the TJ-II stellarator using Langmuir probes [5.13]. Significant edge asymmetries have been observed in electron-root wave-heated plasmas, which are reduced in ion-root beam-heated conditions and when the electron temperature decreases. The order of magnitude (in the order of tens of volts) as well as the observed dependencies on the electric field is consistent by neoclassical Monte Carlo calculations, thus improving confidence in impurity transport predictions. More recently, poloidal asymmetries in the radial electric fields have been found in the plasma gradient region in TJ-II measured using Doppler reflectometry in consistency with predicted plasma potential asymmetries in magnetic flux surfaces [5.14].

This sub-chapter reports on the investigation of core plasma potential asymmetries by studying the core plasma potential response due to external edge biasing. The plasma potential is measured by the dual Heavy ion beam probe located at two toroidally separated locations in the stellarator at TJ-II. The plasma response on the plasma potential due to biasing is also investigated in electron ($E_r > 0$) and ion root ($E_r < 0$) scenarios.

5a.2. Experimental setup

Plasmas discharges were heated by Electron Cyclotron Resonance Heating (ECRH) (2 x 300 kW gyrotrons, at 53.2 GHz, 2nd harmonic, X-mode polarization) and Neutral Beam Injection (NBI) (500 kW port-through power at 33 kV). Central electron temperature and plasma density up to 1 keV and $1.7 \times 10^{19} \text{ m}^{-3}$ are achieved in ECRH plasmas respectively. Whereas in NBI sustained regimes core plasma densities and electron temperatures were in the range $2 \times 10^{19} \text{ m}^{-3}$ and 400 keV, respectively, were observed.

The dual Heavy Ion Beam probe (HIBP I and II) are located at symmetric poloidal sector separated toroidally by $\pi/4$ (Figure 5.1) in the torus. A graphite electrode was installed on a reciprocating probe drive at Sector A8 and biased with respect to a radially movable limiter at sector C3 (as indicated in Figure 5.1). In the present experiments the electrode was inserted 3cm in the edge, corresponding to $\rho \approx 0.85$ ($\rho \sim 0.85$ inside the Last Closed Flux Surface (LCFS)). whereas the limiter was kept at the LCFS ($\rho = 1$). The electrode was biased with respect to the limiter with an AC voltage during plasma discharges. HIBP measurements were used to monitor the core plasma potential response to edge biasing voltage: 340 V / 250 Hz.

A typical time evolution of the target discharges is shown in Figure 5.3. At the first half of the discharge, the plasma is sustained by ECRH with plasma density in the range of $0.5 \times 10^{19} \text{ m}^{-3}$. At the middle of the discharge ($t \approx 1.16 \text{ s}$) the heating scheme is switched to NBI heating with plasma densities in the order of $1 \times 10^{19} \text{ m}^{-3}$. The ECR heated plasma has a lower density and a larger particle transport (reflected in the H_α emission) than the NBI heated plasma (Figure 5.3).

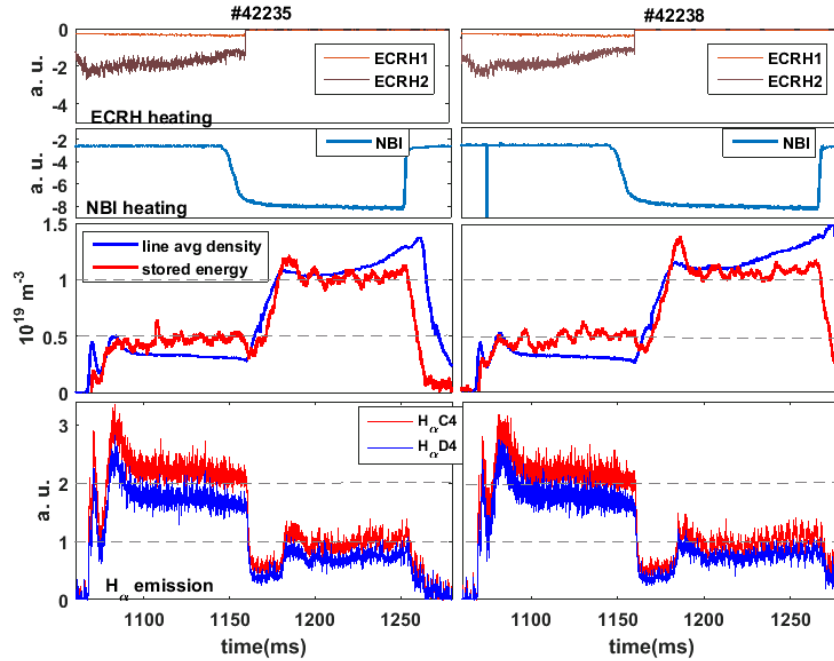


Figure 5.3 Time evolutions of ECRH and NBI heating power, line averaged density and [2.12] H_α emission in the investigated plasma scenarios.

5a.3 Influence of edge biasing on core plasma potential in ECRH and NBI scenarios

Figure 5.4 shows the influence of edge biasing on core plasma potential measured by the HIBP diagnostic at $\rho \approx 0.5$ in NBI heated plasma scenarios for negative biasing voltage. In this particular regime, core plasma potential (ϕ) responds clearly to edge negative biasing (V_{bias}) (with amplitude of -340 V) and induced edge biasing current (I_{bias}) reaching values up to 20 A.

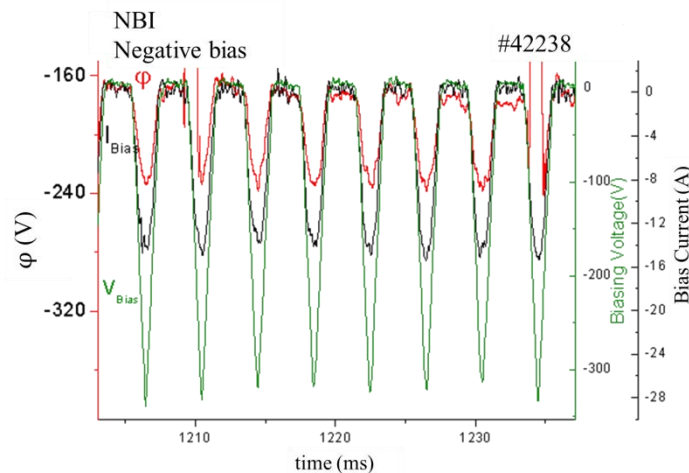


Figure 5.4 Presents the plots for plasma potential (ϕ , red) applied external biasing voltage (V_{bias} , green) and biasing current (I_{bias} , black) for NBI heated plasma for negative biasing.

In Figure 5.5 and Figure 5.6 is shows the response of the plasma potential and bias current, respectively, for ECRH (electron root) and NBI (ion root) heated plasma for positive and negative biasing voltage measured by HIBPI (slit2) and HIBPII (slit3). The response of core plasma potential to edge biasing strongly depends on the heating scenario. Whereas a significant core plasma modulation (in the range of 50 – 100 V) is observed in ECRH and NBI scenarios with positive and negative biasing respectively, the plasma response is weaker in ECRH and NBI scenarios with negative and positive biasing respectively. This phenomenology is consistent with the asymmetric I-V electrode characteristic.

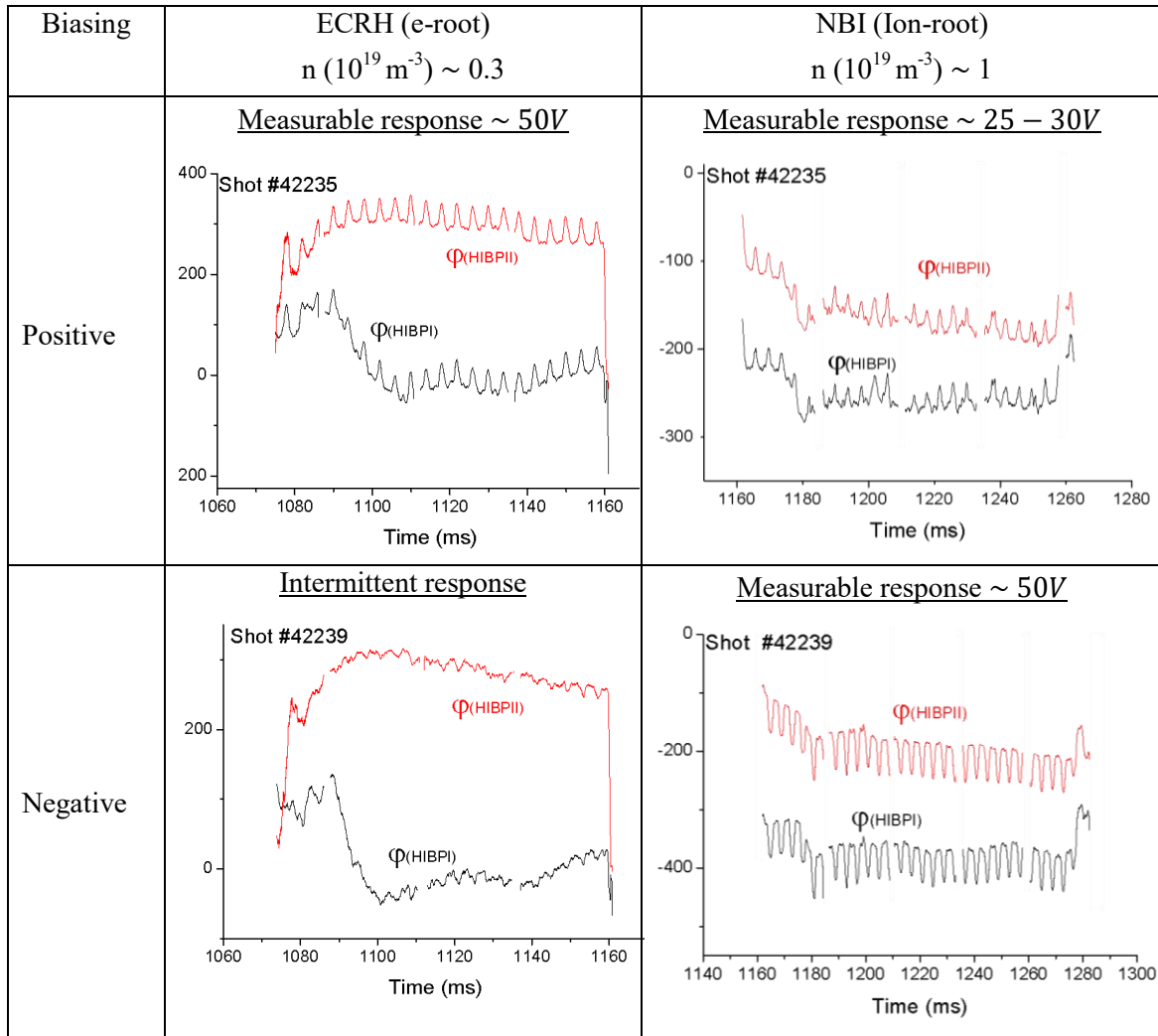


Figure 5.5 Shows evolution (with respect to time) of the plasma potential (ϕ) (in volts on Y axis) obtained from HIBPI (black) and HIBPII (red) in response to external biasing. The response of the plasma potential is presented depending on the sign of the biasing voltage for ECRH and NBI phase of the plasma.

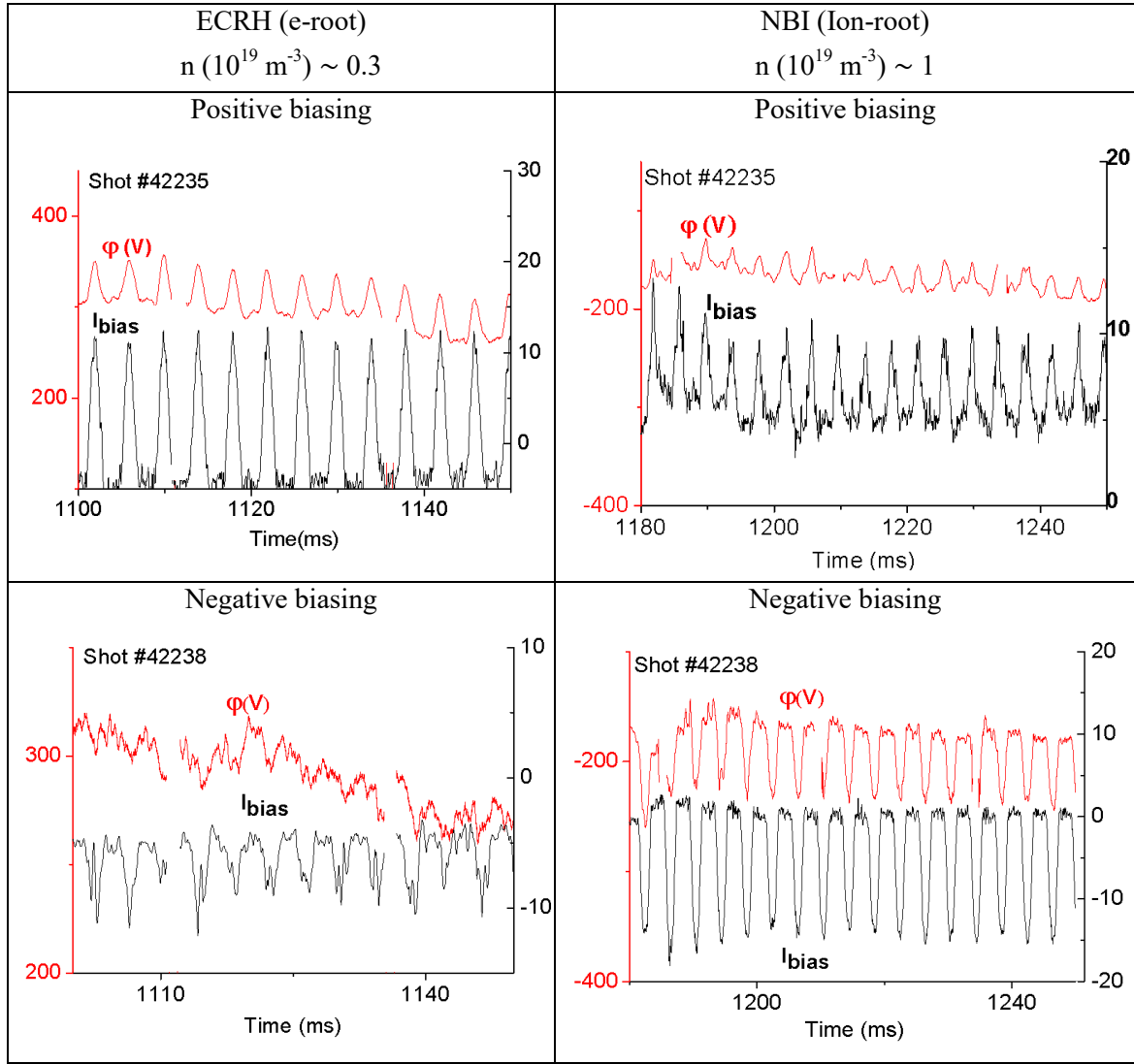


Figure 5.6 shows the similar response of plasma potential measured by HIBPI (ϕ , red) and biasing current (I_{bias} , black) for positive and negative bias voltage with respect to ECRH and NBI heated plasma.

5a.4 Core plasma response to edge plasma biasing and dependence on plasma parameters

The HIBPI and HIBPII systems have been arranged to measure the plasma potential in a fixed plasma sample volume located at $\rho = 0.5$. The potential difference response to edge biasing, $\delta\phi$, between the two HIBP is calculated and its dependence is studied on the plasma density, temperature and mean core plasma potential evolution. Where $\delta\phi$ can be defined by eq. 5.1,

$$\delta\phi = [\phi(hibp1) - \phi(hibp2)] \quad \text{eq. 5.1}$$

The method used to evaluate the $\delta\phi$ value to minimize the error of measurement is demonstrated in Figure 5.7. The difference in the plasma potential response in HIBPI and HIBPII is measured by averaging the value obtain by first aligning the left 'shoulder' joining the

respective base line and measuring the difference between peak to peak. The same procedure is repeated for the right hand side and the difference between the two sides is averaged.

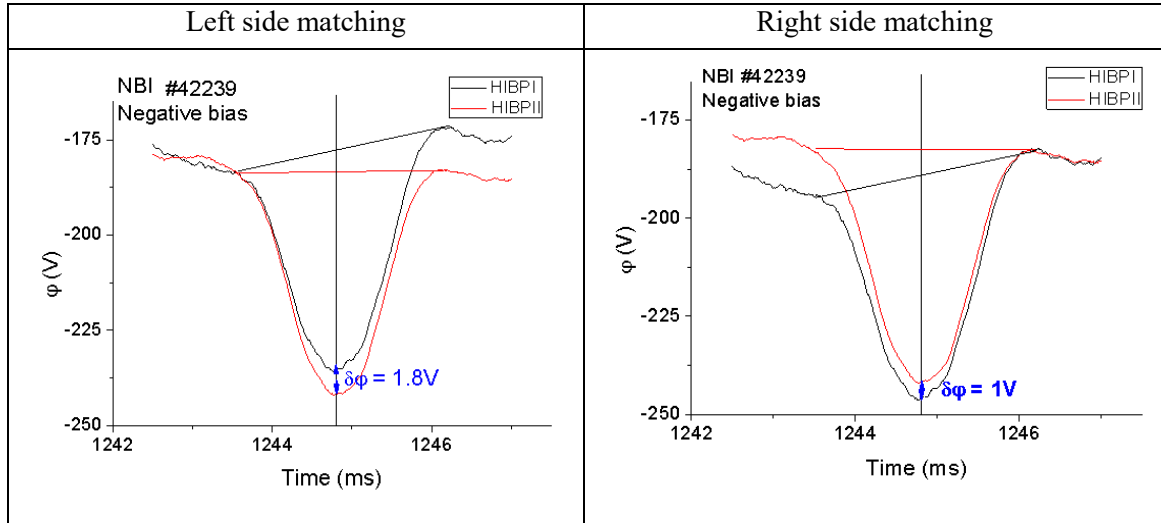


Figure 5.7 Demonstration of measurement difference in potential measured by HIBPI and HIBPII ($\delta\phi$) in response to edge negative biasing. The peak to peak difference is average after aligning the base line for left and right side of the potential response.

Following sections examines the dependency of the above mentioned plasma parameters on the $\delta\phi$ (eq 5.1), when both the HIBP's are fixed to probe position ($\rho = 0.5$) for positive bias and negative biasing for ECRH and NBI heating scenarios, respectively.

i) *Influence of plasma density on $\delta\phi$*

Figure 5.8 shows the dependence of $\delta\phi$ for positive biasing in ECR heated plasmas (electron root) (left) and negative biasing in NBI heated plasma (ion root). The graph on the left shows the evolution of $\delta\phi$ for two different ECRH discharges in the density range: $(0.27-0.35) \times 10^{19} \text{ m}^{-3}$. The evolution of $\delta\phi$ for negative biasing NBI heated plasma in the density range $(0.4-1.5) \times 10^{19} \text{ m}^{-3}$ for two different discharges is presented on the right. It can be inferred from the graphs that the value of variation in $\delta\phi$ is in the order of 5-10 V which is within the error bars of the HIBP diagnostic capabilities.

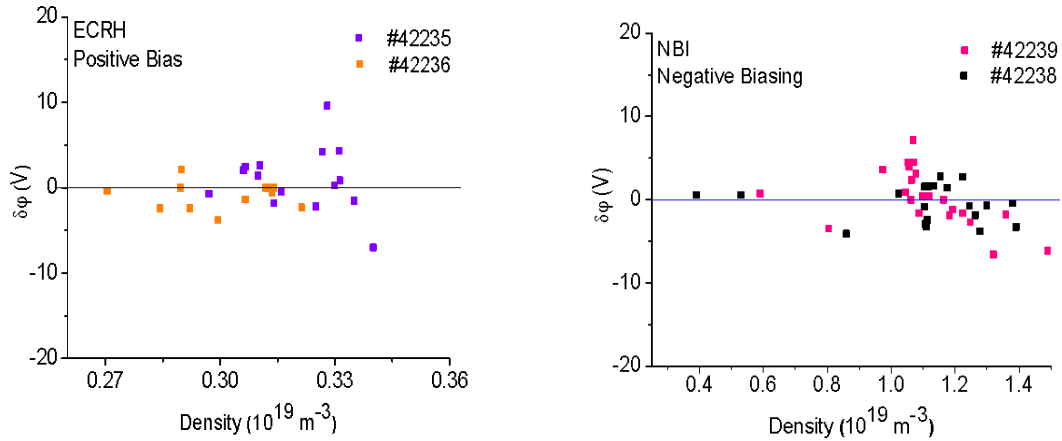


Figure 5.8 Presents the scatter plot of $\delta\phi$ with respect to plasma density for two discharges for positive edge biasing for ECRH plasma (left) and negative edge biasing for NBI heated plasma (right).

ii) Influence of electron temperature on $\delta\phi$

The dependence of $\delta\phi$ on plasma electron temperature for positive biasing for ECR heated plasmas (electron root) (left) and negative biasing NBI heated plasma (ion root) is plotted in Figure 5.9. The graph on the left shows the evolution of $\delta\phi$ for two different ECRH discharges for the temperature (0.6-0.75) keV. The evolution of $\delta\phi$ for negative biasing NBI heated for temperatures (0.24-0.27) keV for two different discharges is presented in the figure 5.9 (right). It can be inferred from the graphs that the value of variation in $\delta\phi$ is in the order of 5-10 V which is again comparable to the error bars in the diagnostic capabilities of HIBP. The electron temperature for ECR heated plasma is measured by ECE diagnostics and NBI heated plasma is measured by Thompson scattering.

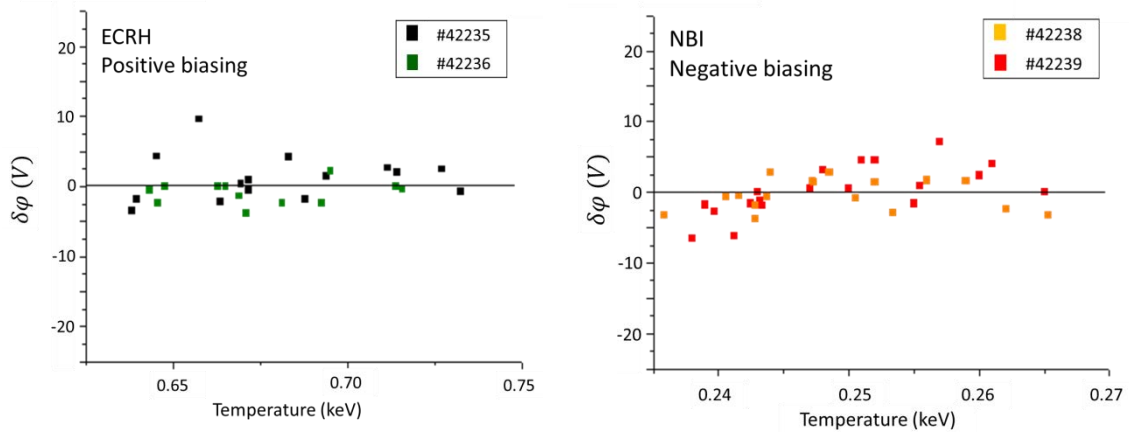


Figure 5.9 presents the scatter plot of $\delta\phi$ with respect to electron temperature for two discharges for positive edge biasing for ECRH plasma (left) and negative edge biasing for NBI heated plasma (right).

iii) *Influence of mean potential on $\delta\phi$*

The Figure 5.10 shows the variation of $\delta\phi$ value for ECRH positive biasing (left) and NBI negative biasing (right) heated plasma with respect to the mean potential measured at fixed $\rho \sim 0.5$. It can be deduced from the plots in Figure 5.10 that the variation in $\delta\phi$ with respect to mean potential is around 5-10 V which is within the diagnostics capabilities of HIBP.

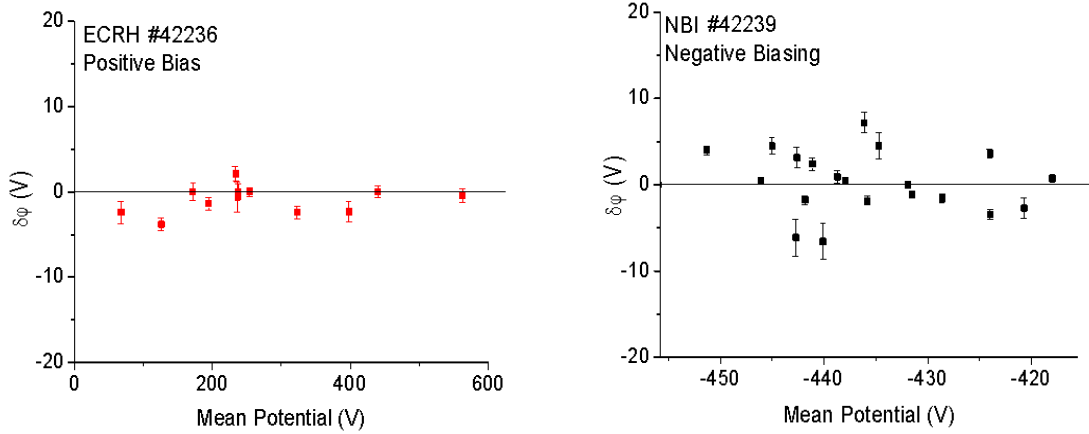


Figure 5.10 presents the scatter plot of $\delta\phi$ with respect to plasma mean potential for a discharges for positive edge biasing for ECRH plasma (left) and negative edge biasing for NBI heated plasma (right).

5a.5 Conclusion

A unique experimental set-up, based on a dual HIBP system, has allowed to measure simultaneously at two different toroidal / poloidal positions the core plasma potential response to edge fluctuations in different ECRH and NBI plasmas scenarios in the TJ-II stellarator. It has been found that the plasma response to edge biasing strongly depends on the heating scenario, being maximum in ECRH and NBI scenarios with positive and negative biasing respectively. This phenomenology is consistent with the asymmetric I-V electrode characteristic. Within experimental uncertainties and in the explored plasma scenarios, no evidence of core plasma potential flux surface asymmetries was found.

5b. Measurements of 2D poloidal plasma profiles and fluctuations in ECRH plasmas using the Heavy Ion Beam Probe system in the TJ-II stellarator

5b.1 Introduction

Understanding and predicting particle and energy transport driven by turbulence is a key research issue in magnetically confined fusion plasmas. Upcoming fusion devices, like ITER, will explore plasma regimes that are far from present devices in many aspects. Therefore, extrapolations from purely empirical data can be misleading, thus reliable data are required to validate models in existing plasma scenarios.

The characterization of plasma potential and its fluctuations is an important topic to understand and validate transport mechanisms in magnetically confined fusion plasmas [5.3]. The search for asymmetries in edge plasma fluctuations has shown the importance of the curvature driven instabilities in the plasma boundary region [5.15]. First direct experimental evidence of strong poloidal Reynold stress asymmetry also pointed out the curvature driven zonal flow, which is similar to the asymmetry observed in turbulent transport [5.16]. In addition, flux-surface variations of electrostatic potential can have a significant impact on high-Z impurity radial fluxes [5.11, 5.12, 5.17]. Radial electric field asymmetries have been measured at the TJ-II stellarator that could be explained to be due to plasma potential variations within the flux surfaces [5.13, 5.14]. Gyrokinetic (GK) simulations in stellarators show a strong localization of unstable modes along flux surfaces [5.14, 5.18, 5.19]. 2D core and edge density fluctuations have been previously investigated using beam emission spectroscopy [5.20] and fast visible cameras [5.21]. The first attempt to measure 2D spatial potential profiles has been done by heavy ion beam probe in the LHD stellarator [5.22] covering less than $\frac{1}{4}$ of the poloidal plasma cross-section.

Another important factor contributing to the particle transport is the density gradient localization, which is closely connected to the refuelling of next step tokamaks and stellarators devices. Fueling of core plasma particles is expected to be achieved with pellet systems that inject particles at high speed deep into the plasma. However, at reactor relevant plasma densities and temperatures, pellets are unable to reach the core plasma region. In fact, pellet ablation will take place in the plasma edge region [5.23, 5.24, 5.25, 5.26] causing plasma bumps with positive and negative density gradient regions where eventually particles could be transported radially inwards by turbulence. Fluid and GK simulations have investigated the level of inward turbulent particle transport in the inverted density gradient region [5.27, 5.28, 5.29], but comparisons of simulations with experimental fluctuation levels and fluxes are still missing. TJ-II stellarator is well suited to investigate the influence of such positive and negative density gradients on plasmas fluctuations and transport due to their unique capabilities to control plasma scenarios and magnetic configuration [5.30].

The unique diagnostic set of dual Heavy Ion Beam Probe [5.2] (HIBPs) in TJ-II has shown the capabilities to simultaneously obtain the local mean and fluctuating measurements of plasma potential, plasma density and poloidal magnetic field component with the spatial resolution of 1-2 cm and sampling rate of 2 MHz. For the first time the HIBP diagnostic has been operated in the energy scanning mode to investigate the 2D poloidal cross-section of TJ-II as the injected primary beam energy is varied. This paper reports on the first attempt to experimentally characterize 2D poloidal structures of plasma profiles using the HIBP diagnostic in low density ECRH plasmas in the TJ-II stellarator. Compared to the recent study of ECRH effects on the plasma potential spatial profiles and turbulence [5.4, 5.31], the present work allows for the production of 2D contour maps of plasma potential and fluctuations from the high field side to the low field side. In addition, the influence of plasma heating on plasma density fluctuations

has been investigated. Both results provide the experimental basis for future model validation of core plasma potential asymmetries and plasma stability in positive and negative gradient regions.

5b.2 Experimental set up

TJ-II stellarator, with major radius $R = 1.5$ m and minor radius $a < 0.20$ m, has a unique experimental arrangement of a dual HIBP system [5.6]. In the experiments reported in this paper both HIBP-I and HIBP-II systems were operated in scanning and fixed point mode from the High to the Low Field Side (HFS to LFS) regions. The point of ionization or sample volume (SV) probed by the injecting beam inside the plasma in a poloidal cross-section depends on the energy of the primary ion beam (Cs^+), determined by beam energy (E_b), and on the control voltages on the four sets of steering plates in the primary beam line to scan the beam from HFS to LFS. Experiments for the 2D poloidal scans were carried out in pure Electron Cyclotron Resonance Heated (ECRH) regimes ($P_{\text{ECRH}} \approx 300$ kW at 53.2 GHz, 2nd harmonic, X-mode polarization) with constant low density in the range $n_e \sim 0.4 - 0.5 \times 10^{19} \text{ m}^{-3}$ and central electron temperature in the range $T_e \sim 1$ keV. Experiments were performed for the standard magnetic configuration of TJ-II with the edge rotational transform value close to 1.6 and discharge duration of about 200 ms.

The experiment was organized as follows. At the first stage the radial plasma profiles were obtained over the 1D detector line [5.3] with a probing beam energy of $E_b = 132$ keV, passing from the LFS through the plasma centre to the HFS, by varying the injection angle into the plasma (control voltage). Then the beam energy was changed in steps of 2 keV from 128 to 148 keV. With each step the beam energy moves the detector line upwards by about 1 cm and forms 2D detector grid. Hence, approximately $10 \times 20 \text{ cm}^2$ of the plasma cross-section was observed from LFS to HFS for this experiment. Measurements of local mean and relative fluctuations in plasma density and potential were obtained using the parallel plate 30° energy analyser in HIBP II. The multi-slit analyser has 5 input slits that observes the 5 neighbouring plasma SVs simultaneously to measure plasma parameters mentioned before.

Figure 5.11 shows the 2D detector grid probed by Cs^+ primary beam in the poloidal cross-section varying the E_b in the range 128 – 148 keV. The primary beam is radially scanned covering HFS and LFS regions in the TJ-II poloidal cross-section. The time for each scan is fixed at 40 ms, so that we obtained 4 scans in the steady-state phase of discharge.

In addition, the experimental data for the investigation of the influence of ECRH scenarios on the plasma fluctuations are also presented. The discharges were carried out for the low density ($n_e \approx 0.4 - 0.6 \times 10^{19} \text{ m}^{-3}$) on-axis ($\rho \approx 0$) and off-axis ($\rho \approx 0.35$) ECRH scenarios. Figure 5.12 shows the temperature and density profiles for on-axis and off-axis discharges. The temperature profile for off-axis ECRH is flattened at the center as compared to the peaked profile at the center for on-axis ECRH. On-axis ECRH plasmas are characterized by peaked electron temperature and hollow density profiles as measured by Thomson Scattering (Figure 5.12). The beam from HIBP-II was scanned from HFS to LFS and power spectral densities for fluctuations were investigated.

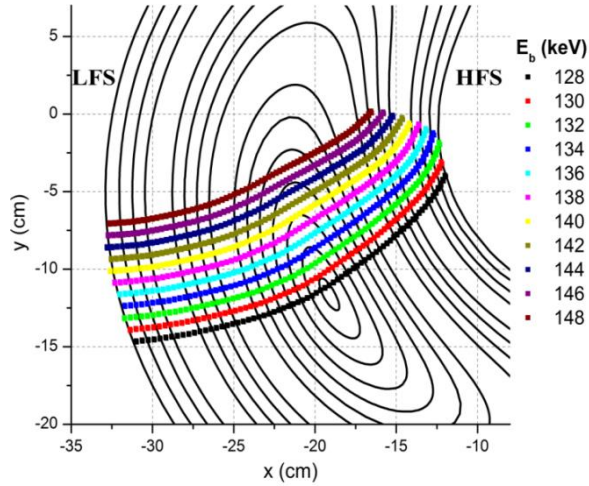


Figure 5.11 HIBP detector grid for the vertical cross-section of TJ-II for Cs^+ probing ions. Detector grid consists of 11 detector lines of equal energy E_b . Each detector line scans plasma vertical cross-sections from HFS to LFS.

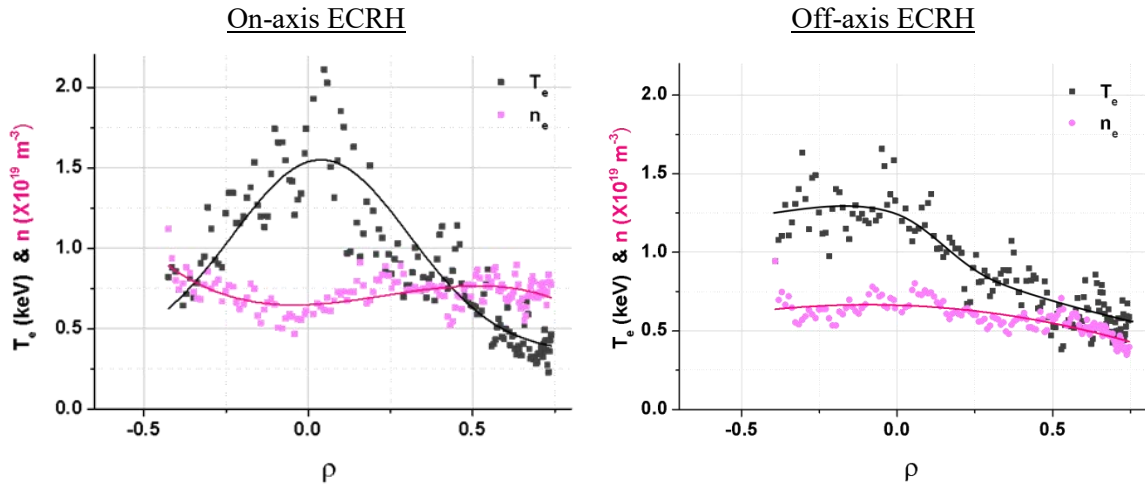


Figure 5.12 (left) On-axis ECRH electron temperature (black curve) and density profile (pink curve) for normalized ρ value obtained by fitting the data from Thomson Scattering profiles; (Left) Off-axis ECRH temperature (black curve) and density profiles (pink curve) as a function of normalized ρ value measured by Thomson Scattering (where positive and negative ρ value corresponds to low and high field side, respectively).

5b.3. Experimental results and discussion

5b.3.1. 2D Poloidal density and potential scans in ECRH on-axis experiments

The 2D analysis of averaged and root mean square (RMS) of fluctuations for plasma potential and secondary ion current (I_{tot}) is shown in Figure 5.13 and Figure 5.14, respectively. Results are plotted over the contour plots of the vacuum magnetic flux surfaces in TJ-II.

In low density plasmas ($n_e \approx 0.4 \times 10^{19} \text{ m}^{-3}$) core plasma potential is positive with values less than 1000 V (± 25 V), as presented in Figure 5.13 which corresponds to a positive radial electric field (E_r) in agreement with neoclassical predictions [5.32, 5.33, 5.34]. It should be noted that the ambipolarity condition (i.e. the equality of ion and electron fluxes) has two stable roots in stellarators: the ion root with typically $E_r < 0$, usually achieved in high density plasmas, and the electron root with $E_r > 0$, that is typically realized when electrons are subject to strong ECRH

heating, as in the plasma scenarios reported in the works [5.32, 5.35, 5.36]. The root mean squared (RMS) of potential fluctuations increases radially inwards from values in the range of 15 V in the edge to 50 V in the plasma centre.

Although the contour plots for potential and RMS of potential fluctuations seems rather close to the magnetic flux surfaces, some discrepancies should be noted. The 2D map for the absolute plasma potential (Figure 5.13, left) have a local maximum that is slightly shifted (1 – 2 cm) upwards from the axis of vacuum magnetic flux surfaces to the high field side. The local maximum of RMS fluctuations of potential (Figure 5.13, right) is also shifted upward. These shifts could be due to uncertainties in the beam trajectory calculations. The shift (in the range of 1 cm) is within the error bar for the calculation of the sample volume position. Moreover, the radial size of the SV is around 1-2 cm. In addition, top – bottom and LFS - HFS poloidal variation of average potential on vacuum magnetic surfaces is on the order of 50V (Figure 5.13). But it should be noted that this is comparable to the peak-to-peak level of experimental error for plasma potential achieved in the present experiments. As shown in Figure 5.13 right, in the explored plasma scenarios and within experimental uncertainties (± 5 V) no evidence of strong spatial localization in RMS fluctuation levels in potential was observed.

The secondary ion current (I_{tot}) measured by the HIBP is proportional to the local plasma density for low-density plasmas, neglecting probing beam attenuation (see sec. III.). Hence, normalized level of secondary ion current fluctuations, $\tilde{I}_{tot}^{rms}/\bar{I}_{tot}$, is proportional to normalised density fluctuations \tilde{n}/n , and I_{tot} measurement is a proxy to the plasma density profile.

Figure 5.14 presents the 2D poloidal map for average (left) and normalized RMS (right) values of I_{tot} . A local minimum in the RMS of I_{tot} fluctuations is located at the position of local maximum of I_{tot} mean value (see sec. 5b.3.2.). The up-down poloidal variation in total secondary current (Figure 5.14, left) could be due to the variation of Cs^+ primary current with the E_b (in the range 128 – 148 keV). The decrease in the Cs^+ ion energy also leads to the increase of primary trajectory length and causes attenuation of the probing beam. The uncertainty in I_{tot} mean value (of the order of 20%) can be accounted for as being due to the variation of the discharges. In agreement with previous studies, edge and core fluctuations are dominated by frequencies below 100 kHz [5.21, 5.37].

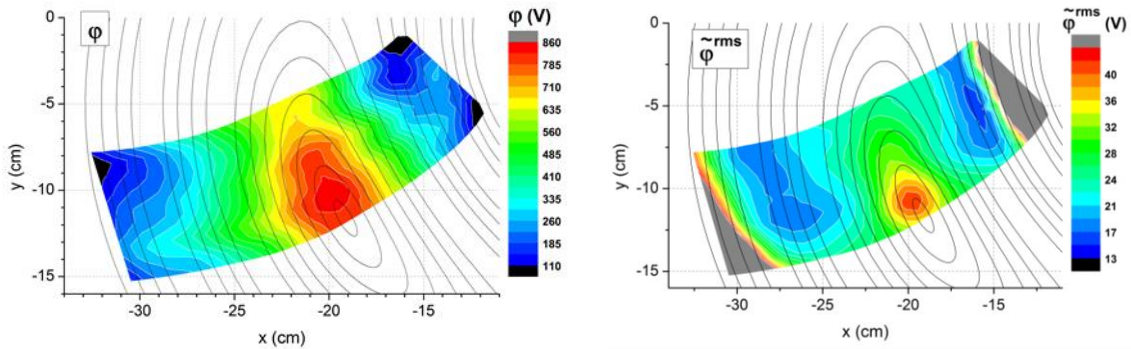


Figure 5.13 2D poloidal map of mean potential (left) and RMS potential fluctuations (right) for the line average densities ranging between $0.43 - 0.47 \times 10^{19} m^{-3}$; discharges presented (E_b changes from 128 keV to 148 keV, respectively): #44393, #44389, #44354, #44356, #44357, #44362, #44364, #44366, #44370, #44380, #44388. Vacuum magnetic flux surfaces are shown in grey.

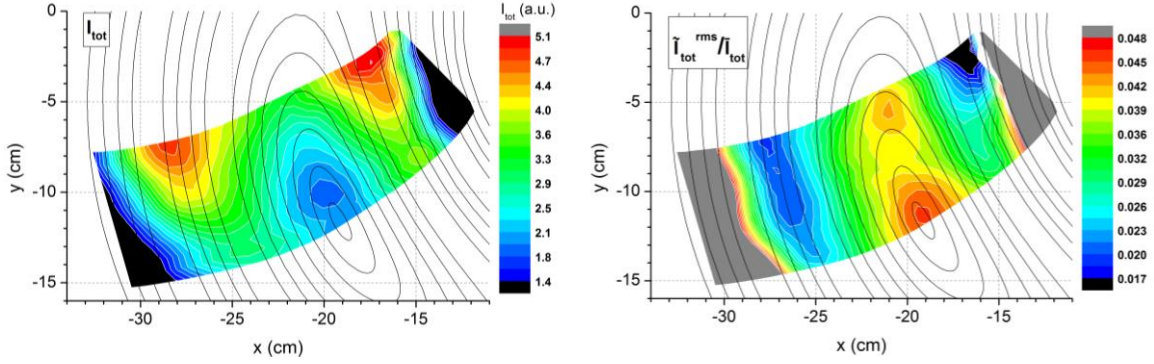


Figure 5.14 2D poloidal map for average (left) and normalized RMS (right) values of secondary ion current I_{tot} , which is a proxy of density fluctuations.

5b.3.2. Effect of ECRH on fluctuations

I. ECRH on-axis experiments

Figure 5.15 (left) presents the radial profiles of the normalized level of secondary ion current fluctuations for different primary beam energies for the results obtained during the 2D poloidal scan (see Figure 5.14). A local minimum in the normalized fluctuation levels ($\tilde{I}_{tot}^{rms} / \bar{I}_{tot}$) appears both in the HFS and LFS at $\rho \sim 0.5-0.6$. This minimum appears for all beam energies (i.e. at different poloidal locations), illustrating the poloidal symmetry and reproducibility of experimental results. The radial location of these minima is correlated with the peaks (maximum) of the I_{tot} profile, i.e. the change from positive to negative radial gradients in I_{tot} profiles as is shown in Figure 5.15 (right). Figure 5.15 (right) also shows the relative RMS fluctuation in secondary ion current for a single scan ($E_b = 132$ keV) from HFS to LFS along with the hollow secondary ion current profile in the low-density ECRH plasma.

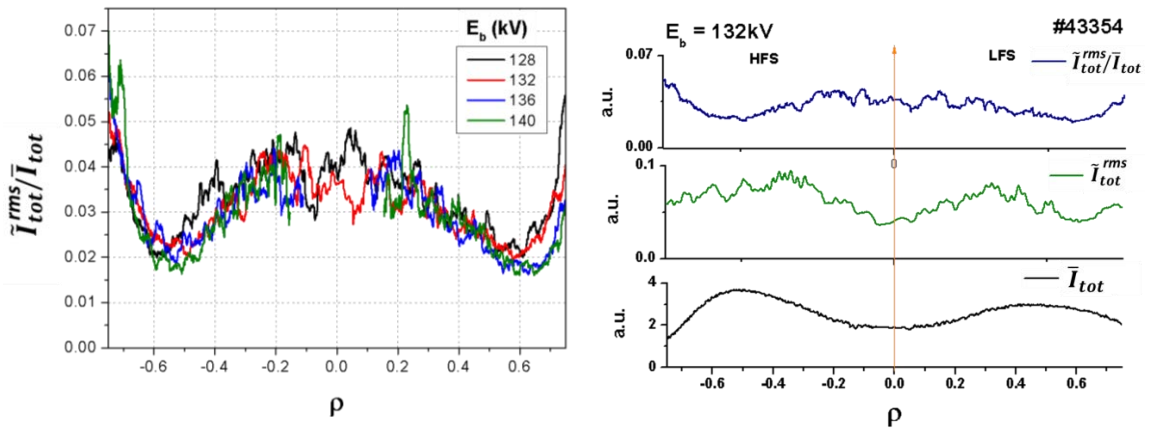


Figure 5.15 Profiles of normalized RMS of beam current fluctuation level for 4 beam energies (left); radial profiles for RMS fluctuation levels in I_{tot} and I_{tot} normalized ($\tilde{I}_{tot}^{rms} / \bar{I}_{tot}$) value in hollow density profile for on-axis ECRH plasma, $E_b = 132$ keV. The local minima are observed in I_{tot} relative fluctuations at the peaks of the I_{tot} profile (right).

The power spectrograms of density fluctuations along with the radial secondary ion current profile for on-axis ($\rho = 0$) ECR heated plasma are presented in Figure 5.16 and the same is plotted with respect to ρ in Figure 5.17. The secondary ion current profile for on-axis ECRH

indicates more peaked shape and higher maximal value in the HFS at the border between negative and positive gradient regions ($\rho \approx -0.5$). The normalized level of density fluctuations (\bar{I}_{rms}/I) is larger in the negative ($\rho = 0.7 - 1$) than in the positive ($\rho = 0.5 - 0.3$) density gradient region, with a minimum in the proximity of the zero density gradient region ($\rho \approx 0.6$). In the frequency range below 100 kHz fluctuations are strongly dominated by quasiscoherent modes [5.38] that are localized in the positive density gradient region, ($|\rho| < 0.5$).

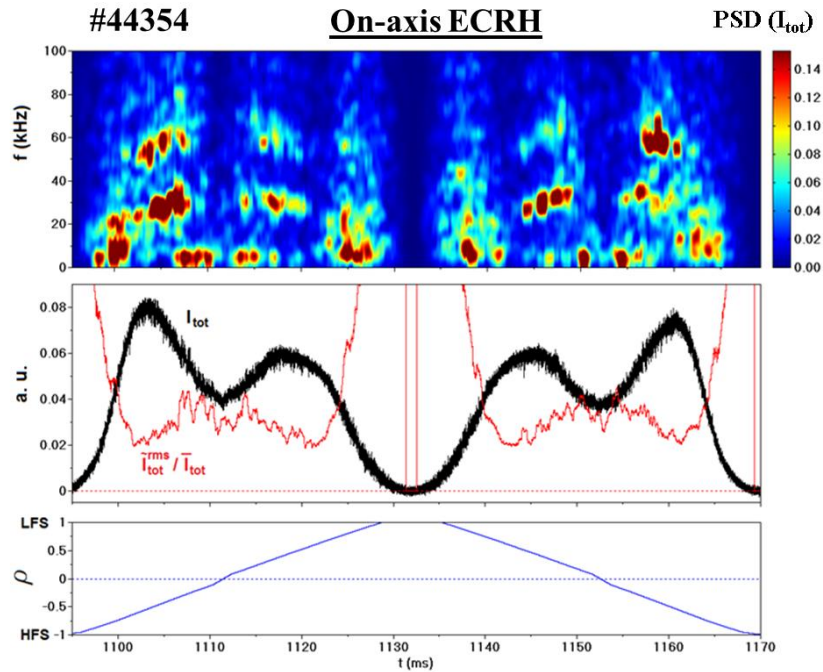


Figure 5.16 On-axis ECR heated plasma ($\rho = 0$). Power spectral density of fluctuations in the secondary ion current with respect to ρ along with the secondary ion current profile (black curve), the normalized RMS of its fluctuations (red curve) and rho position with respect to the time (blue curve), measured by HIBPII for 2 radial scans.

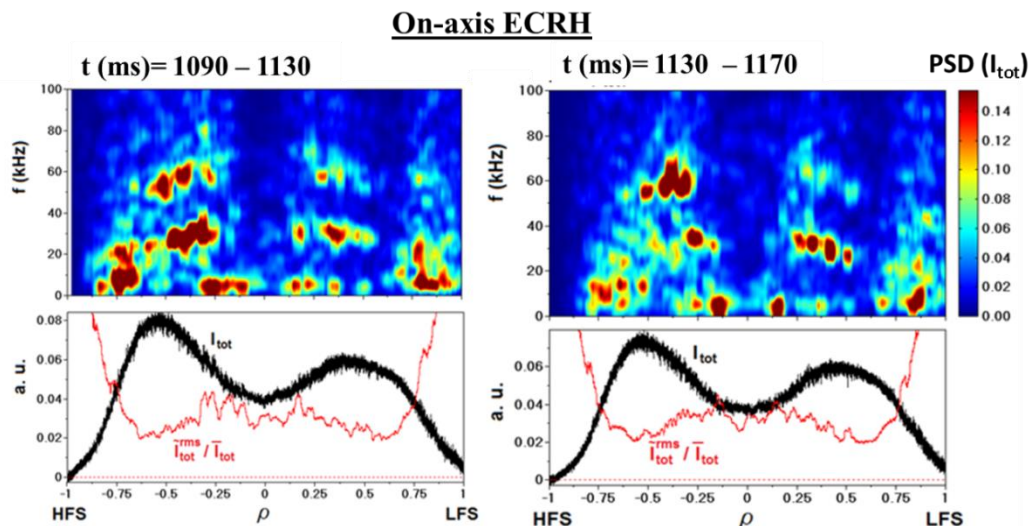


Figure 5.17 On-axis ECR heated plasma ($\rho = 0$). Power spectral density of fluctuations in the secondary ion current with respect to ρ along with the secondary ion current profile (black curve) and the normalized RMS of its fluctuations (red curve), measured by HIBPII plasma for 2 radial scans presented in the Figure 5.16.

II. ECRH off-axis experiments

Figure 5.18 and Figure 5.19 display the mean secondary ion current, normalized level of density fluctuations and power spectrogram of the secondary ion current measured by HIBP-II for off-axis ($\rho = 0.34$) ECR-heated plasmas. Power spectrograms for the two scans presented in figure 5.18 are plotted with respect to the ρ value in Figure 5.19. Fluctuations in the secondary ion current appear both at the positive and negative gradient regions, with the relative amplitude of density fluctuations higher in the negative I_{tot} gradient region (Figure 5.18 and Figure 5.19). Fluctuations are dominated by broadband frequencies (<100 kHz as shown in Figure 5.18) in the negative I_{tot} density gradient region and eventually by quasi-coherent modes in the positive gradient region (off-axis ECRH scenarios). Furthermore, plasma density fluctuations are poloidally asymmetric, showing higher power and broader frequency spectra ($f < 100$ kHz) in the LFS than in the HFS (Figure 5.19). Therefore, experimental results in off-axis ECRH scenarios shows a clear influence of positive & negative I_{tot} gradient regions on plasma fluctuations with quasicohherent modes located in the negative gradient region.

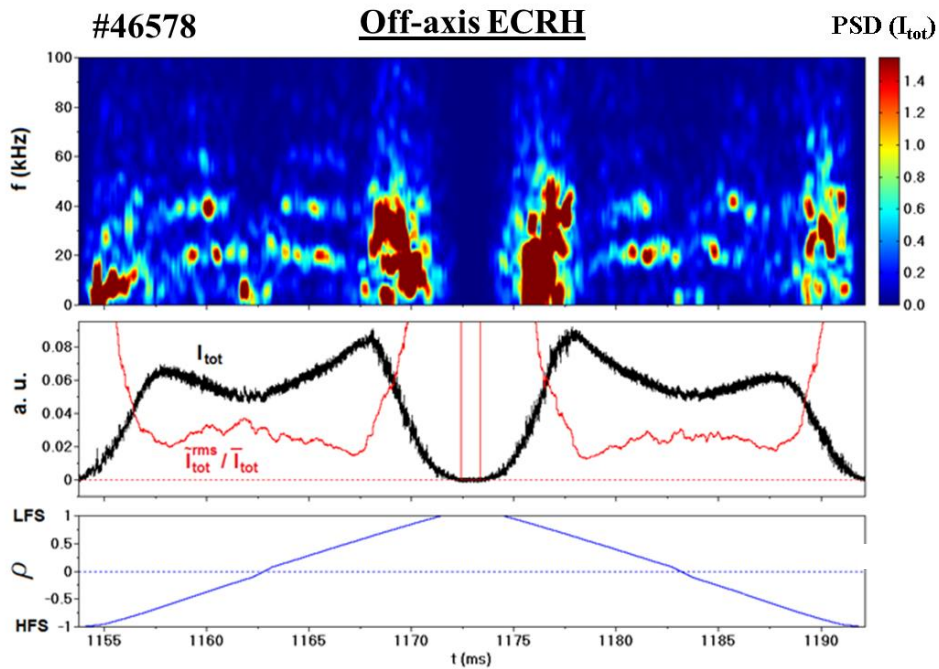


Figure 5.18 Off-axis ECR heated plasma ($\rho = 0.34$). Power spectral density of fluctuations in the secondary ion current with respect to ρ along with the secondary ion current profile (black curve), the normalized RMS of its fluctuations (red curve) and rho position value with respect to time, measured by HIBP-II for 2 radial scans.

Off-axis ECRH

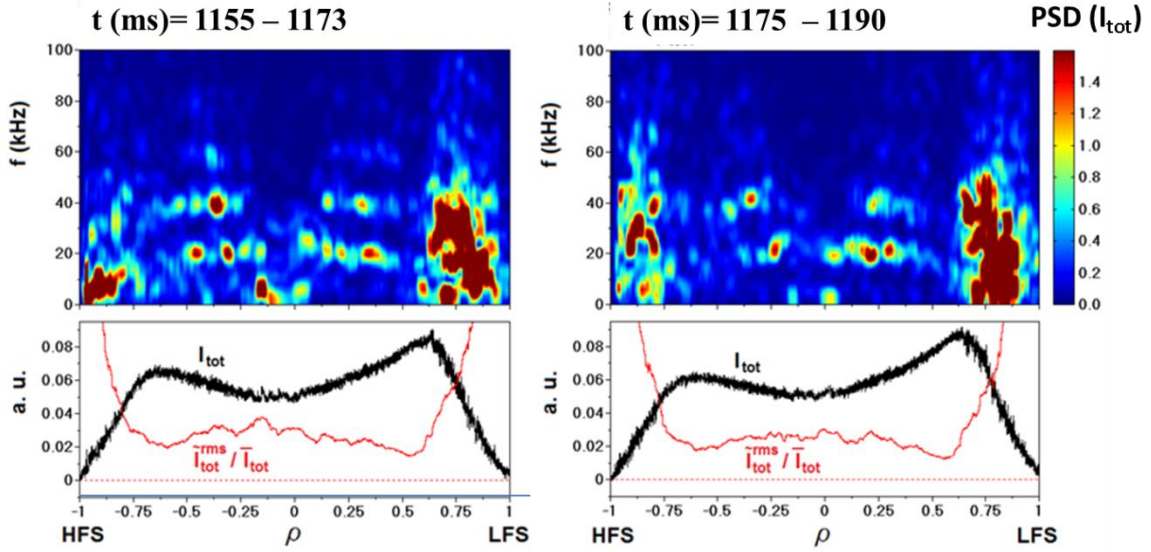


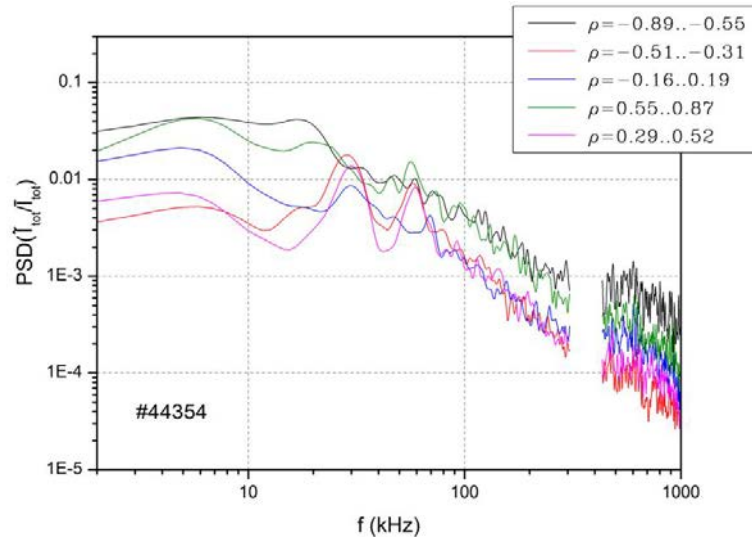
Figure 5.19 Off-axis ECRH heated plasma ($\rho = 0.34$). Power spectral density of fluctuations in the secondary ion current with respect to ρ along with the secondary ion current profile (black curve) and the normalized RMS of its fluctuations (red curve), measured by HIBPII for 2 radial scans as presented in figure 5.18.

III. ECRH on-axis vs off-axis experiments

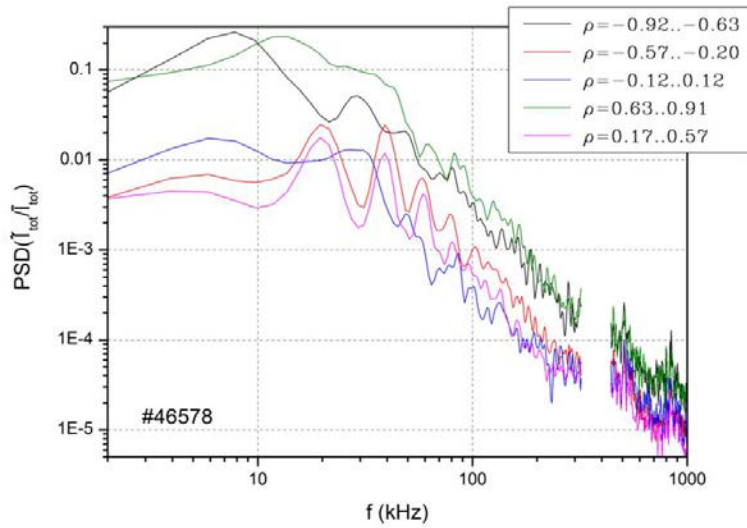
The power spectra of the normalized density fluctuations for on-axis and off-axis experiments are shown in Figure 5.20. The level of fluctuations is larger in the negative ($\rho \approx 0.9 - 0.6$) than in the positive ($\rho \approx 0.5 - 0.2$) I_{tot} gradient in the whole frequency range (1 - 800 kHz) (Figure 5.20.a and Figure 5.20.b). In the negative gradient region ($\rho \approx 0.6 - 0.9$), the amplitude of fluctuations above 100 kHz increases as core electron temperature increases (i.e. for on-axis ECRH). An opposite behavior is observed for frequencies below 100 kHz (Figure 5.20.c).

Finally, it should also be noted that secondary ion current profiles have higher peaked amplitude at the transition from positive to negative gradient regions in LFS for off axis ECRH plasma (see Figure 5.19), unlike the on-axis ECRH profile (see Figure 5.17). The origin of these differences in I_{tot} might be due to different beam trajectories and, as a result, different beam attenuation. It was already noted, the I_{tot} profile is a proxy but not the exact n_e profile. To get a proper n_e profile, even at low density, the inverse problem should be solved assuming the shape of beam trajectories, T_e profile and beam injection current [5.39].

a. On-axis ECRH



b. Off-axis ECRH



c. On-axis vs Off-axis ECRH

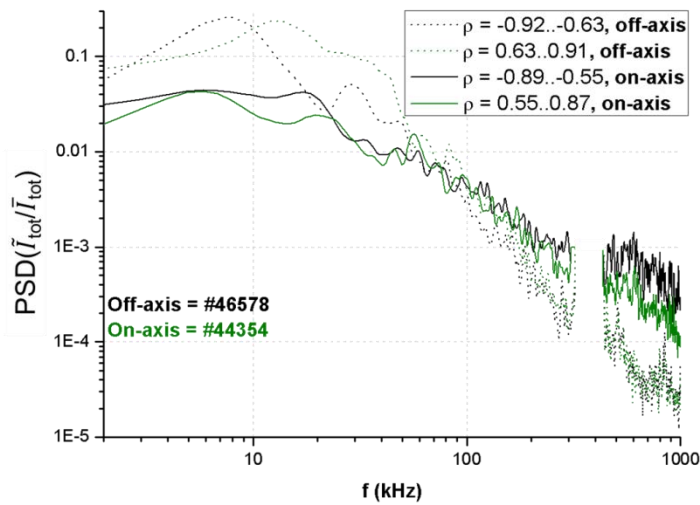


Figure 5.20 Level of fluctuations for on-axis (a) and off axis (b) ECR heated plasma for different radial positions. (c) Over plotting off and on axis fluctuations corresponding to ρ value of gradient region of density.

5b.4 Conclusions

HIBP was used in energy scanning mode to successfully obtain 2D poloidal contour plots of plasma potential and density and their fluctuations measurements in low density plasmas sustained by ECRH in the TJ-II stellarator. The new operational technique of HIBD presented scanned $\sim 1/3^{\text{rd}}$ of the core plasma poloidal area to measure fundamental plasma parameters with the following conclusions:

- a) The 2D map for the absolute plasma potential have a local maximum in the plasma core as expected in low-density high-temperature scenario. It shows about 1 cm mismatch with vacuum magnetic calculations that could be partially explained by instrumental effects. The 2D map for the absolute plasma potential shows poloidal symmetry within the experimental error ± 25 V. The 2D map for the plasma potential RMS shows poloidal symmetry within ± 5 V experimental uncertainty.
- b) Density fluctuations appear both at the positive and negative I_{tot} gradient regions for ECRH plasmas. Normalized density fluctuations are stronger in the negative I_{tot} density gradient than in the positive gradient region. Frequency spectra are dominated by frequencies below 100 kHz with different spectral characteristics in the positive and negative gradient regions that are affected by the ECRH scenario (on vs off-axis heating).

These observations are consistent with linear TEM simulation in ECRH plasma scenarios in the TJ-II stellarator where the most unstable modes appear in negative density and temperature gradients regions [5.40].

The TJ-II innovative experimental set-up, developed using a dual HIBP diagnostic, paves the way to validate models on core plasma potential asymmetries and particle fuelling under positive density gradient scenarios in the TJ-II stellarator. On-going experiments are in progress to quantify systematically the influence of the shape of temperature and density profiles on the level of fluctuations and transport in the positive & negative gradient regions. Future work will include new experiments in order to expand the 2D mapping towards the whole TJ-II poloidal cross-section.

5c. Plasma potential profiles for co and counter NBI operation in the TJ-II stellarator

5c.1. Introduction

Neutral Beam Injection (NBI) is a well-established method for heating fusion plasmas. The main power loss channels affecting NBI efficiency is the neutralization and transmission losses [5.41], and beam power coupling to the plasma as estimated through beam simulation codes [5.42]. NBIs have many applications for fusion plasmas. They are used for density control as the particles injected contribute to the fuelling plasma density. NBIs are also the main source of momentum for the plasma. By setting the injection angle tangential to the plasma the particle beam transfers its momentum to the plasma, thus, generating a current drive.

The confinement time of the ‘Fast ions’ generated by the NBI is one of the indicators of the quality of the overall confinement. The longer the fast ions are confined in the plasma the more energy of the beam is transferred to the plasma. Fast particle driven Alfvénic instabilities constitute a source of major uncertainty for predicting alpha-particle transport, alpha heating profile, and Helium ash accumulation in burning plasmas. Alfvén Eigenmodes (AEs) can have a strong influence on the confinement of fast ions, thus making NBI heating less efficient. High-frequency Alfvénic instabilities driven by fast ions have been reported in tokamak and stellarators. In particular, the HIBP system in operation in the TJ-II stellarator has already provided direct measurements of transport induced by AEs. This is an important open area of research in view of the plasma performance of stellarator / tokamak reactor devices.

The influence of co and counter NBI heating on TJ-II fast ion confinement has been previously investigated in the TJ-II stellarator [5.41, 5.42] considering losses and trapping regions as well as radial electric fields. It was concluded that ions are more efficiently confined in NBI counter-injection scenarios. In this sub-chapter, the influence of co and counter NBI scenarios on plasma potential and fluctuations are reported for TJ-II stellarator.

5c.2. Influence of co and counter NBI scenarios on plasma potential profiles

Experimental setup:

Two NBI lines in tangential Co (NBI1) and Counter (NBI2) configuration inject neutral Hydrogen beams of energies between 30 and 40 keV and total injected power between in the range of 0.4 MW. In co-injection, the beam is injected in the same direction as the magnetic field, in counter injection it is injected anti-parallel to the magnetic field. Figure 5.21 shows a view of TJ-II with the two NBI beam-lines. Plasma potential profiles and fluctuations have been measured in NBI co and counter injection scenarios using the TJ-II HIBP diagnostic.

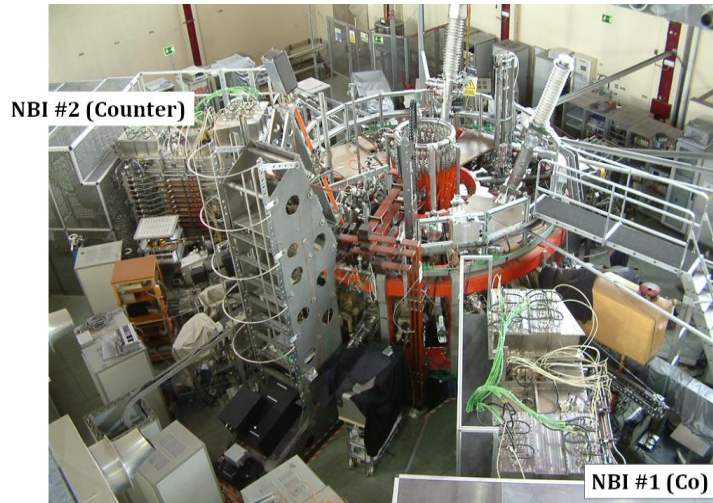
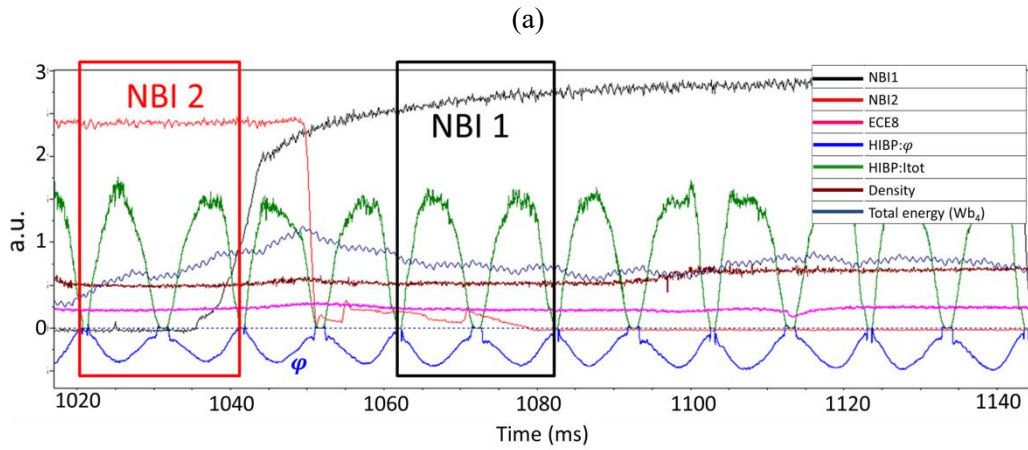


Figure 5.21 View of the two NBI beamlines in the TJ-II stellarator

Experiments were carried out in low density plasma ($0.5 \times 10^{19} \text{ m}^{-3}$) in plasma regimes heated by NBI1 and NBI2 with similar plasma densities and temperatures in a single discharge.

Figure 5.22.a shows a plasma discharge (#39260) where the plasma is sustained first with NBI 2 (420 kW, 29 kV) and later with NBI 1 (580 kW, 32 kV), while maintaining similar plasma densities ($n \approx 0.5 \times 10^{19} \text{ m}^{-3}$) and electron ($T_e \approx 300 \text{ eV}$) and ion temperatures ($T_i(0) \approx 100 \text{ eV}$). The scans highlighted in Figure 5.22 for time intervals (1030-1040 ms) and (1050-1060 ms) are sustained only by NBI2 (red) and NBI1 (black), respectively. Figure 5.22a also plots the evolution of secondary ion current (I_{tot}) and plasma potential (ϕ) measured by HIBP I (slit2), electron temperature measured by ECE (ECE8) and total energy (Wb_4).

HIBPI was operational in scanning mode from HFS to LFS with each scan of roughly 10 ms in these plasma discharges. Figure 5.22b over plots the plasma potential profiles for both co- and counter- NBI regimes versus rho values for the 4 scans highlighted in Figure 5.22a. Figure 5.22b indicates that the plasma potential value for NBI1 is more negative by about 50 V as compared to NBI2 at the center. Although the existing TJ-II data-base comparing NBI1 and NBI2 plasma scenarios with similar plasma parameters is rather limited, results reported in #39260 have been reproduced in other plasma discharges. Figure 5.23 shows the radial profile of secondary ion current and its fluctuations for NBI2 (left) and NBI1 (right) for two scans in Figure 5.22a the value of the fluctuation is comparable for co- and counter- NBI configurations.



(b) Potential in NBI1 and NBI2 for similar density and plasma parameters

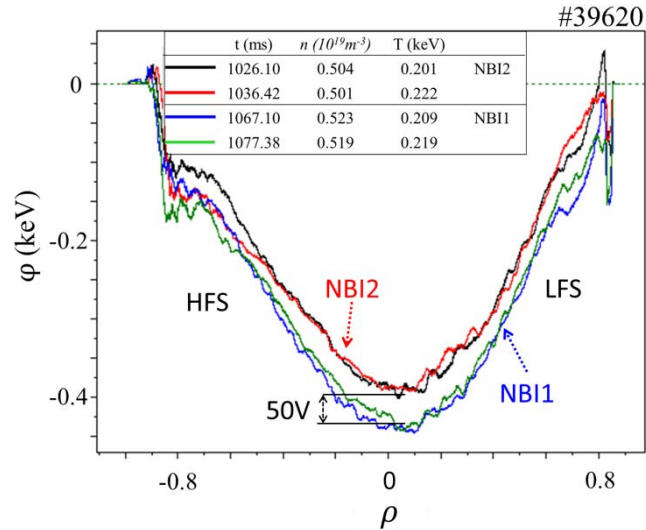


Figure 5.22 (a) Plasma parameters evolution for discharge #39620 sustained by NBI2 (red) and later by NBI 1 (black). The plot presents the electron temperature (ECE8), stored energy (Wb_4), density (n), plasma potential (ϕ) and secondary ion current (I_{tot}) measured by HIBPI (slit2); (b) plasma potential for the 4 scans highlighted in the (a) are over plotted with respect to ρ for $0.504 < n$ ($10^{19}m^{-3}$) < 0.523 , $0.2 < T(keV) < 0.22$.

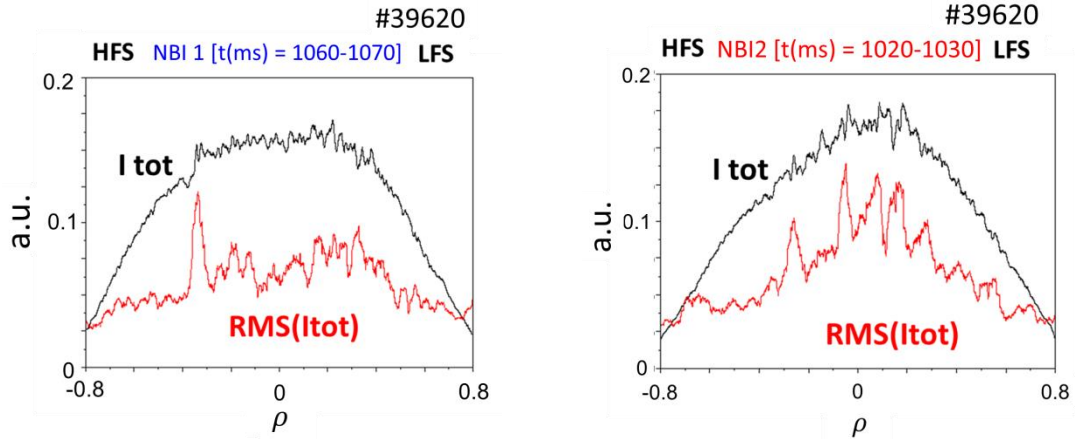


Figure 5.23 Comparison of the level of fluctuations in secondary ion current ($RMS(I_{tot})$, red) for NBI2 (left) and NBI1 (right) corresponding the time-interval corresponding to figure 5.22.

5c.3. Conclusion

Plasma potential profiles have been measured in co and counter NBI scenarios in the TJ-II stellarator. Comparison of potential for the discharges only sustained by NBI1 (co) and NBI2 (counter) shows, in plasmas with similar plasma density and electron and ion temperatures that NBI 2 reaches less negative DC Plasma potential profile as compared to NBI1. These results are in consistency with the predicted better confinement of fast ions in counter- NBI configurations [5.42].

Conclusions

Measurements of plasma potential and density, along with its fluctuations are essential to understand the dynamics of nuclear fusion plasmas. The main objective of this thesis was to enhance the capability of the heavy ion beam diagnostics (HIBD) at ISTTOK tokamak to measure plasma potential by developing an improved high resolution 90° cylindrical energy analyzer. In addition, the thesis uses the heavy ion beam probes (HIBP) setup, already installed in the TJ-II stellarator, to obtain 2D contour maps for the potential and density profiles in different plasma scenarios. These results will contribute to the validation of plasma potential asymmetry models and their fluctuations. The results obtained during the thesis are summarized following.

ISTTOK tokamak

90° CEA was conceptually developed, designed and commissioned on HIBD at ISTTOK. The single-channel prototype tested has demonstrated measurements plasma potential and its fluctuation, being consistent with simulation estimation. The highlights of the design concept, and experimental results obtained at ISTTOK are presented below.

90° cylindrical energy analyzer (CEA)

- 90° cylindrical analyzer has been operated in an innovative deceleration operation mode. In this mode, the central line trajectory is kept at a positive potential resulting in beam retardation. Simulations have estimated a 5 times increase in the coefficient of energy dispersion and 45 times decrease in angular aberration coefficient in deceleration mode in comparison with traditionally used normal mode. Numerical simulation estimates the energy resolution of $\Delta E/E = (3-5) \times 10^{-4}$ with a strong decrease of the angular aberration in the range of $\theta = \pm 2^\circ$ for five times deceleration ($k_E = 5$).
- The 3D layout of the CEA was upgraded by adding following design modifications. i) Additional pair of guard rings were included to compensate for the fringing field distorting the equipotential at the end of the analyzer due to the external SS cross chamber. ii) The deceleration grid is added to maintain the retarding field at the analyzer exit, thus allowing beam detection at ground potential. iii) SEE grid is added to suppress the secondary electron emission from reaching the detector and interfere with real signals.
- A prototype 1/2-size 90° CEA has been investigated both numerically and in experiments with electron beam in a test facility. The experimental results verify the expected higher sensitivity in deceleration mode over conventionally used normal mode.

Electrostatic input module (EIM)

- The internal elements comprising EIM were optimized (geometry and biasing voltages) to achieve a secondary beam dimension of 8 mm × 2.5 mm without any overlapping between the four beams from different slits and without any loss of current at the CEA entrance slit. A new design of Einzel lens is presented that provides additional control over the beam shape at the input of the analyzer (using side strip electrodes).

- A prototype setup of EIM consisting of additional elements necessary during real installation was built and installed on HIBD at ISTTOK to verify and validate the simulations. The alignment parameters obtained in this chapter were crucial to provide reference biasing values for the combined operation of the EIM and 90° CEA.

Potential measurements at ISTTOK

The 90° cylindrical energy analyzer operated in two-times deceleration mode has been successfully applied in ISTTOK HIBD to measure the plasma potential and its fluctuations with the following results.

- An indirect method of calibration estimated absolute plasma potential to be $\varphi \sim -340$ V with estimated calibration error $\Delta\varphi = \pm 70$ V as measured in the plasma core.
- Experimental relative calibration established the CEA resolution of $\Delta E/E \sim 2 \times 10^{-3}$ as obtained with external sinusoidal modulation of beam energy.

The author has designed a customizable workbench in SIMION software for Electrostatic input module and cylindrical energy analyzer for ISTTOK HIBD. It can be used for the charged particle trajectory calculations in the future experiments and upgrade.

TJ-II Stellarator

The thesis reports on the three experiments performed at TJ-II stellarator using the unique dual HIBP installation at TJ-II. The results are summarized below.

- The plasma response to edge biasing strongly depends on the heating scenario, being maximum in ECRH and NBI scenarios with positive and negative biasing, respectively. This phenomenology is consistent with the asymmetric I-V electrode characteristic. However, within experimental uncertainties and in the explored plasma scenarios, no evidence of core plasma potential flux surface asymmetries was found.

The HIBP was used in an energy scanning mode to successfully obtain 2D poloidal contour plots of plasma potential and density and their fluctuations in low density plasmas sustained by ECRH in the TJ-II stellarator for one-third of the core plasma poloidal area with the following conclusions:

- The 2D map for the absolute plasma potential has a local maximum in the plasma core as expected in low-density high-temperature scenarios. It shows about 1 cm mismatch with vacuum magnetic calculations that could be partially explained by instrumental effects. The 2D map for the absolute plasma potential shows poloidal symmetry within the experimental error ± 25 V. The 2D map for the plasma potential RMS shows poloidal symmetry within ± 5 V experimental uncertainty.
- Density fluctuations appear both at the positive and negative I_{tot} gradient regions for ECRH plasmas. Normalized density fluctuations are stronger in the negative I_{tot} density gradient than in the positive gradient region. Frequency spectra are dominated by frequencies below 100 kHz with different spectral characteristics in the positive and negative gradient regions that are affected by the ECRH scenario (on vs. off -axis heating).
- Comparison of plasma potential profile for the discharges sustained only by NBI 1 (co-injection) and NBI 2 (counter-injection) infers less negative DC Plasma potential for NBI 2 as compared to NBI 1. These results are in consistency with the predicted better confinement of fast ions in counter configurations.

Future work

- The future work at HIBD at ISTTOK shall include upgrading the single-channel plasma potential setup (present setup) into multi-channel mode. The half-size CEA ($R_0 = 105$ mm, $H_0 = 60$ mm) shall be replaced with full-size CEA ($R_0 = 215$ mm, $H_0 = 120$ mm) operated in 5 times deceleration (as optimized in the thesis). The upgraded setup would allow measurement of the radial profile of n_e , φ , B_p along with their fluctuations, simultaneously, in a single plasma discharge.
- The new design of the Einzel lens as presented in this thesis shall be tested independently in a test facility to verify the adjustable beam focusing properties of the side strip electrodes.
- Performing new experiments using HIBP at TJI-II in order to expand the 2D mapping towards the whole TJ-II poloidal cross-section.

Conclusiones

La caracterización del potencial y la densidad del plasma, junto con sus fluctuaciones, es esencial para entender la dinámica de plasmas de fusión nuclear. Esta tesis tiene como objetivo principal la mejora de diagnósticos basados en haces de iones pesados (HIBP), mediante el desarrollo de un analizador de energía cilíndrico mejorado de alta resolución en el Tokamak ISTTOK. Complementariamente, la tesis utiliza la configuración dual de sondas de haces de iones pesados ya instalada en el stellator TJ-II para obtener un diagrama de contornos 2D para los perfiles de potencial y densidad en diferentes escenarios de plasma. Estos resultados contribuirán a la validación de modelos de asimetrías de potencial del plasma y sus fluctuaciones. Los resultados obtenidos durante el curso de la tesis se presentan a continuación.

ISTTOK tokamak

Se ha desarrollado el diseño conceptual, la construcción y puesta en operación de un sistema de haces de iones pesados utilizando un sistema analizador cilíndrico [90° CEA] en el Tokamak ISTTOK. El prototipo consta de un único canal para demostrar la medida del potencial de plasma y sus fluctuaciones. A continuación se presentan los aspectos más destacados del trabajo en ISTTOK que comprende el concepto de diseño y los resultados experimentales obtenidos.

Analizador de energía cilíndrica 90° (CEA)

- Esta tesis se centra en el desarrollo innovador de un analizador de energía 90° CEA de alta energía y modo de desaceleración de baja aberración angular. Las simulaciones realizadas con el programa SIMION estiman un aumento de 5 veces en el coeficiente de dispersión de energía y una disminución de 45 veces en el coeficiente de aberración angular en comparación con el modo normal utilizado tradicionalmente. La simulación numérica estima una resolución de energía de $\Delta E / E = (3-5) \times 10^{-4}$ con una disminución de la aberración angular en el rango de $\theta = \pm 2^\circ$ para el modo de desaceleración ($k_E = 5$).
- El diseño 3D del analizador se realizó agregando los siguientes conceptos de diseño. i) Se incluyó un par adicional de anillos de protección para mejorar la uniformidad de las superficies equipotenciales en el extremo del analizador. ii) Se agregó una rejilla de desaceleración para mantener el campo de retardo en el analizador y permitir la detección del haz a potencial de tierra. iii) Se agregó una rejilla [SEE] para evitar que la emisión secundaria de electrones llegue al detector e interfiera con las señales reales.
- Se ha investigado un prototipo a escala $\frac{1}{2}$ del analizador 90° CEA tanto numéricamente como en experimentos con un haz de electrones en una instalación de prueba. Los resultados experimentales han verificado una mayor sensibilidad, esperada en el modo de desaceleración, sobre el modo normal usado convencionalmente.

Módulo de entrada electrostática (EIM)

- Se optimizaron los elementos internos del módulo de entrada electrostática (EIM), tanto en geometría como en voltajes de polarización, para lograr una dimensión del haz secundario de $8 \text{ mm} \times 2.5 \text{ mm}$ sin solapamiento entre los cuatro haces de las diferentes ranuras y sin ninguna pérdida de corriente en la ranura de entrada del CEA. Se desarrolló un nuevo diseño de lente Einzel que proporciona un control adicional sobre la

forma del haz en la entrada del analizador mediante el uso de electrodos de banda lateral.

- Se construyó e instaló un prototipo de configuración EIM que consta de todos los elementos adicionales necesarios en el sistema de iones pesados (HIBD) en el tokamak ISTTOK que permitió verificar y validar las simulaciones. Los parámetros de alineación obtenidos en este capítulo fueron cruciales para proporcionar valores de polarización de referencia para la operación combinada del EIM y 90° CEA.

Medidas del potencial de plasma en el tokamak ISTTOK

Se ha operado exitosamente el analizador de energía cilíndrica (90° CEA) en modo de doble desaceleración en la sonda de iones pesados del tokamak ISTTOK-HIBD para medir el potencial de plasma y sus fluctuaciones con los siguientes resultados:

- Un método indirecto de calibración estima el potencial absoluto de plasma en $\phi \sim -340$ V con un error de calibración estimado $\Delta\phi = \pm 70$ V medido en el núcleo de plasma.
- La calibración relativa experimental estableció la resolución del sistema CEA de $\Delta E / E \sim 2 \times 10^{-3}$ obtenida con la modulación sinusoidal externa de la energía del haz.

El autor ha diseñado un banco de trabajo personalizable de simulación en SIMION para el módulo de entrada electrostática y el analizador de energía cilíndrico para ISTTOK HIBD. Se puede utilizar para los cálculos de trayectorias de partículas cargadas en los futuros experimentos y actualizaciones.

Stellarator TJ-II

La tesis incluye los estudios los tres experimentos realizados en el stellarator TJ-II utilizando la instalación dual de sondas de iones pesados (HIBP). Los resultados obtenidos se resumen a continuación.

- La respuesta del plasma a la polarización en la región periférica depende del escenario de calentamiento, siendo máxima en escenarios de ECRH y NBI con polarización positiva y negativa, respectivamente. Esta fenomenología es consistente con la característica asimétrica de la característica tensión-corriente del electrodo. Dentro de las incertidumbres experimentales y en los escenarios explorados de plasma, no se encontraron evidencias de asimetrías en el potencial del plasma asociado a las superficies del flujo magnético.

El HIBP se operó en un amplio rango de energías para obtener con éxito la distribución de contornos 2D (para un tercio del área poloidal del plasma) de los valores de potencial y densidad del plasma y sus fluctuaciones en plasmas de baja densidad sostenidos por ECRH en el stellarator TJ-II, con las siguiente conclusiones:

- El mapa 2D para el potencial absoluto de plasma tiene un máximo local en el núcleo de plasma en acuerdo con predicciones en escenarios de baja densidad y alta temperatura. Las medidas experimentales muestran aproximadamente 1 cm de desajuste con los cálculos magnéticos de vacío que podrían explicarse parcialmente por efectos instrumentales. El mapa 2D para el potencial del plasma muestra simetría poloidal dentro del error experimental ± 25 V. El mapa 2D para los niveles de fluctuaciones del plasmas (RMS) muestra simetría poloidal dentro de la incertidumbre experimental ± 5 V.

- Las fluctuaciones de densidad aparecen tanto en las regiones de gradiente de densidad de iones secundarios (I_{tot}) positivo como negativo. Las fluctuaciones de densidad normalizadas son más fuertes en el gradiente de densidad negativo que en la región de gradiente positivo. Los espectros de frecuencia están dominados por frecuencias por debajo de 100 kHz con diferentes características espectrales en las regiones de gradiente positivo y negativo que se ven afectadas por el escenario ECRH (calentamiento en eje y fuera de eje).
- La comparación de los perfiles de potencial del plasma para las descargas sostenidas solo por NBI 1 (*co-injection*) y NBI 2 (*counter-injection*) muestra que los perfiles de potencial son menos negativos para el sistema NBI 2 en comparación con NBI 1. Estos resultados son consistentes con un mejor confinamiento de iones rápidos en la configuración NBI 2.

Trabajo futuro

- El trabajo futuro en sistema HIBD en ISTTOK incluirá la actualización de la configuración del potencial de plasma de un solo canal (configuración actual) al modo de operación multicanal. El prototipo CEA de escala $\frac{1}{2}$ ($R_0 = 105$ mm, $H_0 = 60$ mm) debe reemplazarse por un CEA de tamaño completo ($R_0 = 215$ mm, $H_0 = 120$ mm) operado en el modo 5 veces de desaceleración, siguiendo los criterios de optimización desarrollados en la tesis. Esta mejora permitirá la medición del perfil radial y la fluctuación de n_e , ϕ , B_p simultáneamente en una sola descarga de plasma.
- El nuevo diseño de la lente Einzel presentado en esta tesis se probará de forma independiente en una instalación de prueba para verificar las propiedades de enfoque del haz mediante los electrodos de la banda lateral.
- Realización de nuevos experimentos utilizando HIBP en TJI-II para expandir las medidas 2D de potencial y densidad a toda la sección poloidal del stellarator TJ-II.

Bibliography

- 1.1 John Wesson; Tokamaks. Clarendon Press - Oxford, Great Clarendon Street, Oxford OX2 6DP, UK, third edition (2004)
- 1.2 J D Lawson; Some Criteria for a Power Producing Thermonuclear Reactor. Proceedings of the Physical Society Section B, 70(1) 6 (1957)
- 1.3 R. L. Hickok; Plasma Density Measurement by Molecular Ion Breakup. Review of Scientific Instruments, 38(1) 142 (1967)
- 1.4 F. C. Jobes and R. L. Hickok; A direct measurement of plasma space potential. Nuclear Fusion, 10(2):195 (1970)
- 1.5 C. Varandas, et. al. Engineering aspects of the tokamak ISTTOK, Fusion Technology Fusion Technology, 29:1, 105-115, DOI: 10.13182/FST96-A30660 (1996)
- 1.6 J.A.C. Cabral, H. Fernandes, H. Figueiredo, and C.A.F. Varandas; Operation of the tokamak ISTOKK in a multicycle alternating at-top plasma current regime. Nuclear Fusion, 37(11):1575 (1997)
- 1.7 Artur Jorge Louzeiro Malaquias; Analisador da defelexao de um feixe ionico para o tokamak ISTTOK. Master's thesis, Technical University of Lisbon, Instituto Superior Tecnico, Av. Rovisco Pais 1, 1049-001 Lisboa, Portugal (1993)
- 1.8 J. A. C. Cabral, A. Malaquias, A. Praxedes, W. Van Toledo, and C. A. F. Varandas; The heavy ion beam diagnostic for the tokamak ISTTOK. IEEE Transactions on Plasma Science, 22(4):350-358 (1994)
- 1.9 A. Malaquias, I. S. Nedzelskiy, C. A. F. Varandas, and J. A. C. Cabral; Evolution of the tokamak ISTTOK plasma density and electron temperature radial profiles determined by heavy ion beam probing. Review of Scientific Instruments, 70(1):947-950 (1999)
- 1.10 Rafael Bagagem Henriques; ISTTOK plasma characterization and control by the Heavy Ion Beam Diagnostic, Ph.D. thesis, Instituto Superior Tecnico, Av. Rovisco Pais 1, 1049-001 Lisboa, Portugal (2019)
- 1.11 J. A. C. Cabral, I. S. Nedzelskiy, A. J. Malaquias, B. Goncalves, C. A. F. Varandas, I. S. Bondarenko, S. M. Khrebtov, A. D. Komarov, A. L. Kozachok, and L. I. Krupnik; Improved 20 keV injection systems for the heavy-ion-beam diagnostic of the tokamak ISTTOK. Review of Scientific Instruments, 74(3):1853 (2003)
- 1.12 Artur Jorge Louzeiro Malaquias. O diagnostico de feixe de ions pesados do tokamak ISTTOK. PhD thesis, Technical University of Lisbon, Instituto Superior Tecnico, Av. Rovisco Pais 1, 1049-001 Lisboa, Portugal (1999)
- 1.13 A. Malaquias, J.A.C. Cabral, C.A.F. Varandas, and A.R. Canario; Evolution of the poloidal magnetic field profile of the ISTTOK plasma followed by heavy ion beam probing. Fusion Engineering and Design, 34-35:671-674 (1997)
- 1.14 I.S. Nedzelskiy, A. Malaquias, B. Goncalves, C. Silva, C.A.F. Varandas, J.A.C.Cabral; Time-of-flight energy analyzer for the plasma potential measurements

- by a heavy ion beam diagnostic, *Rev. Sci. Instrum.* 75 3514–3516 (2004)
- 1.15 I.S. Nedzelskiy, A. Malaquias, Yu. Tashchev, C. Silva, H. Figueiredo, H. Fernandes, C.A.F. Varandas; Multichannel time-of-flight technique for plasma potential profile measurements by heavy ion beam diagnostic on the tokamak ISTTOK, *Rev. Sci. Instrum.* 77 (3) 033505-033505-9 (2006)
 - 1.16 R. B. Henriques, I. S. Nedzelskiy, A. Malaquias, and H. Fernandes; New detection system and signal processing for the tokamak ISTTOK heavy ion beam diagnostic, *Review of Scientific Instruments* 83, 10D705 (2012)
 - 1.17 I.S. Nedzelskiy, A. Malaquias, J.A.C. Cabral, and C.A.F. Varandas; Influence of a non-uniform magnetic field on the measurement of the ne eff profile by heavy ion beam probing with a multiple cell array detector. In 28th EPS, pages 1253-1256 (2001)
 - 1.18 [Comercial amplifiers] <https://www.femto.de/images/pdf-dokumente/de-lca-400k-10m.pdf>.
 - 1.19 R. B. Henriques, A. Malaquias, I. S. Nedzelskiy, C. Silva, R. Coelho, H. Figueiredo, and H. Fernandes; Radial profile measurements of plasma pressure-like fluctuations with the heavy ion beam diagnostic on the tokamak ISTTOK *Review of Scientific Instruments* 85, 11D848 (2014); <https://doi.org/10.1063/1.4891045>
 - 1.20 G.D. Conway; Turbulence measurements in fusion plasmas. *Plasma Phys. Cont. Fusion* 50 124026 (2008)
 - 1.21 B.N. Breizman and S.E. Sharapov; Major minority: energetic particles in fusion plasma. *Plasma Phys. Cont. Fusion* 53 054001 (2011)
 - 1.22 Alexander V. Melnikov et.al; Plasma Potential in Toroidal Devices: T-10, TJ-II, CHS and LHD. *Plasma and Fusion Research* 7, 2402114 (2012)
 - 1.23 S da Graça, G D Conway, P Lauber, D Curran, V Igochine, I Classen, M Garcia-Muñoz, J Stober, M A Van Zeeland, M E Manso et al; Characterization of Alfvén eigenmodes using NBI during current ramp-up in the ASDEX Upgrade tokamak. *Plasma Phys. Control. Fusion* 54 095014 (2012)
 - 1.24 A.V. Melnikov, L.G. Eliseev, E. Ascasibar, A.A. Chmyga, C. Hidalgo, T. Ido, R. Jiménez-Gómez, A.D. Komarov, A.S. Kozachek, L.I. Krupnik et.al; Alfvén eigenmode properties and dynamics in the TJ-II stellarator. *Nuclear Fusion* 52, 123004 (2012)
 - 1.25 A. V. Melnikov, V. Vershkov, L. Eliseev, S. Grashin et al; Investigation of geodesic acoustic mode oscillations in the T-10 tokamak. *Plasma Phys. Control. Fusion* 48 No 4 S87-S110 (2006)
 - 1.26 G R McKee, R J Fonck, M Jakubowski, K H Burrell, K Hallatschek, R A Moyer, W Nevins, D L Rudakov and X Xu; Observation and characterization of radially sheared zonal flows in DIII-D, *Plasma Phys. Control. Fusion* 45, A477–A485 (2003).
 - 1.27 Davide Galassi, G. Ciraolo, Patrick Tamain, Eric Serre et.al; Tokamak Edge Plasma Turbulence Interaction with Magnetic X-Point in 3D Global Simulations, *Fluids* 4, 50 (2019); <https://doi.org/10.3390/fluids4010050>

- 1.28 G. Van Oost, V. V. Bulanin, A. J. H. Donné, E. Z. Gusakov, A. Kraemer-Flecken, L. I Krupnik, A Melnikov, S Nanobashvili, P Peleman, K A Razumova et.al; Multi-machine studies of the role of turbulence and electric fields in the establishment of improved confinement in tokamak plasmas. *Plasma Phys. Control. Fusion* 49, A29 (2007)
- 1.29 L. Krupnik, A. Alonso, E. Ascasibar et al; Radial electric fields and confinement in the TJ-II stellarator. *Czech J Phys* 55, 317–339 (2005).
<https://doi.org/10.1007/s10582-005-0044-8>
- 1.30 D. Mazon, C. Fenzi and R. Sabot; As hot as it gets. *Nature Phys.* 12, 14–17 (2016).
- 1.31 A.V. Melnikov et.al; Applied and fundamental aspects of fusion science. *Nature Phys* 12, 386–390 (2016). <https://doi.org/10.1038/nphys3759>
- 1.32 K.J. Zhao et al., Toroidal Symmetry of the Geodesic Acoustic Mode Zonal Flow in a Tokamak Plasma, *Phys. Rev. Lett.* 96 255004 (2006)
- 1.33 A.V. Melnikov, L.G. Eliseev, S.V. Perfilov, S.E. Lysenko, R.V. Shurygin, V.N. Zenin, S.A. Grashin, L.I. Krupnik, A.S. Kozachek, R.Yu. Solomatin et.al; The features of the global GAM in OH and ECRH plasmas in the T-10 tokamak. *Nuclear Fusion* Vol. 55, Number 6 (2015)
- 1.34 A.V.Melnikov et al. Proc. 30th EPS Conf. Contr. Fusion and Plasma Phys. ECA Vol. 27A, 3.114 (2003)
- 1.35 T. Ido, M. Osakabe, A. Shimizu, T. Watari, M. Nishiura, K. Toi, K. Ogawa, K. Itoh, I. Yamada, R. Yasuhara et. al; Identification of the energetic-particle driven GAM in the LHD. *Nuclear Fusion* 55 083024 (2015)
- 1.36 M Dimitrova, Tsv K Popov, J Adamek, J Kovačič, P Ivanova, E Hasan, D López-Bruna, J Seidl, P Vondráček, R Dejarnac et al; Plasma potential and electron temperature evaluated by ball-pen and Langmuir probes in the COMPASS tokamak. *Plasma Phys. Control. Fusion* 59 125001 (2017)
- 1.37 I. H. Hutchinson; Principles of plasma diagnostics. Press Syndicate of the University of Cambridge, The Pitt Building, Trumpington Street, Cambridge CB2 1RP, UK, (1992).
- 1.38 A. V. Melnikov et al; Plasma Potential Measurements by the Heavy Ion Beam Probe Diagnostic in Fusion Plasmas: Biasing Experiments in the TJ-II Stellarator and T-10 Tokamak; *Fusion Science and Technology* 46 2, 299-311, DOI: 10.13182/FST04-A568 (2004)
- 1.39 T. Ido, A. Shimizu, M.Nishiura, H. Nakano, S Ohshima, S. Kato, Y. Hamada, Y. Yoshimura, S. Kubo, T. Shimozuma, H. Igami, H. Takahashi, K. Toi, F. Watanabe et.al; Measurement of electrostatic potential fluctuation using heavy ion beam probe in large helical device, *Rev. Sci. Inst.* 79(10):10F318. (2008) DOI: 10.1063/1.2971207
- 1.40 A. Malaquias, C. Varandas, J.A.C. Cabral, L.I. Krupnik, S.M. Khrebtov, I.S. Nedzelskij, Yu. V. Trofimenko, A. Melnikov, C. Hidalgo, I. Garcia-Cortes *Fusion Technology; Engineering Aspects of an Advanced Heavy Ion Beam Diagnostic for the TJ-II Stellarator*, V.1 pp. 869 (1996)

- 2.1 L. Solensten, and K. A. Connor; Heavy ion beam probe energy analyzer for measurements of plasma potential fluctuations. *Review of Scientific Instruments* **58**, 516 (1987); <https://doi.org/10.1063/1.1139262>
- 2.2 T. S. Green, and G. A. Proca; A Parallel Plate Electrostatic Spectrograph. *Review of Scientific Instruments* **41**, 1409 (1970); DOI: 10.1063/1.1684294
- 2.3 A. L. Hughes and V. Rojansky; Second-Order Elastic Deformation of Solids. *Phys. Rev.* **34**, 284-290 (1929).
- 2.4 A.L. Hughes and J. H. Mcmillen; Inelastic and Elastic Electron Scattering in Argon. *Phys. Rev.* **34**, 291-295 (1929).
- 2.5 Deyang Yua; Design of a multichannel 127° cylindrical spectrometer for sputtered ions. <https://arxiv.org/ftp/arxiv/papers/0811/0811.1815.pdf>
- 2.6 I. S. Nedzelskiy et.al; Problems of Atomic Science and Technology № 5. Series: Plasma Physics (8). P. 148-150 (2002)
- 2.7 SIMION® <https://simion.com/>
- 2.8 K. A. Connor, T. P. Crowley, R. L. Hickok, A. Carnevali, P. M. Schoch, J. Resnick, V. Simcic, J. G. Schatz, J. Heard, S. C. Aceto, and J. F. Lewis; Advances in heavy-ion beam probing, *Rev. Sci. Instrum.* **59** 1673–1675. (1988)
- 2.9 A. Fujisava, Y. Hamada, Theoretical study of cylindrical energy analyzers for MeV range heavy-ion beam Probes, *Rev. Sci. Instrum.* **64** 3503–3514 (1993)
- 2.10 A. Fujisava, H. Iguchi, M. Sasao, Y. Hamada; Second-order focusing property of 210° cylindrical energy analyzer, *Rev. Sci. Instrum.* **66** (3) 2524–2527 (1995)
- 2.11 H. Kreckel, H. Bruhns, K. A. Miller, E. Wählin, A. Davis, S. Höckh, and D. W. Savin; A simple double-focusing electrostatic ion beam deflector, *Rev. Sci. Instrum.* **81** 063304-063304-5 (2010)
- 2.12 I.S. Nedzelskiy, A. Malaquias, R. Sharma, R. Henriques; 90° cylindrical analyzer for the plasma potential fluctuations measurements by heavy ion beam diagnostic on the tokamak ISTTOK, *Fusion Engineering and Design*, **123** (2016)
- 2.13 R. Sharma, I. S. Nedzelskiy, A. Malaquias, R. Henriques; Characterization of modified 90° cylindrical energy analyzer with electron beam. *Journal of Instrumentation* Vol. 15 DOI- 10.1088/1748-0221/15/01/C01018 (2020)
- 3.1 R. Sharma, I.S. Nedzelskiy, A. Malaquias and R.B. Henriques; Design and optimization of the electrostatic input module for the ISTTOK Tokamak HIBD cylindrical energy analyzer. *JINST* **12** C11018 (2017)
- 3.2 Liebl, Helmut; *Applied Charged Particle Optics*. Berlin Heidelberg: Springer-Verlag. p. 39. ISBN 978-3-540-71924-3 (2008)
- 4.1 J. J. Zielinski, S. Aceto, J. G. Schwelberger, K. Connor, In situ analyzer calibration methods for heavy ion beam probes installed on stellarator-like devices, *Review of Scientific Instruments* **63** (10) 4574 (1992).
- 4.2 V. J. Simcic, T. P. Crowley, P. M. Schoch, A. Y. Aydemir, X. Z. Yang, K. A.

- Connor, R. L. Hickok, A. J. Wootton, and S. C. McCool; Internal magnetic and electrostatic fluctuation measurements of magneto hydrodynamic modes in the Texas Experimental Tokamak. *Physics of Fluids B: Plasma Physics* **5**, 1576 (1993); <https://doi.org/10.1063/1.860897>
- 4.3 H. Iguchi, *J. Plasma Fusion Res.*, **4**, 82 (2001)
- 4.4 R. Sharma, I.S. Nedzelskiy, A. Malaquias and R. Henriques ; Characterization of modified 90° cylindrical energy analyzer with electron beam. *JINST* **15** C01018 (2020)
- 5.1 C. Hidalgo, C. Alejaldre, A. Alonso, J. Alonso, L. Almoguera, F. de Aragón, E. Ascasibar, A. Baciero et al; Overview of TJ-II experiments *Nucl. Fusion* **45** S266 (2005)
- 5.2 I. S. Bondarenko, A. A. Chmuga, N. B. Dreval, S. M. Khrebtov, A. D. Komarov, A. S. Kozachok, and L. I. Krupnik ; Installation of an advanced heavy ion beam diagnostic on the TJ-II stellarator. *Rev. Sci. Instrum.* **72** 583 (2001)
- 5.3 A.V. Melnikov 2019 *Electric Potential in Toroidal Plasmas*, Springer Nature Switzerland AG 2019, 240 pp, ISBN 978-3-030-03480-1 (2019)
- 5.4 A.V. Melnikov, L.I. Krupnik, L.G. Eliseev, J.M. Barcala, A. Bravo, A.A. Chmyga, G.N. Deshko, M.A. Drabinskij, C. Hidalgo et.al; Heavy ion beam probing - Diagnostics to study potential and turbulence in toroidal plasmas. *Nucl. Fusion* **57** (2017) 072004 (13pp) (2017)
- 5.5 A. V. Melnikov, C. Hidalgo, A. A. Chmyga, N. B. Dreval, L. G. Eliseev, S. M. Khrebtov, A. D. Komarov, A. S. Kozachok, L. I. Krupnik et.al; Plasma Potential Measurements by the Heavy Ion Beam Probe Diagnostic in Fusion Plasmas: Biasing Experiments in the TJ-II Stellarator and T-10 Tokamak, *Fusion Science and Technology*, **46:2**, 299-311 (2017)
- 5.6 A.V. Melnikov, L.G. Eliseev, R. Jiménez-Gómez, E. Ascasibar, C. Hidalgo, A.A. Chmyga, A.D. Komarov, A.S. Kozachok, I.A. Krasilnikov, S.M. Khrebtov et al; Control and data acquisition for dual HIBP diagnostics in the TJ-II stellarator *Fusion Eng. Design* **96-97** 724 (2015)
- 5.7 O.O. Chmyga, E. Ascasibar, J. Barcala, M.A. Drabinskij, L.G. Eliseev, C. Hidalgo et.al; A dual heavy ion beam probe diagnostic on the TJ-II stellarator, problems of atomic science and technology. 2019, № 1. Series: Plasma Physics (25), p. 248-251 https://vant.kipt.kharkov.ua/ARTICLE/VANT_2019_1/article_2019_1_248.pdf
- 5.8 R. Burhenn, Y. Feng, K. Ida, H. Maassberg, K.J. McCarthy, D. Kalinina, M. Kobayashi, S. Morita, R. Burhenn et. al; On impurity handling in high performance stellarator/heliotron plasmas. *Nuclear Fusion* **49** 065005 (2009)
- 5.9 K. McCormick, P. Grigull, R. Burhenn, R. Brakel, H. Ehmler, Y. Feng, F. Gadelmeier, L. Giannone, D. Hildebrandt, M. Hirsch, R. Jaenicke et.al; New Advanced Operational Regime on the W7-AS Stellarator. *Phys. Rev. Lett.* **89** 015001 (2002)
- 5.10 M. Yoshinuma, K. Ida, M. Yokoyama, M. Osakabe, K. Nagaoka, S. Morita, M.

- Goto, N. Tamura, C. Suzuki, S. Yoshimura et al; Observation of an impurity hole in the Large Helical Device. *Nuclear Fusion* 49 062002 (2009)
- 5.11 J. M. García-Regaña, C.D. Beidler, R. Kleiber, P. Helander, A. Mollén, J.A. Alonso, M. Landreman, H. Maaßberg, H.M. Smith, Y. Turkin et al; Electrostatic potential variation on the flux surface and its impact on impurity transport. *Nucl. Fusion* 57 056004 (2017)
- 5.12 I. Calvo, Felix I. Parra, José Luis Velasco, J. Arturo Alonso and J.M. García-Regaña; Stellarator impurity flux driven by electric fields tangent to magnetic surfaces. *Nucl. Fusion* 58 124005 (2018)
- 5.13 M A Pedrosa, J.A. Alonso, J.M. García-Regaña, C. Hidalgo, J.L. Velasco, I. Calvo, R. Kleiber, C. Silva and P. Helander; Electrostatic potential variations along flux surfaces in stellarators. *Nucl. Fusion* 55 052001 (2015)
- 5.14 T. Estrada, E. Sánchez, J.M. García-Regaña, J.A. Alonso, E. Ascasíbar, I. Calvo, A. Cappa, D. Carralero, C. Hidalgo, M. Liniers; Turbulence and perpendicular plasma flow asymmetries measured at TJ-II plasmas. *Nucl. Fusion* 59 076021 (2019)
- 5.15 C. Hidalgo; Edge turbulence and anomalous transport in fusion plasmas. *Plasma Phys. Control. Fusion* 37 A53 (1995)
- 5.16 C. Hidalgo, Joseph Talmadge, Mirko Ramisch and the TJ-II, HXS and TJ-K Teams; Advancing the understanding of plasma transport in mid-size stellarators. *Plasma Phys. Control. Fusion* 59 014051 (2017)
- 5.17 J. L. Velasco, I Calvo, J M García-Regaña, F I Parra, S Satake, J A Alonso and the LHD team; Impact of main ion pressure anisotropy on stellarator impurity transport. *Plasma Phys. Control. Fusion* 60 074004 (2018)
- 5.18 P. Xanthopoulos, G. G. Plunk, A. Zocco, and P. Helander; Intrinsic Turbulence Stabilization in a Stellarator. *Physical Review X* 6 021033 (2016)
- 5.19 E. Sánchez, T. Estrada, J. L. Velasco, I. Calvo, A. Cappa, A. Alonso and J. M. Garcia- Regana; Validation of Global Gyrokinetic Simulations in Stellarator Configurations. 27th IAEA Fusion Energy Conference (FEC 2018) EX/P1-11 (2019)
- 5.20 Z.Yan, G. R. McKee, R. Fonck, P. Gohil, R. J. Groebner, and T. H. Osborne; Observation of the L to H Confinement Bifurcation Triggered by a Turbulence-Driven Shear Flow in a Tokamak Plasma. *Phys. Rev. Lett.* 112 125002 (2014)
- 5.21 S. J. Zweben, J. A. Boedo, O. Grulke, C. Hidalgo, B. LaBombard, R. J. Maqueda, P. Scarin and J. L. Terry; Edge turbulence measurements in toroidal fusion devices. *Plasma Phys. Control. Fusion* 49 S1 (2007)
- 5.22 A. Shimizu, T. Ido, M. Nishiura, S. Kato, K. Ogawa, H. Takahashi, H. Igami, Y. Yoshimura, S. Kubo and T. Shimozuma; 2D spatial profile measurements of potential fluctuation with heavy ion beam probe on the Large Helical Device. *Review of Scientific Instruments* 87 11E731 (2016)
- 5.23 M. Valovic, K. Axon, L. Garzotti, S. Saarelma, A. Thyagaraja, R. Akers, C. Gurl, A. Kirk, B. Lloyd, G.P. Maddison et al; Particle confinement of pellet-fuelled tokamak plasma. *Nucl. Fusion* 48 075006 (2008)

- 5.24 P. Vincenzi, F. Koechl, L. Garzotti, D. B. King, E. Tindale, T. Bolzonella, P. T. Lang, B. Pegourié, M. Romanelli and R. Wenninger; Fuelling and density control for DEMO. *Nuclear Fusion* 55 113028 (2015)
- 5.25 [16] K. McCarthy, N Panadero, S K Combs, N Tamura, E Ascasíbar, M Calvo, A Chmyga, T Estrada, J M Fontdecaba, R García et al; The impact of fast electrons on pellet injection in the stellarator TJ-II. *Plasma Phys. Control. Fusion* 61 014013 (2019)
- 5.26 A. Dinklage, R. Sakamoto, M. Yokoyama, K. Ida, J. Baldzuhn, C.D. Beidler, S. Cats, K.J. Mc Carthy, J. Geiger, M. Kobayashi et al; The effect of transient density profile shaping on transport in large stellarators and heliotrons. *Nucl. Fusion* 57 066016 (2017)
- 5.27 L. Garzotti, J. Figueiredo, C. M. Roach, M. Valovič, D. Dickinson, G. Naylor, M. Romanelli, R. Scannell, G. Szepesi et al; Microstability analysis of pellet fuelled discharges in MAST. *Plasma Phys. Control. Fusion* 56 035004 (2014)
- 5.28 C. Angioni, M. McDermott, E. Fable, R. Fischer, T. Pütterich, F. Ryter, G. Tardini and the ASDEX Upgrade Team; Overview of physics studies on ASDEX Upgrade. *Nucl. Fusion* 57 116053 (2017)
- 5.29 D. Tegnered, M Oberparleiter, H Nordman and P Strand; Fluid and gyrokinetic modelling of particle transport in plasmas with hollow density profiles. *Journal of Physics: Conference Series* 775 012014 (2016)
- 5.30 F. Castejón, D. Alegre, A. Alonso, J. Alonso, E. Ascasíbar, A. Baciero, A. de Bustos, D. Baiao, J.M. Barcala, E. Blanco et al; 3D effects on transport and plasma control in the TJ-II stellarator. *Nucl. Fusion* 57 102022 (2017)
- 5.31 A. V. Melnikov, L I Krupnik, E Ascasibar, A Cappa, A A Chmyga, G N Deshko, M A Drabinskij, L G Eliseev, C Hidalgo, P O Khabanov et al. ECRH effect on the electric potential and turbulence in the TJ-II stellarator and T-10 tokamak plasmas. *Plasma Phys. Control. Fusion* 60 084008 (2018)
- 5.32 A.V. Melnikov, K.S. Dyabilin, L.G. Eliseev, S.E. Lysenko and Yu.N. Dnestrovskij *Problems At. Sci. Technol. Ser. Thermonucl. Fusion.* 54 (2011) (in Russian) (http://vant.iterru.ru/vant_2011_3/4.pdf)
- 5.33 J.L. Velasco, J. A. Alonso, I. Calvo, and J. Arevalo; Vanishing Neoclassical Viscosity and Physics of the Shear Layer in Stellarators. *Phys. Rev. Lett.* 109, 135003 [SEP] (2012)
- 5.34 C. Gutierrez-Tapia, J. J. Martinell, D. López-Bruna, A. V. Melnikov, L. Eliseev, C. Rodríguez, M. A. Ochando, F. Castejón, J. García, B. P. van Milligen et al; Analysis of TJ-II experimental data with neoclassical formulations of the radial electric field. *Plasma Phys. Control. Fusion* 57 115004 (2015)
- 5.35 A. V. Melnikov, C. Hidalgo, L.G. Eliseev, E. Ascasibar, A.A. Chmyga, K.S. Dyabilin, I.A. Krasilnikov, V.A. Krupin, L.I. Krupnik, S.M. Khrebtov et al; Plasma potential and turbulence dynamics in toroidal devices (survey of T-10 and TJ-II experiments). *Nucl. Fusion* 51 083043 (2011)

- 5.36 A. V. Melnikov, Carlos Hidalgo, Takeshi ID, Akihiro Shimzu, Akihide Fujisawa, Konstantin S. Dyabilin and Sergey E. Lysenko; Plasma Potential in Toroidal Devices: T-10, TJ-II, CHS and LHD. *Plasma Fusion Res.* 7 2402114 (2012)
- 5.37 A. Ouroua, T.P. Crowley, K.A.Connor, D.R. Demers, A. Fujisawa, R.L. Hickok, P.E. McLaren, P.M. Schoch; Measurements of broadband fluctuations and plasma potential with the 2 MeV heavy ion beam probe on the TEXT-U Tokamak. *Fusion Engineering Fusion Engineering and Design* 34-35 613 (1997)
- 5.38 A.V. Melnikov, L. G. Eliseev, M. A. Ochando, K.Nagaoka, E. Ascasibar, A. Cappa, F. Castejon, T. Estrada, C. Hidalgo, S. E. Lysenko et al; A Quasi-Coherent Electrostatic Mode in ECRH Plasmas on TJ-II. *Plasma Fusion Res.* 6 2402030 (2011)
- 5.39 Ph.O. Khabanov, L.G. Eliseev, A.V. Melnikov, M.A. Drabinskiy, C. Hidalgo, N.K. Kharchev, A.A. Chmyga, A.S. Kozachek, I. Pastor, J.L. de Pablos et al; Density profile reconstruction using HIBP in ECRH plasmas in the TJ-II stellarator. *JINST* 14 C09033 (2019)
- 5.40 E. Sánchez, T. Estrada, J.L. Velasco, I. Calvo, A. Cappa, A. Alonso, J.M. García-Regaña; Validation of global gyrokinetic simulations in stellarator configurations. *Nuclear Fusion* 59 076029 (2019)
- 5.41 J. Guasp and M. Liniers; Loss cone structure for ions in the TJ-II helical axis stellarator Part I: Properties without a radial electric field. *Nucl. Fusion* 40 397 (2000)
- 5.42 J. Guasp and M. Liniers; Loss cone structure for ions in the TJ-II helical axis stellarator Part II: Radial electric field effects. *Nucl. Fusion* 40 411 (2000)

Appendix 1

A1.1. HIBP has been an applied diagnostics in tokamaks, stellarators and reverse field pinch. Table A.1 presents the timeline of installation of heavy ion beam probe on plasma devices both presently working (in red) and non-operational (in blue).

As summarized in table A.1 the Heavy ion beam probe has been applied on 14 tokamaks (T), 4 stellarators (S), 2 bumpy toruses (BT), 2 plasma mirrors (M) devices and 1 reversed pinch (RP) in different countries around the world, such as USA, Japan, Russia, Canada, Portugal, Spain and Germany. Presently, this diagnostic is under operation (in red color) on 5 tokamaks, 3 stellarators, 1 mirror plasma device and 1 reversed pinch, ranging in beams energy from 25 keV of Xe⁺ beam on small tokamak ISTTOK, to 6 MeV Au⁺ beam on LHD stellarator. Two new HIBP projects to be realized in the near future are 2 MeV HIBP on W-VIIX stellarator in Greifswald, Germany and low energy, 10 keV, HIBP on the small HSX stellarator in Madison, USA.

Country/Year	1960-1970	1970-1980	1980-1990	1990-2000	2000-2010
USA	HIBP cathode arc plasma (R. Hickok F. Jobes)	ST (T) (200, Tl) EBT (BT) (30, Rb) TMX (M) (20, Na)	RENTOR (T) (30, Cs) ISX-B (T) (160, Cs) TEXT (T) (500, Cs)	TEXT-U (T) (2000, Cs, Tl) ATF (S) (160, Cs)	MST (RP) (200, Na)
Former USSR (Russia)			TM-4(T) (100, Cs)	T-10 (T) (250, Cs, Tl)	TUMAN-3M (T) (60, Na)
Japan			NBT (BT) (30, Rb) GAMMA-6, 10 (M) (30, Cs)	JIPPT-IIU (T) (500, Cs) CHS (S) (200, Cs)	JFT -2M (T) (500, Tl) LHD (S) (6000, Au)
Canada				TdV (T) (100, Tl)	
Portugal				ISTTOK (T) (25, Cs, Hg, Xe)	
Spain				TJ-I (T) (100, Cs)	TJ-II (S) (150, Cs)
Germany					WEGA (S) (70, Na)

Table A.1 presents the machines in which HIBP has been installed during past years. The machines in red are functioning till present and in blue are the one that are not operational anymore. The parenthesis with each device includes the beam energy (in KeV) and injected ion.

Appendix 2

A2.1. This section presents the equipotential (Figure A2.1) for ideal 90° CEA simulated in SIMION software. The equipotential lines for the ideal CEA is unperturbed due to absence of input and output plates. The dispersion graphs to determine coefficients for energy (C_E) and angles (C_θ) are 0.8 and 0.56, respectively, as derived from the slope in Figure A2.2.

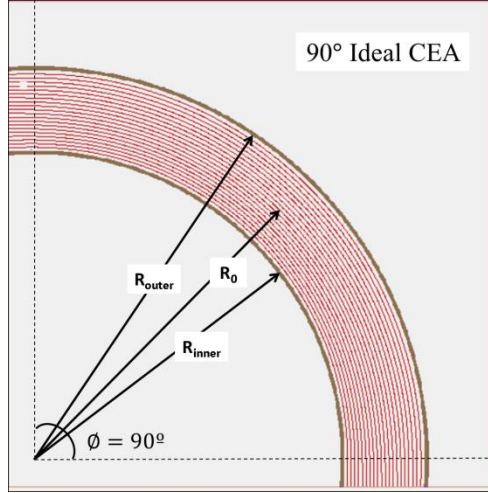


Figure A2.1 Equipotential field lines for ideal 90° CEA.

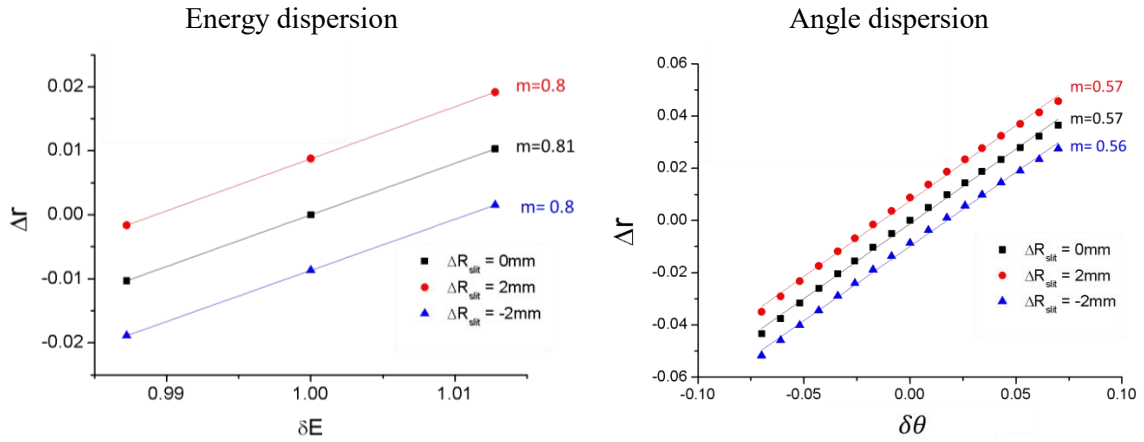


Figure A2.2 Energy (left) and angle (right) dispersion graphs for ideal 90°. The, respectively voltages on the inner and outer electrodes are $V_{inner}/V_{outer} = -2.7/2.7kV$.

A.2.2. This section presents the energy and angle dispersion coefficient for 1/2 size electron beam CEA using SIMION simulation. The voltages on the CEA components are mentioned in Table 2.9 as configuration B and D for normal and deceleration mode, respectively.

In Figure A2.3 is presented the energy dispersion coefficient for the electron for 1/2 size CEA in normal mode (a) and deceleration mode (b) modeled by three trajectories with 2 mm of up (red) –down (blue) relative shift from the standard input (black) at the CEA entrance (effective beam width $w_{b0} = 4$ mm) and varied energy of $E_0 = 1.7 \pm 0.1$ keV.

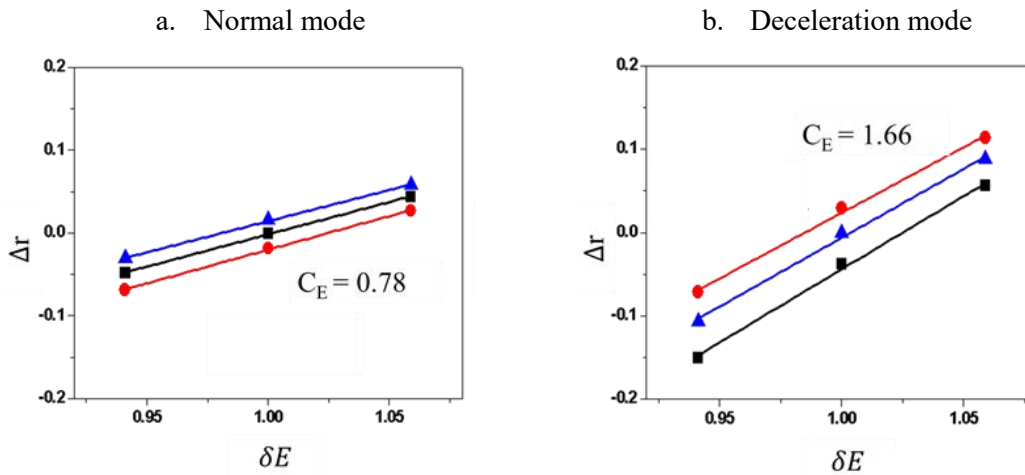


Figure A2.3 Energy dispersion for normal (left) and deceleration (right)

In Figure A2.4 is presented the angle dispersion coefficient for the electron for $\frac{1}{2}$ size CEA in normal mode (a) and deceleration mode (b) modeled by three trajectories with 2 mm of up (red) –down (blue) relative shift from the standard input (black) at the CEA entrance (effective beam width $w_{b0} = 4$ mm and $E_0 = 1.7$) and changing the entrance angle in the $\Delta\theta_{in} = \pm 2^\circ$ range.

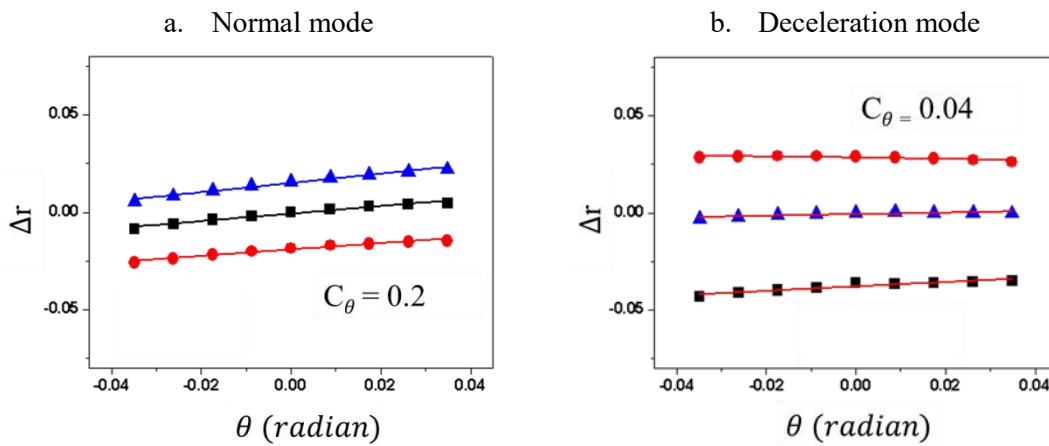


Figure A2.4 Angle dispersion for normal (left) and deceleration (right).

Appendix 3

SIMION Simulation for Combined EIM and full size CEA

A3.1. Geometric arrangement and beam trajectories

The ½ size prototype determines (due to its size) that only one, or in maximum two, channels (sample volumes) can be used. The final goal is to install a larger coverage of the plasma utilizing 4 channels. This appendix presents the simulations performed combining the EIM input module with the full size CEA in order to optimize the voltages for the required beam focus and trajectories.

Figure A3.1a and b depicts the beam trajectories in XZ and XY planes, respectively, for four beam channels. Figure A3.1c presents the beam footprint at the back of the CEA analyzer. The beam simulation parameters are presented in the figures and the applied voltages are given in Table A3.1. The real vacuum chamber shape (a SS 6-way cross chamber) is also included in the geometry. This vacuum chamber has the same shape but the double size of the chamber used for the electron beam experiments in the characterization of the ½ -CEA prototypes (described in chapter 2). It can be seen from Figure A3.1c that the periphery beams profiles, for the 1st (blue) and 4th (brown) channels, shows strong aberration and also its positions are shifted from the plane of alignment (coincident with the 2nd and 3rd channels). This is due to a change on the input angle to CEA (non-perpendicular) induced by the non-symmetric lensing effect at the edges of the Einzel lens (Figure A3.2a). In order to overcome this effect, the design of Einzel lens was modified as explained in next section.

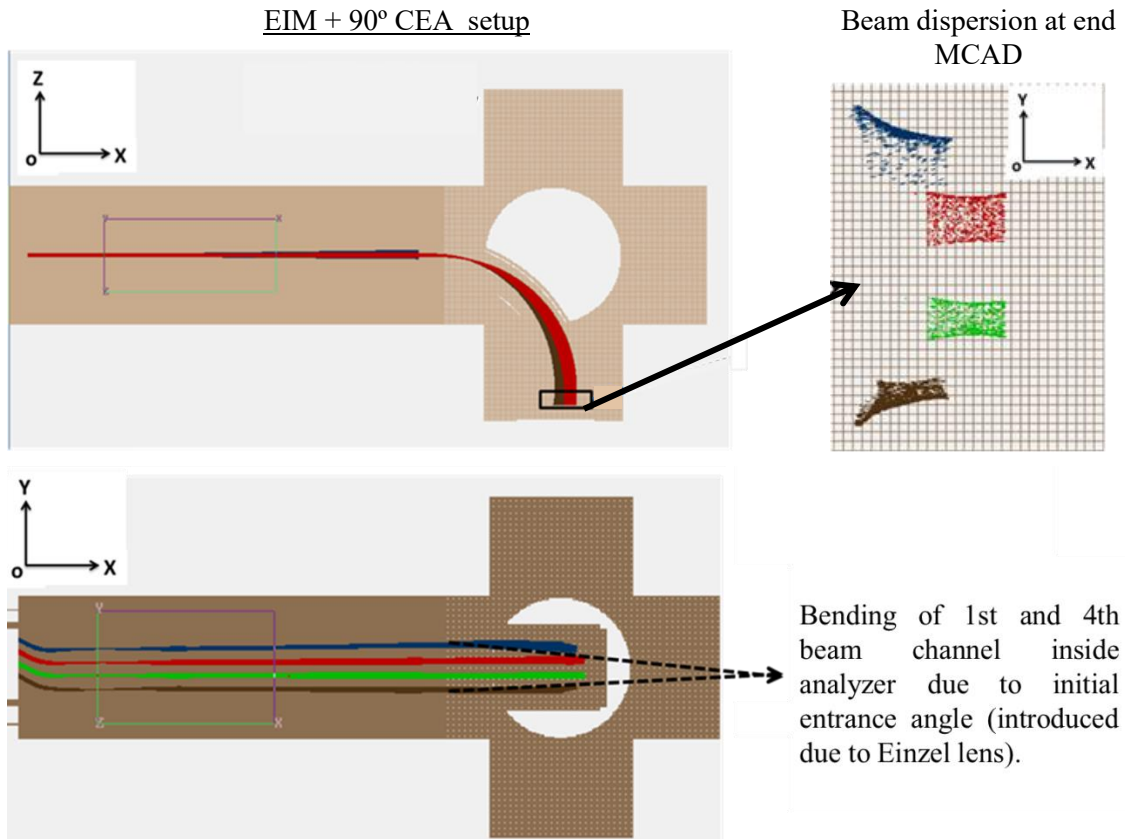


Figure A3.1 Presents the simulated CEA and EIM combined setup. The figure shows the beam from 4 input channels from EIM in X-Z and X-Y plane and also the beam dispersion shape for the end MCAD.

A3.2. Modified Einzel lens

Figure A3.2 shows the beam trajectories in XY plane with the non-modified Einzel lens. It can be observed that the periphery beams (1st and 4th channel) are slightly inclined in Y direction ($\pm 0.5^\circ$ relative to the longitudinal axis) due to the non-symmetric lensing effect in the einzel lens for periphery channels. This beam deviation is propagated and is magnified by the strong analyzing field of the CEA. The Einzel lens has been modified by adding 2 dummy channels at both ends in order to reproduce the same edge conditions as in the core channels. The modified topology of the field lines presents the same up-down symmetry for all four channels. Figure A3.2b shows the 3D view of the modified Einzel lens with the additional channel on both ends. These 2 additional channels are refer as ‘dummy channels’, as their purpose is only to correct the lensing edge asymmetry for the channels 1st and 4th (as seen in Figure A3.3a). Figure A3.3a shows the trajectories with modified Einzel lens producing four parallel beams. Figure A3.3b presents the four beam footprint in the XY plane and as can be seen the optical aberration affecting the beam profile has been corrected. The offsets in the x direction can all be corrected individually during experimental alignment.

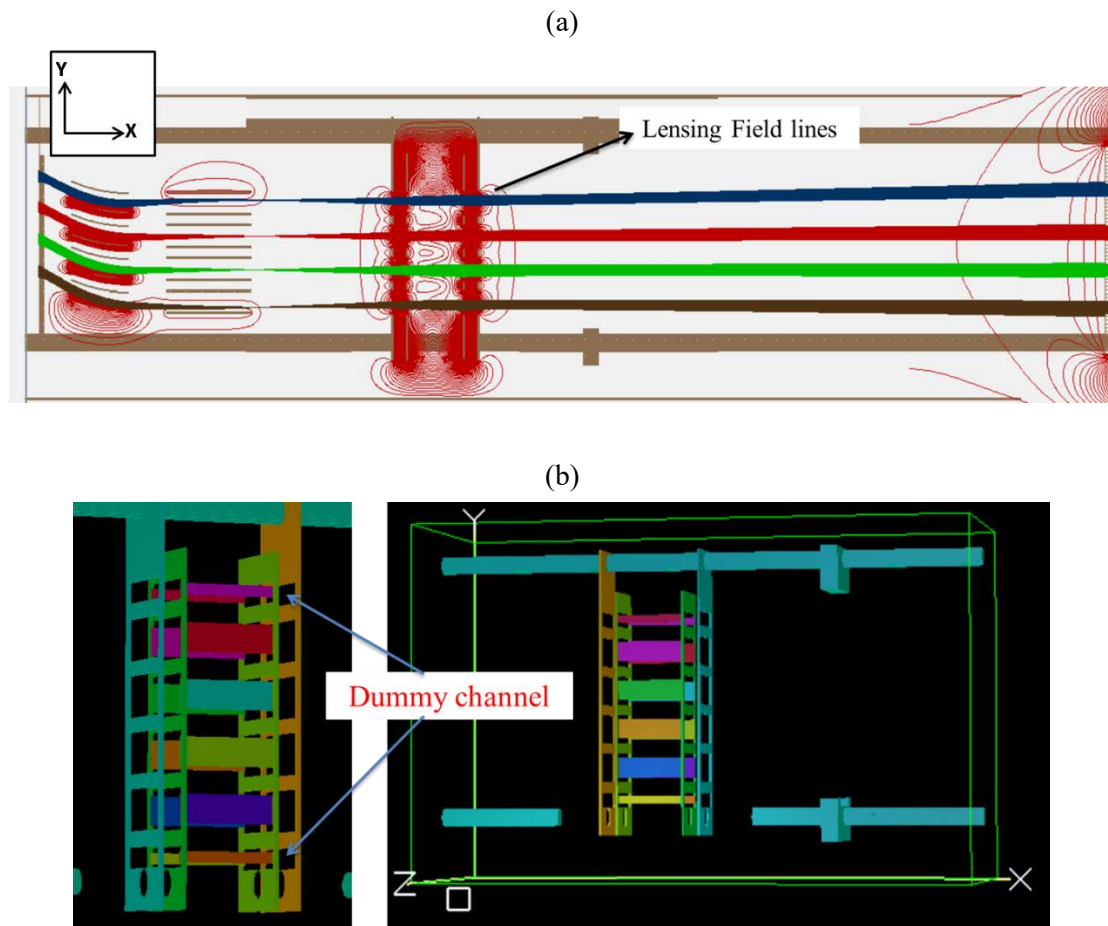


Figure A3.2 Einzel lens modification; (a) beam trajectory from 4 beam channels, (b) modified Einzel lens simulated in SIMION the two pictures side by side shows modified Einzel lens from two view angle with dummy channels on top and bottom;

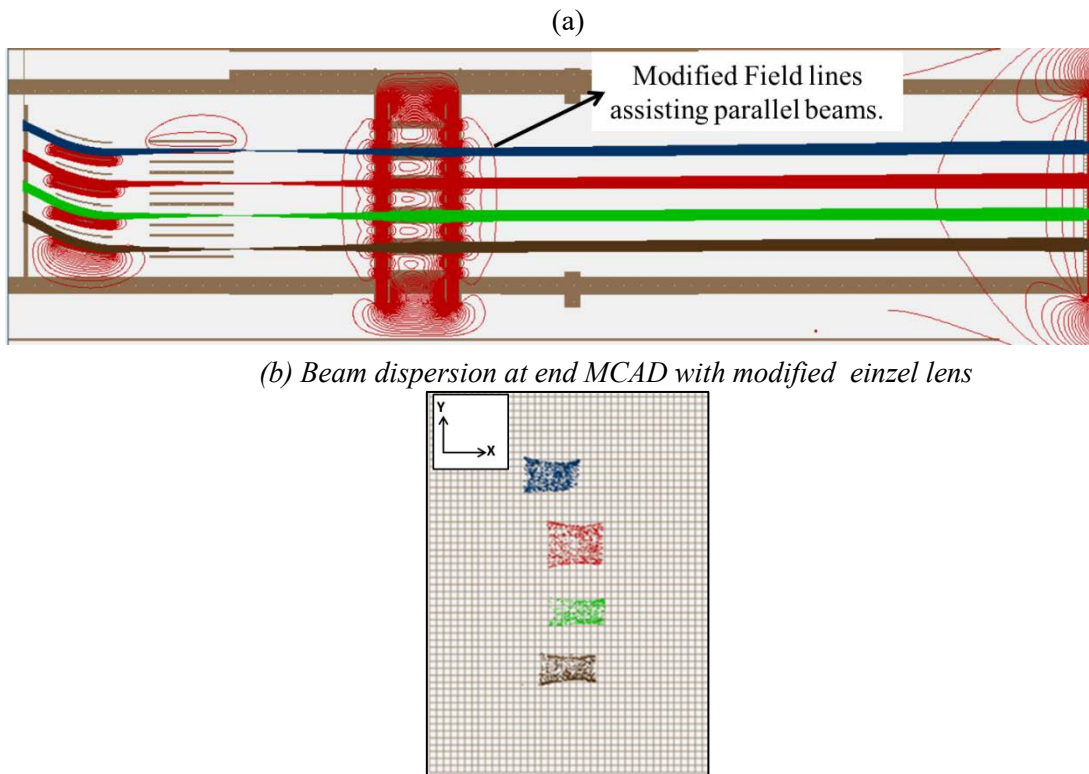


Figure A3.3 Beam trajectory with modified Einzel lens-(a) beam trajectory from 4 beam channels with modified Einzel lens, equipotential at the channel 1st and 4th are less curved; (b) Beam (20keV) dispersion in XY at back MCAD with modified Einzel lens for four channels.

A3.3. Optimization and characteristics of full beam trajectories with modified Einzel lens design

Figure A3.4 shows the four beam trajectories for optimized voltages on the EIM and CEA electrodes. The main observation is that all four beams travel parallel to the longitudinal axis up to the back MCAD. Figure A3.5 shows the beam footprint and position at the end MCAD of energy analyzer for 4 channels with $E_b = 20\text{keV}$. In Figure A3.5 is also depicted the horizontal shift of each of the four beams as a function of their energy for E_0 : 19.7keV, 20keV, 20.3keV. (Simulating plasma +/- 300V plasma potential changes)

The vertical shift (ΔY) observed for each beam channel, with separation in energy, is due to the initial 30° cylindrical plates in the EIM which deflect the beam in the XY direction. This deflection is beam energy dependent. The deflection does not change the beam energy, as the input and output EIM potential is zero. The beam enters the CEA with an initial vertical angle which is recorded in the final vertical position at the back MCAD. However, the energy analyzing field of the CEA induces an energy dependent deflection in the horizontal direction and his not affected by the slight input vertical displacement of the beam.

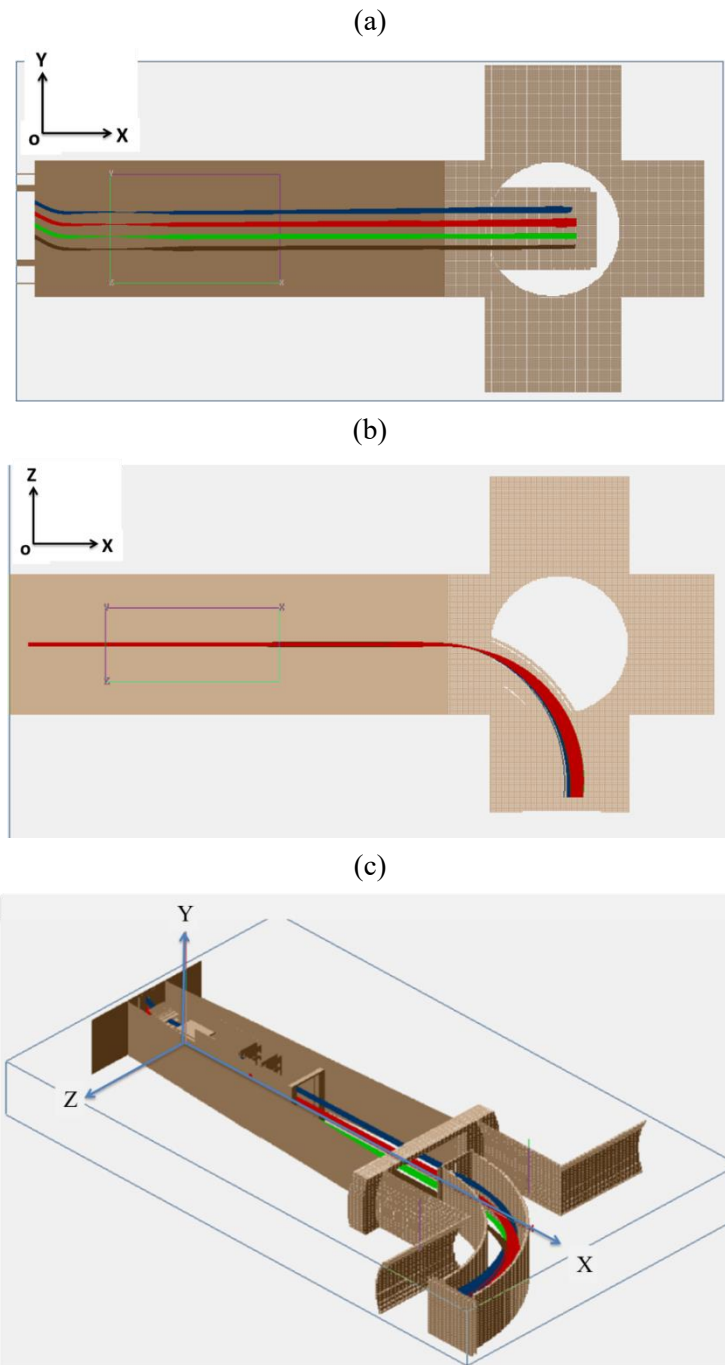


Figure A3.4 Secondary beam trajectory for the four secondary beam channels in the combined setup of EIM and einzel lens with modified einzel lens for XY (a), XZ(b) plane and 3D (c).

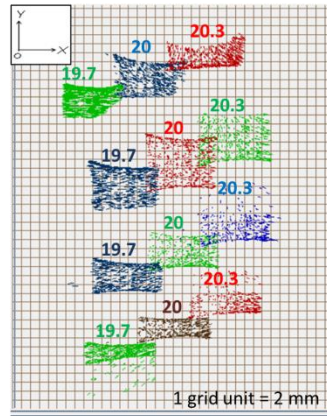


Figure A3.5 Secondary beam distribution at the end MCAD of CEA for the four beam channels (1^{st} , 3^{rd} and 4^{th} have energy of 20keV). The second beam channel has 3 beam input with $E_b = 19.7, 20$ and 20.3 keV (as mentioned in the figure) (1 grid unit = 2mm).

Table A3.1 presents the optimized biased voltages obtain for EIM and CEA internal electrodes for the 4 beam channels for the Figure 3.3, Figure 3.7, Figure A3.3 and Figure A3.4.

Electrode	Biasing Voltage (kV)	
EIM		
a. Cylindrical plates (4pairs)		
Channel 1(U/L)	-1.35 / 1.35	
Channel 2 (U/L)	-1.31 / 1.35	
Channel 3 (U/L)	- 1.335 / 1.335	
Channel 4 (U/L)	-1.24 / 1.24	
b. Parallel plate Arrangement (4pairs)		
Channel 1 (U/L)	0.35 / 0	
Channel 2 (U/L)	0.55 / 0	
Channel 3 (U/L)	0.56 / 0	
Channel 4 (U/L)	0 / 0.22	
c. Einzel like lens		
1 / 4	Grounded	
2 / 3	3.5 / 4.4	
Strip electrode pair (equal voltage)		
Channel 1	3.6	
Channel 2	3.7	
Channel 3	3.68	
Channel 4	3.61	
Dummy	top pair	3.6
	Bottom pair	3.6
90° CEA		
V_{inner} / V_{outer}	7.6 / 8.4	
V_{GR} / V_{DG}	8/8	

Table A3.1 presents the optimized biasing voltage as obtained during the optimization of combined setup of EIM with 90° CEA in SIMION simulations for the four beam channels. Where, U/L refers to upper/ lower electrode plate of the cylindrical or parallel plate; Electrode 1,2,3 and 4 of Einzel lens are indicate d in figure 3.5 b; V_{inner} / V_{outer} is the voltage on inner and outer curved plate of CEA; V_{GR} / V_{DG} is the voltage on guard rings and deceleration grid of CEA.

Appendix 4

A4.1. Detectors arrangement for EIM+CEA setup

The Multichannel detectors installed in the upgraded diagnostic setup are shown in Figure A4.1. Each cell number of the detector corresponds to a channel number in the data acquisition board. Figure A4.2 (left) presents the back MCAD originally consisting of 12 cells and later merged to SPD (right) by short circuiting the individual cells in order to increase the signal to noise ratio (S/N).

Detector	Detector & corresponding Ch. No	No. of cells/channel																		
Primary MCAD	<table border="1" style="margin: auto; border-collapse: collapse;"> <tr><td style="width: 20px; height: 20px;">2</td><td rowspan="2" style="width: 20px; height: 20px;">4</td></tr> <tr><td style="width: 20px; height: 20px;">3</td></tr> </table>	2	4	3	3															
2	4																			
3																				
Front secondary MCAD	<table border="1" style="margin: auto; border-collapse: collapse;"> <tr><td style="width: 20px; height: 20px;"></td><td style="width: 20px; height: 20px;">9</td><td style="width: 20px; height: 20px;"></td></tr> <tr><td style="width: 20px; height: 20px;">10</td><td style="width: 20px; height: 20px;"></td><td style="width: 20px; height: 20px;">11</td></tr> <tr><td style="width: 20px; height: 20px;"></td><td style="width: 20px; height: 20px;">12</td><td style="width: 20px; height: 20px;"></td></tr> <tr><td style="width: 20px; height: 20px;"></td><td style="width: 20px; height: 20px;">13</td><td style="width: 20px; height: 20px;"></td></tr> <tr><td style="width: 20px; height: 20px;"></td><td style="width: 20px; height: 20px;">14</td><td style="width: 20px; height: 20px;"></td></tr> <tr><td style="width: 20px; height: 20px;"></td><td style="width: 20px; height: 20px;"></td><td style="width: 20px; height: 20px;"></td></tr> </table>		9		10		11		12			13			14					6
	9																			
10		11																		
	12																			
	13																			
	14																			
Input secondary CEA	<table border="1" style="margin: auto; border-collapse: collapse;"> <tr><td style="width: 20px; height: 20px;">16</td><td style="width: 20px; height: 20px;">7</td></tr> <tr><td style="width: 20px; height: 20px;">15</td><td style="width: 20px; height: 20px;">8</td></tr> </table>	16	7	15	8	4														
16	7																			
15	8																			
Back CEA secondary MCAD	<table border="1" style="margin: auto; border-collapse: collapse;"> <tr><td style="width: 20px; height: 20px;">28</td><td style="width: 20px; height: 20px;">27</td><td style="width: 20px; height: 20px;">26</td><td style="width: 20px; height: 20px;">25</td></tr> <tr><td style="width: 20px; height: 20px;">24</td><td style="width: 20px; height: 20px;">23</td><td style="width: 20px; height: 20px;">22</td><td style="width: 20px; height: 20px;">21</td></tr> <tr><td style="width: 20px; height: 20px;">20</td><td style="width: 20px; height: 20px;">19</td><td style="width: 20px; height: 20px;">18</td><td style="width: 20px; height: 20px;">17</td></tr> </table>	28	27	26	25	24	23	22	21	20	19	18	17	12						
28	27	26	25																	
24	23	22	21																	
20	19	18	17																	

Figure A4.1

<p>End MCAD (designed initially)</p> <table border="1" style="margin: auto; border-collapse: collapse;"> <tr><td style="width: 20px; height: 20px;">28</td><td style="width: 20px; height: 20px;">27</td><td style="width: 20px; height: 20px;">26</td><td style="width: 20px; height: 20px;">25</td></tr> <tr><td style="width: 20px; height: 20px;">24</td><td style="width: 20px; height: 20px;">23</td><td style="width: 20px; height: 20px;">22</td><td style="width: 20px; height: 20px;">21</td></tr> <tr><td style="width: 20px; height: 20px;">20</td><td style="width: 20px; height: 20px;">19</td><td style="width: 20px; height: 20px;">18</td><td style="width: 20px; height: 20px;">17</td></tr> </table>	28	27	26	25	24	23	22	21	20	19	18	17	<p>Split plate detector (SPD) (modified for better S/N)</p> <table style="margin: auto;"> <tr> <td style="width: 50px; height: 50px; background-color: black; color: white; font-size: 2em; vertical-align: middle;">13</td> <td style="width: 50px; height: 50px; background-color: red; color: white; font-size: 2em; vertical-align: middle;">14</td> </tr> </table>	13	14
28	27	26	25												
24	23	22	21												
20	19	18	17												
13	14														

Figure A4.2 Numeric indicated on each cell corresponds to channel number on the data acquisition.

A4.2. Feedthroughs for data output

Figure 4A.3 shows the picture of one of the output flanges of the 6-way SS cross. This flange is dedicated for obtaining current signals from detectors (in vacuum) and transmits it to the amplifiers (located outside vacuum). The figure shows pinout (#1-13) for both the D25s at the output, where each pin corresponds to specific cell number on the detector. The D25 sends the current signals from the detectors to data acquisition board (sampling rate 2MHz). Thus, each cell on the detector corresponds to specific channel number in on acquisition system.

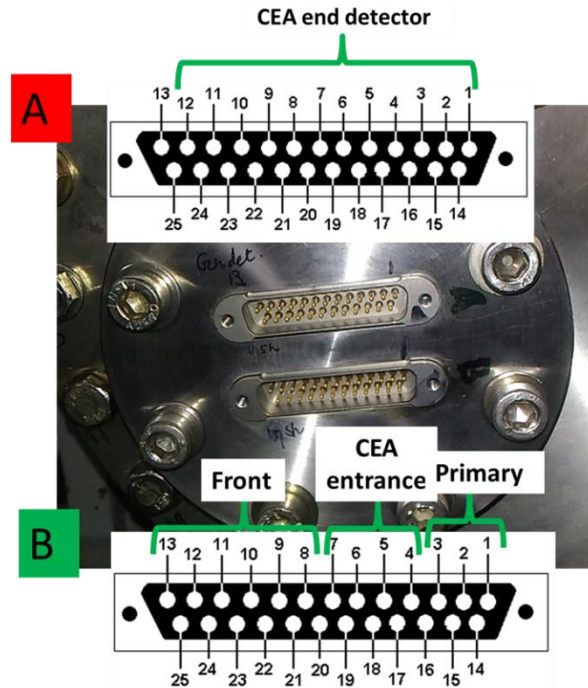


Figure 4A.3

A4.3. Power feedthrough

The Power input to the system is divided into two categories: Low voltage and High voltage feedthroughs.

Low voltage feedthrough- For the electrodes requiring low voltage (EIM electrodes < 2kV), the voltage was fed through BNC connector output. The electrodes of EIMs and the voltage applied to them are presented in the Table 4A.1.

EIM plate	Voltage (V)
Lower Cylindrical plate	-1650
Upper cylindrical plate	0
Upper parallel plate	450
Lower parallel plate	0
Z plate	-150

Table A4.1

High Voltage feedthrough- The high Voltage is fed to the electrodes of Einzel lens and the CEA electrodes. The flange also contains two other HV feedthroughs and also supports the feedthroughs to collect data (shown in Figure A4.4). Figure 4A.4 presents the out pins for the high voltage feedthrough with each pin number corresponding to the electrode shown in the table on the right.

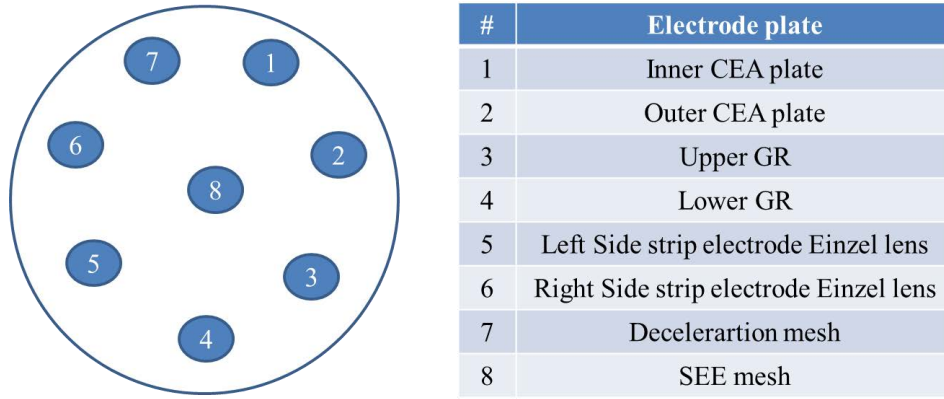


Figure A4.4 HV connections to the diagnostic setup.

A4.4. Measurement of externally applied fluctuations

To estimate the ability of the diagnostic to measure fluctuations, an external modulating voltage was applied to the inner electrode of the CEA. The sinusoidal modulation of 2.5 kHz, 3 kHz, 6kHz and 25 kHz with amplitudes of ± 10 V and ± 20 V has been tested. For an optimized condition of beam balanced at SPD ($\Delta i = i_{14} - i_{13} = 0$), upon application of external modulation on inner electrode, causes modulation of the beam position at the SPD with the same frequency

Figure A4.5 shows the PSD of the difference in current (Δi) in the split plate detector at the end for 6 plasma cycles for ISTTOK AC discharge (left). The amplitude of the external modulation for this figure was 20V with frequency 2.5 kHz. There is clear fluctuation in the PSD current at frequency 2.5 kHz. The signal increases as the amplitude as the plasma current increases imposing a signal to ratio dependency with time. The clear peak at 2.5 kHz (as applied by external source) can be seen on the figure on the right.

These experiments exhibit sensitivity of the analyzer for $\Delta V_{\text{inner}} = \pm 20$ V, Using the conversion coefficient determined by eq. 4.3, corresponds to beam energy fluctuations of $\Delta E_{\text{sin}} = \pm 51$ V ($(\Delta E_{\text{sin}})_{\text{std}} = \pm 36$ V), thus determining an energy resolution of $\Delta E/E \sim 2 \times 10^{-3}$ to the plasma fluctuation measurements.

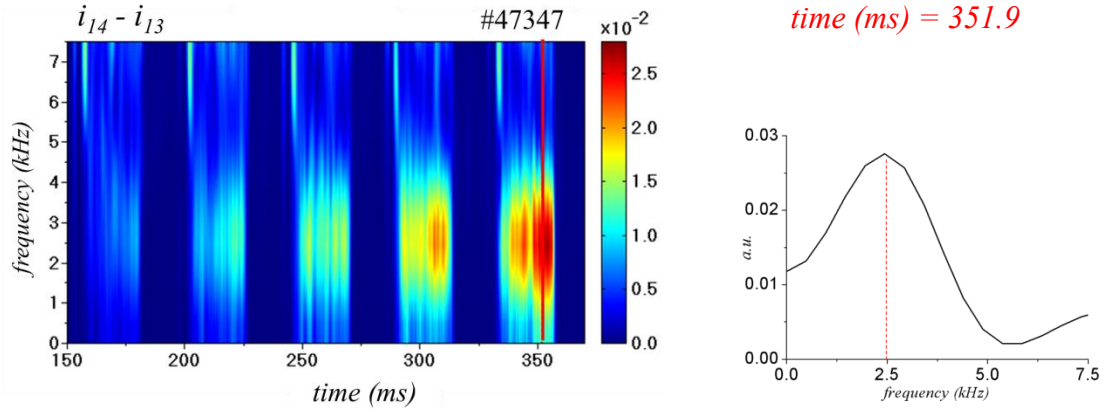


Figure A4.5 Fluctuation measurements for the difference current ($i_{14}-i_{13}$) when applied external modulation to inner electrode.

Results from simulation

The experiment mentioned above was verified with SIMION simulations. Several Gaussian beam, 8mm (dispersion plane) and 2mm (vertical plane), with 500 particles were launched and the beam position was measured for each fly. For each Gaussian beam V_{inner} value was modulated according to sinusoid function of amplitude 20V and frequency 2500Hz;

$$V_{inner} = 20 \text{ Sin } (2\pi ft)$$

Where f is the frequency of modulation = 2500 Hz. The voltages on other CEA electrode are mentioned in the Figure A4.6 (right).

32 Gaussian beams (each corresponding to a V_{inner} value) were launched within one time period of sinusoidal wave (0.0004s). Figure A4.6 uses SIMION simulations to obtain the shift of the beam position (for each V_{inner}) from the central line at the SPD - Δx versus time.

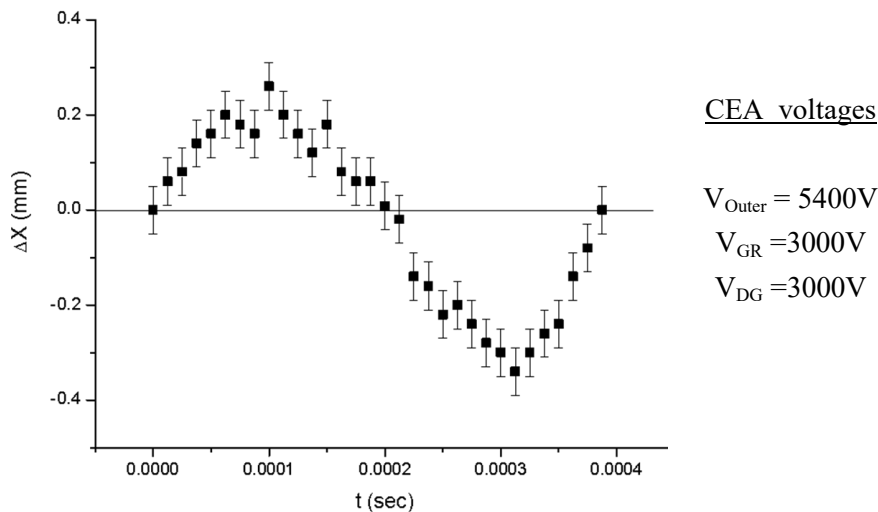


Figure A4.6 Presents the shift of the Gaussian beam at the SPD (Δx) with respect to time. Each point on the graph represents the beam relative position (in mm) from the center for specific V_{inner} . Where, the voltages on the other CEA electrodes is indicated on the right (V_{outer} , V_{GR} , V_{DG} are the voltages in the outer electrode, guard rings and deceleration grid on the CEA). The error bars in Δx on the graph on the left are attributed due to the random generation of the particles at input in the Gaussian beams for each fly.

Such cycles were repeated for $t = 20\text{ms}$ (~ 1 plasma cycle at ISTTOK) and Power spectra density (PSD) for Δx ($\sim i_{14} - i_{13}$) with respect to time as shown in Figure A4.7. A clear frequency fluctuation can be seen around 2.5 kHz. On the left is plotted amplitude of PSD (for $t = 10\text{ms}$) versus frequency. A Gaussian like peak with highest amplitude at 2.5 kHz and FWHM of 2.5 kHz was observed also.

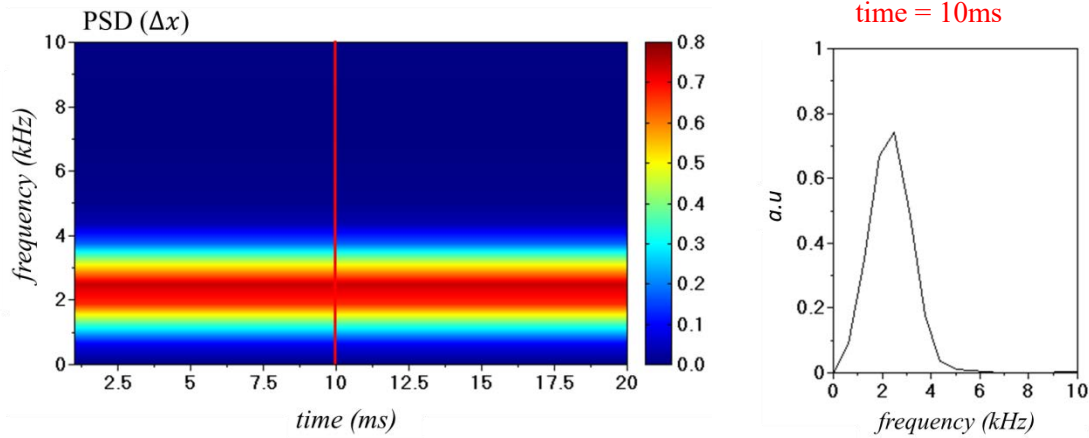


Figure A4.7 Power spectra density for Δx ($\sim i_{14} - i_{13}$) with respect to time (right) and amplitude of these fluctuations w.r.t frequency (0-10 kHz) (left) for time =10 ms (red vertical line in the spectra).

